Acta Universitatis Agriculturae Sueciae

Doctoral Thesis No. 2025:55
Faculty of Forest Sciences

Debondable wood adhesives based on Diels-Alder and Schiff base reactions

Valentin Silveira

Debondable wood adhesives based on Diels-Alder and Schiff base reactions

Valentin Silveira
Faculty of Forest Sciences
Department of Forest Biomaterials and Technology
Uppsala

SLU
SWEDISH UNIVERSITY
OF AGRICULTURAL
SCIENCES

DOCTORAL THESIS
Uppsala 2025

Acta Universitatis Agriculturae Sueciae
2025:55

ISSN 1652-6880
ISBN (print version) 978-91-8124-039-9
ISBN (electronic version) 978-91-8124-085-6
https://doi.org/10.54612/a.115vp2i3dk

Swedish University of Agricultural Sciences, Department of Forest Biomaterials and Technology , Uppsala, Sweden

Print: SLU Grafisk service, Uppsala 2025

Debondable wood adhesives based on Diels-Alder and Schiff base reactions

Abstract

The wood industry relies heavily on thermosetting resins such as urea-formaldehyde, polyurethanes, and epoxies for the manufacturing of engineered wood products. While these adhesives offer strong mechanical performance and moisture resistance, their environmental and health impact raise concerns. Additionally, the irreversible nature of these cross-linked networks prevents efficient material separation and recovery at the product's end-of-life.

Bio-based debondable adhesives, capable of undergoing controlled debonding under specific stimuli, present a promising solution to enable disassembly and recycling of multilayer wood products, improving their sustainability.

In the initial phase of this research, efforts were directed towards modifying potato starch (St) with maleimide moieties (6-maleimidohexanoic acid, 6-MHA). Both suspension and solution methods were explored. Maleimide grafted St (St-6MHA) synthesized via the solution method was selected for further study due to the higher degree of the starch's hydroxyl groups substitution by 6-MHA and the lack of St granule structure preservation of the suspension method .

Kraft lignin (KL) was functionalized with furan groups to enable the formation of a Diels–Alder (DA) network with St-6MHA. Experimental results confirmed the successful formation of a reversible DA network, which formed at 65 °C over 48 h and dissociated at 135 °C after 3 h. Blends of these materials were used to bond furfurylated beech veneer, achieving an average tensile strength of 5.00 ± 0.5 MPa. Controlled debonding was observed at 135 °C after 4 h, demonstrating the system's potential for recyclability of wood products.

In a final step, a Schiff base network was developed using dialdehyde starch (DAS), hexamethylene diamine (HMDA), and amino-functionalized carbon dots. The incorporation of carbon dots showed promise in accelerating the curing process and enhancing the mechanical strength of the DAS:HMDA adhesive system. A tensile strength of 3.96 ± 0.18 MPa was achieved after just 300 sec of pressing at 160 °C, highlighting its potential as a fast-curing, bio-based adhesive.

Keywords: starch, Kraft lignin, click-chemistry, covalent adaptive networks, on-demand debonding, carbon dots

Avbindningsbara trälim baserade på Diels-Alder och Schiff-bas reaktioner

Abstract

Träindustrin är starkt beroende av värmehärdande hartser som urea-formaldehyd, polyuretan och epoxiharts för tillverkning av limmade (konstruerade) träprodukter. Även om dessa lim säkerställer stark mekanisk prestanda och är resistenta mot fukt, väcker deras miljö- och hälsopåverkan oro. Dessutom förhindrar den irreversibla limningen i dessa tvärbundna nätverk effektiv materialseparation och återvinning vid produktens slutliga livscykel.

Biobaserade avbindningsbara lim, som kan genomgå kontrollerad avbindning under specifika stimuli, presenterar en lovande lösning för att möjliggöra återvinning av limmade träprodukter, vilket avsevärt förbättrar hållbarheten.

I den inledande fasen av denna forskning riktades ansträngningar mot att modifiera stärkelse med maleimidenheter (6-maleimidohexanoic acid, 6-MHA) genom att undersöka suspensions- och lösningsmetoder. Maleimid-graftad stärkelse (St-6MHA), syntetiserad genom den lösningsmetoden, valdes för vidare studier på grund av en högre substitutionsgrad av stärkelsens hydroxylgrupp med 6-MHA.

Kraftlignin (KL) funktionaliserades med furangrupper för att möjliggöra bildandet av ett Diels-Alder (DA)-nätverk med St-6MHA. Experimentella resultat bekräftade den lyckade bildningen av ett reversibelt DA-nätverk som bildades vid 65 °C under 48 timmar och blev avbunden vid 135 °C efter 3 timmar. Blandningar av dessa material användes för att binda furfurylerad träfanér, vilket uppnådde en genomsnittlig draghållfasthet på 5.00 ± 0.5 MPa. Kontrollerad avbindning observerades vid 135 °C efter 4 timmar, vilket demonstrerade systemets potential för återvinningsbarhet.

Vidare utvecklades ett Schiff-basnätverk med dialdehydstärkelse (DAS), hexametylendiamin (HMDA) och aminofunktionaliserade carbon dots. Införandet av carbon dots visade lovande resultat när det gällde att accelerera härdningsprocessen och förbättra den mekaniska hållfastheten hos DAS:HMDA-limsystemet. En skjuvhållfasthet på 3.96 ± 0.18 MPa uppnåddes efter bara 300 sekunder pressning vid 160 °C, vilket bekräftar DAS:HMDA-limsystemet potential som ett snabbhärdande, biobaserat lim.

Keywords: starch, Kraft lignin, click-chemistry, covalent adaptive networks, on-demand debonding, carbon dots

Adhésifs pour le bois détachables utilisant les réactions de Diels-Alder et de base de Schiff

Abstract

L'industrie du bois fait largement appel à des résines thermodurcissables comme l'urée-formaldéhyde, le polyuréthane ou l'époxy pour la fabrication de matériaux en bois d'ingénierie. Bien que ces adhésifs offrent d'excellentes performances mécaniques et une bonne résistance à l'humidité, leurs impacts environnementaux et sanitaires suscitent des préoccupations croissantes. Leur caractère irréversible empêche également le démontage et le recyclage efficaces en fin de vie. Les adhésifs biosourcés détachables, capables de se désolidariser de façon contrôlée sous l'effet de stimuli spécifiques, apparaissent comme une solution prometteuse pour favoriser le recyclage des produits bois multicouches et améliorer leur durabilité.

Dans cette étude, l'amidon (St) a d'abord été modifié par greffage de groupements maléimides (acide 6-maleimidohexanoique, 6-MHA), selon des procédés en suspension et en solution. Le produit issu de la voie en solution, présentant un meilleur degré de substitution, a été retenu pour la suite des travaux.

La lignine (KL) a ensuite été fonctionnalisée avec des groupements furaniques afin de former un réseau réversible de type Diels–Alder avec l'amidon modifié (St-6MHA). Les expériences ont confirmé la formation d'un réseau réticulé à 65 °C en 48 heures, réversible à 135 °C en 3 heures. Des placages de hêtre furfurylé ont été collés avec ces mélanges, atteignant une résistance moyenne à la traction de 5.00 ± 0.5 MPa. Un décollement contrôlé a été observé à 135 °C, démontrant la recyclabilité du système.

Enfin, un réseau de base de Schiff a été élaboré à partir d'amidon dialdéhyde (DAS), d'hexaméthylène diamine (HMDA) et de carbon dots amino-fonctionnalisés. L'ajout de ces carbon dots a permis d'accélérer la réticulation et d'améliorer les propriétés mécaniques de l'adhésif. Une résistance de 3.96 ± 0.18 MPa a été obtenue après seulement 300 sec de pressage à 160 °C, mettant en évidence le potentiel de cet adhésif biosourcé à durcissement rapide.

Keywords: starch, Kraft lignin, click-chemistry, covalent adaptive networks, on-demand debonding, carbon dots

Dedication

To Zijia Lu.

Contents

List of publications

This thesis is based on the work contained in the following papers, referred to by Roman numerals in the text:

I. Silveira, V., Jebrane, M., Letoffe, A. and Adamopoulos, S. (2025). Maleimide grafting onto polysaccharides via mild condition esterification and its impact on their structure. Carbohydrate Research, 550, p. 109401. https://doi.org/10.1016/j.carres.2025.109401

II. Silveira, V., Papadakis, R. and Adamopoulos, S. (2025). One-Pot Synthesis of Thermally Reversible Materials Using Maleimide-Polysaccharide and Furan-Lignin Derivatives. RSC advances, 15, p. 28255-28268. https://doi.org/10.1039/D5RA02344K

III. Silveira, V., Pettersson, T., Van Blokland, J., Papadakis, R. and Adamopoulos, S. A starch/lignin network using Diels-Alder reaction for thermally debondable adhesives. (manuscript)

IV. Silveira, V., Papadakis, R. and Adamopoulos, S. (2025). Towards starch-based adhesives involving carbon dots as versatile crosslinkers. The Journal of Adhesion, p. 1-27. https://doi.org/10.1080/00218464.2025.2464051

All published papers are published open access.

The contribution of Valentin Silveira to the papers included in this thesis was as follows:

I. **Silveira**, Jebrane and Adamopoulos designed the concept and structure of the experiments. Preparation and purification of vinyl ester was performed by **Silveira** with Jebrane's advices. FTIR and NMR tests were conducted and results were reported by **Silveira**. Esterification of MCC and St were conducted by **Silveira**. FTIR, NMR, ESEM analysis were conducted and results were reported by **Silveira**. XRD tests were conducted by Gulaim Seisenbaeva at the department of Molecular Sciences, SLU. XRD results were reported by **Silveira**. The first draft of the manuscript was written by **Silveira**, and reviewed by Adamopoulos, Letoffe and Jebrane. Submitted by **Silveira**.

II. **Silveira**, Papadakis and Adamopoulos designed the concept and structure of the experiments. Preparation of St-6MHA was performed by **Silveira** with Papadakis's advices. ESEM, FTIR, NMR, 2D NMR and quantitative NMR tests were conducted and results were reported by **Silveira**. Preparation of KL-FU was conducted by **Silveira**. ESEM, FTIR, NMR and quantitative NMR tests were conducted and results were reported by **Silveira**. Diels-Alder reaction between St-6MHA and KL-FU was conducted by **Silveira**. FTIR, NMR, DSC, TGA and Rheology tests were conducted and results were reported by **Silveira**. The first draft of the manuscript was written by **Silveira**, and reviewed by Adamopoulos and Papadakis. Submitted by **Silveira**.

III. **Silveira**, Pettersson, Van Blokland, Papadakis, and Adamopoulos designed the concept and structure of the experiments. Impregnation of beech and spruce with furfuryl alcohol was conducted and results were reported by **Silveira**. ABES tests were conducted and results were reported by **Silveira**. Lap shear tests were conducted by **Silveira** with Van Blokland's advices and results were reported by **Silveira**. Wood penetration study using microtome and microscopy techniques were conducted and results were reported by **Silveira**. Colloidal probe preparation, sample preparation and AFM tests were conducted and results

were reported by **Silveira**. The first draft of the manuscript was written by **Silveira**, and reviewed by Adamopoulos, Van Blokland, Pettersson and Papadakis. Submitted by **Silveira**.

IV. **Silveira**, Papadakis and Adamopoulos designed the concept and structure of the experiments. Preparation of carbon dots was performed by Papadakis. XPS and UV spectroscopy tests were conducted and reported by Papadakis. ESEM, FTIR, TGA and DSC tests were conducted and results were reported by **Silveira**. Preparation of KL-FU was conducted by **Silveira**. Dialdehyde starch preparation was conducted by Papadakis and **Silveira**. FTIR, DSC and TGA tests were conducted and results were reported by **Silveira**. Preparation of DAS, CD with HMDA blends was conducted by **Silveira**. ABES and reversibility tests were conducted and results were reported by **Silveira**. The first draft of the manuscript was written by **Silveira** and Papadakis, and reviewed by Papadakis and Adamopoulos. Submitted by Papadakis and **Silveira**.

Other scientific contributions

Publications not included in this thesis:

I. Kretschmer, M., Ceña-Diez, R., Butnarasu, C., Silveira, V., Dobryden, I., Visentin, S., Berglund, P., Sönnerborg, A., Lieleg, O., Crouzier, T. and Yan, H. (2022). Synthetic Mucin Gels with Self-Healing Properties Augment Lubricity and Inhibit HIV-1 and HSV-2 Transmission. Advanced Science, p2203898. https://doi.org/10.1002/advs.202203898

II. Miranda-Martínez, A., Yan, H., Silveira, V., Serrano-Olmedo, J. and Crouzier, T. (2022). Portable Quartz Crystal Resonator Sensor for Characterising the Gelation Kinetics and Viscoelastic Properties of Hydrogels. Gels, p718. https://doi.org/10.3390/gels8110718

III. Letoffe, A., Hosseinpourpia, R., Silveira, V. and Adamopoulos, S. (2024). Effect of Fenton reaction parameters on the structure and properties of oxidized wheat starch. Carbohydrate Research, p. 109190. https://doi.org/10.1016/j.carres.2024.109190

IV. Silveira, V. and Papadakis, R. (2025). A highly chromotropic phenacylated dissymmetric bis-viologen and its base-sensing properties. Journal of Molecular Liquids, p127401. https://doi.org/10.1016/j.molliq.2025.127401

Conference:
1st International Conference on Bio-joining, Porto, Portugal, 5-6 December 2024. (Presentation)

Practical teaching on:
DSC, TGA, ESEM, ABES, FTIR, and Microtome.

Abbreviations

6-MHA	6-maleimidohexanoic acid
ABES	Automated bonding evaluation system
AFM	Atomic force microscopy
ASTM	American Society for Testing and Materials
ATR	Attenuated total reflectance
CAN	Covalent adaptive network
CD	Carbon dots
$CDCl_3$	Chloroform
CO	Carbon monoxide
CO_2	Carbon dioxide
CP-MAS NMR	Cross Polarization/Magic Angle Spinning Nuclear Magnetic Resonance
$Cr(acac)_3$	Chromium (III) acetyl acetonate
DAS	Dialdehyde potato starch
DGEBA	Diglycidyl ether bisphenol A
DMAc	Dimethylacetamide
DMF	Dimethylformamide
DMSO	Dimethyl sulfoxide
DMSO-d_6	Deuterated dimethyl sulfoxide
DSC	Differential scanning calorimetry
EN	European norm
ESEM	Environmental scanning electron microscope
EtOH	Ethanol
FA	Furfuryl alcohol

FGE	Furfuryl glycidyl ether
FTIR	Fourier transform infrared spectroscopy
HCl	Hydrochloric acid
HMBC	Heteronuclear Multiple Bond Correlation
HMDA	Hexamethylenediamine
HS157	Chloro(1,5-cyclooctadiene) iridium-(I) dimer
HSQC	Heteronuclear Single Quantum Coherence
KL	Kraft lignin
KL-FU	Kraft lignin modified with furfuryl glycidyl ether
LiCl	Lithium Chloride
MCC	Microcrystalline cellulose
MUF	Melamine-urea-formaldehyde
NaOH	Sodium hydroxide
NMR	Nuclear magnetic resonance spectroscopy
PF	Phenol-formaldehyde
PU	Polyurethane
PVAc	Polyvinyl acetate
rbf	Round bottom flask
SEM	Scanning electron microscope
St	Potato starch
St-6MHA	Potato starch modified with 6-maleimidohexanoic acid
TFA-d_1	Deuterated trifluoroacetic acid
TGA	Thermogravimetric analysis
TMDP	2–chloro-4,4,5,5-tetramethyl-1,3,2-dioxaphospholane
UF	Urea-formaldhyde
UV-Vis	Ultraviolet-visible

XPS	X-ray Photoelectron spectroscopy
XRD	X-ray diffraction

1. Introduction

1.1 Background

1.1.1 Conventional thermosetting adhesives

Adhesives play a crucial role in the manufacturing and performance of wood products, enabling the formation of strong, durable bonds that enhance structural integrity and product longevity. Among the most commonly used adhesives in this field are polyvinyl acetate (PVAc), polyurethane (PU), epoxy, and thermosetting resins such as phenol-formaldehyde (PF) and melamine-urea-formaldehyde (MUF) [1]. Each of these adhesives are designed for specific application. PVAc, known as wood glue, for instance, is a water-based adhesive valued for its ease of use and non-toxic profile, although its moisture sensitivity can limit its use in outdoor or high-humidity environments. Polyurethane, derived from isocyanate-based chemistry, offers strong, flexible bonds, good resistance to water, and temperature, though it may require more cautious handling due to its chemical reactivity. Epoxy adhesives are known for their exceptional bonding strength and chemical resistance, making them ideal for demanding applications, mostly to bond wood with other materials. Thermosetting resins like PF and MUF provide excellent heat and water resistance and are widely used in structural wood products, such as plywood and particleboard. However, the use of formaldehyde can raise health and environmental concerns. These adhesives mostly originate from fossil-based materials, and thus increasing effort has been made to introduce bio-based materials in these adhesives [2] to answer the need for new renewable adhesives.

1.1.2 Demand on debonding adhesives

The use of adhesives in wood products, while essential for ensuring strength and durability, raises several important concerns particularly in terms of health and environmental sustainability. One of the most pressing issues is the potential health risk associated with certain adhesive formulations. Thermosetting resins, such as PF and MUF release formaldehyde, a known carcinogen, especially during manufacturing and under high temperatures or humidity [3]. Prolonged exposure to formaldehyde fumes can lead to

respiratory problems, skin irritation, and other health complications for workers in the wood products industry, and to a lesser extent, for end users [4].

Beyond health concerns, another major challenge lies in the irreversible strength that makes these adhesives so valuable. Thermosetting adhesives, once cured, form irreversible chemical bonds that are resistant to heat, moisture, and mechanical stress. While this ensures excellent performance in structural applications, it also means that bonded wood products cannot be easily separated or reprocessed at the end of their life. This permanent bonding makes recycling or reusing wood components difficult, often resulting in these products being sent to landfills or incinerated. As environmental pressure mounts to reduce waste and enhance material recovery, the inflexible nature of thermosetting adhesives presents a significant barrier to achieve more circular and sustainable wood products [5].

This challenge has created a growing demand for the development of new adhesives that not only provide strong performance but also allow for the easy disassembly and recycling of wood products at the end of their use [6].

1.2 Covalent adaptive networks for the development of debondable adhesives

1.2.1 Definitions

The growing interest in debondable adhesives is marked by the emergence of a variety of new terms, and understanding the distinctions between them is essential to prevent ambiguity. Terms like “reversible”, “switchable”, “on-demand debonding”, “recoverable”, “reprocessable”, “recyclable” and “reusable” are often used interchangeably, yet each carries specific implications (see Table 1 and Figure 1).

Table 1. Evolution of publications on various terms of adhesives from 2015 to 2025 using Scopus (Elsevier, Amsterdam, Netherlands)

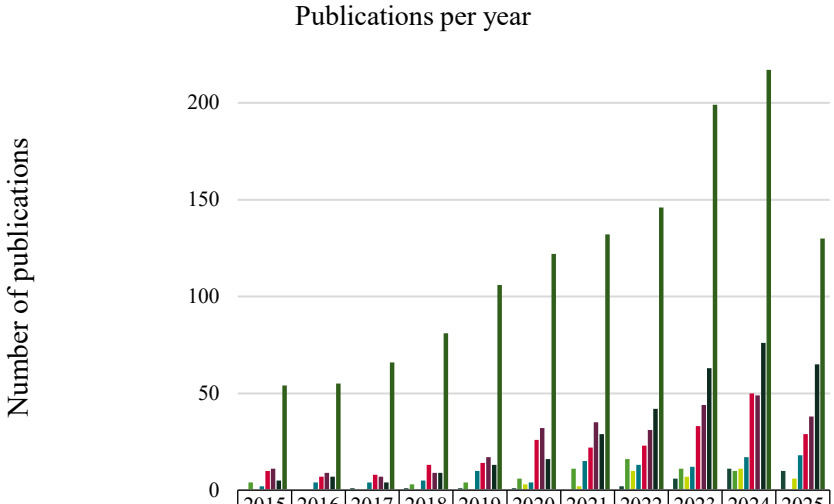

	2015	2016	2017	2018	2019	2020	2021	2022	2023	2024	2025
debondable adhesive	0	0	1	1	1	1	0	2	6	11	10
recoverable adhesive	4	0	0	3	4	6	11	16	11	10	0
reprocessable adhesive	0	0	0	0	0	3	2	10	7	11	6
on demand debonding adhesive	2	4	4	5	10	4	15	13	12	17	18
reusable adhesive	10	7	8	13	14	26	22	23	33	50	29
switchable adhesive	11	9	7	9	17	32	35	31	44	49	38
recyclable adhesive	5	7	4	9	13	16	29	42	63	76	65
reversible adhesive	54	55	66	81	106	122	132	146	199	217	130

Terms such as reversible, reusable, and switchable refer to adhesives capable of undergoing multiple bonding cycles. Reversible and switchable typically indicates that the adhesive can both bond and debond under certain conditions. In contrast, debondable or on-demand debonding refers to adhesives that can lose adhesion when triggered by heat, light, or chemicals but do not necessarily allow for rebonding. Meanwhile, recoverable and reprocessable describe materials that can be reused or reprocessed, often after mechanical separation, without necessarily having intrinsic debonding capabilities. These adhesives may retain their performance upon recycling, but the process does not inherently involve a controlled or reversible bonding mechanism. A recyclable adhesive is more a general term that has been used

to cover all these types of adhesives, more specifically reversible and reusable adhesives.

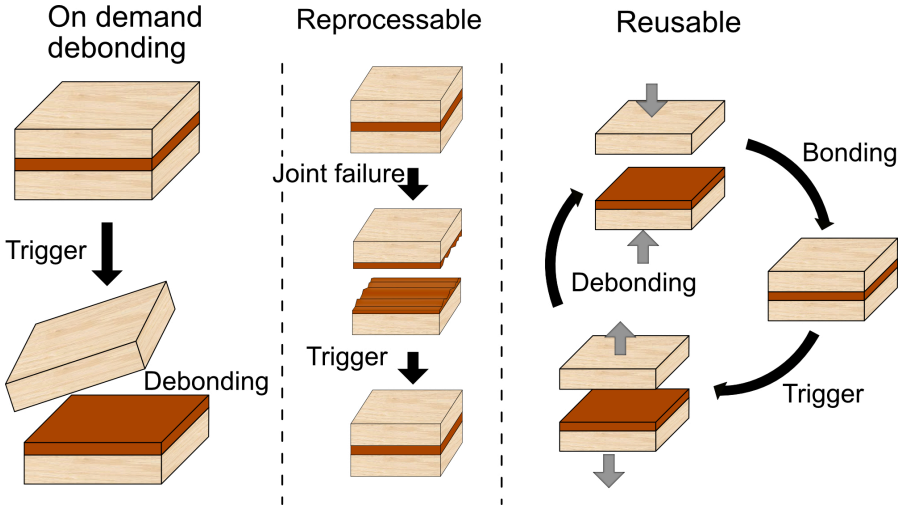

Figure 1. Schematic representation of the different principles of smart adhesives.

Among the various strategies being explored to address the recyclability of bonded wood products, one promising approach involves the development of debondable adhesives based on covalent adaptive networks (CANs) [7]. These innovative polymeric materials incorporate dynamic covalent bonds that can be reversibly broken and reformed under specific conditions and stimuli, such as heat, light, or chemical triggers. This reversible bonding could allow for the controlled disassembly of wood products, making it possible to separate and recycle individual components without compromising their integrity. By combining performance with end-of-life flexibility, adhesives based on covalent adaptive networks represent a significant step towards more sustainable and circular practices in the wood industry.

1.2.2 Different stimuli

Various strategies can lead to debondability (swelling, melting or decomposition of the adhesive for example) using specific stimulus; the

focus will be limited to debondable adhesives made out of dynamic networks. As mentioned earlier, CANs are a class of polymer materials built from dynamic covalent bonds that can reversibly break and reform in response to external stimuli, allowing the network to cleave or self-heal [8]. The dynamic nature of these networks is activated by specific triggers such as heat, light, pH changes (see Figure 2), enabling controlled responses like reshaping, debonding, or reprocessing.

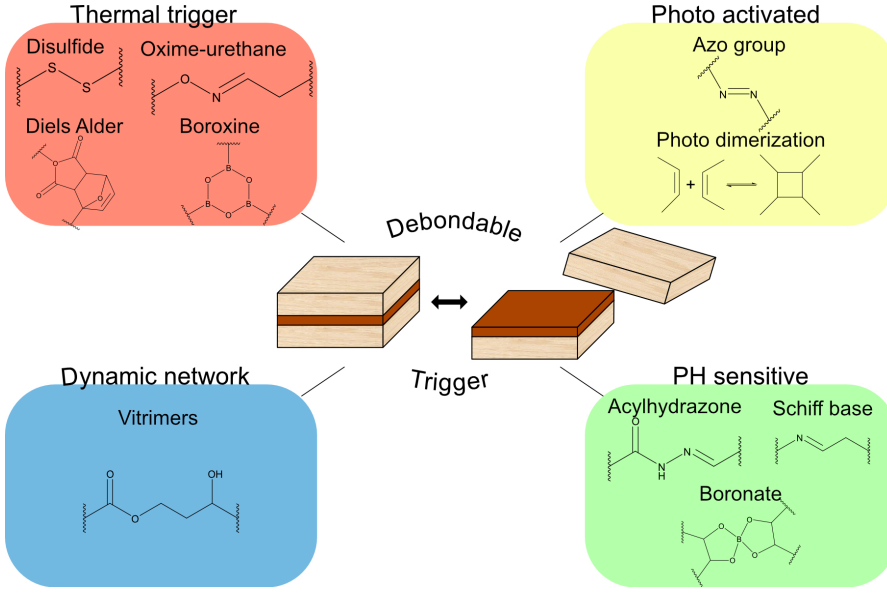

Figure 2. Schematic representation of the different stimuli for debonding.

Here, the debonding mechanism will be limited as occurring through two distinct mechanisms, as illustrated in Figure 3. The first is known as adhesion failure, where the bond at the interface between the adhesive and the substrate is disrupted. The second is named cohesion failure; it involves a loss of mechanical integrity within the adhesive itself. Failures involving damage to the substrate are beyond the scope of this thesis and will not be addressed, as it does not allow the recyclability of the substrates.

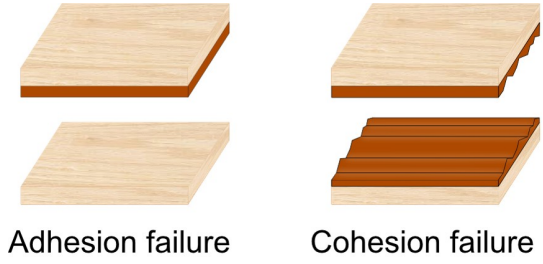

Figure 3. Schematic representation of the different debondable mechanisms.

A critical factor in the design of debondable adhesives is the choice of stimulus used to trigger debonding, as it directly influences both the practical applications and the operational lifespan of the adhesive. Stimuli may be physical or chemical in nature, but they must enable on-demand debonding within a commercially feasible time frame without harming the bonded materials. Ideally, these stimuli should be highly selective, minimizing the risk of unintended activation during normal use, which could result in serious performance failures. Preferred triggers are those unlikely to occur in service environments, such as microwaves or ultrasound.

Currently, ultraviolet (UV) light and heat are the most commonly used debonding stimuli. However, they come with significant limitations, particularly regarding the difficulty of reaching bonded interfaces and the risk of accidental exposure [6].

Photoresponsive networks

A widely explored approach in recent years involves integrating photoresponsive moieties into conventional commercial adhesives. Although this stimulus have not been applied yet for the development of debondable adhesive for wood products, this strategy has been thoroughly reviewed [9] for other materials. Most advancements in this field can be categorized into two main mechanisms: photoinduced overcuring and photodegradation, although other processes, such as isomerization and dimerization have also been studied. These photo-triggered mechanisms

enable fast, on-demand debonding; however, their effectiveness is dependent on the transparency of the substrates to the specific wavelengths used. Additionally, their application is generally restricted to joints that are unlikely to be exposed to these wavelengths during the product's service life, to avoid unintended debonding.

Photoinduced isomerization can be employed to lower the modulus of an adhesive, ultimately leading to cohesive failure. A well-established and stable example is the UV-triggered trans-to-cis isomerization of azobenzene [10]. When azobenzene is incorporated into the polymer matrix, it forms trans-azopolymers that remain solid at ambient conditions. Upon UV exposure, these polymers undergo a phase transition to a liquid state due to the isomerization to the cis form, enabling controlled softening and potential debonding of the adhesive.

Photoinduced dimerization via cycloaddition can serve various functions such as overcuring, cross-link degradation, or photochemical liquefaction, depending on the specific adhesive system.
For instance, a [4π + 4π] cycloaddition reaction involving polymers functionalized with terminal anthracene groups can lead to cross-linking between polymer chains, effectively promoting bonding [11]. The debonding process can be initiated through exposure to ultraviolet light with wavelengths below 300 nm.

Additionally, reversible [2π + 2π] dimerization of 7-hydroxycoumarin derivatives [12] has enabled light-controlled cross-linking in conventional adhesive like polyacrylate and new bio-based adhesives [13]. While less studied, other photoresponsive groups such as cinnamates [14] have also been incorporated into urethane adhesive systems.

Thermal responsive networks

Currently, thermal treatment is the most extensively studied method for developing debondable adhesives. It is often argued that all polymer-based adhesives can be thermally debonded, as they undergo melting or decomposition when exposed to a certain temperature. However, as mentioned earlier, many high-strength structural adhesives for wood are thermosetting polymers, which decompose at very high temperatures without melting. For practical and commercial purposes, temperatures exceeding 250 °C [6] are generally considered unsuitable due to high-energy costs and the potential for damaging wood and other substrates.

One advantage of thermal debonding compared to photoresponsive debonding, is that it does not require substrates to be transparent. However, the substrates must be thermally stable and capable of conducting heat effectively up to the required debonding temperature.

The Diels–Alder (DA) reaction is a [4 + 2] cycloaddition between a diene and a dienophile, resulting in the formation of a six-membered ring adduct. This reaction is thermally reversible. The most common type of DA reaction involves incorporating furan and maleimide groups into the polymer structure as the reaction rate increases when the dienophile contains electron-withdrawing groups and the diene contains electron-donating groups.

Due to its mild conditions, catalyst-free operation, and high yield, the DA reaction is widely utilized in dynamic covalent systems, particularly in self-healing materials and reversible adhesive applications. The current strategy adopted by many research groups consists in introducing a DA network into conventional adhesives. Indeed, Du P. et al. and Carbonell-Blasco M. et al. both achieved thermal debondability by introducing furan moieties at the end chain of polyurethanes later cross-linked using bismaleimide [15, 16]. The same principle was used by Lorero I. [17] to develop debondable epoxies. First, furfurylamine was used to introduce furan moiety on DGEBA, which is supposed to cross-link with bismaleimide. Kuang, X. et al. [18] designed a DA adduct with amine attached to furan and maleimide to make it reacts with DGEBA. These studies demonstrated that incorporating DA adducts does not compromise adhesive strength; in some cases, it even enhances shear strength [18]. This shows the potential to design adhesives that combine the robustness of thermosets with the adaptability of thermoplastics. Indeed, when heated to temperatures generally above 130 °C [19] the retro Diels–Alder reaction is favored, leading to the DA adduct cleavage, resulting in the adhesion or cohesion failure.

Disulfide-containing chemical bonds also present a significant interest for designing debondable adhesives. Despite the main use in reprocessable adhesive or self-healing material, few works reports the use of disulfide bonds in debondable adhesive. Y. Jin et al. reported the development of high-strength; thermally debondable adhesives based on sulfur-modified epoxy networks incorporating both dynamic disulfide linkages and β-hydroxyl ester functionalities. The mechanical performance of these adhesives could be tuned, achieving tensile strengths ranging from 2.5 to 22.8 MPa [20].

Another chemistry that might have potential in this field is the boron–oxygen linkage, valued for its distinctive thermodynamic stability. Among boron-based structures, phenylboronic acid has particularly gathered attention. It can undergo dehydration and condensation with diols or diphenols to form dynamic boronate esters, or it can self-condense to form boroxine rings. The boroxine structure, which exhibits dynamic and reversible behavior, is formed through the dehydration of three phenylboronic acid molecules. Longfang R. et al. [21] designed a polyurethane adhesive cross-linked with boroxines that was able to heal without loss of bonding strength.

pH responsive networks

The research of pH debondable adhesives has mostly been towards the use of pH sensitive polymers [22], which can swell or dissolve depending on pH variations. As thermal trigger, one of the potential risks using pH as a trigger is the damage of the substrate. Indeed, strong acids can degrade wood by hydrolyzing its polymer components (lignin, cellulose, and hemicelluloses). For this reason, researchers have been trying to favor weaker acids such as citric acid or orthophosphoric acid [23]. On the other hand, unlike heat or light treatment, the solution used for debonding might be reused without energy consumption.

Imine bonds, also called Schiff base (named after its discovery by Hugo Schiff in 1864), formed through the condensation of amines and aldehydes or ketones, are dynamic covalent linkages commonly used in self-healing and reversible materials [24]. This bond exhibit pH-dependent reversibility that is stable under neutral to basic conditions but readily hydrolyzed in acidic environments. This reversible nature makes imine chemistry particularly attractive for designing stimuli-responsive and debondable adhesive systems. Türel T. et al. [23] reported the use of imine chemistry in polyurethane adhesives aiming to provide on demand debonding. By introducing imine into the polyol precursor of polyurethane, the adhesive was able to debond when exposed to citric acid at 80°C. When used to bond wood, this adhesive system showed shear strength values from 1.5 to 2.1 MPa.

Boronate bonds, formed between boronic acids and diols, are widely used in dynamic materials due to their reversible covalent nature. These bonds exhibit pH-dependent reversibility: they are stable and form strong linkages

under alkaline to neutral conditions (typically above pH 7), but readily dissociate in acidic environments (below pH 6). Narkar A. et al. designed a polyacrylamide adhesive containing catechol and boronate moieties [25]. They demonstrated the possible formation of a catechol-boronate complex at pH 9 that is able to dissociate at pH 3. The adhesive reversibility was proved over 3 cycles of pH changes, despite the possible oxidation of catechol into quinone at basic pH.

Despite little research in adhesive technology, the acylhydrazone could have potential in development of pH responsive adhesives. This bond is formed through a condensation reaction between hydrazide and aldehyde groups. This linkage demonstrates reversible condensation in response to low pH [26], enabling cyclic reversibility. As a result, so far acylhydrazone linkages has mostly been incorporated in polymer chains for the development of self-healing materials [27].

Vitrimers

Vitrimers represent a distinct class of polymers, apart from traditional thermosets and thermoplastics [28]. Indeed, these polymers integrate the reprocessability and deformability typically associated with thermoplastics as well as the permanent and temperature-stable network of thermosets [29]. This behavior is obtained through their three-dimensional polymer networks containing dynamic covalent bonds that enable rearrangements while maintaining a constant average crosslinking density [29]. Although transesterification is the most widely utilized reaction and first used [30] in vitrimer systems, their dynamic covalent network can also be based on other exchanges. Indeed, these rearrangements can be obtained through various mechanisms such as imine, disulfide, boronic ester or vinylogous urethane exchange, olefin metathesis, transacetalization and transalkylation [28]. The diversity of possible bonds results in a diversity of stimuli to trigger the solid to viscoelastic behavior of vitrimers.

In recent years, there has been increasing interest in utilising vitrimers as adhesive materials, primarily due to their potential for self-healing and reprocessability. Recent attempts have been made on developing epoxy-vitrimers. Surós M. et al. [31] designed an epoxy adhesive including vitrimer network that could debond at 180°C for 2 h by hand-pulling and even be recycle through alcoholysis of the esters at 197°C. Different formulations were evaluated for bonding aluminum sheets, achieving lap shear strengths

up to 25.8 ± 2.9 MPa. Santiago D. et al. [32] also reported a similar epoxy-vitrimer debondable adhesive based on the same reaction between DGEBA and glutaric anhydride.

Recent studies have focused on lignin-based vitrimers for debondable wood adhesives. Indeed, Liu J. et al. [33] developed an on-demand debonding adhesive based on vinylogous urethane network between polyamine and ketone functionalized lignin, after bonding two pieces of wood, debonding could be triggered by thermal treatment of 170°C for 3 min. Relatively high shear stress of 12.7 MPa were measured on wood samples. Yang Y. et al. [34] reported another vitrimer network based on phenol-functionalized lignin able to debond using photo-thermal stimuli. The dynamic network was based on transacetalization of acetal groups formed between phenol-lignin and divynil ether. A shear stress of 12.87 MPa was recorded when bonding wood samples.

1.3 Bio-based adhesives for wood

Although most adhesives used nowadays are derived from fossil-based materials, historically, adhesives were primarily sourced from natural, bio-based substances. First developed adhesives often relied on animal protein (albumin, collagen, and casein), starches, and natural proteins or resins extracted from crops and trees [35]. These bio-based adhesives were widely used for centuries. However, with the rise of the petrochemical industry, synthetic adhesives made from fossil fuels became dominant because of their superior strength, durability, low cost and ease of production. Today, there is a renewed interest in returning to bio-based adhesives driven by legislation changes due to health risks and individual growing awareness to promote sustainability and reduce environmental impact.

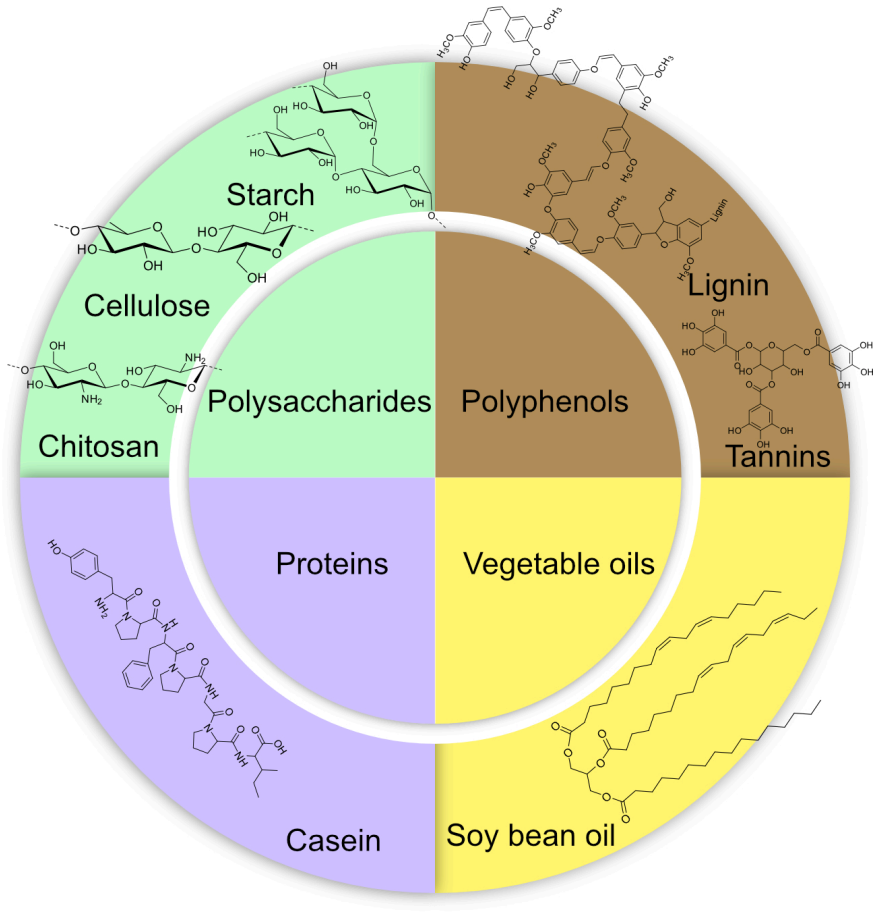

Figure 4. Schematic representation of bio-based alternatives for adhesives.

Bio-based polymers for adhesives can be sourced from a wide range of renewable wastes, including marine, agricultural, and industrial wastes or by-products. Common candidates can be divided in four families including proteins, vegetable oils, polysaccharides and polyphenols as illustrated in figure 4. Marine bio-waste, such as crustacean shells and seafood processing residues, provides chitin, a valuable polysaccharide when turn into chitosan with potential as a wood adhesive [36]. Other polysaccharides derived from plants such as cellulose and starch, which are abundant, renewable, and biodegradable have raised significant interest in adhesive application [37]. Plant-derived proteins [38], resins such as rosin [39] and oils such as soybean

oil [40, 41], are also being explored for their adhesive properties. The wood and pulp industry generates lignins [42], tannins [43], and celluloses [44] from sawdust and bark, while agricultural waste offers starch [45], cellulose, and proteins from crop residues. The food industry generates proteins from discarded produce and oilseed by-products. Dairy coproducts such as the curds from skimmed milk are rich in a protein called casein that has been widely used as wood adhesive. Despite its replacement by fossil-based adhesives, casein still raise interests for its use in wood adhesives [46]. These diverse, often underutilized resources offer promising, sustainable alternatives for developing eco-friendly adhesives. However, the low water resistance and poor bonding strength often limits the direct use of these bio-based materials as adhesive, necessitating the use of cross-linking agents; many of which are fossil-derived thereby reducing the overall bio-based content of the final adhesive formulation.

Another solution to improve bio-based adhesives properties is the use of additives. Graphene and its derivatives, such as graphene oxide and reduced graphene oxide, and carbon dots (CD) have attracted growing interest in adhesive technologies due to their good mechanical, thermal, and electrical properties. When incorporated into adhesive formulations, graphene materials can enhance bonding strength [47], dispersability [48], and thermal conductivity [49]. Their large surface area and strong interfacial interactions with polymer matrices contribute to improved load transfer and cohesive performance. Moreover, CDs are of particular interest as they can be synthesized from bio-based materials (citric acid, vegetable oil, etc.) [50].

1.4 Aim of the thesis

The aim of the present research work was to investigate the potential use of polysaccharides more specifically potato starch, in the design of debondable adhesives for wood products. In order to achieve a proof of concept, the following research questions were formulated:

(1) Which debonding stimuli (e.g., heat, pH, light, etc.) are more appropriate to wood?

(2) Which chemical reactions can provide debonding property to starch-based adhesives under specific stimuli while maintaining performance suitable for wood bonding applications?

(3) How can starch be chemically modified to enable controlled debonding for the recyclable assembly of wood products?

(4) Which bio-based materials could be used to crosslink starch?

The primary objectives of this research were to develop (i) a thermally debondable adhesive system based on starch (St) and Kraft lignin (KL), and (ii) a pH-responsive, starch-based debondable adhesive. These objectives were addressed through four studies, each presented as separate articles in the thesis.

The first article explores the modification of St with 6-maleimidohexanoic acid (6-MHA) in dispersion. The second article examines the solution-phase modification of St with 6-MHA and the functionalization of KL with furfuryl glycidyl ether (FGE), leading to the formation of a Diels–Alder (DA) network between the two modified biopolymers. The third article investigates the performance of the St-6MHA:KL-FU network as a thermally debondable adhesive for wood substrates. The final study assesses the incorporation of carbon dots as multifunctional components to enhance curing behavior and mechanical strength in the development of a Schiff base-based, pH-responsive debondable adhesive.

2. Materials and methods

2.1 Materials

2.1.1 Chemicals

For synthesis: Potato starch (St), kraft lignin (KL), oxalyl chloride, 6-maleimidohexanoic acid (6-MHA), dimethylacetamide (DMAc), dimethylsulfoxide (DMSO), furfuryl glycidyl ether (FGE), sodium hydroxide (NaOH), hydrochloric acid (HCl), lithium chloride (LiCl), chloro(1,5-cyclooctadiene) iridium(I) dimer ($[Ir(cod)Cl]_2$, HS157), potassium carbonate, sodium acetate, vinyl acetate, dichloromethane, dimethylformamide (DMF), acetone and ethanol were purchased from Sigma-Aldrich (Stockholm, Sweden).

For extraction and purification of vinyl ester: dichloromethane, chloroform, acetonitrile and Silica gel 60 (0.063-0.200 mm) were purchased from Sigma-Aldrich (Stockholm, Sweden).

For NMR analysis: deuterated DMSO (DMSO-d_6, 99.80% atom D), deuterated chloroform ($CDCl_3$-d 99.8% atom D), 2–chloro-4,4,5,5-tetramethyl-1,3,2-dioxaphospholane (TMDP, 95%), chromium (III) acetylacetonate ($Cr(acac)_3$, 97%), cholesterol (greater than 99%) and deuterated trifluoroacetic acid (TFA-d_1, 99.5% atom D) were purchased from Sigma-Aldrich (Stockholm, Sweden).

For wood veneer furfurylation: furfuryl alcohol and tartaric acid were purchased from Sigma-Aldrich (Stockholm, Sweden).

2.1.2 Solid wood and wood veneer

Wood materials used in this study were European beech (*Fagus sylvatica*) veneer with 0.6 mm thickness cut to dimensions 0.6 x 20 x 120 mm^3 using ABES sample cutter (see Figure 6) and Scots pine (*Pinus sylvestris*) solid wood with an angle between annual growth ring of 45° with dimensions of 30 × 15 × 5 mm^3 was used for adhesive penetration investigation.

2.2 Methods

2.2.1 St esterification with vinyl ester derivative in suspension

Synthesis of vinyl ester of 6-MHA

The vinyl ester of 6-MHA was synthesized by dissolving 37.40 mmol of 6-MHA in 20 mL of DMF, followed by the addition of vinyl acetate in a 10-fold molar excess. The reaction was carried out in a three-necked round-bottom flask equipped with a reflux condenser and thermometer. Prior to initiating the reaction, the mixture was degassed with argon for 15 minutes. Subsequently, the catalyst HS157 (0.01 equivalents) and sodium acetate (0.03 equivalents) were added. The reaction was maintained under magnetic stirring at 110 °C for 24 hours in a dry argon atmosphere.

Upon completion, the reaction mixture was poured into water and extracted with dichloromethane. The organic fraction was then concentrated using rotary evaporation. The resulting viscous liquid was dissolved in a 4:1 (v:v) mixture of chloroform and acetonitrile and purified by silica gel column chromatography. After purification, the solvent was removed via rotary evaporation. The final product, the vinyl ester of 6-MHA, was characterized using FTIR and NMR spectroscopy.

Polysaccharide activation

St was activated through a mercerization process. A total of 20 g of St were added to a beaker containing 1 L of 4 M sodium hydroxide solution. The mixture was stirred for 1 hour, followed by filtration and sequential washing with dehydrating solvents: methanol, acetone, and hexane. The treated samples were then freeze-dried and stored under vacuum in a desiccator.

Synthesis of St-6MHA in suspension

Activated St (1 g) was dispersed into a 100 mL round-bottom flask containing a solution of the vinyl ester (1 equivalent to the hydroxyl groups of the polysaccharides), 0.15 g of potassium carbonate as a catalyst, 15 mL of DMF, and 5 mL of DMAc. After degassing the mixture with argon, the reaction was carried out under reflux with vigorous magnetic stirring at 110 °C for 24 hours. Upon completion, the reaction mixture was cooled to room temperature, filtered, and thoroughly washed with water to remove the catalyst, followed by ethanol to eliminate residual reagents and solvents. The

resulting maleimide-grafted polysaccharides were characterized using FTIR and NMR spectroscopy, XRD, TGA, and ESEM.

2.2.2 St esterification with acyl chloride derivative in solution

Preparation of acyl chloride

6-MHA was dissolved in DMAc, and oxalyl chloride (1 equivalent) was added dropwise to the solution while maintaining the temperature in an ice bath. Following the addition, the reaction mixture was stirred at room temperature under an inert argon atmosphere for 3 hours. Gaseous by-products, including HCl, CO, and CO_2, were allowed to escape from the reaction vessel. Upon completion, the resulting acyl chloride intermediate was used directly without further purification.

Modification of St with acyl chloride in solution

A total of 3.2 g of oven-dried St was placed in a round-bottom flask containing 50 mL of dry DMAc. The mixture was stirred at 140 °C for 1 hour. Subsequently, the temperature was reduced to 100 °C, and 1 g of lithium chloride was added. Upon addition, the suspension became instantly transparent with a noticeable increase in viscosity, forming a slurry. The mixture was then heated overnight at 50°C to ensure complete dissolution of the St.

The resulting St solution was added to a solution of the previously prepared acyl chloride in DMAc, using a molar ratio corresponding to two equivalents of acyl chloride per hydroxyl group of the anhydroglucose unit. The reaction mixture was stirred at room temperature for 24 hours under a continuous flow of argon. Upon completion, the modified St was precipitated by the addition of methanol. Then, the modified St was washed/centrifuged with methanol 3 to 5 times and then freeze-dried.

2.2.3 St oxidation

DAS was synthesized following a previously published protocol reported by our group [51]. A 5% solution of oven-dried St (dried at 40 °C for 48 hours in oven) was prepared by dispersing the St in distilled water under magnetic stirring. Sodium periodate ($NaIO_4$) was added to the suspension at a weight ratio of 1:1.65 (St to $NaIO_4$). To protect $NaIO_4$ from photodegradation, the

reaction vessel was wrapped in multiple layers of aluminum foil. The oxidation reaction was carried out at 35 °C for 24 hours.

Following the reaction, acetone was added to quench the process, and the mixture was centrifuged at 5000 rpm for 5 minutes. The precipitate was washed thoroughly with distilled water and centrifuged twice, first for 5 minutes and then for 10 minutes at 5000 rpm. A final wash with ethanol was performed, followed by centrifugation for 10 minutes at the same speed to ensure the removal of residual oxidizing agents. The resulting DAS was dried under vacuum at 35 °C for 48 hours, and the dried material was used for further analyses.

2.2.4 KL etherification with furfuryl glycidyl ether

KL (1 g) was dissolved in water containing sodium hydroxide (200 mg, 5 mmol), corresponding to one equivalent relative to the total acidic groups in KL (including phenolic OH and carboxylic groups). After stirring for 1 hour, FGE was added in an amount equivalent to 1.5 times the phenolic hydroxyl content of KL. The reaction mixture was then stirred at 50 °C for 24 hours. Upon completion, the mixture was cooled to room temperature and acidified to pH 2 using 10% (v/v) aqueous hydrochloric acid. The resulting suspension was centrifuged to collect the precipitated KL. The functionalized lignin was washed three times with 50 mL portions of acidified water (pH 2) and subsequently freeze-dried.

2.2.5 Carbon dots synthesis

CD1 was synthesized via a hydrothermal method. Citric acid (2.0 g) was first wetted with 1.0 g of formamide, followed by the addition of 1.0 g of freshly distilled aniline. The resulting slurry was ground using a mortar and then dissolved in 25 mL of Milli-Q water. This solution was transferred to a 50 mL Teflon-lined autoclave and heated at 185 °C for 24 h. After the reaction, the mixture was transferred to a 100 mL round-bottom flask, and the solvent was removed via rotary evaporation. The resulting dark orange residue was purified by size exclusion chromatography using Sephadex G-10 to eliminate unreacted starting materials and low molecular weight impurities. The purified sample was then freeze-dried to yield a fluffy, deep yellow powder. Final yield: 1.75 g.

CD2 was synthesized via microwave-assisted post-functionalization (amidation) of CD1. Specifically, 0.50 g of CD1 was dissolved in 5 mL of DMF, followed by the addition of a freshly prepared DMF solution of polyethyleneimine (PEI; 0.10 g in 5 mL). The reaction mixture was distributed equally into four 5 mL Biotage microwave reaction vials, which were sealed and subjected to microwave irradiation at 300 W for 20 minutes. Upon completion, the vials were cooled to room temperature, and their contents were combined. The brown reaction product was purified by size exclusion chromatography using Sephadex G-25 to remove unreacted materials and low molecular weight by-products. The collected fractions were concentrated by rotary evaporation to remove residual DMF. The resulting red solid was dried in a vacuum oven at 50 °C for 16 hours, yielding 0.55 g of product. Due to its limited solubility in water, the final CD2 material was analyzed using solid-state characterization techniques.

Various mixtures were prepared for Automated Bonding Evaluation System (ABES) testing. DAS was first dissolved in DMAc and divided into four portions. Carbon dots (CD1 or CD2) were added to the DAS solution at a concentration of 5% by weight relative to starch. The mixtures were theated at 120 °C overnight. Despite the initial insolubility of CD2 in DMAc, a homogeneous dark brown solution was obtained. This tends to confirm the reaction between the aldehyde groups of DAS and the amine functionalities on CD2. Following ABES testing, an excess of hexamethylenediamine (HMDA) was added to the mixtures at a molar ratio of 4:1 (amine to aldehyde) to promote crosslinking of DAS. Additionally, a 70% HMDA solution was tested separately as a reference.

2.2.6 Furfurylation of veneer and solid wood

European beech (*Fagus sylvatica*) veneers, with dimensions of $0.6 \times 20 \times 120\ mm^3$, were oven-dried at 100 °C until a constant weight was achieved. The dried veneers were then immersed in a solution of furfuryl alcohol (FA) containing 5% (w/w) tartaric acid, used as a polymerization catalyst, and left to soak for 24 hours (Figure 5). Following impregnation, the samples were wrapped in aluminum foil and cured in an oven at 103 °C for 24 h to initiate in situ polymerization of FA. To remove any residual unreacted FA, the samples were then unwrapped and left in the oven for an additional hour.

After curing, the final weight of the veneers was recorded, and the weight percent gain (WPG) was calculated using the following equation:

$$WPG = \frac{(m_1 - m_0)}{m_0} * 100 \quad (1)$$

Here, m_1 represents the weight of the veneer after furfurylation and m_0 the weight of the oven-dried veneer.

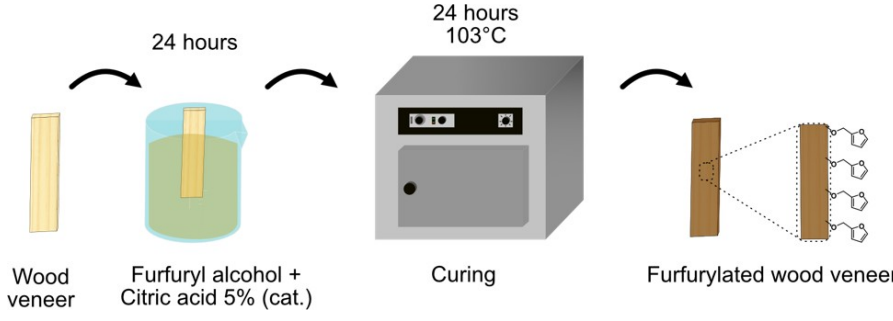

Figure 5. Schematic representation of furfurylation process.

2.3 Characterization techniques

2.3.1 Spectroscopy

FTIR

FTIR spectra were recorded using a Spectrum Two spectrometer (PerkinElmer, Waltham, USA) equipped with a Universal ATR (UATR) diamond accessory, enabling direct analysis of solid samples without the need for prior preparation. A pressure arm was employed to apply a consistent force (monitored via software), ensuring optimal contact between the sample and the diamond crystal for effective interaction with the IR beam. Spectra were acquired with a resolution of 4 cm^{-1}, averaging 32 scans over a spectral range of 4000 to 450 cm^{-1}.

NMR

All NMR spectra (^{1}H, ^{13}C, ^{13}C DEPT, ^{31}P, and 2D NMR) were recorded on a Bruker Avance III 600 MHz spectrometer (Bruker, Billerica, USA).

For ^{1}H NMR measurements, Ttetramethylsilane (TMS) was used as an internal reference. Spectra were acquired with 16 scans and a relaxation delay of 30 seconds. For sample preparation, 100-150 mg of St was suspended in 800 µL of dry DMSO-d_6. The mixture was shaken overnight at 80 °C using a bidirectional mixer to ensure complete dissolution, then transferred to a 5 mm NMR tube for analysis at room temperature. When deuterated trifluoroacetic acid (TFA-d_1) was used, 1-2 drops were added just before measurement. The degree of substitution (DS) for St-6MHA was determined by ^{1}H NMR following a commonly reported method [52]. This approach involves comparing the integrated peak areas corresponding to the protons of grafted 6-MHA with those of the starch backbone. After the addition of TFA-d_1, each anhydroglucose unit theoretically contributes seven protons. However, due to residual moisture in the starch and incomplete deuteration by TFA-d_1, only the signal at 5.19 ppm assigned to a specific starch proton was reliably used. The DS was calculated based on the following equation:

$$DS = \frac{I_{\text{grafted 6-MHA}}}{2 \cdot I_{\text{starch}}} \quad (2)$$

Where $I_{\text{grafted-6MHA}}$ corresponds to the intensity of the protons from 6-MHA and I_{starch} corresponds to the intensity of the starch proton at 5.19 ppm.

Attempts to study the reaction between DAS and CDs were made using ^{13}C CP-MAS NMR recorded at room temperature using a Bruker Avance III 600 MHz CCD (Bruker, Billerica, USA) equipped with a 4-mm 1H/13C high-resolution magic angle spinning (HR-MAS) probe. The samples were packed into 4 mm zirconia rotors. The sample spinning speed was set to 12.0 MHz, with a contact time of 1 msec, and a relaxation delay of 5 sec between acquisitions.

^{1}H and ^{13}C NMR spectra of 6-MHA samples in chloroform-d were recorded using TMS as reference.

The amount of furan groups grafted onto KL was quantified using ^{31}P NMR spectroscopy. A 0.1 M solution of cholesterol, prepared in an anhydrous pyridine/$CDCl_3$ mixture (1.6:1, v:v), served as the internal standard. Chromium (III) acetylacetonate was added to this solution as a relaxation agent to ensure accurate signal integration. Phosphorylation was carried out using 2-chloro-4,4,5,5-tetramethyl-1,3,2-dioxaphospholane (TMDP), in accordance with established protocols [53] 128 scans were recorded with 10 sec delay and a spectral width of 100 ppm.

Analysis of the DA and rDA reactions between St-MHA and KL-FU was made using ^{1}H NMR. St-6MHA and KL-FU were dissolved in DMSO-d_6 with an equimolar ratio of maleimide and furan functions. The reaction was carried out at 65 °C for 4 days to ensure the total formation of the DA adduct. The intensity of the peak at 7.62 ppm assigned to furan double bonds protons was integrated to compare the area of the peak before and after reaction.

XPS

X-ray Photoelectron spectroscopy (XPS) X-ray photoelectron spectra of CDs samples were recorded on a Quantum 2000 Scanning ESCA instrument using a monochromatic Al K-Alpha X-ray (1486.7 eV) excitation source.

XRD

XRD patterns of starch samples were recorded on a Bruker D8 CCD (Bruker, Billerica, USA) powder diffractometer with Mo Kα radiation in the angular range of $2\theta = 5{-}70°$ at 25 °C.

2.3.2 Microscopy

Stereomicroscope

A Zeiss Discovery V12 stereomicroscope (Zeiss, Oberkochen, Germany) was employed to examine the surface of beech veneer before and after furfurylation, as well as following the lap shear test.

Light and fluorescence microscope

To investigate adhesive penetration into wood, a blend of St-6MHA and KL-FU was prepared in a 2:1 ratio based on their respective functional group

contents. This mixture was uniformly applied to the tangential surfaces of both untreated Scots pine (*Pinus sylvestris*) and furfurylated pine specimens (WPG = 22.2 ± 0.1%) with dimensions of 30 × 15 × 5 mm³. Application was carried out manually using a brush at a loading of 200 g·m^{-2}. Following application, the samples were pressed under previously described conditions.

As for the beech sample, the moisture content of the specimens was measured using the oven-dry method resulting in an average moisture content of 9.5±0.1% for untreated pine and 5.2±0.1% for furfurylated pine. The average density was measured to be 0.50 ± 0.01 g·cm^{-3} for untreated pine and 0.91 ± 0.01 g·cm^{-3} for furfurylated pine.

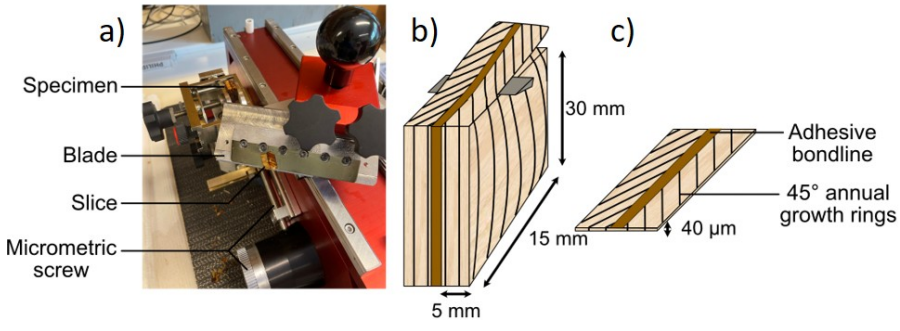

Figure 6. Microtome set up a) and schematic representation of specimen b) and thin section c).

To examine radial adhesive penetration into the porous wood structure, 40 µm-thick sections were prepared (Figure 6) using a sliding microtome (WSL, Zürich, Switzerland) to expose the glue line on transverse surfaces within either earlywood or latewood regions of pine. These sections were mounted onto glass slides and analysed using a Zeiss Axio Imager 2 fluorescence microscope (Zeiss, Oberkochen, Germany) equipped with Neofluar and Apochromat optics, DAPI filter and an Axiocam 8 digital camera.
Images of the samples were also made using a Leica DMLB Light microscope (Leica, Wetzlar, Germany).

ESEM

The surface morphology of the samples was examined using an Environmental Scanning Electron Microscope (ESEM, Philips XL-30,

HITACHI, Japan) operated at an accelerating voltage of 10 kV with a spot size of 4.3. Secondary electron imaging was performed at different magnifications. Prior to imaging, the samples were coated with a thin layer of gold using a sputter coater (Emitech K550X, Quorum Emitech, England) to enhance conductivity and image quality.

2.3.3 Bond development and mechanical tests

ABES

The bond strength development and curing properties of the various DAS adhesives was evaluated using lab-shear bonds subjected to tensile loading through the ABES technique (Adhesive Bond Evaluation System, Corvalis, USA). This apparatus enables the assessment of strength development characteristics for various adhesive types in shear mode between two thin veneer pieces. It offers a rapid, cost-effective, and immediate method to characterize various bond-influencing parameters, notably the curing speed of adhesives. The device consists of a hot-pressing unit associated with a displacement module enabling to cure and test the adhesion on a single device, as shown in Figure 7. Adhesives were applied to a single side of one beech veneer (20 × 5 mm² overlapping area) using spatula to put approximatively around 20 mg of adhesive. The veneers were then hot-pressed under controlled conditions of temperature and time. The temperature was set to 160°C to enable solvent evaporation and avoid reagent evaporation. After curing, the pressure was released, and the bond was immediately subjected to shear testing. Shear strength was recorded at different pressing time. Each condition was tested with ten replicates.

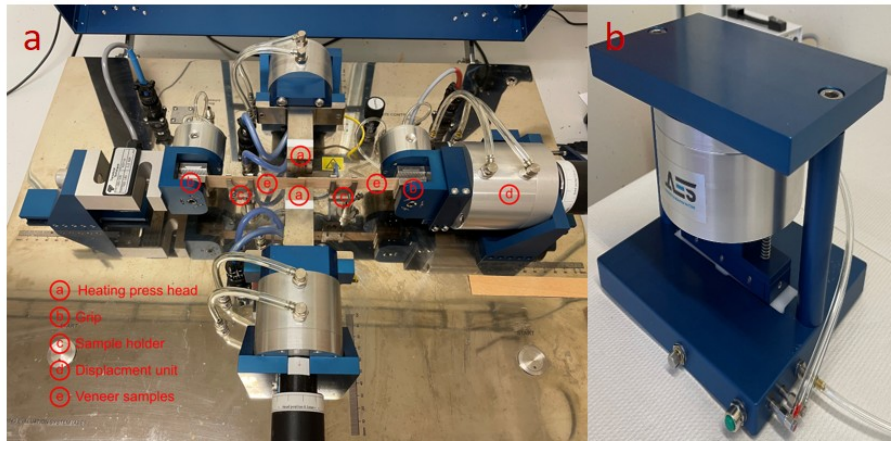

Figure 7. ABES set up (a) and ABES sample cutter (b).

Lab shear test

In order to evaluate the influence of lignin on the bonding strength of the adhesive various compositions of St-6MHA:KL-FU were tested to bond furfurylated beech veneer. The shear strength of the specimens produced was evaluated using a universal testing machine (see Figure 8).

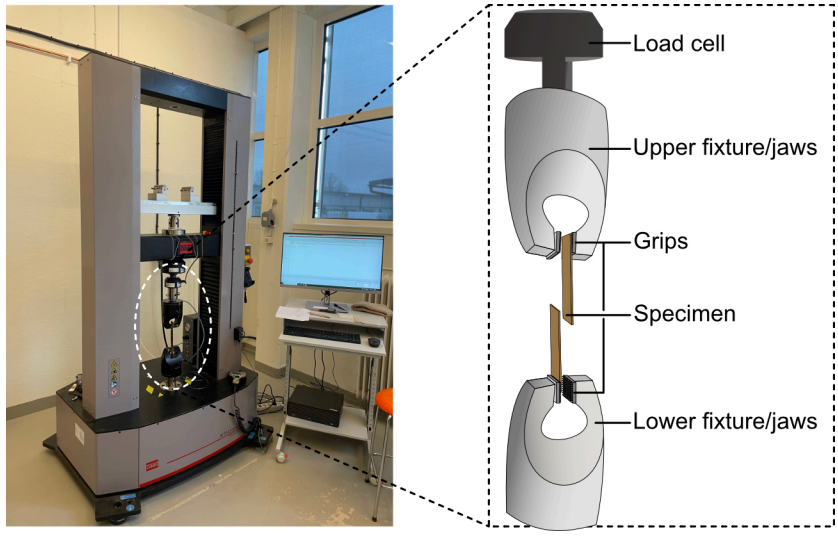

Figure 8. Picture (left) and schematic representation (right) of the universal testing machine set up.

Furfurylated European beech (*Fagus sylvatica*) veneer with dimensions of 0.6 x 20 x 120 mm³ was placed in a climate chamber at 20°C and 65% relative humidity until an equilibrium moisture content at the respective climate was reached.

To form the lap shear specimen, two veneers were bonded together (overlap area 5 x 20 mm^2) with adhesive containing a different ratio of St-6MHA and KL-FU using ABES device to press them at 0.8 MPa and 160°C for 3 min. The specimens were further cured in an oven for 48 h at 65°C.

After gluing, the lap shear specimens were put in a climate chamber at 20°C and 65% relative humidity until moisture content stabilized (less than 0.1% change in weight over 2 h interval) prior to testing. The moisture content of the specimens was measured using the dry weight method, leading to an average moisture content of 9.2 ± 0.1% for untreated beech and 3.1 ± 0.1% for furfurylated beech. The average density was measured at 0.66 ± 0.03 $g.cm^{-3}$ and 0.97 ± 0.03 $g.cm^{-3}$ for untreated and furfurylated beech, respectively.

Lap shear tests were performed in an MTS universal test machine (MTS Criterion C45.105Y, MTS systems, Eden Prairie, USA) with a 1 kN load cell (see Figure 8). The following load procedure was adopted: force was set to

zero, the specimen was mounted in the lower jaw, and then the upper jaw was closed and if a change in force was observed the crosshead was moved carefully manually to bring it back to zero. Then, the loading procedure was started. The preloading was done in crosshead control at 0.10 $mm.min^{-1}$ until a force of 1 N was reached. Then, the loading proceeded with a speed of 0.25 $mm.min^{-1}$ while recording force, crosshead displacement and time at 10 Hz. The test rate was chosen based on pre-tests aiming to reach failure between 1 to 2 min in line with EN 302-1. Fracture surfaces were visually examined to determine whether failure was due to shear and to determine if failure occurred in the wood substrate ('wood failure') or in the adhesive interface ('adhesive or cohesive failure'). Shear strength values corresponding to the different mode of failures as described in Figure 9 of the specimens are included in the reported data. In total, 10 data points were recorded per sample set.

Figure 9. Schematic representation of failure modes.

Thin veneers of 0.6 mm, similar to those used in the ABES system, were employed to reduce adhesive consumption by minimizing the overlap area compared to the requirements of standard EN302-1. Using the ABES sample cutter set to 120 × 20 mm^2 dimensions minimizes the risk of cutting errors often associated with the more complex specimen geometry in EN302-1 (see Figure 10), as reported by Derikvand et al. [54]. The use of thin veneers also reduces issues related to specimen eccentricity without requiring grooves. Notably, lap-shear specimens are highly sensitive to even minor deviations from standard cutting procedures. Accurate groove cutting is essential, as deviations of ± 0.5 mm in depth can significantly affect tensile shear strength results. This setup also allows the use of the ABES heating press for 5 mm

overlap bonding, leading to more reproducible sample preparation. Additionally, the reduced thickness (0.6 mm vs. 5 mm specified in EN302-1) improves curing efficiency due to enhanced thermal transfer from the wood to the bondline.

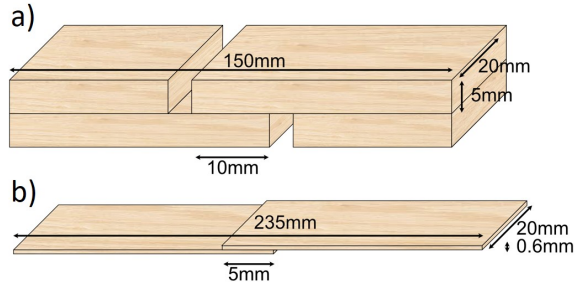

Figure 10. Schematic representation of specimen dimensions used in standard EN 302-1 a), and used in our method b).

Atomic force microscope

Colloidal probe AFM measurements were conducted to investigate the interaction forces between the uncoated and CNF-coated SiO_2 colloidal probe and various starch and lignin materials. These interactions were monitored as a function of time in contact (surface delay) and of the chemical environment.

The widths and lengths of the selected cantilevers (tip A of HQ:NSC35/tipless/No Al, MikroMasch, Wetzlar, Germany) were initially measured using a reflectance optical microscope (Nikon, Tokyo, Japan). The resonance frequency and quality factor of each cantilever were then determined using the TuneIT software (Järna, Sweden) on a MultiMode 8 AFM system (Bruker, Billerica, USA). These parameters were later used for calibration of the spring constant.

A dilute suspension of silica particles (Lot no: 31443, Dry Borosilicate Glass Microspheres, Duke Scientific Corporation) with a diameter of 9.6 ± 1.0 µm, in Milli-Q water (0.005–0.01 wt%) was prepared, and a few drops were deposited onto a microscope slide using a glass capillary. The droplets were allowed to air dry. The low concentration of the suspension effectively

minimized microsphere aggregation during the drying process. Separately, hot melt glue (EPIKOTE 1001, Shell Chemical Co.) and the cantilever chip were applied onto individual microscope slides. These were placed on a hot plate maintained at 120 °C and positioned under an optical microscope equipped with long working distance objectives.
Prior to the gluing process, the particles were dispersed in 1 M NaOH for 15 min to activate their surfaces. They were then thoroughly rinsed with Milli-Q water until the suspension reached a neutral pH.
Using an etched tungsten wire, a small drop of molten glue was transferred to the tip end of a previously calibrated cantilever (Figure 11a, 11b and 11c). A second tungsten wire was employed to pick up a single silicon oxide microsphere and position it precisely onto the glue droplet (Figure 11d, 11e and 11f). This microsphere placement was carried out with the aid of a manual micromanipulator (HS 6 Manuell, Märzhäuser Wetzlar GmbH & Co KG, Wetzlar, Germany), ensuring high positional accuracy. Microspheres with a uniform diameter of approximately 9 µm were carefully selected. The completed probe consisting of the cantilever with the attached microsphere was then stored in a protective cantilever box until use.

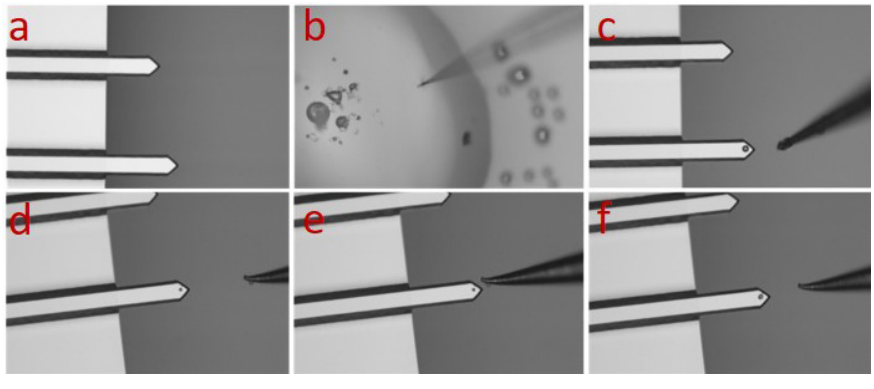

Figure 11. Microscope images of colloidal probe preparation. a, b, c deposition of glue droplet on clean tip. d, e, f deposition of particle on the glue droplet.

CNF coated probes were prepared. The colloidal probes were successively immersed in a polyethylenimine (PEI) solution (100 mg·L^{-1} in deionized water, pH 6.5) for 2 min, followed by rinsing in deionized (DI) water for 1

min. They were then immersed in a CNF suspension (100 mg·L^{-1} in DI water, pH 6.5) for 10 minutes, and again rinsed in DI water for 1 min. This coating cycle was repeated twice to ensure uniform surface coverage. After the final rinse, the cantilevers were dried using a stream of nitrogen gas before subsequent use.

A droplet of sample to analyze dissolved in DMAc was placed on a round mounting glass and dried over nitrogen gas for 3 h prior to measurement.

To identify regions of interest, force spectroscopy measurements were conducted using a MultiMode 8 AFM equipped with a PicoForce extension (Figure 12). The cantilever, modified with a glued microsphere, was positioned over previously prepared thin film samples. A total of 25 individual force-distance curves, each consisting of 6144 data points, were acquired by scanning the cantilever across the sample in a 5 × 5 grid pattern, with a lateral spacing of 1000 nm between points in both x and y directions. The ramp size was set to 3 µm, with an approach/retract speed of 3 µm·s^{-1}. Additional parameters included a trigger threshold of 1.5 V (~ 55.65 nm), a retraction delay of 100 msec, and no surface delay. These measurements were performed in ambient air at room temperature. The area where highest adhesion was recorded was used to study the influence of time on adhesion by using different surface delays ranging from 0 to 60 sec.

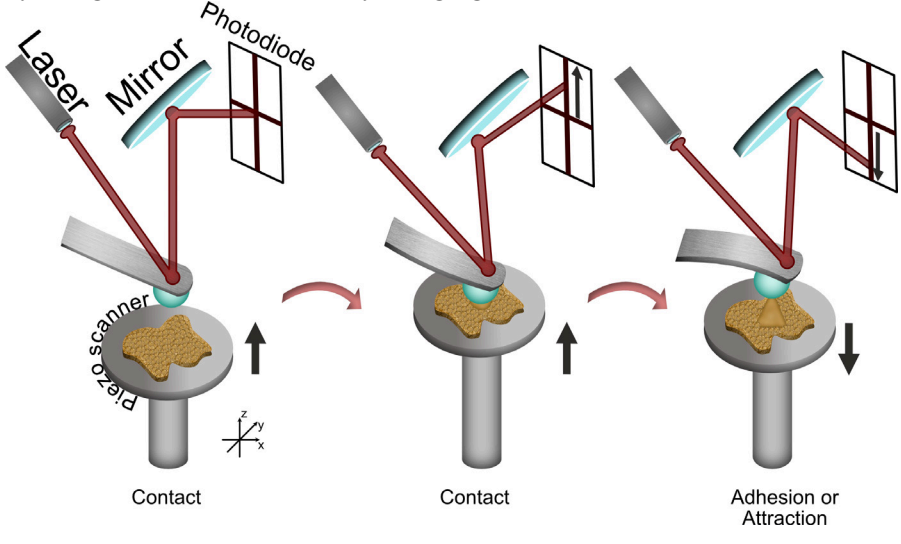

Figure 12. Schematic representation of AFM force measurement principle.

Unprocessed raw data from the AFM was converted to force curves (i.e. force vs separation data) and the adhesion values were extracted with the AFM ForceIT v3 software (Järna, Sweden). The adhesion was extracted as displayed in the following equation:

$$F_{adh} = \frac{F_{pull-off}}{R_{probe}} = \frac{k\alpha U}{R_{probe}} \quad (3)$$

Here, F_{adh} represents the normalized adhesion force, calculated from the pull-off force $F_{pull\text{-}of}$, the microsphere radius R_{probe}, the cantilever spring constant k, the deflection sensitivity α, and the deflection voltage recorded by the photodiode U. The deflection sensitivity was determined directly from the force–distance data for each measurement. It was obtained from the slope of the linear region indicated in green in Figure 13, where the absence of nonlinearity confirms that deformation of both the probe and the sample was negligible.

For each sample, 3 areas of interest were studied and 10 replicates per surface delay were made.

All the glass slides and glass sample holders used in this procedure were prior cleaned using an UV/ozone cleaner (ProCleaner, BioForce Nanosciences, Virginia Beach, USA) before use.

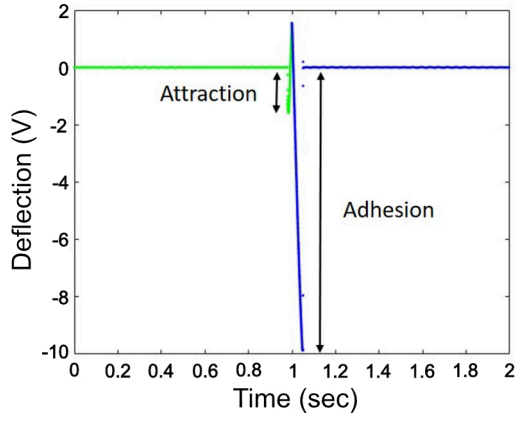

Figure 13. Typical deflection-time curve of KL using a CNF coated probe (surface delay= 60s).

2.3.4 Thermal analysis

TGA

TGA and DTG thermograms of samples were made with a TGA2 analyzer (Mettler Toledo, Greifensee, Switzerland), under nitrogen with a flow rate of 40 mL.min^{-1}, using alumina pans. 5 to 10 mg of each sample were put in a standard TGA alumina crucible pan and heated from 30°C to 600 °C at a heating rate of 10 °C.min^{-1}.

DSC

DSC thermograms of samples were performed using a DSC3+ analyzer (Mettler Toledo, Greifensee, Switzerland). The samples were heated from −30 to 200 °C at a heating rate of 30 °C min^{-1} followed by a cooling from 200 to -30°C at -20°C.min^{-1} under a nitrogen flow of 10 mL·min^{-1}. This cycle was repeated 3 times and only curves corresponding to the 2nd or 3rd heating were analyzed. Approximately 5 mg of oven-dried sample (at 50 °C for 24 h) was used for each analysis.

The rDA of St-6MHA with KL-FU sample was analyzed using the same instrument. A mixture containing St-6MHA and KL-FU with an equimolar quantity of functionalizing group in DMSO were heated at 65°C for 3 days to ensure that the DA reaction occurred. Approximately 5 mg of this mixture was accurately weighed by a balance with a resolution of 0.00001 g and put into an aluminum crucible of 100 µL with the empty aluminum crucible (with lead pierced) as reference. The samples were heated from -30 to 200°C and subsequently cooled down to −50 °C for 5 min at a rate of 30 °C min^{-1}. Then, it was immediately heated from −50 to 200 °C at a rate of 30°C min^{-1}. Only the first heating curve was analyzed. Dry nitrogen gas flow of 10 mL.min^{-1} was used to purge the furnace chamber of the DSC instrument.

2.3.5 Titration

Hydroxyl number

In order to calculate the necessary amount of 6-MHA required for maximum degree of substitution in suspension, the number of available hydroxyl on St was measured using the titration method described in the standard ASTM D 4274. It is a standardized test method for determining the hydroxyl (OH) content of polyurethane raw materials, specifically polyols. The St samples

were acetylated by reacting them with a solution of acetic anhydride in pyridine inside a pressure bottle at 98°C. Afterward, any excess reagent was hydrolyzed with water, and the resulting acetic acid was titrated using a standard solution of sodium hydroxide. The hydroxyl content is determined by calculating the difference between the titration volumes of the blank and the sample solutions. It was measured that St contains 3.56 $mmol.g^{-1}$ of available hydroxyl groups in suspension.

Amylose/amylopectin content

The amylose/amylopectin content of St was determined by a colorimetric method previously described [55]. It consists of measuring the absorbance at 620 nm using an ultraviolet–visible spectrophotometer (Lambda 35 UV/VIS spectrometer, PerkinElmer, Waltham, USA) of a standard solution of pure amylopectin/amylose bound with iodine salt at different ratio to build a standard curve on the evolution of absorbance for the different amylose compositions. The St amylose content was evaluated by the absorbance peak at 620 nm and compared with the standard curve. An amylose content of 17.1 % was measured for St.

Carbonyl content

The carbonyl content was determined using the hydroxylamine procedure [56]. First, 0.2 g of St was gelatinized in water and subsequently cooled to 40 °C. The pH of the solution was adjusted to 3.2 using a 0.1 M hydrochloric acid solution. Following this, 15 mL of hydroxylamine reagent was added, and the mixture was stirred at 40 °C for 4 h. The excess hydroxylamine was then immediately titrated with 0.1 M HCl at pH 3.2. A blank titration was carried out under the same conditions for reference.

The hydroxylamine reagent was prepared by dissolving 25 g of hydroxylamine hydrochloride in 100 mL of 0.5 M sodium hydroxide solution. The volume was then brought to 500 mL with distilled water. A carbonyl content of 85.1 % was measured for DAS.

2.3.6 Debondability evaluation

Thermal debondability test

Bonding evaluations were performed using ABES device. Untreated and furfurylated European beech veneer (0.6 x 20 x 120 mm^3) were bonded together using different mixtures of modified and unmodified St and KL dissolved in DMAc. Approximately 20 mg of solution was applied at the extremity of one veneer on a length of 5 mm, another veneer was placed on top and the bond line was pressed at 65°C with a constant loading pressure of 1 MPa for 48 h.

In a next step, the bonded specimens were placed in the ABES apparatus to evaluate shear strength. In order to evaluate thermal debondability of the adhesive, another batch of bonded veneers was placed in an oven at 135°C for 4 hours prior to be tested. Experiments were performed with 20 replicates.

pH debondability test

Samples of veneer were pressed using the ABES for 300 sec at 160°C with the different adhesives formulated. The bonded veneer was then immersed in a different solution. A first batch of bonded veneer was placed in a water solution at pH 7 and a second batch in a solution at pH 4. The shear strength was measured using ABES after 1 h and 4 h of immersion (see figure 14). The experiment was done in triplicates.

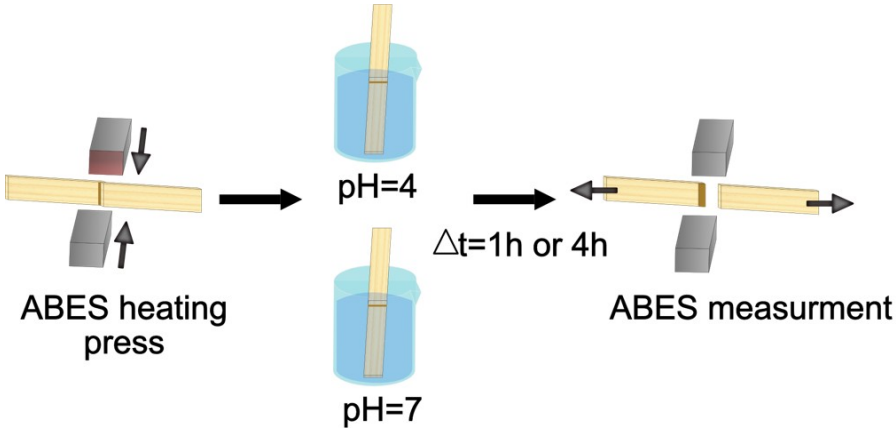

Figure 14. Schematic representation of pH debondability test.

3. Results and discussion

3.1 Starch reversible network (papers I, II and IV)

3.1.1 Diels-Alder reaction between starch and Kraft lignin (papers I and II)

St-6MHA synthesis in suspension

The maleimide moiety consists in an unsaturated cyclic imide, creating an electron-deficient dienophile system. This electron-withdrawing character enhances the compound's susceptibility to undergo cycloaddition with electron-rich diene. The conjugation within the maleimide structure not only increases its reactivity but also contributes to the reaction's stereoselectivity. Diels–Alder reactions involving maleimides generally follow a concerted mechanism, where the electron-deficient nature of the dienophile plays a critical role in guiding the stereochemical outcome of the resulting cyclohexene ring. Although the maleimide can potentially participate in both [2+2] and [2+4] cycloadditions, the [2+4] addition is preferred when heat is applied, largely due to orbitals and steric considerations and the tendency to form more thermodynamically stable products [19]. Thus, we aim to graft 6-MHA on St for the reactivity and selectivity of the maleimide group in Diels-Alder reaction.

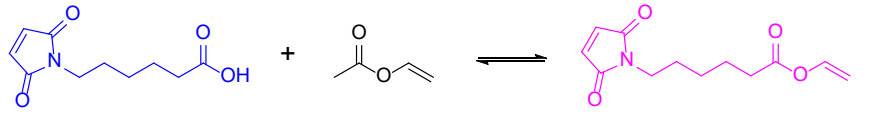

Figure 15. Schematic representation 6-MHA ester synthesis.

Hydroxyl groups in starch exhibit limited reactivity toward direct esterification with carboxylic acids; therefore, either the hydroxyl or carboxylic acid groups must be activated to enhance their reactivity. In this method, 6-MHA was first converted into its corresponding vinyl ester to facilitate the reaction following the procedure illustrated in Figure 15.

Chemical characterization of 6-MHA ester

The structure of the synthesized vinyl ester was confirmed using FTIR and NMR spectroscopy. Comparison of both FTIR spectrum shown in Figure 16, of 6-MHA and MHA ester, showed new, distinctive absorption bands. These bands, attributed to the vinyl functional group, included signals at approximately 3095 cm^{-1} for vinyl C–H stretching, 2938 and 2863 cm^{-1} for saturated CH_2 stretching, 1644 cm^{-1} for non-conjugated C=C stretching, and 948 cm^{-1} for out-of-plane C–H deformation of the $CH=CH_2$ group. Additionally, the formation of an ester bond was evidenced by a new peak at 1750 cm^{-1} corresponding to C=O stretching in the vinyl ester, and another at 1135 cm^{-1} attributed to ester C–O stretching. The disappearance of the characteristic carboxylic acid C=O stretch at 1680 cm^{-1} further supported the successful conversion of 6-MHA into its vinyl ester derivative.

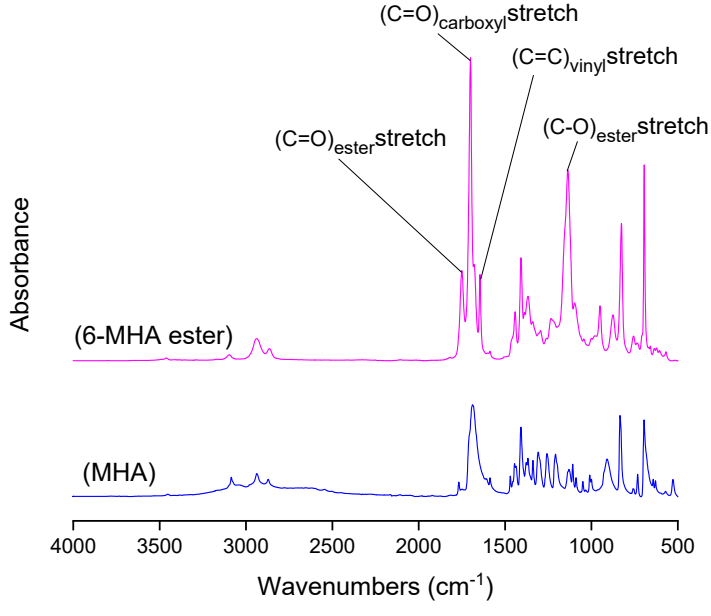

Figure 16. FTIR absorbance spectra of unmodified 6-MHA and 6-MHA ester.

The successful transvinylation of 6-MHA with vinyl acetate was confirmed through both ^{1}H and ^{13}C NMR spectroscopy. In Figure 17, displaying the ^{1}H

NMR spectra of 6-MHA and its corresponding vinyl ester, new peaks appeared at 4.5, 4.8, and 7.2 ppm, associated with the vinyl protons.
Further confirmation was provided by ^{13}C NMR analysis shown in Figure 18. Additional signals than the one observed on 6-MHA spectrum at 97.0 and 141.0 ppm were respectively attributed to the methylenic and methinic carbons of the vinyl group. These observations align with previously reported study [57], supporting the successful formation of the vinyl ester.

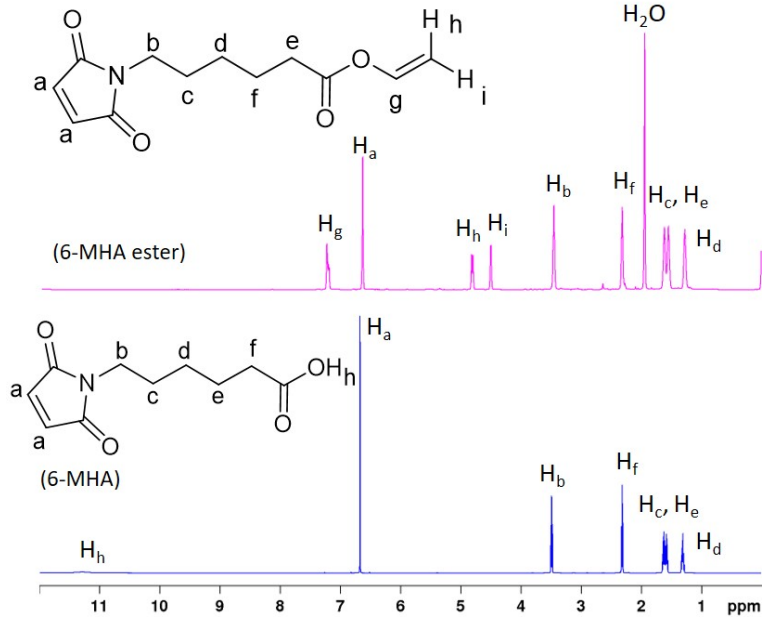

Figure 17. ^{1}H NMR spectra of unmodified and modified 6-MHA (6-MHA ester).

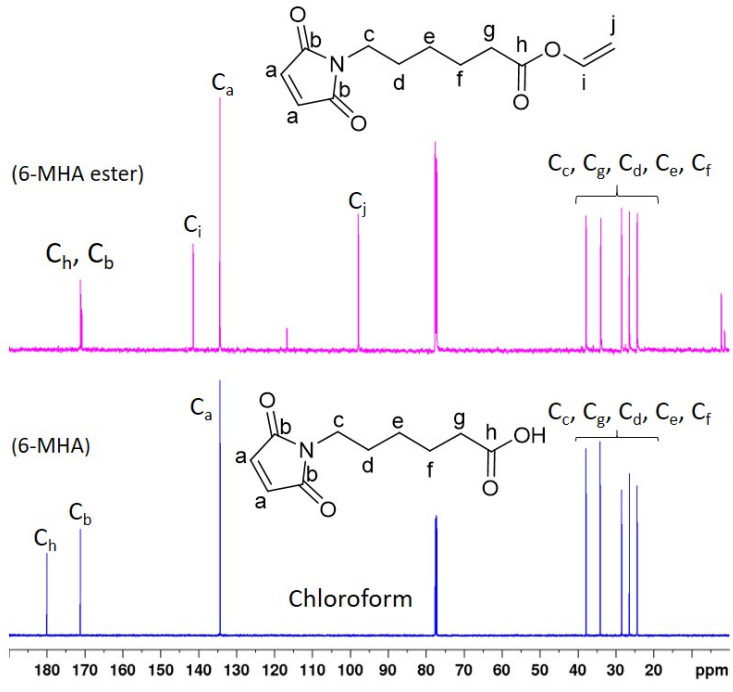

Figure 18. ^{13}C NMR spectra of unmodified 6-MHA and 6-MHA ester.

Chemical characterization of St-6MHA synthesized in suspension

St was modified with 6-MHA ester via transesterification using potassium carbonate as a mild catalyst, as illustrated in Figure 19. This reaction was conducted in suspension to try to preserve its native structure, which is supposed to contribute positively to mechanical performance in adhesive application. This approach is considered less aggressive than traditional methods, as it avoids the production of hydrochloric acid, which could hydrolyze St chains. Unlike conventional esterification techniques involving acyl chlorides or anhydrides, this transesterification method uses vinyl esters, producing acetaldehyde as the only byproduct, which can be easily removed during the reaction due to its low boiling point (21 °C). The results from previous research [57] suggested to fix the temperature and time of reaction at 110°C and 24 h as optimum conditions.

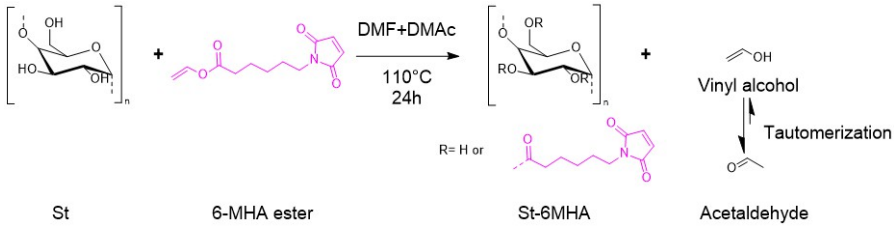

Figure 19. Schematic representation of polysaccharides esterification synthesis in suspension.

Figure 20 presents the FTIR spectra of both unmodified and esterified St. The starch sample modified via transesterification exhibited several new absorption bands, confirming the successful grafting of 6-MHA moieties.

A sharp peak at 1740 cm^{-1} corresponds to the stretching vibration of ester carbonyl groups (C=O), while the band at 1695 cm^{-1} is associated with the carbonyl group of the maleimide functionality [58]. Additionally, the absorption band in the range of 1560–1600 cm^{-1} is attributed to C=C stretching vibrations. A band at 1236 cm^{-1} indicates C–O stretching, characteristic of newly formed ester bonds. Other distinct features include C–H bending vibrations at 1440 cm^{-1} and 1400–1410 cm^{-1}, and C–N stretching vibrations around 1360 cm^{-1}, all of which are consistent with the structure of 6-MHA. These spectral changes are in agreement with previous literature [57, 59]. The modified St also displayed new absorption bands in the 2800–3000 cm^{-1} region, corresponding to C–H stretching vibrations from the introduced acyl groups, further evidence of successful esterification.

One of the most notable changes observed is the reduction in the intensity of the broad hydroxyl absorption bands. This decrease suggests that hydroxyl groups on the starch backbone were successfully replaced by ester functionalities through the transesterification process.

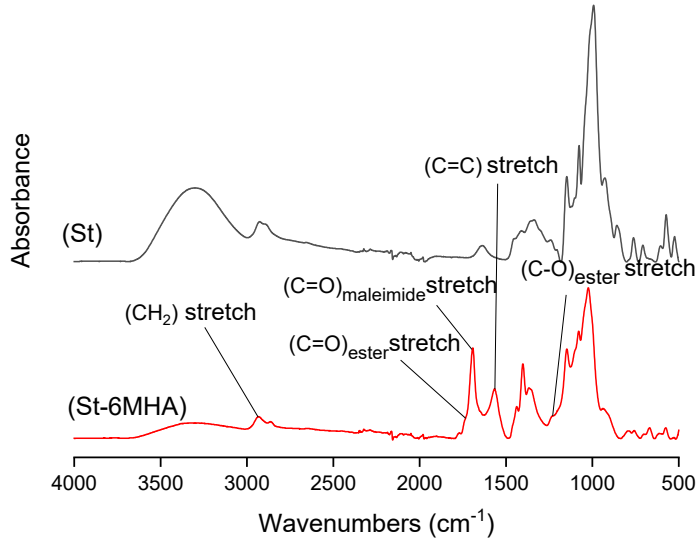

Figure 20. FTIR absorbance spectra of St and St-6MHA synthesized in suspension.

The NMR spectroscopic analysis of St-6MHA (Figure 21 and 22) revealed relatively low signal intensities for the St characteristic peaks. This was primarily attributed to the poor solubility of the modified starch in various deuterated solvents, as well as the broad distribution of chemical environments introduced by the modification. Notably, the signal corresponding to the hydroxyl proton at the C_6 position (annotated as H_9) was markedly reduced. This observation is consistent with expectations, as the primary alcohol at C_6 is generally more reactive than the secondary hydroxyls under standard conditions.

The ^{1}H NMR spectrum of St-6MHA displayed characteristics peaks from 6-MHA carbon chains' protons between 1.0 and 3.5 ppm (Figure 17) annoted as b, c, d, e and f on Figure 21. Moreover, a clear singulet appeared at 7.0 ppm associated to maleimide protons. The disappearance of the vinyl protons at 4.5, 4.8, and 7.2 ppm further confirm the transesterification.

The ^{13}C DEPT NMR spectrum of St-6MHA (Figure 22) enabled to clearly differentiate the secondary carbons from the grafted 6-MHA aliphatic chain as they appeared with a negative signal between 20 and 40 ppm (annoted as c, d, e, f and g). Moreover, a peak in the deshielded region of the spectrum is displayed at 134.7 ppm corresponding to the carbons involved in the double bonds of the maleimide.

The DS was determined by ^{1}H NMR and estimated to be 0.27. While this may be considered a relatively low DS, it actually corresponds to the modification of approximately 47 % of the available hydroxyl groups, based on the hydroxyl content of starch measured through titration (3.56 $mmol \cdot g^{-1}$). It is also important to note that the DS value may be underestimated due to the limited solubility of the modified starch in DMSO-d_6, which could hinder accurate peak integration in the NMR spectrum.

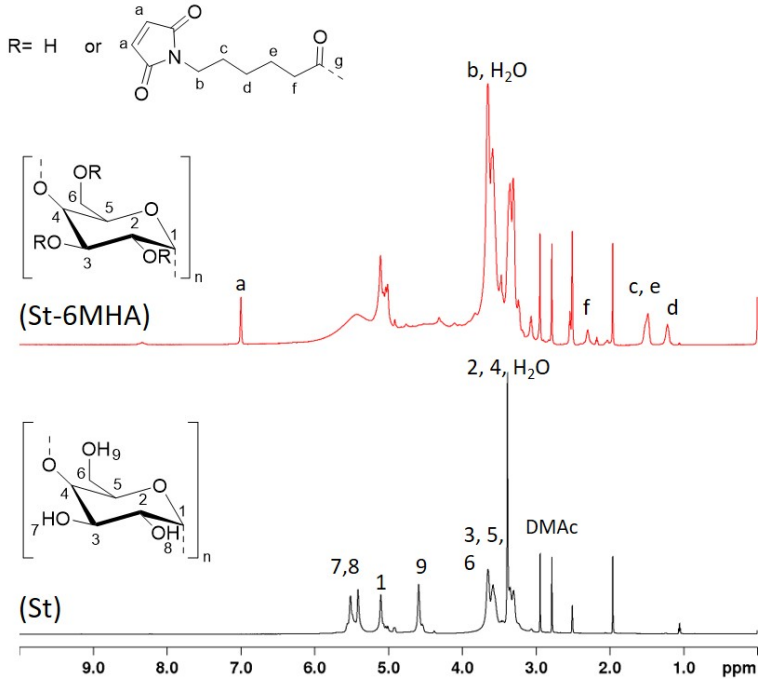

Figure 21. ^{1}H NMR spectra of St and St-6MHA synthesized in suspension.

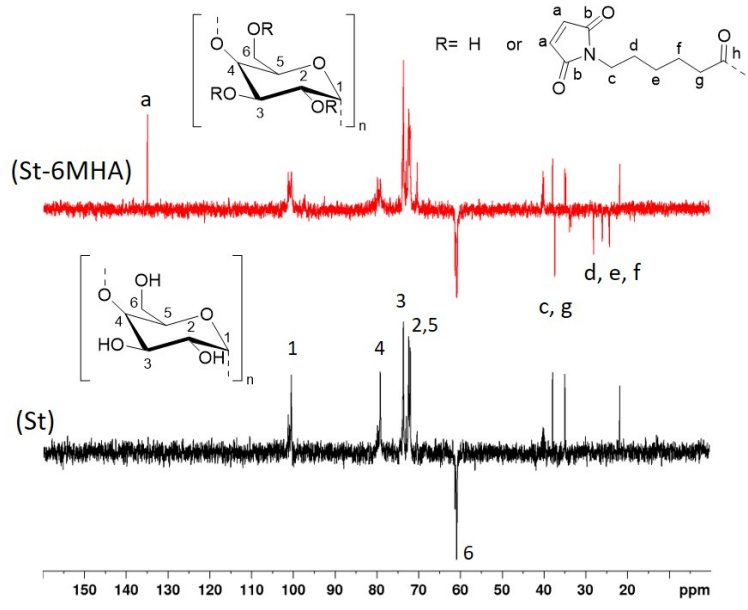

Figure 22. ^{13}C DEPT NMR spectra of St and St-6MHA synthesized in suspension.

Structural analysis of St-6MHA synthesized in suspension

Figure 23 displays the X-ray diffraction (XRD) patterns of St before and after esterification. The native St exhibited distinct crystalline peaks at 2θ values of 7.8° and 10.5°, along with overlapping peaks at 13.7°, 15.5°, 16.45°, and 21°, which are characteristic of its semi-crystalline structure. After reaction with the 6-MHA ester, these peaks were either greatly diminished or completely absent. In their place, a broad amorphous halo emerged around 2θ = 9.65°, along with a weaker peak at approximately 20°, suggesting a significant reduction in crystallinity and a transition toward a more amorphous structure within the starch matrix.

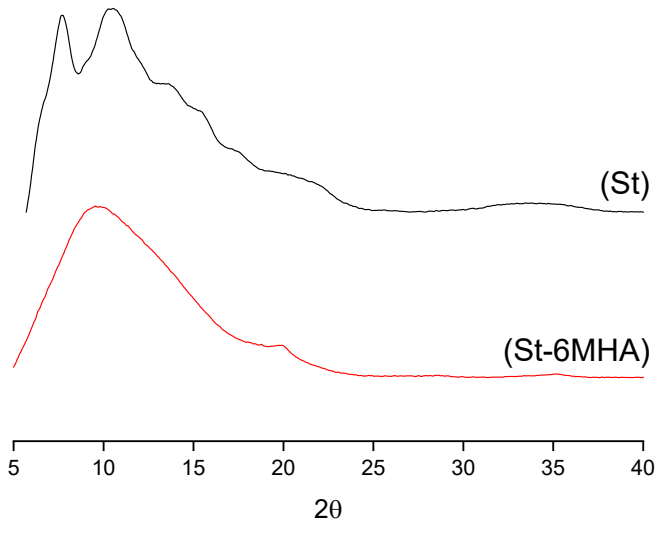

Figure 23. XRD patterns of St and St-6MHA synthesized in suspension.

This loss of crystallinity aligns with previous findings [60], which report that esterification typically disrupts the ordered structure of St. Crystalline regions in St are mainly formed by double helical arrangements in amylopectin, stabilized by intermolecular hydrogen bonds. The introduction of ester groups during the modification process partially replaces hydroxyl groups, thereby weakening both intra- and intermolecular hydrogen bonding. This substitution compromises the ability of St chains to maintain their crystalline packing, ultimately leading to a more disordered, amorphous structure [61]. To further investigate morphological changes occurring during the reaction, ESEM images were taken (Figure 24).

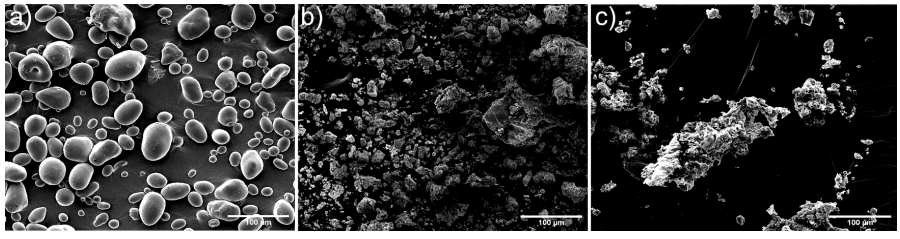

Figure 24. ESEM images of St before modification a), after mercerization process b) and after reaction c).

Alkaline pretreatment followed by esterification likely altered the microstructure and molecular interactions within St, as previously indicated by XRD analysis. Consequently, morphological changes can be expected. Figure 24 presents the ESEM images of St in its native form, after alkaline mercerization, and following esterification.

In its unmodified state, St appeared as oval or ellipsoidal granules, typically flattened along one axis, with diameters ranging from a few micrometers to about 100 µm. The granule surfaces were apparently smooth, showing minimal irregularities most of which were due to contact between granules.

After alkaline treatment and subsequent freeze-drying, the St exhibited a substantial loss of its organized granule structure. The gelatinization caused by the alkaline conditions led to a breakdown of the native morphology [62], resulting in irregularly shaped particles and agglomerates with rough surfaces. These altered structures size were comparable to St. Similar morphological changes were observed in the esterified St, though the surface of the particles appeared smoother. Comparable transformations in starch morphology have been reported in prior studies involving acid-catalyzed esterification processes [63, 64]. These changes showed the significant structural impact of both alkaline and esterification treatments on starch. Attempt to modify St following the same procedure without mercerization treatment were made but no changes in NMR or FTIR spectra were observed thus other synthetic routes were investigated to obtain higher DS despite loss of St native structure.

St-6MHA synthesis in solution

Polysaccharides like starch commonly require high DS for being used in advanced materials [64]. One effective strategy to increase DS involves carrying out esterification in a non-aqueous medium [65]. The innovation in the approach illustrated in Figure 25 lies in conducting the esterification in a one-pot reaction at room temperature without the need for hazardous catalysts. It is supposed that the solvent used in the process also acts as a catalyst, similar to the catalytic role of DMF reported in the literature [66] and can be recovered after the reaction, enhancing the sustainability of the method.

Before modifying St, 6-MHA was converted into its corresponding acyl chloride to enhance its reactivity with St hydroxyl groups. This step was carried out under an inert atmosphere to prevent moisture from reacting with the freshly formed acyl chloride. The high sensitivity of acyl chlorides to moisture makes their isolation and analysis challenging. While conventional FTIR is difficult to perform without risking hydrolysis from ambient moisture, NMR analysis has been successfully conducted by other researchers under strictly inert conditions [67]. To minimize the risk of hydrolysis, the acyl chloride was used immediately without purification. The St, pre-dissolved in DMAc, was added directly into the reactive mixture. Both St and St-6MHA were characterized by FTIR and NMR to confirm successful modification.

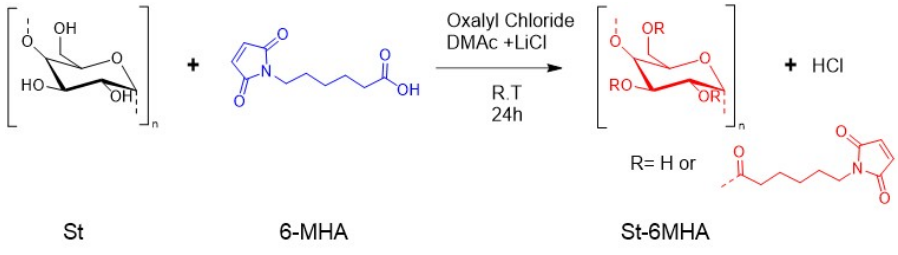

Figure 25. Schematic representation of St-6MHA synthetic route in solution.

Chemical characterization of St-6MHA

Absorption bands in FTIR spectra shown in Figure 26 were similar to those observed with the suspension method. However, the FTIR spectrum of St-

6MHA exhibited relatively higher peak intensities, suggesting a potentially higher DS. This was confirmed by quantitative ^{1}H NMR with a DS measured of 0.97 ± 0.02. Additionally, new absorption bands appeared at 826 cm^{-1} and 696 cm^{-1}, which were attributed to C–H bending and ring bending vibrations of the maleimide group, respectively.

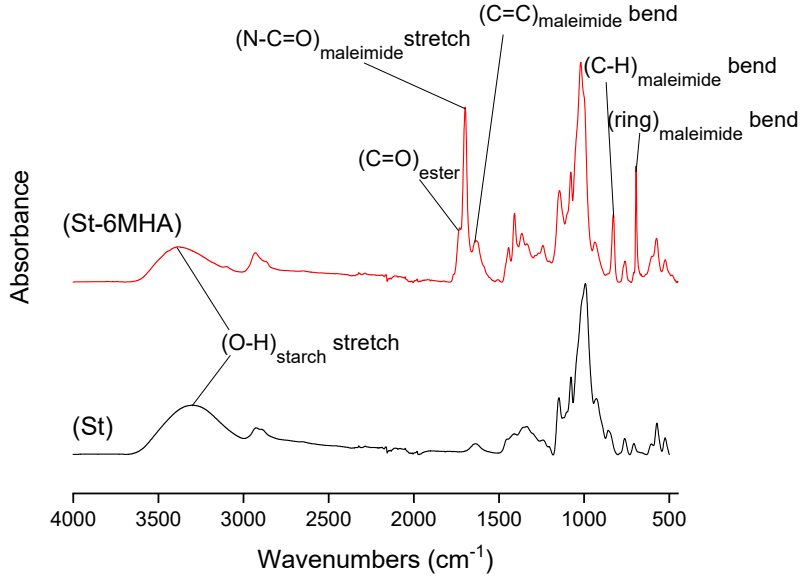

Figure 26. FTIR absorbance spectra of St and St-6MHA synthesized in solution.

The successful grafting of maleimide groups onto St was confirmed using both ^{1}H NMR (Figure 27) and ^{13}C NMR (Figure 28) analyses. In the ^{1}H NMR spectrum of St-6MHA, as observed previously for the suspension method distinct peak at 6.90 ppm was observed, corresponding to the protons on the maleimide ring from the grafted 6-MHA. In addition to observations made for St-6MHA in suspension (Figure 22), in the ^{13}C NMR spectrum (Figure 28), signals between 171.5 and 173.2 ppm were identified, representing the carbonyl (C=O) carbons of both the maleimide and the ester groups,

confirming successful esterification. These new peaks might be more intense with this synthetic strategy due to higher DS and the higher number of scans used for the analysis. Indeed, the lower natural abundance and sensitivity of ^{13}C nuclei required a high number of scans to obtain detectable signals in the ^{13}C NMR spectrum.

As mentioned earlier for the suspension method, in both ^{1}H and ^{13}C NMR spectra of the St-6MHA, the signals associated with the native St structure appeared broadened and reduced in intensity. This is attributed to partial esterification, which introduces greater structural diversity and increases the number of chemically non-equivalent proton environments, leading to signal broadening and decreased peak intensity [68].

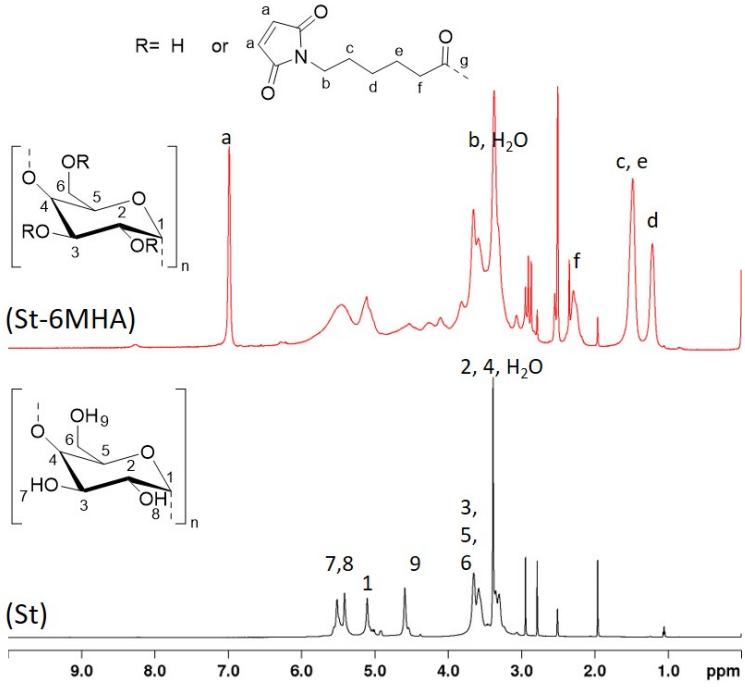

Figure 27. ^{1}H NMR spectra of St and St-6MHA synthesized in solution.

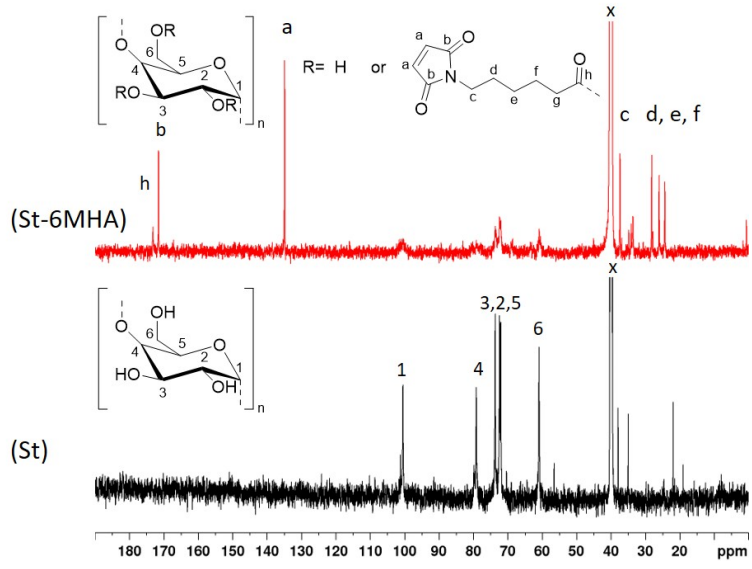

Figure 28. ^{13}C NMR spectra of St and St-6MHA synthesized in solution.

KL-FU synthesis

KL was modified with FGE to introduce furan moieties, primarily targeting the phenolic hydroxyl groups located at the chain ends, as depicted in Figure 29. The reaction was carried out in a basic aqueous medium to ensure dissolution. The amount of NaOH was calculated based on the total content of acidic groups in KL, including both carboxylic and phenolic hydroxyl groups. It was expected that due to their considerably higher pKa, aliphatic hydroxyl groups would not react, leading phenolate to act as a nucleophile with the epoxy ring.

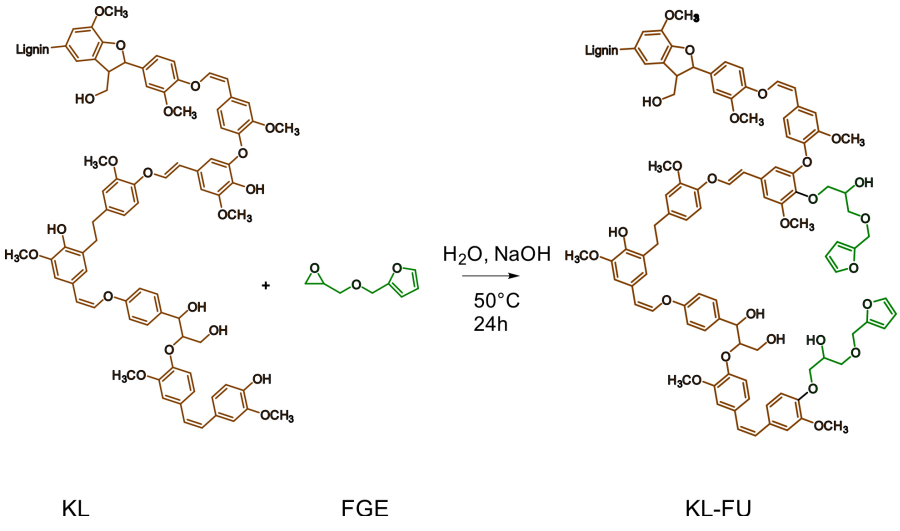

Figure 29. Schematic representation of KL-FU synthetic route.

Chemical characterization of KL-FU

FTIR spectra of KL and KL-FU were recorded, as shown in Figure 30. Characteristic absorption bands in the spectrum of KL-FU appeared at 1711 cm^{-1}, 1588 cm^{-1}, 918 cm^{-1}, and 750 cm^{-1}, corresponding to C=C stretching in the furan ring, aromatic C=C stretching, furan ring deformation, and C=C out-of-plane bending, respectively [69].

Moreover, furan grafting led to an increase in the intensity of the broad absorption band between 3000 and 3600 cm^{-1}, associated with O–H stretching vibrations. This change can be attributed to the opening of the epoxide ring during the grafting reaction, resulting in the formation of new aliphatic hydroxyl groups (see Figure 29 and 30).

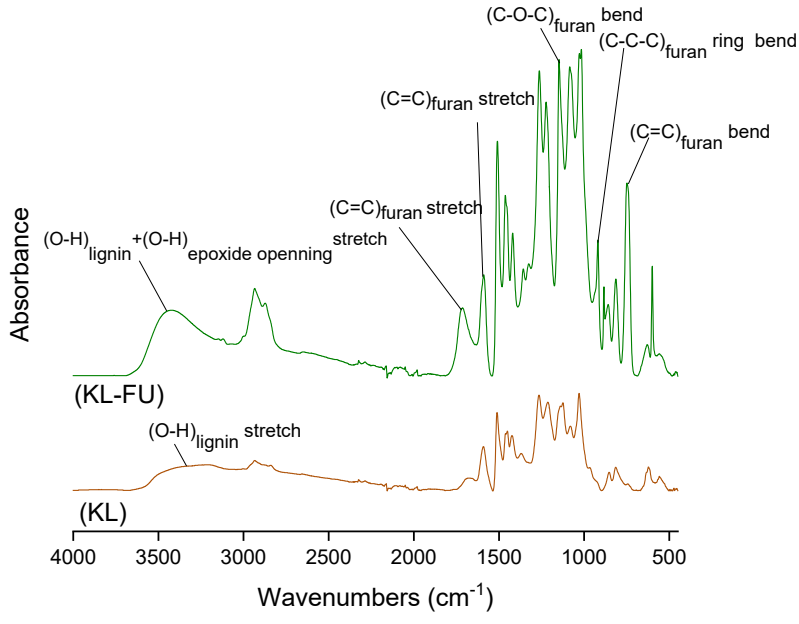

Figure 30. FTIR absorbance spectra of KL and KL-FU.

The success of this reaction was further confirmed by ^{1}H (Figure 31) and ^{13}C (Figure 32) NMR. Identical peaks to those displayed in FGE NMR spectra were observed. Indeed, the ^{1}H NMR spectra of KL-FU, displayed new peaks at 7.60, 6.40 and 4.20 ppm characteristic of protons belonging to the furan ring and the aliphatic chain of FGE. The ^{13}C NMR spectrum of KL-FU revealed the presence of all the carbon from FGE at 142, 110 and between 60 and 70 ppm. A shift of the peak characteristic of carbon labelled as C_1 and C_2 due to the ring opening of the epoxy group.

The signals corresponding to KL structure appear significantly broadened and less intense, as it was observed earlier for St-6MHA. Again, this reduced peak sharpness and intensity can be attributed to the greater number of chemically distinct proton environments.

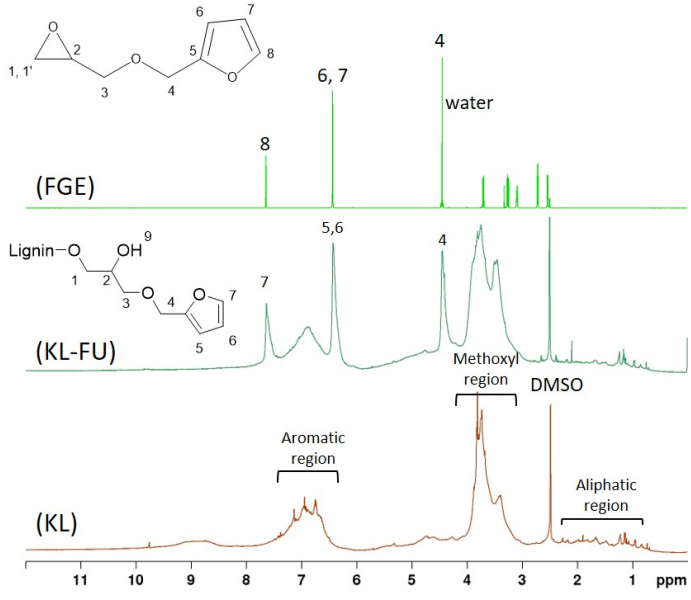

Figure 31. [1]H NMR spectra of FGE, KL and KL-FU.

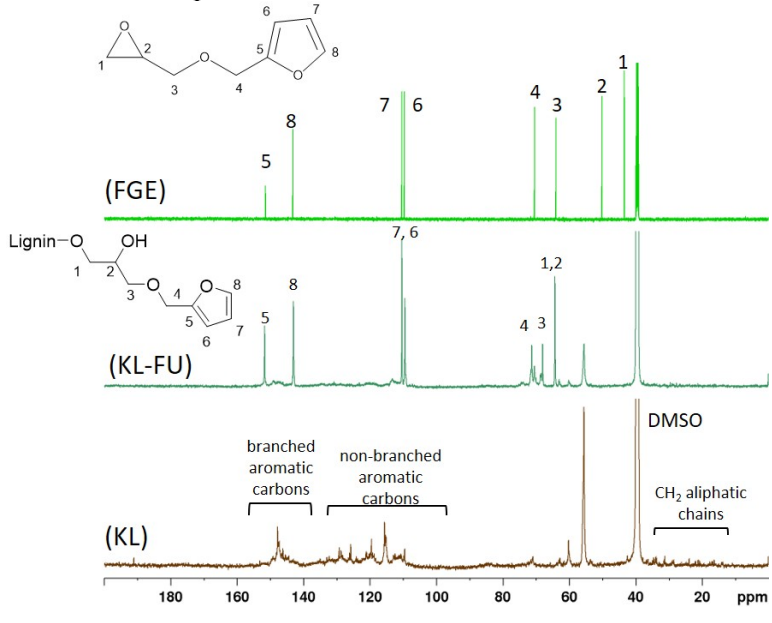

Figure 32. [13]C NMR spectra of FGE, KL and KL-FU.

As mentioned earlier, the opening of the epoxide ring during the reaction introduces new aliphatic hydroxyl groups, thereby increasing the overall aliphatic OH content in KL-FU. This is evidenced by the emergence of a relatively high-intensity peak around 143 ppm in the ^{31}P NMR spectrum (see Figure 33), separate from the native aliphatic OH signals of KL and is consistent with previous findings [69].

The furan content in KL-FU was determined using quantitative ^{31}P NMR, following the method described by Argyropoulos et al. [53]. The value calculated at 2.30 mmol.g^{-1} was consistent with findings by Duval et al. [69] claiming that the total phenolic groups in KL are capable of reacting when a slight excess of FGE is used.

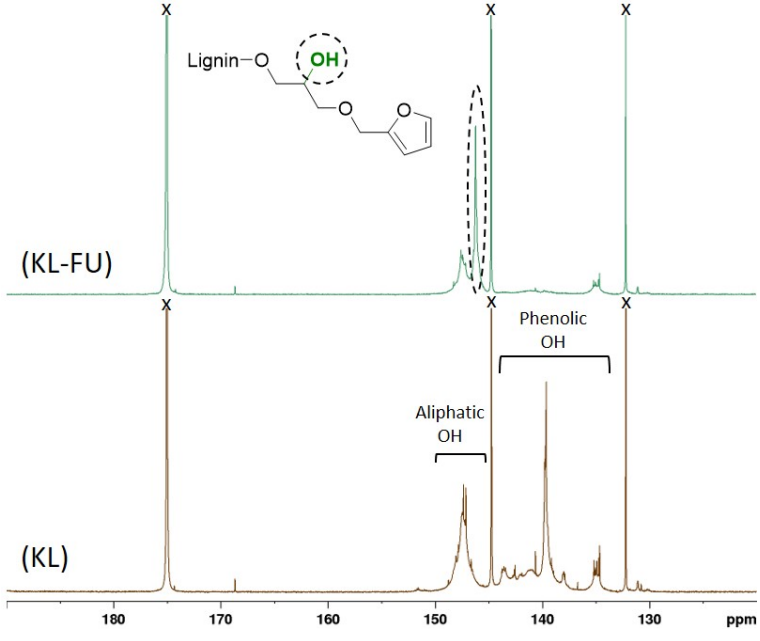

Figure 33. ^{31}P NMR spectra of KL and KL-FU.

Characterization of the network based on Diels-Alder reaction

St-6MHA and KL-FU were combined in equimolar amounts based on their maleimide and furan functionalities to study the DA adduct formation as illustrated on Figure 34.

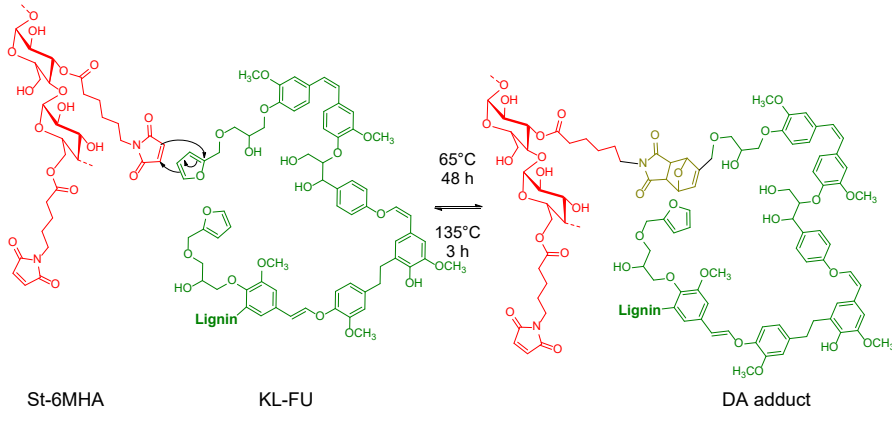

Figure 34. Schematic representation of Diels-Alder reaction between St-6MHA and KL-FU.

A solution in DMSO was made at a low viscosity to enable clear observation of gel-formation during forward DA reaction, as St-6MHA can form itself a viscous solution at high concentrations. The mixture was heated to 65 °C and stirred overnight, leading to visible gel formation. Upon heating at 135 °C for at least 2 hours, the gel turns back into a darker solution. In more dilute systems, phase separation was observed between the formed gel and the excess solvent, highlighting the role of concentration in network formation.

^{1}H NMR spectroscopy was performed before and after DA reaction (see Figure 35). To ensure clear signal resolution and to prevent gelation, St-6MHA and KL-FU were dissolved in DMSO-d_6 at low concentrations. Bands characteristic of maleimide and furan moieties could be observed between 6.0 and 8.0 ppm. Indeed, the resulting spectra showed a noticeable decrease in the signal at 7.62 ppm, which corresponds to the furan double bonds. This reduction indicates their consumption during the formation of the DA adduct. Based on the integration of signals associated with maleimide

groups around 7.0 ppm, the reaction conversion was estimated to be approximately 70%.

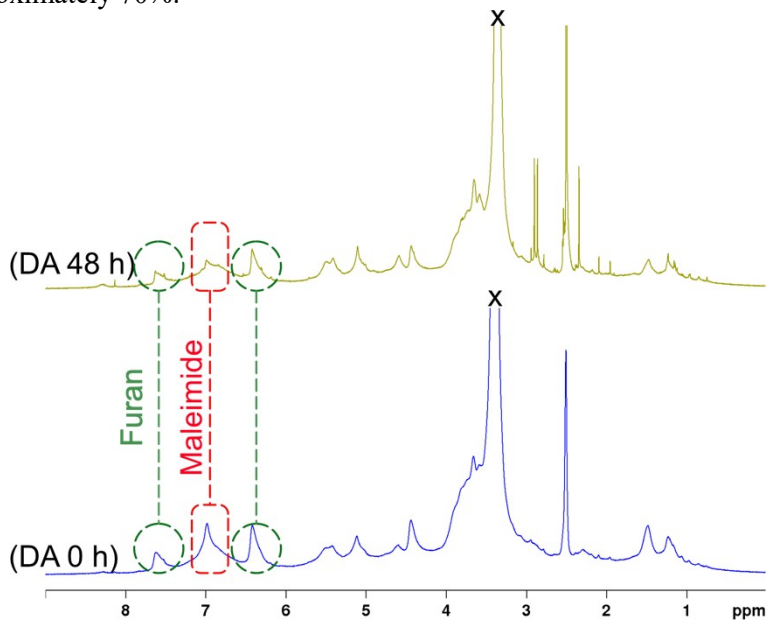

Figure 35. ^{1}H NMR spectra of St-6-MHA/KL-FU mixture before and after heating at 65°C for 48 h.

St-6MHA and KL-FU were dissolved in DMSO and subjected to thermal cycle to study both the forward and retro DA reactions. The samples were heated at 65 °C for 48 h to promote the forward reaction and then at 135 °C for 3 h to trigger the retro reaction. This heating cycle was repeated twice, and FTIR spectra were collected at regular time intervals. A gradual decrease in the absorbance band between 1640 and 1680 cm^{-1} attributed to the maleimide group indicated the formation of the DA adduct [70]. The changing intensity between the maleimide band and the DMSO reference band confirmed both the consumption of maleimide during the forward reaction and its formation during the retro reaction.

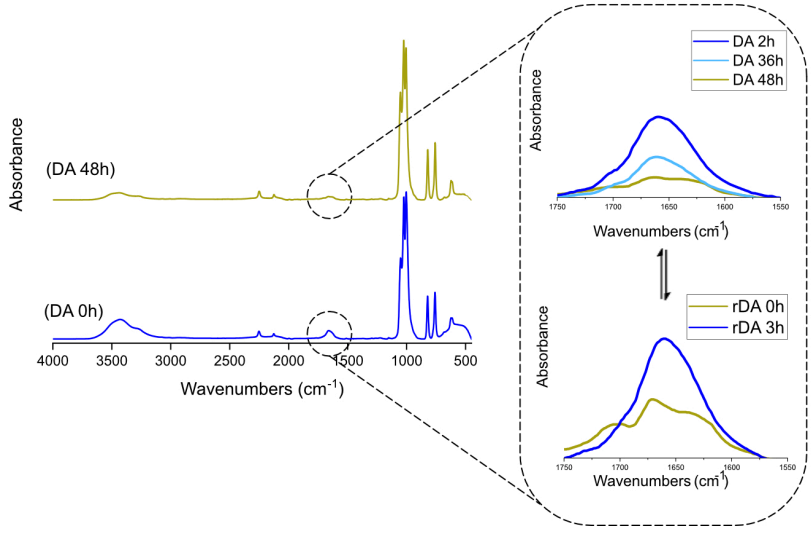

Figure 36. FTIR absorbance spectra of St-6MHA/KL-FU mixture before and after heating at 65°C for 48 h, (left) and of forward and retro DA reaction of St-6MHA/KL-FU mixture.

DSC thermograms of St-6MHA, KL-FU and the DA adduct of those two materials in order to show the retro DA reaction are shown in Figure 37. Two peaks not present in the thermograms of references were observed at 80 and 110°C in the thermogram of the DA adduct. Indeed, two stereoisomeric adducts endo and exo can be produced. The endo isomer forms when the electron-withdrawing group on the dienophile is oriented toward the diene, enabling favorable secondary orbital interactions. This pathway is kinetically favored due to its lower activation energy, allowing the endo product to form more rapidly. The exo product, while forming more slowly, is typically more thermodynamically stable. It is also known that the exo adduct undergoes rDA cleavage at a higher temperature than the endo [67]. The enthalpy energy of the two peaks were measured using the star-e software (Metler Toledo, Greifensee, Switzerland), confirming the considerably higher contribution from endo product. Surprisingly, this indicates the favored formation of the kinetic product [71] in contradiction with previous work reported by Morinval A. et al. [67]. This could be explained by the baseline irregularities obtained for St-6MHA and KL-FU around 100°C for which

trapped water might be responsible for. Moreover, in some cases, the formation of the endo product can be favored, typically at low temperatures for bulky materials as polysaccharides and lignin [71].

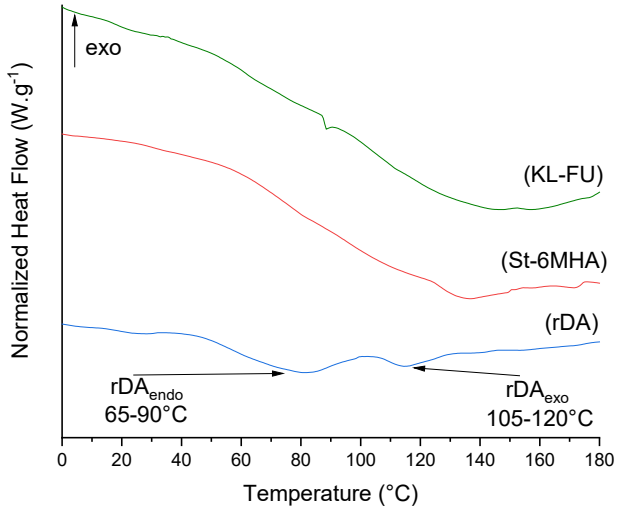

Figure 37. DSC thermograms of St-6MHA/KL-FU mixture after heating at 65°C for 48 h (rDA) and of St-6MHA and KL-FU as references.

3.1.2 Schiff base reaction between starch and carbon dots (paper IV)

DAS synthesis

St was oxidized into DAS as illustrated in Figure 38 to functionalize St with aldehyde functions able to react with amino group of carbon dots described later.

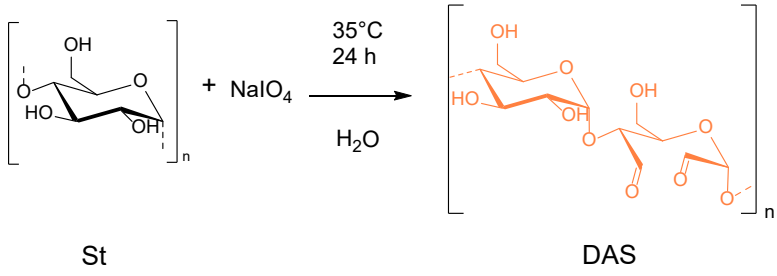

Figure 38. Schematic representation of DAS synthetic route

Chemical characterization of DAS

Figure 39 presents the FTIR spectra of St and DAS. It shows the presence of peaks at 1740 cm^{-1} and 1679 cm^{-1} corresponding to C=O stretching vibrations, which were absent in the spectrum of St. Moreover, characteristic peaks related to C–O stretching in St at 990, 1075, and 1150 cm^{-1} decreased in intensity or disappeared following its oxidation to DAS [72]. A signal at 875 cm^{-1} also appeared, suggesting the presence of hemiacetal bonds formed between dialdehyde groups and non-oxidized hydroxyls.

The C–H stretching band initially observed around 2960 cm^{-1} in St shifts to 2880 cm^{-1} after oxidation.

Carbonyl content was measured using a common titration procedure based on hydroxylamine [56] to further confirm the oxidation. The carbonyl content reached 85.1%.

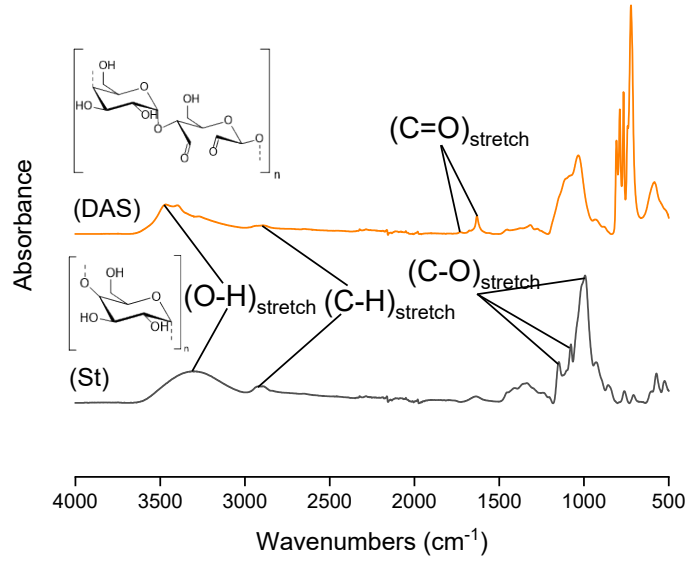

Figure 39. FTIR absorbance spectra of St and DAS.

Morphology of DAS

ESEM images of St and DAS at different magnifications are shown in Figure 40. As already shown in Figure 24, St typically appears as smooth particles with oval shape morphologies. In contrast, the images of DAS display distinct morphological characteristics compared to St. At lower magnification, DAS appears as individual particles with an irregular surface, dispersed throughout the field. When observed at higher magnification, the particles show more complex surface with tubular-like clustered structures. Similar structures of DAS have previously been reported [73]. Such changes can have an impact on the reactivity of DAS, particularly in the context of adhesive formulations with carbon dots described further.

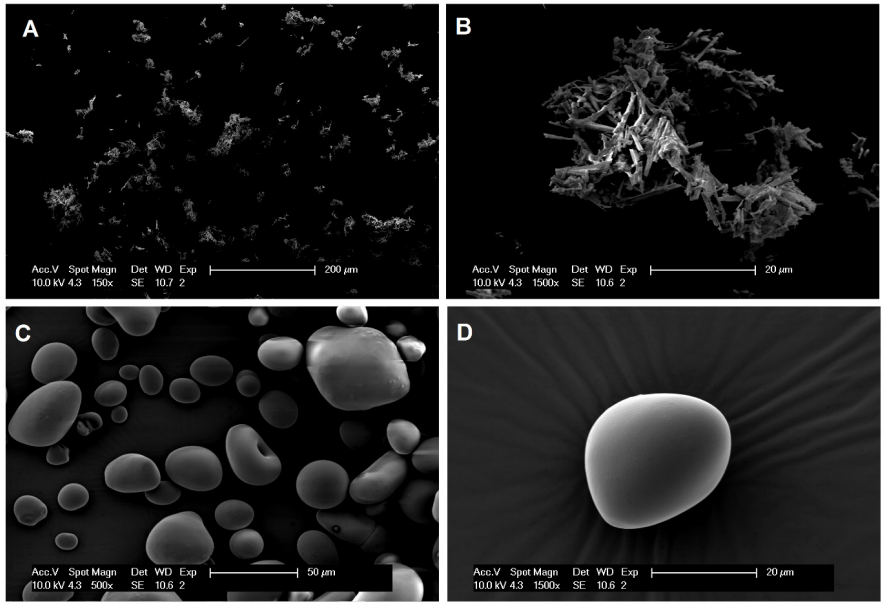

Figure 40. ESEM images of DAS (A-B) and of St (C-D).

CDs synthesis

As shown in Figure 41, CD1 was synthesized using citric acid, a bio-based precursor commonly employed in the preparation of graphene quantum dots and carbon nanomaterials [50]. Formamide and aniline were used to incorporate nitrogen-containing functional groups such as amines and amides. These nitrogen-rich functionalities enable crosslinking, which is essential for designing bio-based adhesive systems. In a next step, CD1 was further functionalized through microwave-assisted amidation with branched PEI, resulting in the formation of CD2.

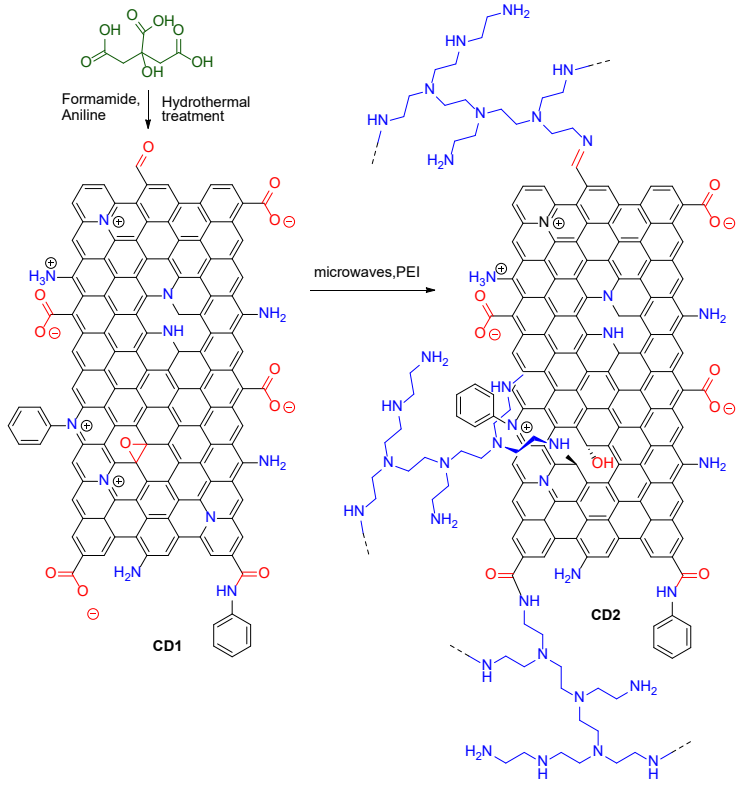

Figure 41. Schematic representation of the synthetic route used for the preparation of CD1 and CD2.

Chemical characterization of CDs

The FTIR spectra of CD1 and CD2 (see Figure 42) show relatively complex signals, confirming the presence of multiple functional groups. Concerning CD1, peaks corresponding to N–H stretching at 3379 cm^{-1}, aromatic C–H stretching in the 3100–3000 cm^{-1} range were observed. A strong peak displayed at 1697 cm^{-1} is attributed to the C=O stretching vibration of amide groups. A distinct signal at 1497 cm^{-1} indicates the presence of pyridinic nitrogen atoms, suggesting nitrogen doping. Stretching vibrations of carboxylate groups appear at 1345 and 1399 cm^{-1}.

The FTIR spectrum of CD2 shares similarities with CD1 but also reveals characteristic signals confirming successful incorporation of PEI. A broad N–H stretching band around 3366 cm^{-1} is observed, corresponding to

primary and secondary amine groups introduced by PEI. Additionally, peaks at 2931 and 2858 cm^{-1} can be attributed to the C–H stretching vibrations from the aliphatic chains of PEI. Strong N–H bending vibrations further support evidence of amine functionalization. Indeed, band at 1566 cm^{-1} and several overlapping bands in the 1560–1600 cm^{-1} range were present. Furthermore, multiple C–N stretching vibrations were detected between 1000 and 1300 cm^{-1}.

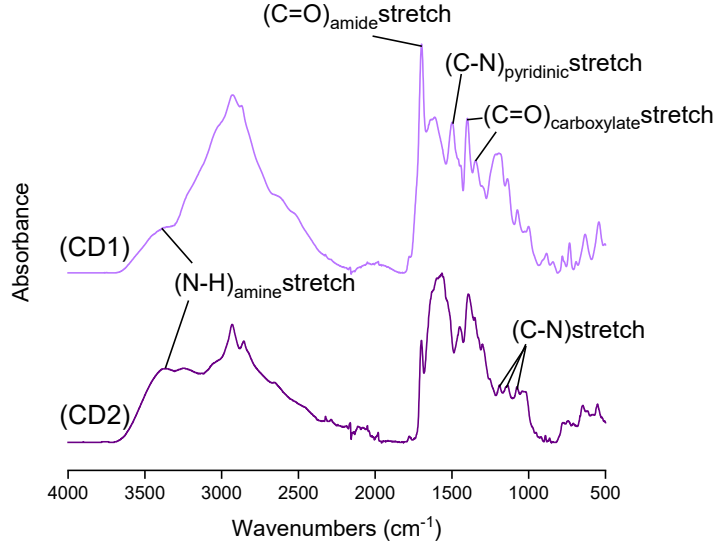

Figure 42. FTIR absorbance spectra of CD1 and CD2.

Figure 43 shows the high-resolution C1s XPS spectra of CD1 and CD2, while detailed values of integrals and percentage contribution of the four deconvoluted signals can be found in Table 2. The presence of various carbon bonding environments was confirmed, including sp^2 and sp^3 hybridized carbon atoms, carbon bonded to nitrogen (from amines or amides), and carbonyl groups associated with carboxylate and amide functionalities.

The XPS spectrum of CD1 shows considerable C–N contributions, indicating the presence of amide and amine functionalities, which aligns with the FTIR findings. Moreover, deconvolution of the spectra confirmed the

functionalization of CD1 with PEI to form CD2 as a notable increase in C–N bonding was observed, particularly evident from the enhanced signal at 286.5 eV. Indeed, it can be seen in Table 2, a rise in the C–N signal area from 3.497 in CD1 to 3.897 in CD2. Additionally, the signal corresponding to sp^3 carbon (285.5 eV) also increased in CD2, consistent with the methylene-rich structure of branched PEI being introduced onto the CD1 surface.

Both CD1 and CD2 displayed broad C=O signals around 288-288.5 eV, attributed to carbonyl-containing groups such as carboxylates, amides, or esters. Interestingly, CD2 exhibited a slight increase in the intensity of this band, likely resulting from additional oxidation or partial carbonization during the microwave-assisted PEI functionalization process.

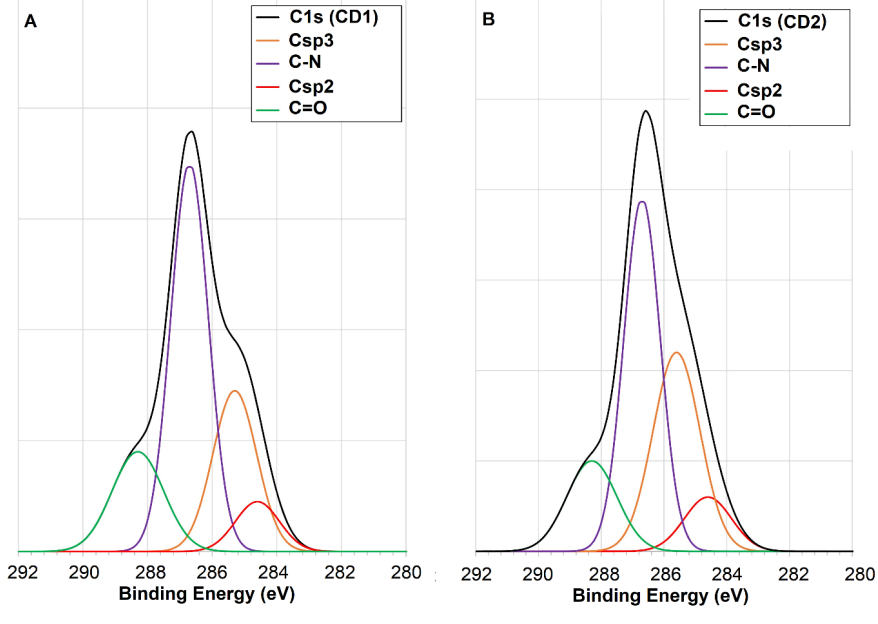

Figure 43. HR-C1s spectra of CD1 and CD2 and their deconvolution.

Table 2. Integrals and percentage contribution of the four deconvoluted signals of the HR-C1s XPS spectra of CD1 and CD2.

		CD1		CD2	
Signal	Band Energy (eV)	Integral	Percentage	Integral	Percentage
Csp2	285.0	0.759	11.7	0.899	9.9
Csp3	285.5	1.349	20.7	3.297	36.3
C-N	286.5	3.497	53.8	3.897	42.9
C=O	288.0 - 288.5	0.899	13.8	0.999	10.9

Morphology of CDs

The ESEM images of CD1 and CD2 are presented in Figure 44. Images of CD1 showed quasi-spherical particles with relatively smooth surfaces and sizes between 1 to 100 µm, some of which appear merged. This morphology is consistent with observations from recent studies on CDs [74], and it aligns with the structural effects of freeze-drying processes [75].

In contrast, CD2 displayed a relatively different morphology. As illustrated in Figure 44.C, flakes with sharp, well-defined edges appeared tightly arranged, possibly suggesting partial crystallinity. These structures may result from processes such as exfoliation or layer-by-layer assembly.

These distinct morphological features between CD1 and CD2 could have an impact on their functional properties. Specifically, they may affect particle volume and surface area, both of which are critical for adhesive penetration and bonding efficiency in various applications.

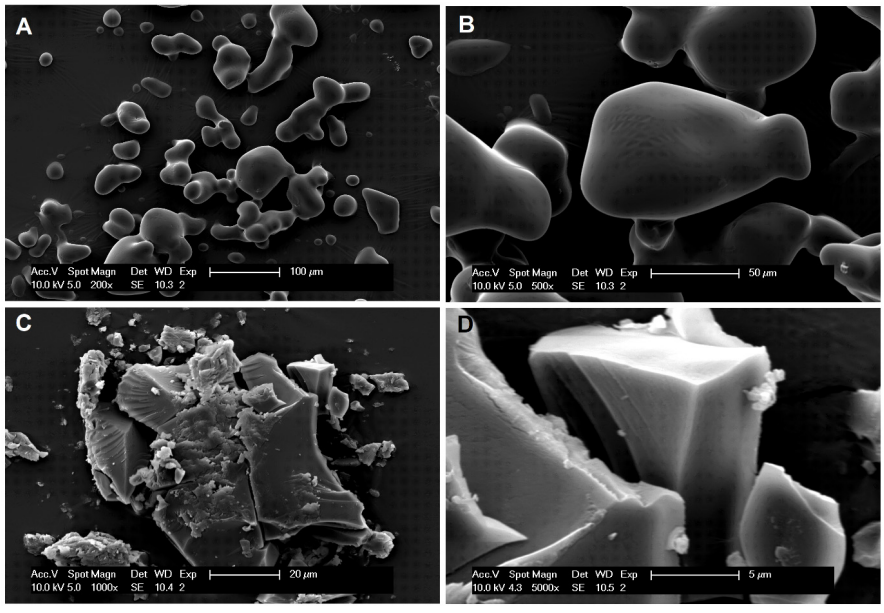

Figure 44. ESEM images of CD1 (A-B) and of CD2 (C-D).

Characterization of the network based on Schiff base reaction

Due to the mixture's insolubility in common deuterated solvents after reaction, NMR analysis could not be performed in solution. Attempts to analyze these materials using CP-MAS NMR were also unsuccessful. Despite careful packing of the powdered samples, the rotor failed to spin at the required speed. This issue might be associated with the starch component, as similar problems were encountered during trials with both St and DAS.

As a result, FTIR spectroscopy was employed to investigate the chemical structure of DAS and its cross-linked networks with CDs and HMDA, as shown in Figure 45. Although the spectra were complex and featured overlapping signals, a consistent trend was observed across all samples. Notably, a distinct peak corresponding to the C=O stretching vibration of amide groups appeared at 1698 cm^{-1} in each of the two DAS-based mixtures.

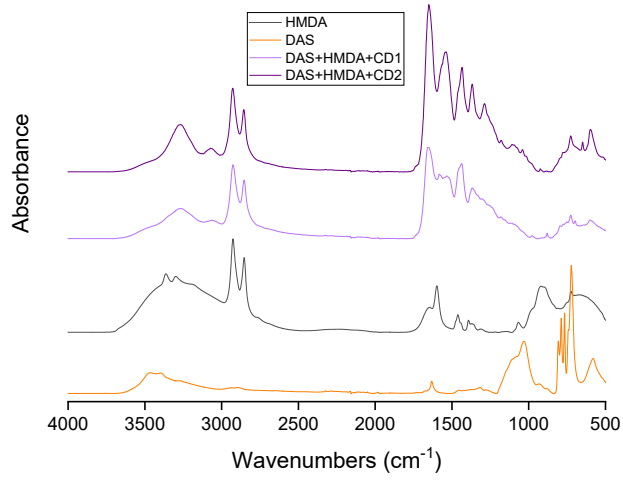

Figure 45. FTIR absorbance spectra of the DAS/CDs/HMDA conjugated system.

3.2 Debondability of reversible networks for use in wood adhesives (papers III and IV)

3.2.1 Diels-Alder reaction (paper III)

When designing debondable adhesives, there is a competition between adhesion (bonding to the substrate) and cohesion (internal strength of the adhesive). For debonding to occur, failure must happen either within the adhesive itself or at the interface with the substrate, as illustrated in Figure 3. Therefore, to achieve controlled debonding, the adhesion or the cohesion must rely importantly on the reversible bonds incorporated into the adhesive system.

Here, it was designed a debondable adhesive system based on the formation of a thermally reversible bond within the adhesive as well as between the adhesive and the wood substrate to bond (see Figure 46).

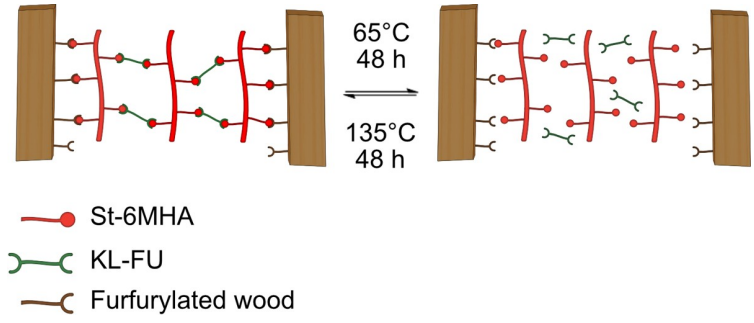

Figure 46. Schematic representation of debondable adhesive principle based on Diels-Alder reaction.

Furan functionalization of wood

To enable the formation of a DA adduct between St-6MHA and the wood surface, wood veneers were first furfurylated; a conventional wood protection process that introduces furan groups onto the wood surface.

Under 103°C, furfuryl alcohol undergoes a complex polymerization process characterized by multiple reactions, which lead to the development of a highly cross-linked and structurally heterogeneous polymer network [76, 77]. The different mechanisms reported lead to the formation of polymer chains containing furfuryl alcohol dimer, furfuryl ether, 2,5-dihydrofuran ending with levulinic acid [76].

Evidence of the furan presence on the furfurylated wood surface was made through FTIR of furfurylated and untreated beech veneer. The spectra are shown in Figure 47. A cured solution of FA was used as a reference. Characteristic peaks of furan were found in the spectrum of the furfurylated specimen at 1710, 1600, and 1418 cm^{-1} corresponding to C=O stretching vibration, [78] C=C stretching [79], and C–H bending in oxygenated aromatic compounds.

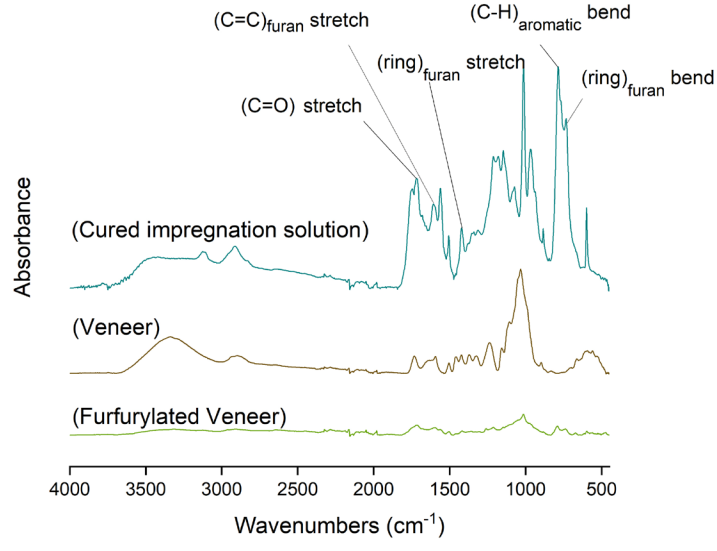

Figure 47. FTIR absorbance spectra of furfurylated and raw beech veneer, and of the cured solution used for furfurylation.

Thermal stability of St-6MHA an KL-FU

Thermograms of St-6MHA and KL-FU are presented in Figure 48 with their respective unmodified materials. It is important to ensure that materials involved in the adhesive system can resist to degradation under the curing condition used in the adhesion process. It can be seen, according to Figure 48 that the thermal stability profiles of St-6MHA and KL-FU differ from those of their original materials. However, in both cases, thermal degradation begins only above 200 °C, which confirms that debonding tests at 65 °C and 135 °C, as well as shear testing after curing at 160 °C, can be safely conducted without compromising the materials.

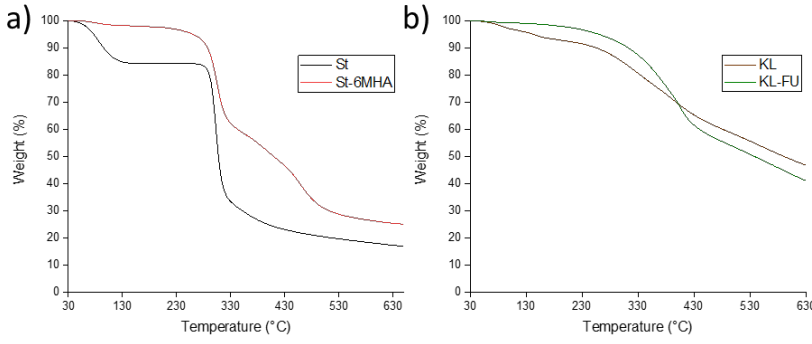

Figure 48. TGA thermograms of St and St-6MHA a) and of KL and KL-FU b).

Mechanical properties of different formulations

In order to study the potential use of St-6MHA and KL-FU as an adhesive, the shear strength of different blends bonding furfurylated beech veneers was measured. The average maximum shear strength values can be found in Figure 49.

Overall, the addition of KL-FU to St-6MHA was found to enhance shear strength value, reaching a maximum of 5.00 ± 0.5 MPa when the formulation contained a 2:1 ratio of maleimide to furan groups. However, increasing the proportion of furan groups beyond this ratio resulted in a slight decrease in shear strength. This diminution suggests that maleimide groups play a dominant role in adhesion, likely through DA adduct formation with furan functionalities introduced on the surface of furfurylated wood veneers.

Thus, altering the St-6MHA to KL-FU ratio, impacts the balance between adhesion and cohesion associated with DA adduct formation.

Increasing KL-FU content enhanced cohesion by forming more DA cross-linked St-6MHA but reduced the number of maleimide groups available to bond with the wood surface, thereby slightly diminishing adhesion.

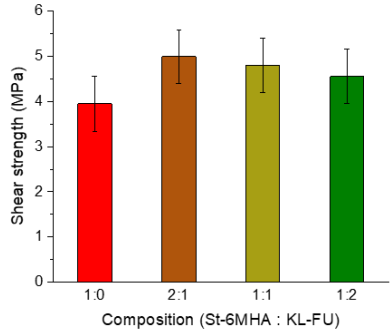

St-6MHA	KL-FU	Shear strength (Mpa)
1	0	3,95 ± 0,7
2	1	5,00 ± 0,5
1	1	4,80 ± 0,6
1	2	4,56 ± 0,6

Figure 49. Shear strength values of different St-6MHA:KL-FU compositions.

A direct comparison with other starch-based debondable adhesives for wood was not possible, as no prior studies on such systems were found in the literature. Nonetheless, the shear strength values obtained in this study are within the range typically reported for some conventional commercial adhesives. Stöckel et al. [80] evaluated the tensile shear strength of beech veneer bonded with urea-formaldehyde and melamine-urea-formaldehyde adhesives. Using similar curing techniques (ABES), they reported maximum shear strengths between 4.0 and 6.0 MPa, depending on curing time. Similarly, Hosseinpourpia et al. [81] found that birch veneers bonded with a commercial polyurethane adhesive reached shear strength of approximately 3.2 MPa.

Accurate comparison of adhesive strength requires standardized testing under identical conditions. Adhesive performance is highly dependent on factors such as wood species, curing methods, surface preparation, and testing protocols. As a result, the values cited should be seen as indicative rather than directly comparable.

Debondability evaluation

ABES was used to evaluate the thermal debondability of St-6MHA:KL-FU adhesive when used to bond furfurylated beech veneers (Figure50.b). Measurements on untreated beech veneers were also made as references (Figure 50.a).

The functionalized system demonstrated relatively higher shear strength on untreated beech veneers, reaching 3.3±0.3 MPa compared to 2.7±2 MPa for the mixture of unmodified materials (Raw St:KL). Despite the reduced number of hydroxyl groups after functionalization, the bonding strength did not decrease. The aliphatic hydroxyl groups (see Figure 29) formed during modification of KL along with the hydrogen bond acceptor character of maleimide and furan seem to have compensated the hydrogen bonding loss from hydroxyl groups' substitution. The functionalized adhesive seemed to benefit from new bonding mechanisms and improved network formation, resulting in superior shear strength.

In the absence of a DA network (mixture of St:KL), a slight increase in shear strength was observed, indicating that the heat exposure alone does not weaken adhesion when no DA adducts are formed. On the opposite, in samples bonded with the functionalized St-6MHA and KL-FU on untreated veneer, a drop in shear strength from 3.3 MPa to 2.5 MPa after thermal treatment was observed. This suggests the rDA reaction occurred, breaking the covalent DA adducts and converting them back to their respective maleimide and furan groups. The loss of these crosslinks likely weakened the internal cohesion of the adhesive, making it more prone to failure at lower shear strength. However, the adhesive did not fully debond after heating, implying that the DA adducts do not contribute predominantly to either adhesion or cohesion in this configuration.

The same experiment was repeated using furfurylated beech veneers (see Figure 50.b), which introduced reactive furan groups on the wood surface. None of the samples bonded with the control St:KL mixture performed well enough to be tested in the ABES apparatus, with all failing during handling. This result is attributed to the hydrophobic nature of PFA, which fills the wood's porous structure and blocks native hydroxyl groups, thereby limiting adhesive penetration and preventing hydrogen bonding. Prior research [82, 83] supports these findings, reporting that PFA can act as a protective barrier that block hydrogen bonding with wood cellulose, hemicelluloses or lignin.

When St-6MHA:KL-FU adhesive was applied to furfurylated veneers, a significant drop in shear strength from 3.6 MPa to 1.3 ± 0.2 MPa after thermal treatment was observed. The residual bonding strength indicates some DA bonds might be able to reform upon cooling. This was confirmed by manually separating immediately after removal from the oven, demonstrating the thermally reversible nature of the DA linkage.

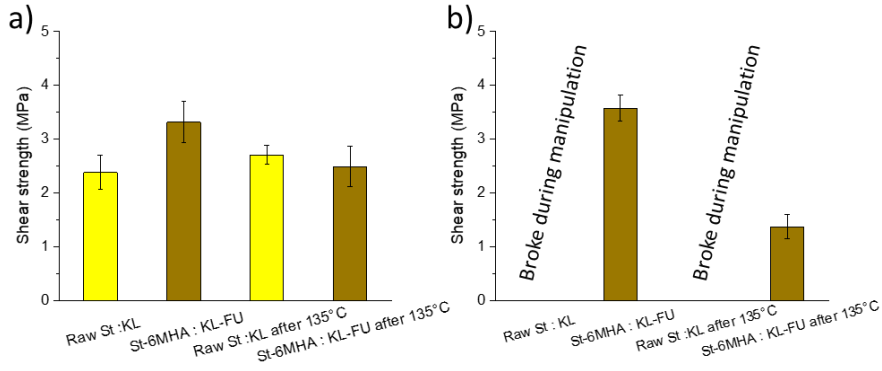

Figure 50. Shear strength measurements using ABES of St:KL and St-6MHA:KL-FU (2:1 ratio of maleimide to furan groups) mixture in DMAc before and after heat treatment at 135°C for 4 h using a) untreated beech veneers and b) furfurylated beech veneers.

Wood penetration

Images of the bond line between untreated and furfurylated pine samples bonded with the St-6MHA:KL-FU adhesive, captured with a fluorescence microscope, are presented in Figure 51.

Penetration is often regarded as a key factor influencing bond strength [84]. Indeed, it was reported that a deeper adhesive penetration enhances mechanical interlocking and overall bond performance [85].

As mentioned earlier, multiple studies have explored the incorporation of DA bonds into conventional adhesives such as polyurethanes [86, 87], and epoxies [88, 89] where the adhesive network is formed from low molecular weight monomers that polymerize into a larger, cross-linked structure. The small molecular size of these starting compounds allows them to effectively penetrate the porous wood structure, including the cell walls. Upon polymerization, they interlock with the substrate, forming a strong bond. In that case triggering DA adduct cleavage can simultaneously weaken both cohesion and adhesion. Moreover, it has to be noted that despite the PFA formed during furfurylation (dark brown region in Figure 51.c and 51.d);

previous studies reported the possibilities of conventional wood adhesives to penetrate wood structure [85].

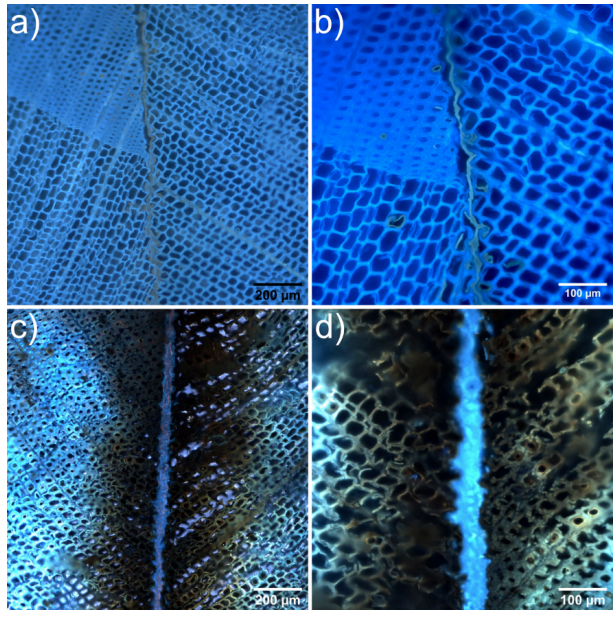

Figure 51. Images of cured adhesives on transverse surfaces of untreated and furfurylated pine using a fluorescence microscope.

The relatively high molecular weight of starch (amylose Mw ~10^5 g.mol^{-1} and amylopectin Mw~10^6–10^7 g.mol^{-1} [90]) compared to conventional wood adhesives limits its ability to deeply penetrate the wood cell walls. This limitation is clearly reflected in the microscopy images, which show no evidence of adhesive penetration into the cell wall structure. Instead, bulky adhesive accumulation is visible along the bond line and open cells at the interface. Nonetheless, in untreated pine, minor adhesive migration was observed along the ray cells, indicating some localized penetration.

Interestingly, the bond line in furfurylated samples appeared thicker compared to the one in unmodified pine. This might be the result of a stronger network able to trap residues of solvent during the curing.

Micromechanical study

The resulting lack of penetration in wood structure, suggests that the adhesion mechanism in starch-based systems fundamentally differs from adhesives based on small molecules. Rather than mechanical interlocking through deep penetration, bonding relies predominantly on hydrogen bonding between the hydroxyl groups of starch and the hydroxyl-rich components of wood and surface interlocking. Micromechanical investigation was made using AFM to understand the contribution of St-6MHA and KL-FU in the adhesion mechanism.

At this scale, the forces detected between the probe and the sample primarily arise from four types of interactions: electrostatic forces, van der Waals forces, capillary forces, and chains interlocking [91, 92]. Electrostatic forces are generally considered negligible in air, especially when compared to capillary forces and van der Waals forces. Moreover, as the surfaces prepared were dried with nitrogen gas, capillary forces can also be considered as negligible.

A colloidal probe was coated with CNF to better mimic the natural interactions between wood and the samples studied.

Figure 52 and 53 show that CNF-coated probe had mostly a visible influence on lignin samples. For a contact time of 10 sec, the maximum adhesion force increased from 590 ± 19 with SiO_2 probe to 654 ± 56 mN/m with coated probe. The chemical diversity of KL (aromatic rings, phenolic hydroxyls, and carbonyl) compared to starch seems to enable more interaction mechanisms with the CNF-coated probe.

The influence of time on recorded adhesion forces of KL, St, and silica reference using the two types of colloidal probes are shown in Figure 52.

Adhesion forces increased with longer contact times (called “surface delays” on Figure 52), reflecting the time-dependent nature of weak interactions such as physical entanglements, and hydrogen bonding. For St, after approximately one second, the adhesion force quickly reached a maximum. KL exhibited a continuous rise in adhesion until 20 sec. This might found an explanation in the difference in structure between KL and St. In one hand, the rich accessible hydroxyl from St and on the other hand, the more various functionalities but more hindered from KL lead to different behavior.

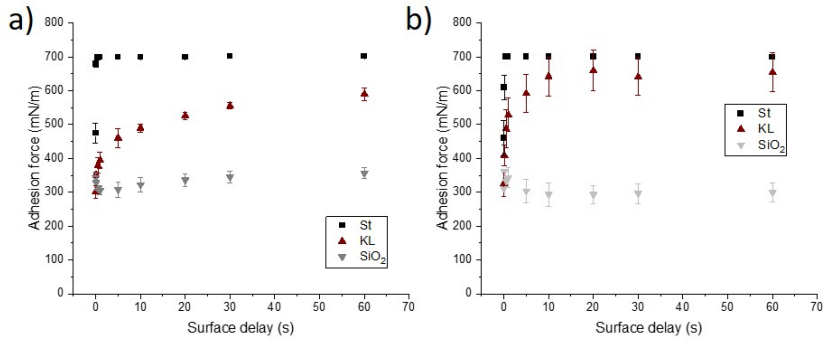

Figure 52. Normalized adhesion force from AFM adhesion measurement of St and KL at different surface delays using a) $Si0_2$ colloidal probe b) CNF coated $Si0_2$ colloidal probe.

The influence of time on recorded adhesion forces of KL-Fu, St-6MHA, and silica reference using the two types of colloidal probes are shown in Figure 53.

The plots reveal a clear reduction in adhesion following the chemical modification of St. This can be the result of weaker hydrogen bonds and compatibility with the probes as grafting 6-MHA onto St reduces the number of free hydroxyl groups as well as potentially increasing hydrophobicity.
KL-FU demonstrated higher adhesion than KL. This increase can be related to the formation of new aliphatic hydroxyl groups in KL-FU. Indeed, these hydroxyl groups are located on side chains, potentially more flexible and exposed compared to the native hydroxyl groups in KL, resulting in improved van der Waals interactions.

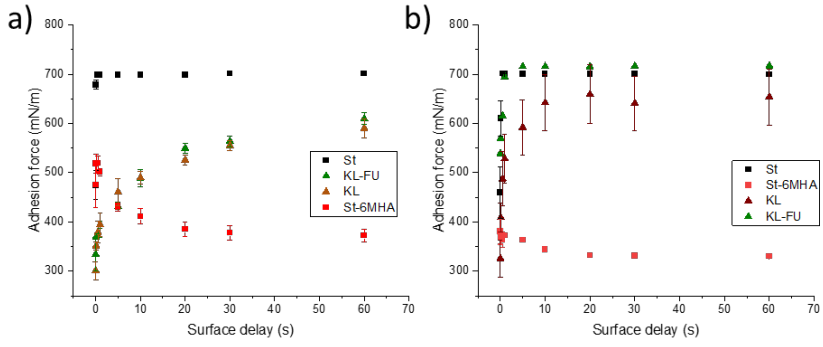

Figure 53. Normalized adhesion force from AFM adhesion measurement of St, KL, St-6MHA and KL-FU at different surface delays using a) $Si0_2$ colloidal probe b) CNF coated $Si0_2$ colloidal probe.

3.2.2 Schiff base reaction (paper IV)

As illustrated in Figure 54, the adhesive formulation is based on the blend of DAS, CDs and HMDA. The formation of an imine (Schiff base) network between the aldehyde of DAS and the imine functions of CDs and HMDA along with solvent evaporation are responsible for the adhesive curing.

The internal cohesion of the adhesive primarily arises from this imine-based cross-linked network. On the other hand, physical interlocking of DAS chains within the surface of wood, as well as hydrogen bonding might be responsible for adhesion with wood. Indeed, hydrogen bonds can form between hydroxyl and carbonyl groups on DAS, amino groups on HMDA and CDs, and the various hydroxyl groups naturally present in lignin, cellulose, and hemicelluloses within the wood structure.

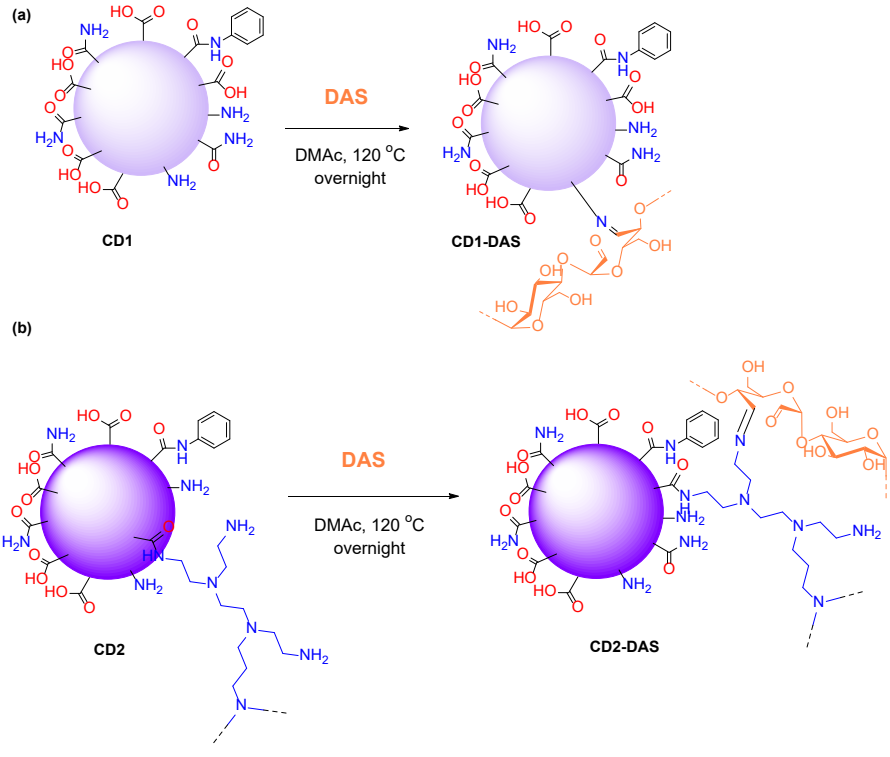

Figure 54. Schematic representation of the conjugation between CDs and DAS resulting in CD1-DAS a) and CD2-DAS b).

Thermal stability of DAS and CDs

As for St-6MHA and KL-FU, the thermal stability of DAS and CDs was evaluated using TGA. The thermograms of St, DAS, CD1, and CD2 are shown in Figure 55. Since these materials will be subjected to elevated temperatures both to facilitate imine bond formation and to ensure solvent evaporation, it is essential to confirm their stability under the 160 °C conditions used in further bonding testing with ABES.

As illustrated in Figure 55, both St and DAS showed a two-step thermal degradation that can be associated with the evaporation of trapped water followed by the decomposition of starch backbone. DAS began to thermally degrade at a lower temperature (approx. 175°C) compared to St. This may be attributed to the breakdown of starch's semi-crystalline structure following oxidation. A previous study suggests that a higher amylopectin-to-

amylose ratio enhances the thermal stability of starch [93], likely due to the greater crystallinity commonly associated with amylopectin, which forms the crystalline regions within starch granules.

Thermograms of both CDs showed that both materials remained thermally stable up to approximately 150°C. As for starch samples, the observed mass losses below this temperature were primarily attributed to the evaporation of water. The multiple steps observed in both CDs thermograms above 200°C attributed to the wide variety of functional groups makes their interpretations difficult. However, within the context of this study, the thermal stability of both CDs up to 200°C suggests they are well suited for curing conditions needed for solvent evaporation.

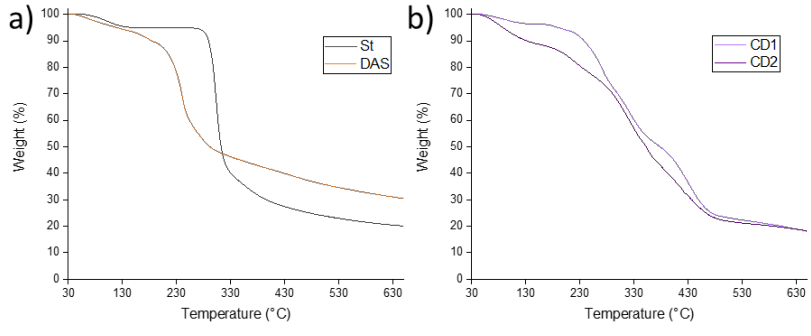

Figure 55. TGA thermograms of St and DAS a) and of CD1 and CD2 b).

Curing properties of DAS adhesive systems

The influence of pressing time, HMDA and CDs on the shear strength of the different formulations were investigated using ABES; results are shown in Figure 56. Pressing time plays a crucial role in adhesive performance, influencing not only bond strength but also manufacturing speed and energy consumption. As expected [94], longer pressing times led to increased shear strength values, likely due to enhanced curing and more complete solvent evaporation.

The effect of imine bond formation on shear strength was demonstrated by the enhanced adhesion observed when DAS was combined with HMDA.

This mixture achieved a relatively higher average maximum shear strength of 3.63 ± 0.44 MPa, compared to 2.40 ± 0.11 MPa for DAS alone and 2.95 ± 0.12 MPa for HMDA alone.

DAS solutions with CDs showed faster curing compared to solutions containing only DAS. Indeed, DAS+CD2 reached the maximum shear strength of the DAS solution within just 30 sec (2.47 ± 0.10 MPa), while CD1 reached 2.19 ± 0.09 MPa in 120 sec. One explanation can be found in the good thermal conductivity of graphene like materials. Moreover, the added amino groups present on the surface of both CDs, enable crosslinking with DAS while increasing number of hydrogen bonding with the wood surface. The higher reactivity observed with CD2 may be attributed to the branched PEI structure, offering more accessible amino groups for imine formation.

Interestingly, in the presence of HMDA, the curing properties trends were reversed. CD1 led to faster initial bonding than CD2. This may be explained by the reduced availability of free aldehyde groups in the DAS+CD2 mixture, as more aldehydes are involved in crosslinking with PEI. This limits HMDA's interaction with DAS. However, given enough time (after 300 sec), the hindered aldehyde groups in DAS+CD2 might react, resulting in a higher final shear strength of 3.96 ± 0.18 MPa.

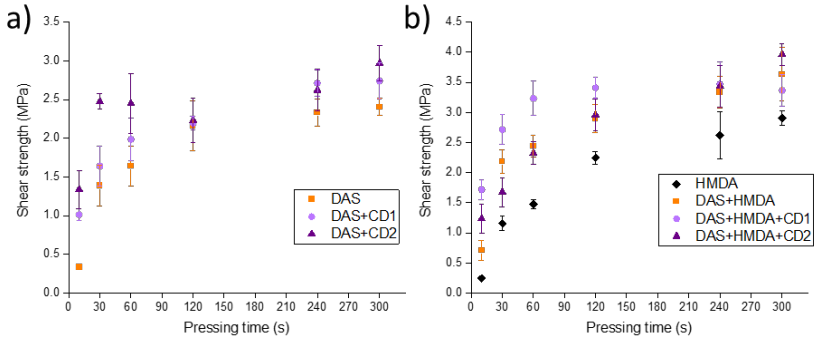

Figure 56. Plots of shear strength as a function of pressing time (at set temperature 160 ˚C) for DAS, DAS+CD1 and DAS+CD2 without HMDA a) and with HMDA b).

Debondability evaluation

Imine bonds are known to be reversible, particularly under acidic conditions [95], where they hydrolyze back into their corresponding amine and aldehyde. This property has potential to enable controlled debonding of the adhesive when exposed to an acidic environment.

To evaluate potential debondability of this adhesive system, the bond strength of wood veneers bonded with three different formulations: DAS+HMDA, DAS+HMDA+CD1, and DAS+HMDA+CD2 was tested using the ABES apparatus following immersion in both neutral and acidic aqueous solutions. Results of these experiments are presented in Table 3. A general decrease in shear strength was observed after immersion in both media, which can be attributed to the DAS poor water resistance. Nonetheless, only the DAS+HMDA+CD1 formulation showed complete debonding after 1 h in acidic solution.

In contrast, the DAS+HMDA+CD2 adhesive retained a measurable bond strength averaging 1.81 MPa in neutral water and decreasing to an average 1.27 MPa after 4 h in acidic water. This improved resistance to hydrolysis in CD2-based systems is likely due to the presence of PEI, whose hydrophobic and highly branched structure may avoid water access to DAS and enhance the network's stability.

Table 3. ABES results obtained after the debondability test performed at pH 4 and pH 7.

pH 7	Time (h)	Shear strength (Mpa)	Adhesive	pH 4	Time (h)	Shear strength (Mpa)	Adhesive
	1	1.95±0.21	DAS+ Amin		1	1.49±0.21	DAS+ Amin
	1	0.71±0.05	DAS+Amin+CD1		1	0	DAS+Amin+CD1
	1	2.11±0.20	DAS+Amin+CD2		1	1.06±0.05	DAS+Amin+CD2
	4	1.64±0.36	DAS+ Amin		4	1.50±0.17	DAS+ Amin
	4	0	DAS+Amin+CD1		4	0	DAS+Amin+CD1
	4	1.81±0.13	DAS+Amin+CD2		4	1.27±0.15	DAS+Amin+CD2

4. Concluding remarks

This study presents an initial step towards the development of bio-based and debondable adhesives for wood products. Two distinct dynamic networks were designed to reversibly crosslink starch with either lignin or carbon dots.

A novel, method for starch esterification was established. St-6MHA was synthesized through a one-pot synthesis process without heating or using potential harmful catalysts, aligning with green chemistry principles.

The DA network synthesized demonstrated the ability of starch and lignin to form reversible covalent bonds. The DA adduct was successfully formed at 65 °C over 48 h and cleaved at 135 °C within 4 h. However, the reversibility only contributed to debonding when the adhesive system had a significant role in either adhesion or cohesion. Indeed, without furfurylating the wood surface to introduce reactive furan groups, no effective debonding occurred, even though a decrease in shear strength was observed.

Shear strength performance of the DA system was comparable to conventional adhesives according to literature. The shear strength reached up to 5.0 ± 0.5 MPa when St-6MHA and KL-FU were combined in a 2:1 molar ratio, respectively based on maleimide and furan reactive groups. Despite starch's limited ability to penetrate wood due to its high molecular weight, micromechanical testing provided insights into other adhesion mechanisms; mainly physical interlocking at the surface and hydrogen bonding. Functionalization of both St and KL was found to influence these interactions.

To explore pH-responsive debonding, a second system was developed using imine chemistry. DAS was synthesized, and citric acid, formamide, and aniline were used in a bottom-up approach to prepare amino-functionalized CDs. Successful grafting of PEI onto CD1 was confirmed, resulting in CD2. FTIR analysis confirmed the formation of imine linkages between DAS, CDs, and HMDA.

When applied as adhesives for bonding wood veneers, the CDs formulations not only reduced curing time but also improved shear strength, indicating the promising role of such additives in adhesive formulation. Debondability tests under acidic conditions revealed that only mixtures

containing CD1 successfully debonded, even though all imine-based systems showed a reduction in bonding strength.

5. Future perspectives

The work presented in this thesis is a first step towards the development of bio-based debondable adhesives for wood products. The use of a reversible network in adhesive design could lead not only for debondability but has some potential to develop reusable adhesive. Thus, repeated bonding and debonding cycles should be investigated.

A study on the importance of the chain length of maleimide or furan grafted moieties and the influence of the degree of substitution will be interesting.

As a continuation of the present work on AFM characterization of the starch and lignin network, it will be interesting to prepare colloidal probes with functionalized CNF with maleimide or with furan to evaluate the strength of Diels Alder adduct between the probe and St-6MHA or KL-FU.

As a continuation of the work on carbon dots, it will be interesting to investigate further the potential of CD1 and CD2 as fluorescent marker to study adhesive penetration into wood structure. Moreover, it will be interesting to further investigate their potential to improve Diels-Alder-based adhesive curing time.

References

1. Frihart, C.R., Wood adhesion and adhesives. Handbook of wood chemistry and wood composites, 2005: p. 255-313.
2. Tian, W., et al., Recent progress of biomass in conventional wood adhesives: a review. Green Chemistry, 2023. 25(24): p. 10304-10337.
3. Yang, M. and K.A. Rosentrater, Life cycle assessment of urea-formaldehyde adhesive and phenol-formaldehyde adhesives. Environmental Processes, 2020. 7: p. 553-561.
4. Kim, K.-H., S.A. Jahan, and J.-T. Lee, Exposure to formaldehyde and its potential human health hazards. Journal of Environmental Science and Health, Part C, 2011. 29(4): p. 277-299.
5. Besserer, A., et al., Cascading Recycling of Wood Waste: A Review. Polymers (Basel), 2021. 13(11).
6. Mulcahy, K.R., et al., Debondable adhesives and their use in recycling. Green Chemistry, 2022. 24(1): p. 36-61.
7. Jarach, N. and H. Dodiuk, Debondable, Recyclable and/or Biodegradable Naturally-Based Adhesives, in Biobased Adhesives. 2023. p. 427-461.
8. Avshalomov, R., N. Jarach, and H. Dodiuk, Breaking the unbreakable bond: Towards sustainable adhesives' future. European Polymer Journal, 2024. 209: p. 112920.
9. Hohl, D.K. and C. Weder, (De) bonding on demand with optically switchable adhesives. Advanced Optical Materials, 2019. 7(16): p. 1900230.
10. Zhang, P., et al., Light-switchable adhesion of azobenzene-containing siloxane-based tough adhesive. ACS Applied Polymer Materials, 2021. 3(5): p. 2325-2329.
11. Mulcahy, K.R., et al., Debondable adhesives and their use in recycling. Green Chemistry, 2022. 24(1): p. 36-61.
12. Trenor, S.R., T.E. Long, and B.J. Love, Development of a light-deactivatable PSA via photodimerization. The Journal of Adhesion, 2005. 81(2): p. 213-229.
13. Boga, K., et al., Eco-friendly photoreversible adhesives derived from coumarin-functionalized epoxy soybean oil. ACS Applied Polymer Materials, 2023. 5(7): p. 4644-4653.
14. Cashion, M.P., T. Park, and T.E. Long, Influence of Hydrogen Bonding on the Adhesive Properties of Photo-Curable Acrylics. The Journal of Adhesion, 2009. 85(1): p. 1-17.
15. Du, P., et al., Diels–Alder-based crosslinked self-healing polyurethane/urea from polymeric methylene diphenyl diisocyanate. Journal of Applied Polymer Science, 2014. 131(9).

16. Carbonell-Blasco, M.P., et al., Polyurethane Adhesives with Chemically Debondable Properties via Diels–Alder Bonds. Polymers, 2023. 16(1): p. 21.
17. Lorero, I., et al., Thermally remendable, weldable, and recyclable epoxy network crosslinked with reversible Diels-alder bonds. Polymer, 2022. 259: p. 125334.
18. Kuang, X., et al., Facile fabrication of fast recyclable and multiple self-healing epoxy materials through diels-alder adduct cross-linker. Journal of Polymer Science Part A: Polymer Chemistry, 2015. 53(18): p. 2094-2103.
19. Gandini, A., The furan/maleimide Diels–Alder reaction: A versatile click–unclick tool in macromolecular synthesis. Progress in Polymer Science, 2013. 38(1): p. 1-29.
20. Jin, Y., et al., Chemically debondable, high-strength and tough adhesives from sulfur-modified epoxy networks. Green Chemistry, 2023. 25(3): p. 1157-1168.
21. Longfang, R., L. Congcong, and Q. Taotao, Preparation of boroxine-based self-healing polyurethane with repeatable adhesive property under mild conditions. Materials Today Chemistry, 2022. 26: p. 101126.
22. Muqaddas, M., et al., Advances in Debondable Adhesives: A Focus on pH-Dependent Reversible Bonding Technologies. Polymer Reviews: p. 1-46.
23. Türel, T., et al., Harnessing Imine Chemistry for the Debonding-on-Demand of Polyurethane Adhesives. ACS Applied Materials & Interfaces, 2025. 17(1): p. 2656-2665.
24. Belowich, M.E. and J.F. Stoddart, Dynamic imine chemistry. Chemical Society Reviews, 2012. 41(6): p. 2003-2024.
25. Narkar, A.R., et al., pH Responsive and Oxidation Resistant Wet Adhesive based on Reversible Catechol–Boronate Complexation. Chemistry of Materials, 2016. 28(15): p. 5432-5439.
26. Ramimoghadam, D., et al., Towards Sustainable Materials: A Review of Acylhydrazone Chemistry for Reversible Polymers. Chemistry – A European Journal, 2024. 30(49): p. e202401728.
27. Qiao, L., et al., Self-healing, pH-sensitive and shape memory hydrogels based on acylhydrazone and hydrogen bonds. European Polymer Journal, 2022. 162: p. 110838.
28. Schenk, V., et al., Vitrimer composites: current status and future challenges. Materials Advances, 2022. 3(22): p. 8012-8029.
29. Van Zee, N.J. and R. Nicolaÿ, Vitrimers: Permanently crosslinked polymers with dynamic network topology. Progress in Polymer Science, 2020. 104: p. 101233.
30. Montarnal, D., et al., Silica-Like Malleable Materials from Permanent Organic Networks. Science, 2011. 334(6058): p. 965-968.

31. Surós, M., et al., Reversible adhesives from epoxy-based transesterification-induced vitrimers. Polymer, 2024. 299: p. 126939.
32. Santiago, D., et al., Recyclable and Reprocessable Epoxy Vitrimer Adhesives. ACS Applied Polymer Materials, 2023. 5(3): p. 2006-2015.
33. Liu, J., A. Pich, and K.V. Bernaerts, Preparation of lignin-based vinylogous urethane vitrimer materials and their potential use as on-demand removable adhesives. Green Chemistry, 2024. 26(3): p. 1414-1429.
34. Yang, Y., et al., Green and ultrastrong polyphenol lignin-based vitrimer adhesive with photothermal conversion property, wide temperature adaptability, and solvent resistance. Chemical Engineering Journal, 2023. 477: p. 147216.
35. Keimel, F.A., Historical development of adhesives and adhesive bonding. Handbook of Adhesive Technology, 2003: p. 1-12.
36. Chen, Y., et al., High-Performance Wet Adhesion of Wood with Chitosan. ACS Sustainable Chemistry & Engineering, 2024. 12(12): p. 4946-4956.
37. Heinrich, L.A., Future opportunities for bio-based adhesives – advantages beyond renewability. Green Chemistry, 2019. 21(8): p. 1866-1888.
38. Yue, H., et al., Recent advancement in bio-based adhesives derived from plant proteins for plywood application: A review. Sustainable Chemistry and Pharmacy, 2023. 33: p. 101143.
39. Zhou, Y., et al., A novel rosin-based non-isocyanate polyurethane with high-strength, self-healing, and recyclable properties for wood adhesives. Industrial Crops and Products, 2024. 211: p. 118203.
40. Li, C., et al., Strong and recyclable soybean oil-based epoxy adhesives based on dynamic borate. European Polymer Journal, 2022. 162: p. 110923.
41. Silva, I.D.S., et al., Synthesis and Performance of Biobased Polyurethane Adhesives from Epoxidized Soybean Oil and Isosorbide. ACS Applied Engineering Materials, 2024. 2(4): p. 919-934.
42. Huang, C., et al., Unlocking the role of lignin for preparing the lignin-based wood adhesive: A review. Industrial Crops and Products, 2022. 187: p. 115388.
43. Dunky, M., Wood Adhesives Based on Natural Resources: A Critical Review: Part III. Tannin- and Lignin-Based Adhesives, in Progress in Adhesion and Adhesives. 2021. p. 383-529.
44. Vineeth, S., R.V. Gadhave, and P.T. Gadekar, Chemical modification of nanocellulose in wood adhesive. Open Journal of Polymer Chemistry, 2019. 9(04): p. 86.
45. Din, Z.-u., et al., Starch: An Undisputed Potential Candidate and Sustainable Resource for the Development of Wood Adhesive. Starch - Stärke, 2020. 72(3-4): p. 1900276.

46. Raydan, N.D.V., et al., Recent Advances on the Development of Protein-Based Adhesives for Wood Composite Materials—A Review. Molecules, 2021. 26(24): p. 7617..
47. Yang, P., et al., Developing carbon dots as green modifiers for improving the bonding performance of low-molar-ratio urea-formaldehyde resin. International Journal of Adhesion and Adhesives, 2023. 125: p. 103416.
48. Wan, J. and D. Ye, Waterborne polyurethane adhesives grafted with carbon dots for enhancing dispersion, cohesion, and adhesion. International Journal of Adhesion and Adhesives, 2025. 140: p. 104031.
49. Fu, Y.-X., et al., Thermal conductivity enhancement of epoxy adhesive using graphene sheets as additives. International Journal of Thermal Sciences, 2014. 86: p. 276-283.
50. Jelinek, R., Carbon-Dot Synthesis, in Carbon Quantum Dots: Synthesis, Properties and Applications, R. Jelinek, Editor. 2017, Springer International Publishing: Cham. p. 5-27.
51. Nicolas, N., H. Reza, and A. Stergios, A Dialdehyde Starch-Based Adhesive For Medium-Density Fiberboards. BioResources, 2023. 18(1): p. 2155-2171.
52. Elomaa, M., et al., Determination of the degree of substitution of acetylated starch by hydrolysis, 1H NMR and TGA/IR. Carbohydrate Polymers, 2004. 57(3): p. 261-267.
53. Argyropoulos, D.S., N. Pajer, and C. Crestini, Quantitative 31P NMR Analysis of Lignins and Tannins. J Vis Exp, 2021(174).
54. Derikvand, M. and G. Fink, Bond Strength of Wood Adhesives: The Sensitivity of Standard Test Methods to Imperfections. 2020.
55. Zhu, T., et al., Comparison of Amylose Determination Methods and the Development of a Dual Wavelength Iodine Binding Technique. Cereal Chemistry, 2008. 85(1): p. 51-58.
56. Letoffe, A., et al., Effect of Fenton reaction parameters on the structure and properties of oxidized wheat starch. Carbohydrate Research, 2024. 542: p. 109190.
57. Jebrane, M., N. Terziev, and I. Heinmaa, Biobased and Sustainable Alternative Route to Long-Chain Cellulose Esters. Biomacromolecules, 2017. 18(2): p. 498-504.
58. Liu, Y.-L. and Y.-H. Wang, Preparation and characterization of multifunctional maleimide macromonomers and their cured resins. Journal of Polymer Science Part A: Polymer Chemistry, 2004. 42(13): p. 3178-3188.
59. Wolfs, J., et al., Determination of the degree of substitution of cellulose esters via ATR-FTIR spectroscopy. Journal of Polymer Science. n/a(n/a).

60. Han, F., et al., Synthesis, characterization and functional properties of low substituted acetylated corn starch. International Journal of Biological Macromolecules, 2012. 50(4): p. 1026-1034.
61. Diop, C.I.K., et al., Effects of acetic acid/acetic anhydride ratios on the properties of corn starch acetates. Food Chemistry, 2011. 126(4): p. 1662-1669.
62. Zhu, F. and P. Liu, Starch gelatinization, retrogradation, and enzyme susceptibility of retrograded starch: Effect of amylopectin internal molecular structure. Food Chemistry, 2020. 316: p. 126036.
63. Cuenca, P., S. Ferrero, and O. Albani, Preparation and characterization of cassava starch acetate with high substitution degree. Food Hydrocolloids, 2020. 100: p. 105430.
64. Imre, B. and F. Vilaplana, Organocatalytic esterification of corn starches towards enhanced thermal stability and moisture resistance. Green Chemistry, 2020. 22(15): p. 5017-5031.
65. Grote, C. and T. Heinze, Starch Derivatives of High Degree of Functionalization 11: Studies on Alternative Acylation of Starch with Long-chain Fatty Acids Homogeneously in N,N-dimethyl acetamide/LiCl. Cellulose, 2005. 12(4): p. 435-444.
66. Mohammadkhani, L. and M.M. Heravi, Oxalyl Chloride: A Versatile Reagent in Organic Transformations. ChemistrySelect, 2019. 4(20): p. 6309-6337.
67. Morinval, A. and L. Avérous, Responsive sustainable and biodegradable systems based on Diels-Alder reaction from amylomaize starch. European Polymer Journal, 2023. 198: p. 112391.
68. Junistia, L., et al., Synthesis of Higher Fatty Acid Starch Esters using Vinyl Laurate and Stearate as Reactants. Starch - Stärke, 2008. 60(12): p. 667-675.
69. Duval, A., et al., Reversible crosslinking of lignin via the furan–maleimide Diels–Alder reaction. Green Chemistry, 2015. 17(11): p. 4991-5000.
70. Wang, T., et al., Kinetic Study of the Diels–Alder Reaction between Maleimide and Furan-Containing Polystyrene Using Infrared Spectroscopy. Polymers, 2024. 16(3): p. 441.
71. Li, Y.-H., J.-H. Chen, and Z. Yang, Exo-Selective Diels–Alder Reactions. Chemistry – A European Journal, 2024. 30(17): p. e202304371.
72. Hosseinpourpia, R., et al., Modification of Pea Starch and Dextrin Polymers with Isocyanate Functional Groups. Polymers, 2018. 10(9): p. 939.
73. Wannous, A., et al., New approach for starch dialdehyde preparation using microwave irradiation for removal of heavy metal ions from water. SN Applied Sciences, 2022. 4(5): p. 133.
74. Ngafwan, N., et al., Study on novel fluorescent carbon nanomaterials in food analysis. Food Science and Technology, 2021. 42: p. e37821.

75. Andreana, I., et al., Freeze drying of polymer nanoparticles and liposomes exploiting different saccharide-based approaches. Materials, 2023. 16(3): p. 1212.
76. Iroegbu, A.O.C. and S.S. Ray, On the chemistry of furfuryl alcohol polymerization: A review. Journal of Polymer Science, 2024. 62(6): p. 1044-1060.
77. Delliere, P., A. Pizzi, and N. Guigo, Structural Variations in Biobased Polyfurfuryl Alcohol Induced by Polymerization in Water. Polymers, 2023. 15(7): p. 1745.
78. Tondi, G., et al., A Simple Approach to Distinguish Classic and Formaldehyde-Free Tannin Based Rigid Foams by ATR FT-IR. Journal of Spectroscopy, 2015. 2015: p. 1-8.
79. Conley, R.T. and I. Metil, An investigation of the structure of furfuryl alcohol polycondensates with infrared spectroscopy. Journal of applied polymer science, 1963. 7(1): p. 37-52.
80. Stöckel, F., et al., Tensile shear strength of UF- and MUF-bonded veneer related to data of adhesives and cell walls measured by nanoindentation. Holzforschung, 2010. 64(3): p. 337-342.
81. Hosseinpourpia, R., A. Eceiza, and S. Adamopoulos, Polyurethane Wood Adhesives Prepared from Modified Polysaccharides. Polymers, 2022. 14(3): p. 539.
82. Elder, L.G.T.T., Moisture in untreated, acetylated, and furfurylated norway spruce monitored during drying below fiber saturation using time domain nmr. Wood and Fiber Science, 41(2), 2009, pp. 194–200, 2009. 41(2): p. 194-200.
83. Shen, X., et al., Water vapor sorption mechanism of furfurylated wood. Journal of Materials Science, 2021. 56(19): p. 11324-11334.
84. Frihart, C.R., Wood structure and adhesive bond strength. Characterization of the cellulosic cell wall, 2006: p. 241-253.
85. Froidevaux, V., et al., Study of the Diels–Alder and retro-Diels–Alder reaction between furan derivatives and maleimide for the creation of new materials. Rsc Advances, 2015. 5(47): p. 37742-37754.
86. Turkenburg, D.H., et al., Polyurethane adhesives containing Diels–Alder-based thermoreversible bonds. Journal of Applied Polymer Science, 2017. 134(26).
87. Yang, S., et al., Recyclable and self-healing polyurethane composites based on Diels-Alder reaction for efficient solar-to-thermal energy storage. Chemical Engineering Journal, 2020. 398: p. 125654.
88. Mcelhanon, J.R., et al., Removable foams based on an epoxy resin incorporating reversible Diels–Alder adducts. Journal of Applied Polymer Science, 2002. 85(7): p. 1496-1502.

89. Ramimoghadam, D., et al., Thermally reversible prototype adhesive via the furan–maleimide Diels–Alder reaction. International Journal of Adhesion and Adhesives, 2024. 128: p. 103522.
90. Domene-López, D., et al., Influence of Starch Composition and Molecular Weight on Physicochemical Properties of Biodegradable Films. Polymers (Basel), 2019. 11(7).
91. Fukunishi, A. and Y. Mori, Adhesion force between particles and substrate in a humid atmosphere studied by atomic force microscopy. Advanced Powder Technology, 2006. 17(5): p. 567-580.
92. Eastman, T. and D.-M. Zhu, Adhesion Forces between Surface-Modified AFM Tips and a Mica Surface. Langmuir, 1996. 12(11): p. 2859-2862.
93. Liu, X., et al., Thermal degradation and stability of starch under different processing conditions. Starch - Stärke, 2013. 65(1-2): p. 48-60.
94. Gurr, J., et al., The bond strength development of coconut wood in relation to its density variations. The Journal of Adhesion, 2022. 98(10): p. 1520-1533.
95. Zhang, H., Z. Su, and X. Wang, Starch-based rehealable and degradable bioplastic enabled by dynamic imine chemistry. ACS Sustainable Chemistry & Engineering, 2022. 10(26): p. 8650-8657.

Popular science summary

Wood products are everywhere from furniture and flooring to construction panels. However, there is a hidden challenge behind their durability: the adhesives that hold them together. Most conventional wood adhesives are designed to create strong, permanent bonds, often using synthetic, fossil-based chemicals. While this ensures long-lasting performance, it also makes recycling nearly impossible. Once bonded, wood components cannot be easily separated without damage, and many end up in landfills or incineration.

In this work, we are trying to tackle this problem with an innovative, eco-friendly solution: going towards **biobased debondable adhesives**. These new adhesives are made from renewable materials like plant-derived polymers or by-product from industries (food, agriculture, pulp, etc.) and are designed to be both strong and smart. Unlike traditional glues, they can "let go" of the bond on demand, using external triggers such as heat, or pH. This smart debonding allows wood products to be disassembled at the end of their life, so the materials can be reused or recycled instead of thrown away.

By combining sustainability with functionality, these biobased debondable adhesives could help transform the wood industry, making it more circular and less wasteful. It's a breakthrough that sticks until we want it not to.

Populärvetenskaplig sammanfattning

Träprodukter används överallt, från möbler och golv till byggpaneler. Det finns dock en dold utmaning bakom deras hållbarhet: limmet som håller ihop dem. De flesta konventionella trälim är utformade för att skapa starka, permanenta bindningar, ofta med hjälp av syntetiska, fossilbaserade kemikalier. Även om detta säkerställer långvarig prestanda, gör det också återvinning nästan omöjlig. När träkomponenter är limmade kan de inte lätt separeras utan att skadas, och många hamnar på soptippar eller förbränning.

I detta arbete försöker vi ta itu med detta problem med en innovativ, miljövänlig lösning: att gå mot biobaserade avbindningsbara lim. Dessa nya lim är tillverkade av förnybara material som växtbaserade polymerer eller biprodukter från industrier (livsmedel, jordbruk, massa, etc.) och är utformade för att vara både starka och ”smarta”. Till skillnad från traditionella lim kan de "släppa taget" om bindningen vid behov, med hjälp av externa utlösare som värme, ljus eller pH. Denna smarta avbindning gör att träprodukter kan demonteras i slutet av sin livslängd, så att materialen kan återanvändas eller återvinnas i stället för att kastas bort.

Genom att kombinera hållbarhet med funktionalitet kan dessa biobaserade, avbindbara lim bidra till att omvandla träindustrin och göra den mer cirkulär och mindre slösaktig.

Acknowledgements

I would like to express my deepest gratitude to my supervisor, Prof. Stergios Adamopoulos, for giving me this opportunity. His insightful feedback and patience helped me to become a better scientist.

I also extend my sincere thanks to my co-supervisor Dr. Raffaello Papadakis, for his invaluable guidance, continuous support, and encouragement throughout the course of this research.

I also want to thank Dr. Joran Van Blokland, Dr. Meysam Nazari for their expertise, constructive comments, helpful suggestions and friendly support.¨

I am also grateful to Prof. Geoffrey Daniel, Prof. Nasko Terziev and Prof. Gulaim Seisenbaeva, whose expertise support made this research possible.

A special thanks to my colleagues and lab mates at Department of Forest Biomaterials and Technology/Division of wood science for the stimulating discussions and the collaborative spirit that made this journey enjoyable and enriching, especially Dr. Jie Gao and Dr. Dinesh Fernando.

I also want to thank Prof. Arantxa Eceiza, Associate Prof. Nagore Gabilondo and Dr. Kizkitza González for their warm welcome and help during my stay at the University of the Basque Country.

Enfin, je tiens à remercier ma famille et mes amis en France pour leur soutien inconditionnel et leurs encouragements tout au long de mon parcours académique. Vous avez été pour moi une source constante de force et de motivation.

Appendix

I

Carbohydrate Research 550 (2025) 109401

Contents lists available at ScienceDirect

Carbohydrate Research

journal homepage: www.elsevier.com/locate/carres

Maleimide grafting onto polysaccharides via mild condition esterification and its impact on their structure

Valentin Silveira [a], Mohamed Jebrane [a,b,*], Adrien Letoffe [a], Stergios Adamopoulos [a]

[a] Department of Forest Biomaterials and Technology, Swedish University of Agricultural Sciences, Box 7008, 750 07, Uppsala, Sweden
[b] Sustainable Materials and Packaging, RISE Research Institutes of Sweden AB, Stockholm, Sweden

ARTICLE INFO

Keywords:
Microcrystalline cellulose
Functional groups
6-Maleimidohexanoic acid
NMR
Acylation
Esterification
Starch
Thermal stability
Crystallinity

ABSTRACT

This study proposes an innovative approach to tailor the properties of two polysaccharides, microcrystalline cellulose (MCC) and potato starch, through chemical modification in dispersion. The methodology involves the grafting of 6-Maleimidohexanoic acid (6-MHA) moieties onto hydroxyl groups of the polysaccharides without dissolving them in order to keep their native structure preserved. To overcome the slow and inefficient reaction between carboxylic acids of 6-MHA and hydroxyl groups of the polysaccharides, a vinyl ester of 6-MHA was synthesized through the transvinylation of 6-MHA acid with vinyl acetate. The resulting 6-MHA ester was employed to introduce a new functionality to polysaccharides' hydroxyl groups via transesterification, catalyzed by potassium carbonate. To enhance the reactivity, the polysaccharides were mercerized prior to modification process. The efficiency of the transesterification reaction between the vinyl ester of 6-MHA and the hydroxyl groups of the polysaccharides was confirmed using Fourier-transform infrared spectroscopy (FTIR) and nuclear magnetic resonance spectroscopy (NMR). Thermal behavior analysis was carried out using thermogravimetric analysis (TGA), while changes in crystallinity resulting from the modification were assessed through X-ray diffraction analysis (XRD). Finally, the impact of the modification on the morphology of polysaccharides was examined with environmental scanning electron microscopy (ESEM). Despite changes in microstructure, MCC kept its macrostructure remained morphologically unchanged while the granular structure of starch was damaged. Maleimide grafting onto MCC and starch has the potential to turn them into thermally reversible materials for various applications such as debondable adhesive or coating.

1. Introduction

Polysaccharides, as a class of natural biopolymers, have attracted considerable attention across various scientific disciplines due to their abundance, availability, biodegradability, and versatile properties [1]. Among them, starch and cellulose have emerged as promising materials, with numerous applications spanning from food [2] and pharmaceuticals [1] to materials science [3,4] and biotechnology [1]. However, despite their inherent advantages, both starch and cellulose often require tailored modifications to meet the specific properties for the intended applications.

One class of modification that has gained attention in recent years is the grafting of maleimide groups [5,6] into the polysaccharides' backbones. Maleimide functionalization offers a versatile platform for the attachment of various biomolecules, drugs, or other compounds to polysaccharides. These modifications can impart new functionalities, such as improved drug delivery [7], enhanced adhesion properties [8], or the introduction of responsive elements, thereby expanding the applications of starch and cellulose in diverse fields.

Starch or cellulose grafted with 6-Maleimidohexanoic acid (6-MHA) will enable click chemistry between maleimide and other alkene or furan-grafted molecules through a Diels-Alder reaction. The Diels-Alder reaction stands as a cornerstone in organic chemistry, recognized for its efficiency and versatility in forming carbon-carbon bonds. It belongs to the category of cycloaddition reactions, specifically classified as a [4 + 2] cycloaddition. In this reaction, a conjugated diene reacts with a dienophile to form a new six-membered ring structure. The reaction proceeds through a concerted mechanism, where the π electrons of the diene and dienophile interact to form two new σ bonds, resulting in the formation of a cyclic product known as a cycloadduct. Click chemistry is an approach of chemical synthesis that focuses on developing efficient and selective chemical reactions that can be used to quickly and easily

* Corresponding author. Department of Forest Biomaterials and Technology, Swedish University of Agricultural Sciences, Box 7008, 750 07, Uppsala, Sweden.
E-mail address: Mohamed.jebrane@slu.se (M. Jebrane).

https://doi.org/10.1016/j.carres.2025.109401
Received 2 August 2024; Received in revised form 20 January 2025; Accepted 21 January 2025
Available online 27 January 2025

join two molecular building blocks together. This approach was first introduced by K. Barry Sharpless and his colleagues in 2001 as a way to accelerate drug delivery and material science research [9]. Click chemistry has gained significance due its efficiency and versatility [10, 11]. Click reactions are specifically designed to occur under mild, non-toxic conditions, enduring high efficiency and selectivity. This allows for rapid synthesis of complex molecules with fewer synthetic steps, minimizing waste and reducing environmental impact. The grafting of maleimide moieties onto polysaccharides subsequently unlocks a range of applications [12,13] such as debondable adhesive or coating which would further enable recycling of bonded and coated materials.

Among the various reactions available for grafting new functionalities onto polysaccharides such as starch and cellulose, esterification stands out as one of the most common utilized chemical reactions [14–20]. Esterification involves the introduction of ester functional groups into the polymer structure by reacting carboxylic acid derivatives with hydroxyl groups, typically abundant in polysaccharides. This reaction results in the formation of ester bonds, thereby altering the physicochemical properties of the polysaccharides. Esterification can be tailored to achieve specific modifications, such as enhanced solubility, hydrophobicity, improved film-forming capabilities, and biocompatibility [21]. Nonetheless, this functionalization has its limits, as it may lead to the degradation of the microstructure of polysaccharides. The microstructure is crucial in determining the inherent characteristics of starch and cellulose, such as mechanical strength, solubility, rheological behavior, and crystallinity [22]. Therefore, it is desirable to develop modification techniques that minimize the damage on the microstructure.

To effectively utilize polysaccharides as advanced materials, a high degree of substitution is required [19]. The esterification of polysaccharides can be performed in aqueous or non-aqueous media [21]. Despite being cost-effective, safe, and environmentally friendly, the method suffers from low reaction efficiency and degree of substitution (DS). In the case of starch, this is attributed to its crystalline structure and extensive intra- and intermolecular hydrogen bonding, rendering it nearly insoluble in cold water. Even for small-molecules, it is difficult to penetrate into the interior of starch granules [21]. The limited modification capabilities of starch in an aqueous environment can be remedied through the application of metal catalysts, which however are associated with health issues.

In order to achieve higher DS, starch can be esterified in a non-aqueous environment [23]. In this case, starch in its dry form undergoes modification using a solvent or the reagent as the medium, typically at elevated temperatures ($\geq$100 °C). Liquid acid anhydride is often utilized in excessive quantities, serving both as the reactive agent and as a reaction solvent alongside acidic or alkaline catalysts. The esterification of polysaccharides is traditionally achieved through acyl chlorides or anhydrides reactions [4,24–27] owing to the limited reactivity between carboxylic acid groups and hydroxyl groups present in polysaccharides. Unfortunately, these reactions generate hydrochloric acid or acids as a byproduct, leading to hydrolysis of glycosidic bonds. The consequence of hydrolysis on polysaccharides structure is characterized by a transformation in the macromolecular architecture and properties of these carbohydrate polymers. Indeed, starch or cellulose are both organized in semi crystalline and amorphous areas, and their amorphous area is more prone to degradation. In an attempt to mitigate this acid-induced degradation in polysaccharides, base such as pyridine are frequently employed to neutralize the generated acid [28]. Although the use of a nitrogen stream can help in eliminating gaseous hydrogen chloride as it forms, it is important to note that even brief exposure to localized acid conditions may result structural damage to cellulose or starch. Continuous development in researching new solvent systems for non-water soluble polysaccharides, such as cellulose or certain type of starch is important for performing modification with high degree of substitution. In recent years, lithium chloride/N,N-dimethylacetamide (LiCl/DMAc) has gained widespread popularity. Initially, it has been recognized for its ability to dissolve polyamides and chitin while its application expanded rapidly, with McCormick [29] and Turbak [30] independently demonstrating its capability to dissolve cellulose. The challenge of finding suitable solvents to perform the reaction is to avoid the dissolution of polysaccharides but at the same time swell them to increase their reactivity.

This article explores the feasibility of grafting maleimide groups onto starch and cellulose while preserving their microstructure intact. The study employs an innovative esterification procedure [31] that has proven to be successful in producing long chain fatty acid cellulose esters, with a high degree of substitution. This new process is based on the transesterification reaction between the hydroxyl groups present at the surface of polysaccharides and the vinyl ester of a carboxylic acid. In contrast to conventional esterification methods using acyl chlorides or anhydrides, the novel transesterification approach employing vinyl esters represents a potential mild acylation technique. Moreover, this method generates acetaldehyde as a byproduct that can be easily removed from the reaction medium due to its low boiling point (21 °C). To our knowledge, this process has not been used to graft maleimide moieties onto polysaccharides.

In this study, we investigated the modification of microcrystalline cellulose (MCC) and potato starch (hereafter referred as starch) using the vinyl ester of 6-MHA under mild conditions. The adjusted reaction parameter previously reported by Ref. [31], which resulted in the highest degree of substitution, were used to graft 6-MHA moieties onto cellulose and starch. Our goal was to graft 6-maleimidohexanoic acid moieties onto starch and MCC, enhancing their functionalities without compromising the integrity of these polysaccharides.

The initial step consists in the synthesis of vinyl ester through the transvinylation of 6-MHA with vinyl acetate. The synthetized ester was then used to functionalize MCC and starch through a transesterification reaction, using potassium carbonate (K_2CO_3) as mild catalyst and a mixture of dimethylformamide (DMF) and dimethylacetamide (DMAc) as solvent. This solvent mixture was chosen for its inability to dissolve starch or MCC, and its capacity to swell polysaccharide structures, thereby increasing the degree of substitution. The esterification of MCC and starch was investigated by Fourier-transform infrared spectroscopy (FTIR) and nuclear magnetic resonance (NMR) spectroscopy. Thermal characteristics of modified MCC and starch were determined by thermogravimetric analysis (TGA). The impact of the reaction on the macromolecular chains and microstructure of MCC and starch was studied by X-ray diffraction (XRD). Finally, scanning electron microscopy (SEM) was employed to investigate the morphology of the functionalized polysaccharides.

2. Materials and methods

2.1. Materials

Microcrystalline cellulose (MCC, powder 20 μm), potato starch, 6-maleimidohexanoic acid, chloro(1,5-cyclooctadiene) iridium-(I) dimer (Ir 57.2 %) ([Ir(cod)Cl]2, HS157), potassium carbonate, sodium acetate, vinyl acetate, acetonitrile, chloroform, dichloromethane, dimethylacetamide (DMAc), and dimethylformamide (DMF), Deuterated DMSO (DMSO-d_6, 99.80 % atom D), deuterated trifluoroacetic acid (d_1-TFA, 99.5 % atom D, were purchased from Sigma-Aldrich (Stockholm, Sweden). All other solvents were American Chemical Society (ACS) grade and used as received.

2.2. Instrumentation

2.2.1. FTIR spectroscopy

A Fourier-transform infrared (FTIR) spectrophotometer FTIR (Spectrum Two, PerkinElmer, Llantrisant, UK) was equipped with a Universal Attenuated Total Reflectance (UATR) diamond accessory, which allows

collection of spectroscopy FTIR spectra directly on a sample without any special preparation. The "pressure arm" of the instrument was used to apply a constant pressure (monitored by software) to the sample positioned on top of the diamond crystal to ensure a good contact between the sample and the incident IR beam. All FTIR spectra were collected at a spectrum resolution of 4 cm^{-1}, with 32 scans over the range from 4000 to 500 cm^{-1}.

2.2.2. Nuclear magnetic resonance (NMR) spectroscopy

2.2.2.1. Liquid state NMR. ^{1}H and ^{13}C NMR spectra of starch samples in dimethyl sulfoxide-d_6 (DMSO-d_6) and ^{1}H and ^{13}C NMR spectra of 6-MHA samples in chloroform-d ($CDCl_3$) were recorded in a Bruker Avance III 600 MHz CCD (Bruker, Billerica, USA) using TMS as reference. Multiplicities were abbreviated as follows: s = singlet, d = doublet, dd = doublet of doublets, t = triplet, q = quartet, and m = multiplet.

The degree of substitution (DS) of starch 6-MHA was measured using ^{1}H-NMR spectroscopy, following a procedure similar to that commonly reported in the literature [32]. The DS was determined as the ratio between the integrated areas of the peaks assigned to the grafted 6-MHA and those of the starch backbone. The addition of deuterated trifluoroacetic acid (d-TFA) facilitated the exchange of labile protons from hydroxyl groups, leaving each α-D-glucopyranose unit with only seven protons. However, since starch inherently contains traces of water that d-TFA cannot completely deuterate, only the peak corresponding to the anomeric proton of starch, located around 5.20 ppm, was used for the calculation. The DS was then determined using the following equation

$$DS = \frac{\text{Igrated 6} - \text{MHA}}{2Istarch}$$

2.2.2.2. Solid state NMR. The ^{13}C CP-MAS NMR spectra of modified and unmodified MCC samples were recorded at room temperature using a Bruker Avance III 600 MHz CCD (Bruker, Billerica, USA) equipped with a 4-mm $^{1}H/^{13}C$ high-resolution magic angle spinning (HR-MAS) probe. The samples were packed into 4 mm zirconia rotors. The sample spinning speed was set to 12.0 MHz, with a contact time of 1 msec, and a relaxation delay of 5 s between acquisitions.

2.2.3. Thermogravimetric analysis (TGA)

TGA plots were acquired using a Mettler-Toledo TGA2 (Mettler Toledo, Greifensee, Switzerland), under nitrogen with a flow rate of 40 mL min^{-1}, using alumina pans. For each TGA run, a sample of weight in the range 5–10 mg was introduced in a standard TGA alumina crucible pan and heated from 30 °C to 600 °C at a heating rate of 10 °C min^{-1}.

2.2.4. X-ray diffraction (XRD) analysis

XRD patterns were recorded on a Bruker D8 CCD (Bruker, Billerica, USA) powder diffractometer with Mo Kα radiation in the angular range of $2\theta = 5–70°$ at 25 °C.

2.2.5. Environmental scanning electron microscopy (ESEM)

After coating MCC and starch samples with gold using sputter coater (Emitech k550X, Quorum Emitech, England), images were taken using a PhilipsXL-30 ESEM (HITACHI, Chiyoda, Japan) at an accelerative voltage of 10 KV, with a spot size of 4.3 using the secondary electrons detector for a magnification of ×200 and × 1000.

2.3. Synthetic strategies

2.3.1. Hydroxyl numbers by titration

In order to calculate the necessary amount of 6-MHA required for maximum degree of substitution, the hydroxyl numbers of polysaccharides was measured using the titration method described in the standard ASTM D 4274 [33]. In this standard test method, the hydroxyl (OH) content of polyurethane raw materials, specifically polyols, is determined. Starch samples were acetylated by reacting them with a solution of acetic anhydride in pyridine inside a pressure bottle at 98 °C. After the reaction, any excess reagent was hydrolyzed with water, and the resulting acetic acid was titrated with a standard sodium hydroxide solution. The hydroxyl content was calculated based on the difference in titration volumes between the blank and the sample solutions.

2.3.2. Synthesis of vinyl ester of 6-MHA

Vinyl ester of 6-MHA was synthesized by mixing 37.40 mmol 6-MHA in 20 mL DMF with a 10 equivalent excess of vinyl acetate in a three-necked round-bottomed glass flask equipped with a reflux condenser and thermometer, and thereafter degassed with argon for 15 min prior to reaction. The catalyst HS157 (0.01 equiv.), along with sodium acetate (0.03 equiv.), was then added, and the reaction mixture was kept under magnetic stirring in a dry argon atmosphere at 110 °C for 24 h. After reaction, the mixture was poured in water and extracted with dichloromethane, and then the organic fraction was concentrated by a rotary evaporation. The obtained viscous sample was dissolved in a mixture of chloroform/acetonitrile (4:1, v:v), and purified using silica-gel column chromatography. After purification, the solvent was removed by rotary evaporation. The obtained vinyl ester of 6-MHA was characterized by FTIR and NMR spectroscopy.

FTIR (cm^{-1}) 3095 (vinyl C–H stretching), 3006 (chain unsaturation C–H stretching), 2938 and 2863 (saturated CH_2 stretching modes), 1750 (C═O stretching of vinyl ester), 1644 (non-conjugated C═C stretching), 1464 (H bending of CH_2 groups), 1135 (ester C–O stretching), 949 (CH out of plane deformation of CH═CH_2), 948 (CH_2 out-of-plane deformation of –CH═CH_2).

^{1}H NMR (600 MHz, $CDCl_3$): δ(ppm) = 7.18 (H_i, t, 1H, (C═O)OCH), 6.62 (H_a, s, 2H, CH═CH), 4.8 (H_j, d, 1H, CH═C), 4.8 (H_k, d, 1H, CH═CH), 3.5 (H_b, t, 2H, N–CH_2–CH_2), 2.3 (H_f, q, 2H, CH_2-(C═O)O), 1.61 (H_c, q, 2H, CH_2–CH_2–CH_2), 1.54 (H_e, q, 2H, CH_2–CH_2–CH_2), 1.54 (H_d, q, 2H, CH_2–CH_2–CH_2). ^{13}C NMR (600 MHz, $CDCl_3$): δ(ppm): 171.1 (C═O ester), 170.4 (C═O maleimide), 141.4 (O–CH =), 134.4 (C═C maleimide), 97.8 (CH═CH_2 vinyl), 37.8–24.3 (aliphatic CH_2).

2.3.3. Polysaccharides activation

MCC and starch were activated by mercerization. 20 g of the polysaccharides were placed in a beaker containing 1 L of sodium hydroxide solution (4 M). The mixture was stirred for 1 h and then filtered and washed by a series of dehydrating solvents, methanol, acetone and hexane. The samples were freeze-dried and kept under vacuum in a desiccator.

2.3.4. Grafting maleimide moieties onto polysaccharides

The activated polysaccharides (1 g) were placed in a 100 mL round-bottomed flask, containing a solution of vinyl ester (1 equivalent of polysaccharides hydroxyl groups), 0.15 g potassium carbonate (catalyst), and 15 mL of DMF and 5 mL of DMAc. After degassing with argon, the mixture was then heated under reflux with vigorous magnetic stirring for 24 h at 110 °C. At the end of reaction, the flask content was cooled down to room temperature and filtered, and excessively washed with water to remove the catalyst and then with ethanol to remove residual reagent and solvents. The obtained maleimide grafted polysaccharides were characterized by FTIR and NMR spectroscopy, XRD, TGA, and ESEM.

MCC 6-MHA: FTIR (cm^{-1}): 2929 and 2860 (saturated CH_2 stretching modes), 1770 (C═O stretching of vinyl ester), 1692 (C═O stretching of maleimide), 1618 (non conjugated C═C stretching), 1438 (H bending of CH_2 groups), 1141 (ester C–O stretching), 783 (C═C bending), and 740 (CH_2 bending).

^{13}C CP MAS NMR (600 MHz): δ(ppm): 182.9 (C_h, C_b, C═O), 110.0 (C═C), 42.2–24.6 (aliphatic CH_2).

Starch 6-MHA: FTIR (cm^{-1}): 2929 and 2857 (saturated CH_2 stretching modes), 1766 (C═O stretching of vinyl ester), 1690 (C═O stretching of maleimide), 1563 (non-conjugated C═C stretching), 1435

(H bending of CH_2 groups), 1100 (ester C–O stretching), 800 (C═C bending), and 707 (CH_2 bending). ^{1}H NMR (600 MHz, $(CD_3)_2SO$): δ(ppm): 5.5–4.5 (m, 6, glucose unit), 1.1 (m, alkyl chain), 4.38 (m, alkyl chain).

3. Results and discussion

3.1. Chemical synthesis and spectroscopic characterization of precursor

The commercially available 6-MHA underwent functionalization through transvinylation with vinyl acetate, resulting in the formation of a new vinyl ester: vinyl 6-maleimidohexanoate denoted as MHA ester, following the procedure outlined in Fig. 1. The confirmation of the structure of the synthesized vinyl ester was achieved through a combination of spectroscopic analyses, as described earlier.

Comparing the FTIR spectra of the starting 6-MHA with the spectra of the synthesized corresponding vinyl ester revealed the appearance of new characteristic absorption bands (Fig. 2). These newly emerged absorption bands attributed to the vinyl group were situated around 3095 cm^{-1} representing vinyl C–H stretching, 2938 and 2863 cm^{-1} indicating saturated CH_2 stretching modes, 1644 cm^{-1} associated with non-conjugated C═C stretching, and 948 cm^{-1} corresponding to C–H out-of-plane deformation of CH═CH_2. The presence of a new ester bond was shown with new bands at 1750 cm^{-1} indicative of C═O stretching in the vinyl ester and 1135 cm^{-1} related to ester C–O stretching. The disappearance of C═O stretching band at 1680 cm^{-1} was also observed and related to carbonyl groups of the acid, confirming the successful transformation of 6-MHA into its corresponding vinyl ester (MHA ester).

The transvinylation reaction between 6-MHA and vinyl acetate was further confirmed by ^{1}H NMR and ^{13}C NMR. The ^{1}H NMR spectra of the synthesized vinyl ester displayed new resonances characteristic of the vinyl ester protons (δ 4.5, 4.8, and 7.2 ppm) in addition to those of the starting fatty acid precursor (Fig. 3).

The ^{13}C NMR analysis of the synthesized vinyl ester (Fig. 4) verified the findings from the ^{1}H NMR (Fig. 3). Alongside the unchanged resonances related to the fatty acid carbons, the spectra of the synthesized vinyl ester exhibited a new group of signals resonating at δ 97.0 and 141.0 ppm, corresponding to the methylenic and methinic carbons of the vinyl ester group. This was consistent with results reported by Ref. [31].

3.2. Esterification of MCC and starch by MHA ester

6-MHA has been chosen as a diene for further Diels Alder reactions for both its reactivity and selectivity [5,34]. The maleimide group is an electron-deficient diene. It consists of a double bond conjugated with an imide functional group. This conjugation increases its reactivity as a diene in Diels-Alder reactions. The imide functionality is electron-withdrawing, making the diene electron-poor. This electron deficiency facilitates its reaction with electron-rich dienophiles in Diels-Alder reactions, where the diene and the dienophile undergo a cycloaddition reaction to form a cyclic compound. Maleimide-based dienes often lead to high stereoselectivity in the Diels-Alder reaction. The reaction typically proceeds through a concerted mechanism, and the electron-withdrawing nature of the maleimide helps control the stereochemistry of the newly formed cyclohexene ring. The maleimide group can undergo a Diels-Alder reaction at both the 1,2- and 1,4-positions of the double bond. However, in many cases, the 1,4-addition (ortho-addition) is favored due to steric hindrance and the possibility of forming a more stable product [5].

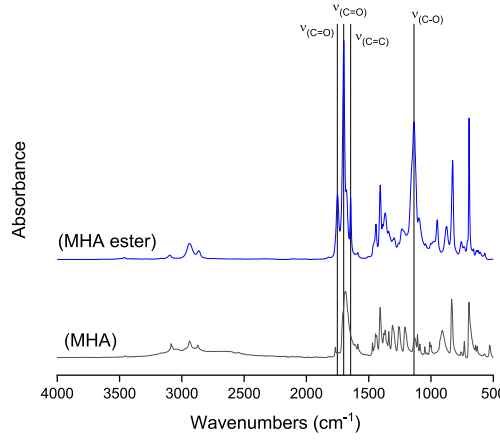

Fig. 2. FTIR absorbance spectra of unmodified and modified 6-MHA (MHA ester).

The reactions were conducted following the procedure outlined in Fig. 5, using potassium carbonate as a mild catalyst. In previous research [31], the degree of grafting of fatty chains onto MCC's hydroxyl groups was measured as a function of reaction time and temperature. The results in that work revealed that increasing both reaction time and temperature led to a higher level of esterification in the MCC. Notably, the effect of reaction temperature was more significant than that of reaction time. In other words, raising the reaction temperature favored the diffusion of the vinyl ester into the MCC hydroxyl groups to a greater extent.

This disparity in the effects of temperature and time could be attributed to the diffusion mechanism governing the accessibility of hydroxyl groups and the size of the reagent. Specifically, the three hydroxyl groups present in an anhydroglucose unit of MCC are not equally accessible. Without using specific conditions [35], the primary hydroxyl group can be more reactive compared to the two secondary hydroxyl groups, primarily due to stereochemical hindrance factors.

The result of the previous research lead us to choose the optimum reaction condition as 24 h duration and temperature 110 °C. The reaction temperature was chosen considering the anticipated polymerization of maleimide, which is known to occur at temperatures above 120 °C [36].

3.2.1. Spectroscopic characterization of the synthesized MCC and starch esters

Figs. 6 and 7 show the FTIR spectra of unmodified and esterified MCC and starch. The MCC polymer modified through transesterification

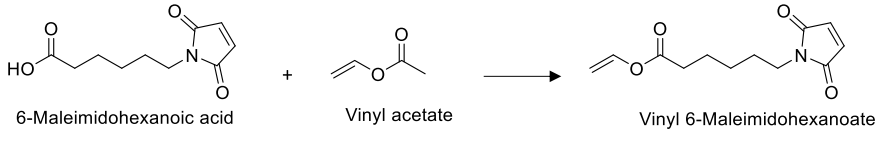

Fig. 1. Synthesis of MHA ester.

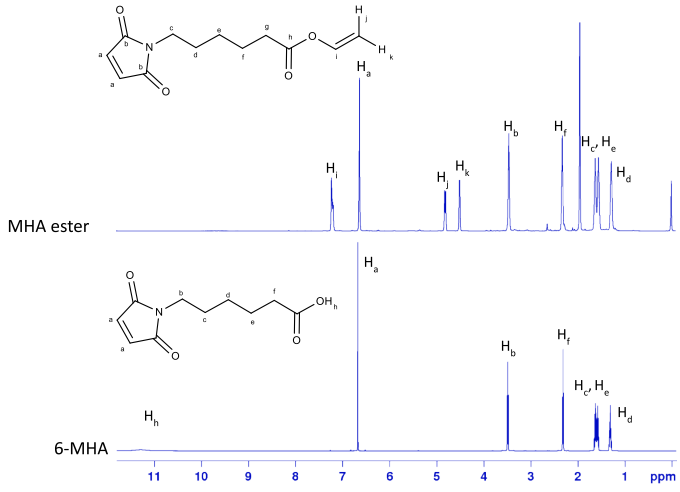

Fig. 3. ^{1}H NMR spectra of unmodified and modified 6-MHA (6-MHA ester).

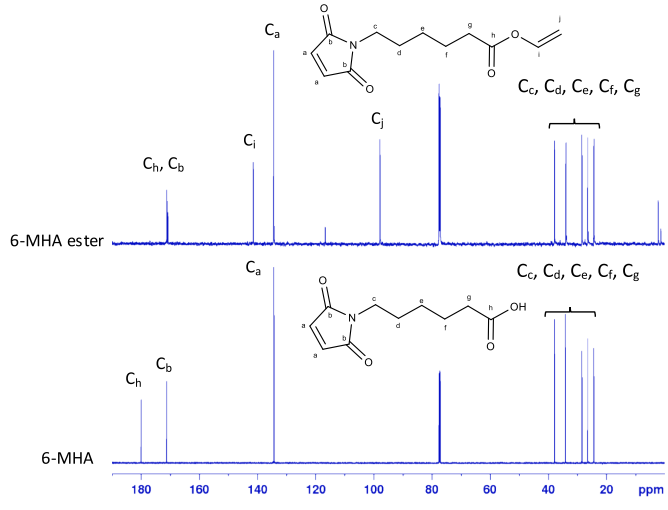

Fig. 4. ^{13}C NMR spectra of unmodified and modified 6-MHA (6-MHA ester).

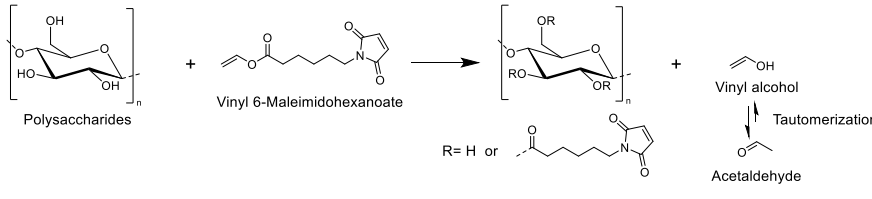

Fig. 5. Synthesis of esterified polysaccharides.

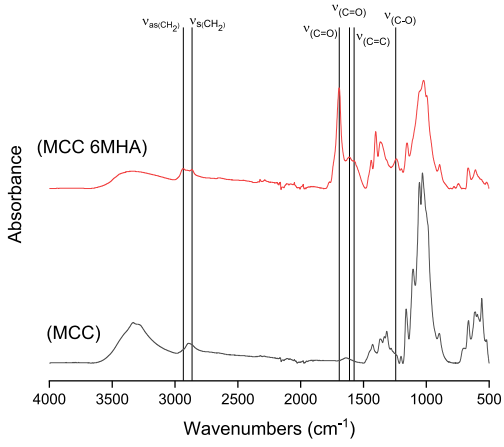

Fig. 6. FTIR absorbance spectra of MCC and esterified MCC (MCC 6-MHA).

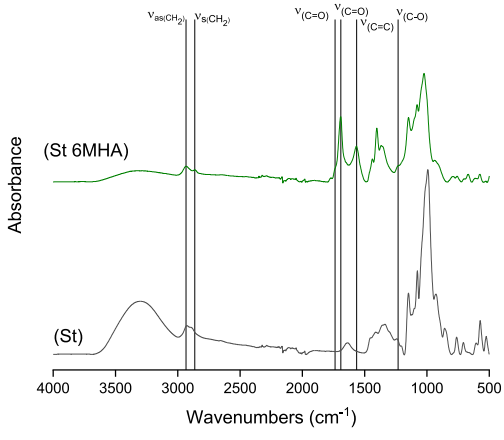

Fig. 7. FTIR absorbance spectra of starch (St) and esterified starch (St 6-MHA).

reaction showed new absorption bands at 1741 cm^{-1} that is attributed to the stretching of the ester carbonyl group (C═O), the band at 1695 cm^{-1} is assigned to the stretching of the carbonyl group in the maleimide group, while the band around 1560-1600 cm^{-1} is attributed to C═C stretching. The band at 1236 cm^{-1} is attributed to the C–O stretching associate to new formed ester groups. Some new bands were identified as characteristics for the 6-MHA such as: C–H bonding absorption bands at 1440 cm^{-1} and 1400-1410 cm^{-1} and the C–N stretching absorption bands at 1360 cm^{-1}. These results were found to be in accordance with previous studies [31,37]. The appearance of new absorption bands in the region between 2800 and 3000 cm^{-1} corresponds to the stretching vibrations of the C–H bonds in the acyl groups. This indicates the presence of acyl substituents in the modified MCC. The spectra of starch samples displayed the same absorption bands with a notable difference in the carbonyl stretching vibrations at 1740 cm^{-1} and the C═O stretching at 1690–1700 cm^{-1} assigned to the maleimide group [38]. Additionally, on both MCC and starch spectra, one of the most significant changes is the decrease in the intensity of the hydroxyl groups absorption bands. This is indicative of successful transesterification, where 6-MHA moieties have been grafted into the polysaccharides backbone, thus reducing the available hydroxyl groups. The observed vibrations related to unchanged hydroxyl groups in the spectra can be explained as the reaction is performed in dispersion. MCC and starch were not dissolved, this type of chemical modification would not affect the hydroxyl OH groups protected inside their respective fibrous or granule structure. These hydroxyl groups are important as they maintain the internal organization of the polysaccharides, if affected, the disruption of hydrogen bond between chains or between traces of water would not enable the fibrous or granular structure to maintain.

The modified MCC samples underwent additional characterization using ^{13}C CP-MAS NMR spectroscopy (Fig. 8). Apart from the primary pattern corresponding to cellulose carbons, distinct signals corresponding to the newly introduced 6-MHA moieties were visible in the spectra of modified MCC. These signals were directly assigned on the modified MCC spectra based on the nomenclature provided in the associated structure. These signals were in accordance with studies made by others [31,39]. The new signals corresponding to the alkyl chains were located in the region of 20–50 ppm while a weak signal was observed around 180 ppm assigned to carbonyl groups.

The NMR spectroscopic analysis of the modified starch samples (Fig. 9) showed relatively low intensity of the different peaks associated to starch due to the challenging issue of their low solubility in various deuterated solvents. It should also be noted that while the reaction may modify a significant portion of the accessible hydroxyl groups on the starch surface, it represents only a small fraction of the total hydroxyl groups present in the starch. As a result, the ratio between the remaining and modified hydroxyl groups tends to make the intensity of the new peaks relatively low. Consequently, alternative strategies or solvents that enhance solubility may be necessary to more effectively interrogate the structural alterations and characteristics of these modified starch samples using NMR techniques. It should be noted that the peaks corresponding to the protons of the hydroxyl groups attached to carbon C6 (H9) and C3 (H8) are significantly decreased. This is expected, as the primary alcohol linked to carbon C6 is generally more reactive than the secondary alcohol at carbon C3, unless under specific conditions. ^{13}C NMR showed no signal of starch neither and trials of ^{13} CP MAS NMR were made but unsuccessful. Despite the low intensity of the peaks observed, the spectra showed the apparition of two new peaks at 1.1 ppm and 4.38 ppm that can be respectively attributed to alkyl group and methoxy group that tends to confirm the modification according to literature [32,40].

The degree of substitution (DS) of starch was determined using ^{1}H NMR (see Fig. S1) and was estimated to be 0.27. While this represents a relatively low DS, it corresponds to a modification of 47 % of the

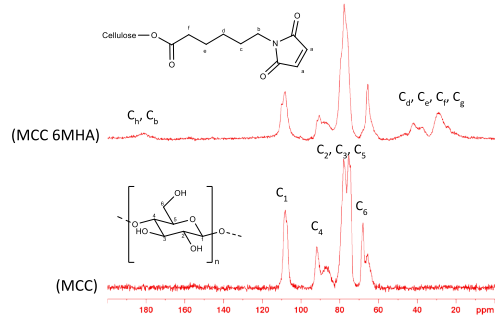

Fig. 8. ^{13}C CP-MAS NMR spectra of unmodified and modified MCC with 6-MHA ester for 24h at 110 °C.

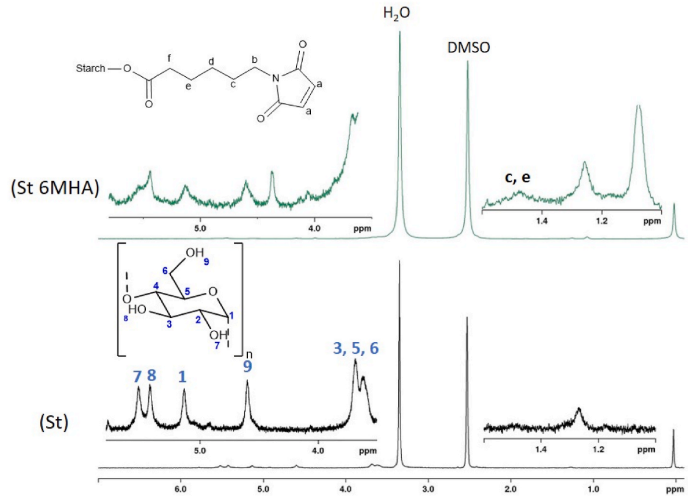

Fig. 9. ^{1}H NMR spectra of unmodified (St 6MHA) and modified starch (St) with 6-MHA ester for 24h at 110 °C.

available hydroxyl groups when considering the 3.56 mmol/g hydroxyl content of starch, as determined by titration in dispersion. It is worth noting that the calculated DS may underestimate the actual value due to the limited solubility of the modified starch in DMSO-d_6.

3.2.2. *Thermal properties of the synthesized MCC and starch esters*

Figs. 10 and 11 present the TGA and DTG thermograms of both starch and MCC before and after modification. Continuous nitrogen was used to study the decomposition properties of the MCC samples by performing TGA at optimum reaction time and temperature according to previous study (Jebrane et al., 2017). The weight loss reported was normalized against the initial weight of the samples analyzed (Fig. 10). The results indicated that the thermal degradation of native MCC began at 295 °C and showed a single weight-loss step. In contrast, modified MCC was less stable and began to decompose at relatively lower temperatures than unmodified MCC. This was expected because the grafting acyl groups into MCC's hydroxyl groups affect its crystallinity contributing to its thermal instability [31]. Additionally, modified MCC displayed two distinct degradation steps visible on the DTG thermogram, attributed at 159 °C to the degradation of the grafted 6-MHA and a second peak attributed to degradation of the MCC backbone starting at 230 °C reaching a maximum at 322 °C (Fig. 11a). Similar results have been reported in the literature [31].

The thermal stability of esterified starch was significantly improved in comparison to unmodified starch. For native starch, a two step degradation pattern was observed (Fig. 10b). It can be interpreted as a first step linked to the water evaporation that was trapped into starch structure, and a second step related to the starch backbone degradation at 300 °C. Modified starch initiated its decomposition at around 230 °C but at a significantly lower rate than native starch since the degradation of starch is not complete at 630 °C. Although the thermal stability of esterified starch outperformed that of native starch, modified samples exhibited a similar decomposition process with the initial stage starting at a lower temperature compared to unmodified starch. The thermal stability behavior of starch can be explained in two different ways. A first explanation is that starch can perform retrogradation [41]. This

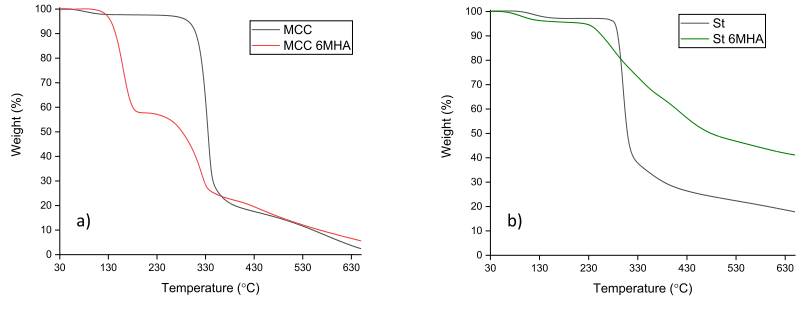

Fig. 10. TGA thermograms of (a) unmodified and modified (MCC 6-MHA) MCC and (b) unmodified and modified (St 6-MHA) starch (St) with 6-MHA ester for 24 h at 110 °C.

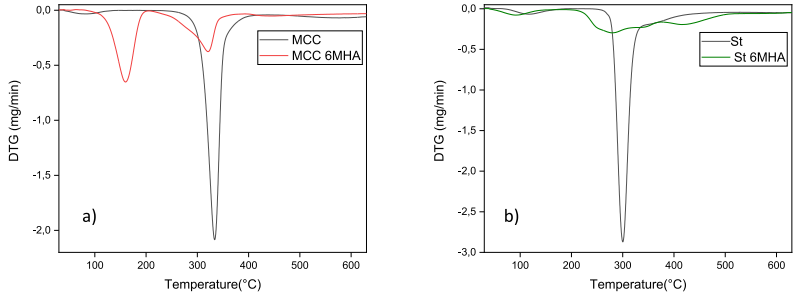

Fig. 11. DTG thermograms of (a) unmodified and modified(MCC 6-MHA) MCC and (b) unmodified and modified (St 6-MHA) starch with 6-MHA ester for 24 h at 110 °C.

complex phenomenon occurs when a starch gel, formed after gelatinization, undergoes structural changes upon cooling and aging. During retrogradation, amylose and amylopectin molecules re-associate and form ordered structures. When starch retrogrades, the reformation of crystalline structures occurs, resulting in a more ordered and stable structure, resistant to heat [42]. This phenomenon might have happened during the first step of the chemical process, when mercerized, starch gelatinized in contact with sodium hydroxide solution, and after precipitation and filtration the gel like material was freeze-dried. A second explanation for the observed enhanced thermal stability, consists in supposing that it was achieved a relatively high degree of substitution, meaning a significant reduction of hydroxyl number within the starch molecules after esterification. Given that the primary decomposition mechanism of starch relies on inter- or intra-molecular dehydration reactions involving water as a primary decomposition product, the reduction in the number of remaining hydroxyl groups resulted in an improvement of thermal stability at lower temperatures. Similar observations have been done by Ref. [43].

3.2.3. *XRD analysis of MCC and starch esters*

Fig. 12a presents the XRD patterns of MCC before and after esterification. The XRD pattern of native MCC exhibited three main diffraction peaks at 7, 10, and 15.6°, associated respectively to the crystalline cellulose I structure 101, 10 $\bar{1}$, and 002 diffraction planes. Following the reaction with MHA ester, the main characteristic planes of cellulose were significantly weakened or entirely disappeared. Instead, a new amorphous halo appeared between $2\theta = 7$ and 18°, which can be attributed to an increase of amorphous phase in the cellulosic backbone. These observed changes were consistent with similar findings reported in the literature for esterified cellulose, which were associated with an increasing intermolecular distance of the backbone chain due to the length of grafted entities [44]. Nonetheless, the mercerization performed to increase MCC reactivity might have affected its morphology and crystallinity. In order to investigate the morphology of MCC before and after mercerization and modification, observations were performed under an ESEM.

The main characteristic peak observed for native starch (Fig. 12b) at 7.8 and 10.5° following by overlapping peaks at 13.7, 15.5, 16.45 and 21° disappeared on the XRD pattern of modified starch. Only a broad peak centered at 9.65° and a small peak at 20° were visible. This result indicates the total loss of crystallinity of the esterified starch contradicting the idea of starch retrogradation. Indeed, previous work performed by Ref. [45] showed that freeze dried starch samples that undergo retrogradation can show a broad peak in their XRD pattern, but it will still be centered at the position of native starch peaks. The examination of XRD data from various starch acetylation methodologies [46] reveals a consistent trend. The crystalline structure of native starch is typically destroyed during esterification processes, as documented by

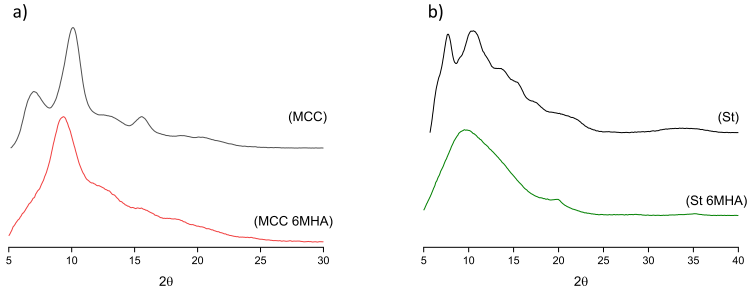

Fig. 12. XRD patterns of unmodified (MCC) and modified MCC (MCC 6-MHA) with 6-MHA ester for 24 h at 110 °C (a) and unmodified (St) and modified potato starch (St 6MHA) with 6-MHA ester for 24 h at 110 °C (b).

Ref. [18]. In starch, crystallinity is predominantly attributed to the formation of double helices facilitated by intermolecular hydrogen bonds within amylopectin chains. Consequently, the reduction in crystallinity observed during acylation is frequently attributed to the diminished formation of both inter- and intra-molecular hydrogen bonds. This decrease arises due to the partial substitution of starch hydroxyl groups with ester groups, ultimately leading to the destruction of the original ordered crystalline structure, as elucidated by Ref. [47].

The disappearance of well-defined crystalline structures was reported with a high degree of substitution. The decrease in the number of hydroxyl groups inhibited the capacity for inter-molecular hydrogen bond formation, resulting in the emergence of amorphous patterns characterized by broad peaks, as documented by Ref. [20]. Moreover, the degradation of the microstructure of both polysaccharides indicates that not only their surfaces undergo modification but also the core. This was possible due to the ability of DMAc to swell polysaccharides and open up their structures [48].

3.2.4. Morphology of MCC and starch before and after modification

The alkaline pre-treatment of starch and MCC followed by the esterification reaction might have changed the microstructure and interaction between their macromolecules as shown previously in the XRD analysis, and thus morphological changes could be expected. The morphology of MCC and starch as revealed by ESEM in their unmodified states, after mercerization, and after esterification are shown in Figs. 13 and 14.

The ESEM images of native MCC showed rough surfaces of linear micro particles of varied sizes not exceeding 100 μm. The mercerization treatment did not seemed to have any particular effect on the shape or size of the MCC particles, showing a resistance of cellulose to alkaline treatment [52]. The esterified MCC particles showed similar shape with the unmodified MCC ones with an increase of the number of small particles that can be explained by the mechanical stress caused by a long time agitation at 110 °C. The ESEM images of native starch granules showed oval or ellipsoidal shape particles, flattened along one axis, ranging from few μm to 100 μm in diameter. The surface of granules appeared mostly smooth and lacked pronounced surface irregularities. The only irregularities appeared to be the result of contact from one granule onto another. Unlike MCC, mercerized starch showed a loss of organised microstructure. It seems that the gelatinization of starch due to alkaline treatment caused, after freeze-drying, a disintegration of starch microstructure [49]. The oval granules merged or melted into random shaped particles and agglomerates with rough surfaces with sizes ranging from few μm to more than 100 μm. Same observations were made for esterified starch, although the surface of particles appeared to be smoother. A similar starch morphology has been reported in studies where starch was esterified under acid conditions [19, 40].

The differential response of MCC particles and starch granules to alkaline treatment, such as mercerization, can be attributed to the differences in their chemical structure and molecular arrangement, as presented in supporting information (FS2 and FS3).

Cellulose fibers have a fibrous, thread-like structure. This structure, with its strong intermolecular interactions, contributes to the overall stability of cellulose fibers. Cellulose molecules are arranged in highly ordered, crystalline structures, held together by extensive hydrogen bonding between adjacent cellulose chains. This crystalline structure provides significant stability and resistance to chemical treatments, including alkaline solutions [52]. Cellulose is a linear polysaccharide composed of repeating glucose units linked by β-1,4-glycosidic bonds [50]. These glucose units are connected in a way that forms long, straight chains. The β-1,4-glycosidic bonds in cellulose are highly stable and resistant to hydrolysis under alkaline conditions.

In contrast, starch granules are composed of both amorphous and semi-crystalline blockets. The amorphous blockets, composed of amylose, are more likely to be modified in a first place. The amorphous regions in the semi-crystalline blockets, which contain the branching points of amylopectin, are more susceptible to hydrolysis. These amorphous regions can be more easily disrupted under alkaline conditions, leading to changes in granule crystallinity and morphology [53]. At a molecular level, starch is a mixture of two different polysaccharides, amylose and amylopectin. Amylose consists of linear chains of glucose

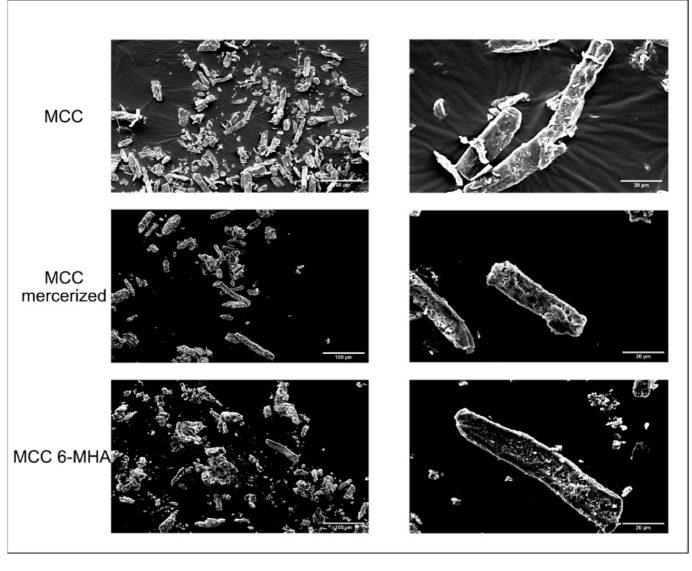

Fig. 13. ESEM images of MCC before and after modification (MCC 6-MHA).

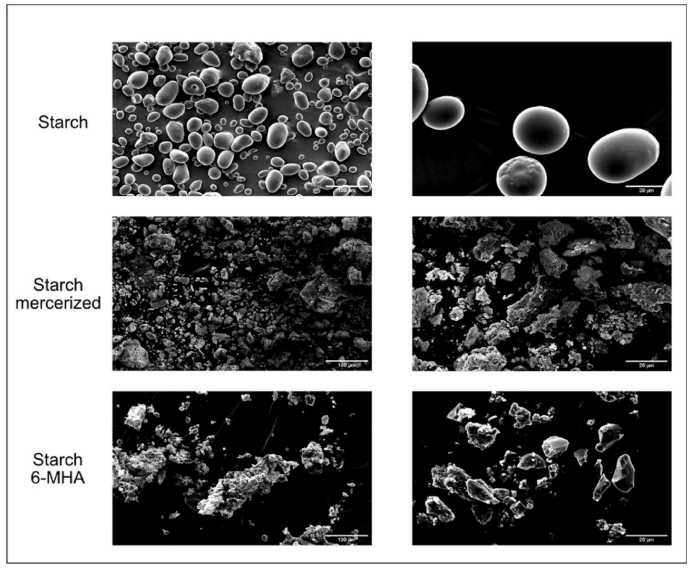

Fig. 14. ESEM images of starch before and after modification (Starch 6-MHA).

units, but amylopectin has branched structures with both α-1,4 and α-1, 6-glycosidic bonds [43,51]. The presence of α-1,4-glycosidic bonds in starch makes it more susceptible to hydrolysis under alkaline conditions [53].

In summary, MCC's strong, linear, and highly crystalline structure, as well as the stability of its β-1,4-glycosidic bonds and extensive hydrogen bonding, make it more resistant to alkaline treatment. Starch, with its branched, less organized structure and α-1,4-glycosidic bonds, is more vulnerable to the effects of alkaline solutions. The differences in chemical composition and structural organization between MCC and starch may explain why cellulose fibers appear to have similar size and shape when after alkaline treatment starch granules are degraded.

Grafting maleimide into polysaccharides open a wide range of possibilities to develop new materials for various applications (coatings, paintings, adhesives, composites, …) as it enables these latter to undergo click chemistry with furan grafted molecules or polymers. As mentioned earlier, the traditional esterification generate or occurs in presence of hydrogen chloride that can hydrolyze glycosidic bonds and thus destroy polysaccharides native structure. We believe that these organized structures have interesting mechanical properties to develop new materials. As the morphology and microstructure of MCC remains similar after modification, we believe that cellulose has mostly kept his mechanical properties and could be a good candidate to perform Diels Alder reaction to develop thermally responsive materials.

4. Conclusions

6-MHA was grafted on the surface of both MCC and starch using a mild condition transesterification reaction. The evidence of the grafting was shown by FTIR and NMR spectroscopy. The thermal analysis alongside with XRD analysis and ESEM observations brought a new understanding of the impact of this process on the stability and microstructure of the modified polysaccharides.

This modification had a significant impact on the crystallinity of the polysaccharides, which lead to different evolution of their microstructures.

Indeed, if ESEM images corroborated the alteration of starch granules after the activation of starch hydroxyl groups by mercerization, the morphology of MCC seemed relatively unchanged.

Opposite effect of modification were observed concerning thermal analysis. TGA analysis of both polysaccharides before and after modification revealed that the partial loss of crystallinity of MCC make it degrade at lower temperature when starch seemed to have gain thermal stability with its full carbon backbone degradation still not reached at 600 °C.

These findings pave the way for further research into a tailored utilization of modified starch and MCC in a variety of industrial applications such as the development of debondable adhesive or coating promoting the recyclability of bonded materials.

CRediT authorship contribution statement

Valentin Silveira: Writing – review & editing, Writing – original draft, Visualization, Methodology, Investigation, Formal analysis, Conceptualization. **Mohamed Jebrane:** Writing – review & editing, Validation, Methodology, Conceptualization. **Adrien Letoffe:** Writing – review & editing, Validation. **Stergios Adamopoulos:** Writing – review & editing, Validation, Resources, Conceptualization.

Informed consent statement

Not applicable.

Data availability statement

The data presented in this study are available from the corresponding author upon request.

Funding

Not applicable.

Declaration of competing interest

The authors declare that they have no known competing financial interests or personal relationships that could have appeared to influence the work reported in this paper.

Acknowledgments

Not applicable.

Appendix A. Supplementary data

Supplementary data to this article can be found online at https://doi.org/10.1016/j.carres.2025.109401.

Data availability

Data will be made available on request.

References

[1] V. Gopinath, et al., Multifunctional applications of natural polysaccharide starch and cellulose: an update on recent advances, Biomed. Pharmacother. 146 (2022), https://doi.org/10.1016/j.biopha.2021.112492.
[2] W.A.J.P. Wijesinghe, N. Wedamulla, Application of polysaccharides in food technology: a review, Trends in Carbohydrate Research 13 (2021) 35–49.
[3] A. Patel, J.-D. Mathias, P. Michaud, Polysaccharides as adhesives, Reviews of Adhesion and Adhesives 3 (2013) 312–345, https://doi.org/10.7569/RAA.2013.097310.
[4] P. Wang, B.Y. Tao, Synthesis of cellulose-fatty acid esters for use as biodegradable plastics, J. Environ. Polym. Degrad. 3 (1995) 115–119, https://doi.org/10.1007/BF02067487.
[5] A. Gandini, The furan/maleimide Diels–Alder reaction: a versatile click–unclick tool in macromolecular synthesis, Prog. Polym. Sci. 38 (2013) 1–29, https://doi.org/10.1016/j.progpolymsci.2012.04.002.
[6] G. Griffini, B. Rigatelli, S. Turri, Diels-alder macromolecular networks in recyclable, repairable and reprocessable polymer composites for the circular economy – a review, Macromol. Mater. Eng. 308 (2023), https://doi.org/10.1002/mame.202300133.
[7] T. Mohan, K.S. Kleinschek, R. Kargl, Polysaccharide peptide conjugates: chemistry, properties and applications, Carbohydrate Polymers 280 (2022), https://doi.org/10.1016/j.carbpol.2021.118875.
[8] C. Pornpitchanarong, et al., Maleimide-functionalized carboxymethyl cellulose: a novel mucoadhesive polymer for transmucosal drug delivery, Carbohydrate Polymers 288 (2022), https://doi.org/10.1016/j.carbpol.2022.119368.
[9] H.C. Kolb, M.G. Finn, K.B. Sharpless, Click chemistry: diverse chemical function from a few good reactions, Angew. Chem. Int. Ed. 40 (2001) 2004–2021, https://doi.org/10.1002/1521-3773(20010601)40:11<2004::AID-ANIE2004>3.0.CO;2-5.
[10] H. Nandivada, X. Jiang, J. Lahann, Click chemistry: versatility and control in the hands of materials scientists, Adv. Mater. 19 (2007) 2197–2208, https://doi.org/10.1002/adma.200602739.
[11] J.E. Moses, A.D. Moorhouse, The growing applications of click chemistry, Chem. Soc. Rev. 36 (2007) 1249–1262, https://doi.org/10.1039/B613014N.
[12] N. Sahatsapan, et al., 6-Maleimidohexanoic acid-grafted chitosan: a new generation mucoadhesive polymer, Carbohydrate Polymers 202 (2018) 258–264, https://doi.org/10.1016/j.carbpol.2018.08.119.
[13] A. Duval, et al., Reversible crosslinking of lignin via the furan–maleimide Diels–Alder reaction, Green Chem. 17 (2015) 4991–5000, https://doi.org/10.1039/C5GC01319D.
[14] T. Aziz, et al., A review on the modification of cellulose and its applications, Polymers 14 (2022), https://doi.org/10.3390/polym14153206.
[15] J. Fang, et al., The chemical modification of a range of starches under aqueous reaction conditions, Carbohydrate polymers 55 (2004) 283–289, https://doi.org/10.1016/j.carbpol.2003.10.003.
[16] J. Fang, et al., The preparation and characterisation of a series of chemically modified potato starches, Carbohydrate polymers 47 (2002) 245–252, https://doi.org/10.1016/S0144-8617(01)00187-4.
[17] S.C. Fox, et al., Regioselective esterification and etherification of cellulose: a review, Biomacromolecules 12 (2011) 1956–1972, https://doi.org/10.1021/bm200260d.
[18] F. Han, et al., Synthesis, characterization and functional properties of low substituted acetylated corn starch, Int. J. Biol. Macromol. 50 (2012) 1026–1034, https://doi.org/10.1016/j.ijbiomac.2012.02.030.
[19] B. Imre, F. Vilaplana, Organocatalytic esterification of corn starches towards enhanced thermal stability and moisture resistance, Green Chem. 22 (2020) 5017–5031, https://doi.org/10.1039/D0GC00681E.
[20] Y. Xu, V. Miladinov, M.A. Hanna, Synthesis and characterization of starch acetates with high substitution, Cereal Chem. 81 (2004) 735–740, https://doi.org/10.1094/CCHEM.2004.81.6.735.
[21] M.A. Otache, et al., Advances in the modification of starch via esterification for enhanced properties, J. Polym. Environ. 29 (2021) 1365–1379, https://doi.org/10.1007/s10924-020-02006-0.
[22] Y.I. Cornejo-Ramírez, et al., The structural characteristics of starches and their functional properties, CyTA - J. Food 16 (2018) 1003–1017, https://doi.org/10.1080/19476337.2018.1518343.
[23] C. Grote, T. Heinze, Starch derivatives of high degree of functionalization 11: studies on alternative acylation of starch with long-chain fatty acids homogeneously in N,N-dimethyl acetamide/LiCl, Cellulose 12 (2005) 435–444, https://doi.org/10.1007/s10570-005-2178-z.
[24] J.W. Mullen, E. Pacsu, Starch studies. Preparation and properties of starch triesters, Ind. Eng. Chem. 34 (1942) 1209–1217.
[25] H.S. Kwatra, J.M. Caruthers, B.Y. Tao, Synthesis of long chain fatty acids esterified onto cellulose via the vacuum-acid chloride process, Ind. Eng. Chem. Res. 31 (1992) 2647–2651, https://doi.org/10.1021/ie00012a004.
[26] J. Aburto, I. Alric, E. Borredon, Preparation of long-chain esters of starch using fatty acid chlorides in the absence of an organic solvent, Starch - Stärke 51 (1999) 132–135, https://doi.org/10.1002/(SICI)1521-379X(199904)51:4<132::AID-STAR132>3.0.CO;2-Z.
[27] N. Masina, et al., A review of the chemical modification techniques of starch, Carbohydrate Polymers 157 (2017) 1226–1236, https://doi.org/10.1016/j.carbpol.2016.09.094.
[28] T.B. Grindley, Esterification of polysaccharides, J. Am. Chem. Soc. 129 (2007) 2195–2196, https://doi.org/10.1021/ja069801d.
[29] T.R. Dawsey, C.L. McCormick, The lithium chloride/dimethylacetamide solvent for cellulose: a literature review, J. Macromol. Sci. 30 (1990) 405–440, https://doi.org/10.1080/07366579008050914.
[30] A.F. Turbak, et al., Solvent System for Cellulose, Google Patents, 1981.
[31] M. Jebrane, N. Terziev, I. Heinmaa, Biobased and sustainable alternative route to long-chain cellulose esters, Biomacromolecules 18 (2017) 498–504, https://doi.org/10.1021/acs.biomac.6b01584.
[32] M. Elomaa, et al., Determination of the degree of substitution of acetylated starch by hydrolysis, 1H NMR and TGA/IR, Carbohydrate Polymers 57 (2004) 261–267, https://doi.org/10.1016/j.carbpol.2004.05.003.
[33] A.I.W. Conshohocken, ASTM Standard D4274, Standard Test Methods for Testing Polyurethane Raw Materials: Determination of Hydroxyl Numbers of Polyols, 2023.
[34] B. Briou, B. Améduri, B. Boutevin, Trends in the Diels–Alder reaction in polymer chemistry, Chem. Soc. Rev. 50 (2021) 11055–11097, https://doi.org/10.1039/D0CS01382J.
[35] Z. Zhai, K.J. Edgar, Polysaccharide aldehydes and ketones: synthesis and reactivity, Biomacromolecules 25 (2024) 2261–2276, https://doi.org/10.1021/acs.biomac.4c00020.
[36] Y.-L. Liu, J.-M. Yu, Cocuring behaviors of benzoxazine and maleimide derivatives and the thermal properties of the cured products, J. Polym. Sci. Polym. Chem. 44 (2006) 1890–1899, https://doi.org/10.1002/pola.21290.
[37] J. Wolfs, et al., Determination of the degree of substitution of cellulose esters via ATR-FTIR spectroscopy, J. Polym. Sci. (2023), https://doi.org/10.1002/pol.20230220.
[38] Y.-L. Liu, Y.-H. Wang, Preparation and characterization of multifunctional maleimide macromonomers and their cured resins, J. Polym. Sci. Polym. Chem. 42 (2004) 3178–3188, https://doi.org/10.1002/pola.20162.
[39] L. Duchatel-Crépy, et al., Substitution degree and fatty chain length influence on structure and properties of fatty acid cellulose esters, Carbohydrate Polymers 234 (2020), https://doi.org/10.1016/j.carbpol.2020.115912.
[40] P. Cuenca, S. Ferrero, O. Albani, Preparation and characterization of cassava starch acetate with high substitution degree, Food Hydrocolloids 100 (2020), https://doi.org/10.1016/j.foodhyd.2019.105430.
[41] J.J.G. Van Soest, et al., Retrogradation of potato starch as studied by fourier transform infrared spectroscopy, Starch - Stärke 46 (1994) 453–457, https://doi.org/10.1002/star.19940461202.
[42] Y.-Y. Xie, et al., Effect of repeated retrogradation on structural characteristics and in vitro digestibility of waxy potato starch, Food Chem. 163 (2014) 219–225, https://doi.org/10.1016/j.foodchem.2014.04.102.
[43] L. Zhang, et al., Study on the morphology, crystalline structure and thermal properties of yellow ginger starch acetates with different degrees of substitution, Thermochim. Acta 495 (2009) 57–62, https://doi.org/10.1016/j.tca.2009.05.019.
[44] H. Winkler, W. Vorwerg, R. Rihm, Thermal and mechanical properties of fatty acid starch esters, Carbohydrate Polymers 102 (2014) 941–949, https://doi.org/10.1016/j.carbpol.2013.10.040.
[45] T. Taguchi, et al., Evaluation of starch retrogradation by X-ray diffraction using a water-addition method, LWT 173 (2023) 114341, https://doi.org/10.1016/j.lwt.2022.114341.
[46] M. Tupa, et al., Simple organocatalytic route for the synthesis of starch esters, Carbohydrate Polymers 98 (2013) 349–357, https://doi.org/10.1016/j.carbpol.2013.05.094.
[47] C.I.K. Diop, et al., Effects of acetic acid/acetic anhydride ratios on the properties of corn starch acetates, Food Chem. 126 (2011) 1662–1669, https://doi.org/10.1016/j.foodchem.2010.12.050.
[48] A.-L. Dupont, Cellulose in lithium chloride/N,N-dimethylacetamide, optimisation of a dissolution method using paper substrates and stability of the solutions, Polymer 44 (2003) 4117–4126, https://doi.org/10.1016/S0032-3861(03)00398-7.
[49] F. Zhu, P. Liu, Starch gelatinization, retrogradation, and enzyme susceptibility of retrograded starch: effect of amylopectin internal molecular structure, Food Chem. 316 (2020), https://doi.org/10.1016/j.foodchem.2019.126036.

[50] Z. Peter, Order in cellulosics: historical review of crystal structure research on cellulose, Carbohydrate Polymers 254 (2020), https://doi.org/10.1016/j.carbpol.2020.117417.
[51] A. Buléon, et al., Starch granules: structure and biosynthesis, Int. J. Biol. Macromol. 23 (1998) 85–112, https://doi.org/10.1016/S0141-8130(98)00040-3.
[52] S.-Q. Chen, et al., The influence of alkaline treatment on the mechanical and structural properties of bacterial cellulose, Carbohydrate Polymers 271 (2021), https://doi.org/10.1016/j.carbpol.2021.118431.
[53] S. Wang, L. Copeland, Effect of alkali treatment on structure and function of pea starch granules, Food Chem. 135 (2012) 1635–1642, https://doi.org/10.1016/j.foodchem.2012.06.003.

Maleimide grafting onto polysaccharides via mild condition esterification and its impact on their structure

Valentin Silveira[a], Mohamed Jebrane [†,*✉], Adrien Letoffe[a], and Stergios Adamopoulos[a]

[a]*Department of Forest Biomaterials and Technology, Swedish University of Agricultural Sciences, Box 7008, 750 07 Uppsala, Sweden*

✉Mohamed Jebrane, Mohamed.jebrane@slu.se, +46 (0) 76 59 59 861

Supporting Information

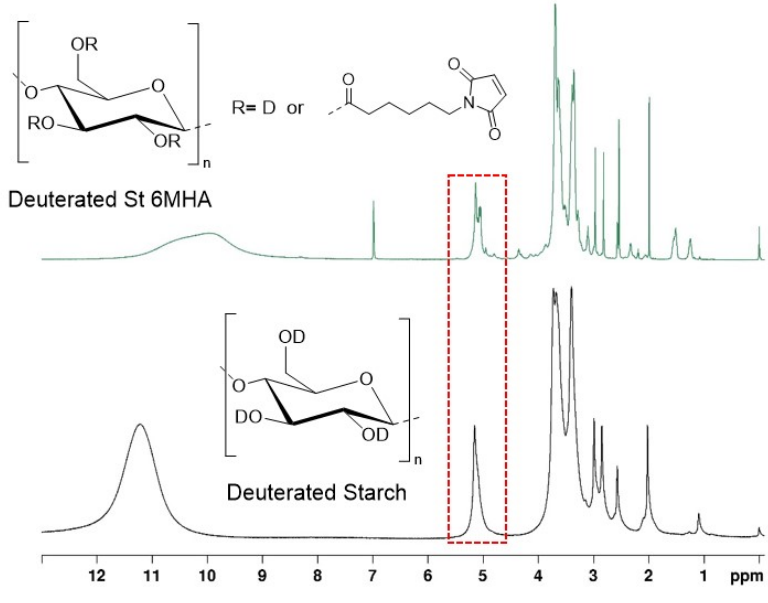

Figure S1 – ^{1}H NMR of starch and modified starch after adding d_1-tfa in DMSO-d_6.

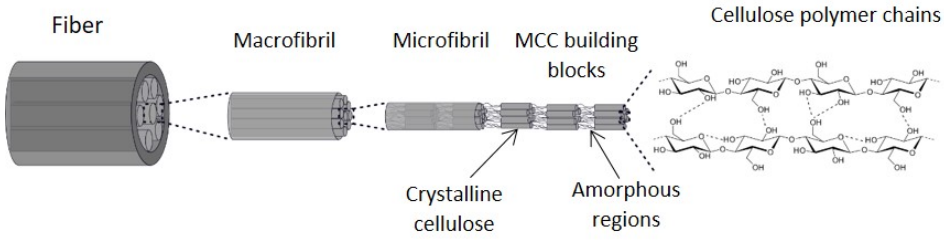

Figure S2 – Structure of cellulose fibers

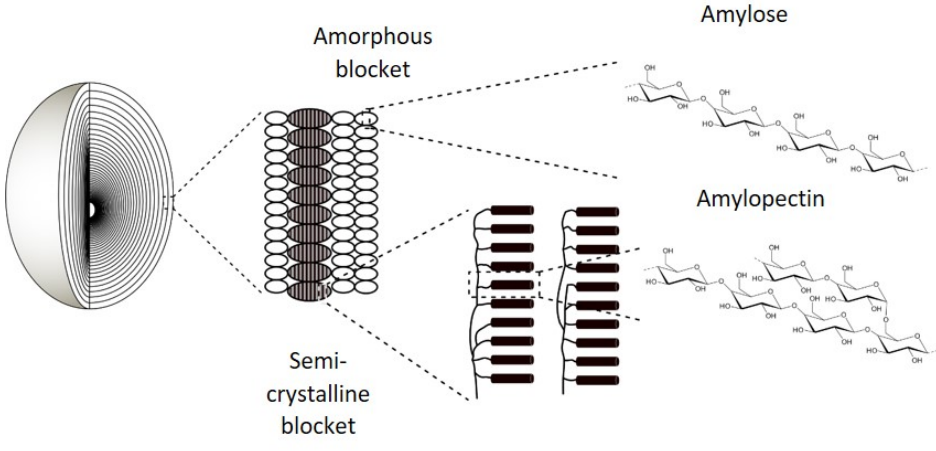

Figure S3 – Structure of starch granule

II

RSC Advances

PAPER

View Article Online
View Journal | View Issue

Cite this: *RSC Adv.*, 2025, **15**, 28255

One-pot synthesis of thermally reversible materials using maleimide-polysaccharide and furan-lignin derivatives

Valentin Silveira, Raffaello Papadakis and Stergios Adamopoulos*

The bio-based materials potato starch (St) and Kraft lignin (KL) were chemically modified to create a thermally responsive network through a reversible Diels–Alder (DA) reaction between maleimide and furan groups present in St and KL, respectively. To achieve this, St was esterified in a one-pot synthesis at room temperature with 6-maleimidohexanoic acid (6-MHA) to produce St 6MHA aligning with the 12 principles of green chemistry, which was confirmed by FTIR, ^{1}H, ^{13}C, and 2D NMR spectroscopy. Furan (Fu) groups were introduced to KL by reacting furfuryl glycidyl ether with the phenol entities of KL, forming KL-Fu. The structures of the KL-Fu derivatives were characterized using FTIR, ^{1}H, ^{13}C, and ^{31}P spectroscopy, as well as TGA. St 6-MHA and KL-Fu were then subjected to thermal cycloaddition through the DA reaction. Furthermore, controlled retro-DA reactions were induced thermally and confirmed by FTIR and ^{1}H NMR spectroscopy. DSC analysis of the final products revealed the thermally responsive nature of the system. This study highlights the significant potential of such a thermally responsive system, demonstrating that effective chemical modification of abundant renewable feedstock can enable the development of high-value materials thereof.

Received 4th April 2025
Accepted 4th August 2025

DOI: 10.1039/d5ra02344k

rsc.li/rsc-advances

1 Introduction

The persistent use of fossil fuel-based materials has led to significant environmental challenges, including pollution and resource depletion. As a sustainable alternative, biopolymers have emerged as promising solutions due to their biodegradability and renewable nature. Among these, starch and lignin, derived from plant biomass, have gained attention for their potential applications.[1,2] However, these biopolymers often exhibit poor performance when used in material applications in terms of mechanical properties, thermal stability, water resistance and others, limiting their broader use.[3,4] When used alone, these biopolymers lack sufficient mechanical strength or water resistance to function effectively as standalone materials. Consequently, they have primarily been utilized as fillers in traditional materials for enhancement of their bio-based content or similar.[5] To address these limitations, researchers have explored various modification techniques. For starch, esterification[6] and oxidation have traditionally been employed to enhance water resistance[7] and facilitate crosslinking. Meanwhile, research on lignin has primarily focused on alkylation, oxidation, and polymerization for applications as coatings, adhesives, and emulsifiers.[8,9] The growing interest in biopolymers as replacements for conventional durable fossil fuel-based materials reflects a global shift towards sustainable solutions[10] driven by environmental concerns and regulatory pressures.[11] Concerns about the accumulation of waste have heightened the focus on sustainable alternatives with more circular end-of-life options.

Starch, a natural polysaccharide derived from renewable agricultural resources such as corn, potato, and cassava, is widely regarded as a promising biopolymer for replacing fossil-fuel based materials, such as adhesives, films, and resins.[12–14] Its inherent biodegradability, abundance, and low cost make it an attractive candidate for producing eco-friendly packaging, disposable items, and films.[13,15] Moreover, the film-forming ability of starch, when processed through plasticization or blending, enables the creation of flexible, lightweight materials suitable for a range of applications. However, the thermoplastic character of starch presents significant challenges to replacing thermoset resins. Its hydrophilic nature leads to high moisture sensitivity, resulting in poor water resistance and limited durability under humid conditions.[16] Starch-based plastics also exhibit brittleness and insufficient mechanical strength compared to conventional plastics,[17] necessitating the use of plasticizers or blending with other polymers to improve flexibility and toughness. Additionally, processing starch requires specific conditions to avoid thermal degradation, and its compatibility with industrial-scale production processes remains an ongoing area of research. Despite these challenges, advancements in modification techniques and composite formulations continue to expand the potential of starch as

Department of Forest Biomaterials and Technology, Swedish University of Agricultural Sciences, Vallvägen 9C, 756 51 Uppsala, Sweden. E-mail: stergios.adamopoulos@slu.se; Tel: +46 73-572 27 86

a viable, sustainable alternative to traditional synthetic materials.[18]

On the other hand, lignin is a complex biopolymer found in plant cell walls, providing structural support and resistance to degradation. It is primarily composed of aromatic macromolecules derived from three monolignols: *p*-coumaryl alcohol, coniferyl alcohol, and sinapyl alcohol. These form hydroxyphenyl, guaiacyl, and syringyl units, which determine lignin's properties.[19] Lignin, being one of the most abundant biopolymers on our planet, also exhibits potential to replace aromatic fossil fuel-based resources. Of the 100 million tons of lignin generated annually through biomass processing, only approximately 2% are commercially utilized[20] for diverse applications such as binders, emulsifiers, and adhesives.[21] Currently, the majority of lignin is still being burned in pulping plants for energy production. As lignin is a by-product of the pulping process and not the primary product, its quality and purity can be relatively low. The specific production method influences its composition, often resulting in a mixture of impurities, including carbohydrates, proteins, and inorganic salts.[22] Moreover, the structural complexity and wide variability of lignin remain significant challenges for its direct use in application for high-value products. Although significant efforts have been made over the past few decades to characterize its structure, a clear understanding of its molecular composition has only recently emerged.[23] Controlling lignin's multifunctional nature is a crucial step in its refinement and valorization. For this reason, chemical modification has been recognized as a key strategy to address these issues, primarily by enhancing chemical reactivity, reducing polymer brittleness, improving solubility in organic solvents, and facilitating the processing of lignin.[24–26] Like polysaccharides, the modification of lignin relies on the presence of multiple hydroxyl groups, whether aliphatic or phenolic. Attempts to crosslink lignin to produce materials with higher bio-based content have been reported through esterification with diacids,[27] acetal formation with aldehyde,[28] and urethane formation with diisocyanate.[29]

Combining starch with lignin has been investigated as an effective strategy to address starch's deficient properties compared to fossil fuel-based materials, such as moisture sensitivity, thermal stability, and mechanical properties. Research has primarily focused on enhancing water resistance and decreasing the hydrophilicity of starch-based materials by integrating lignin into the starch matrix.[30] Several attempts have been reported to combine these two polymers. The focus has been towards the development of starch blends, more specifically thermoplastic starch, in which lignin is incorporated to improve both the film properties and the resistance to degradation of the film.[30] Indeed, lignin is a naturally occurring material with exceptional UV absorption capabilities, attributed to its aromatic structure and the presence of phenolic groups, ketones, and intramolecular hydrogen bonds.[31] For example Majeed *et al.*[32] tried to introduce lignin in urea cross-linked starch to improve coating properties. However, lignin's compatibility with other biopolymers and polymers, including starch, is limited due to its weak interfacial bonding, which often results in particle aggregation and phase separation. To overcome this issue, attempts to chemically bond starch and lignin have been made. Indeed, crosslinking of starch with lignin has been reported by using ammonium zirconium carbonate,[33] glutaraldehyde,[34] and urea after modifying both materials with aldehyde.[35] More recently, Rashedi *et al.*[36] crosslinked starch and lignin using a diepoxy crosslinker to improve the rheological and thermal properties of starch. The resin was produced through the formation of stable and resistant ether bonds, which prevent material degradation and enhance the recyclability of the bonded material.

Over the past years, research has increasingly been focused on integrating dynamic bonds into polymer structures, utilizing a click chemistry approach.[37,38] These bonds can form and break in response to external stimuli, such as heat, pH changes, or light irradiation, enabling reversible cross-linking in polymers.[39] This property leads to the creation of self-healing, debondable, and reprocessable materials. These architectures, known as covalent adaptable networks (CANs), can be either associative or dissociative, depending on the nature of bond formation.[40] One of the most widely used reactions in CAN formation is the Diels–Alder (DA), a [4 + 2] cycloaddition between a diene and a dienophile, offering 100% atom efficiency. For bio-based applications, the DA cycloaddition between furan and maleimide groups, acting as diene and dienophile respectively, provides a versatile approach to form reversible bonds.[41] This reaction offers several benefits, including its relatively low reaction temperatures around 60 to 70 °C for bond formation and 110 to 120 °C for the reverse reaction, which is well-suited to the thermal stability of starch and lignin.[42] In response to this, numerous such as lignin, tannins, alginate, and various other polysaccharides.[43–45] Indeed, several studies have employed the DA reversible reaction to create starch hydrogels, either by using a bismaleimide molecule to cross-link furan-modified starch or by reacting furan-modified starch with maleimide-modified starch.[46,47] The focus of the past years has been on introducing DA in thermoset resins, such as polyurethanes and epoxies, to maintain good mechanical properties and enable recyclability.[48] Nevertheless, little work has been done on developing fully bio-based reversible systems. The main interest in using DA reaction lies in the possibility of designing smart materials able to debond from each other or a given substrate, to debond back to initial components, to be reprocessed, and even self-healed.[49] This enables an easier recycling of composite materials if used as an adhesive, and offering composites a longer service-life if used as a coating. This approach enhances the structural integrity and functional properties of starch and lignin, rendering them more suitable for advanced applications. The DA reaction, a type of click chemistry,[41,50] is particularly advantageous due to its efficiency, mild reaction conditions, and eco-compatibility.[51] We believe that by incorporating click chemistry, these biopolymers can be tailored to exhibit improved compatibility and advanced properties, paving the way for their use in innovative and sustainable materials. Indeed, by crosslinking a polysaccharides with a phenolic compound it is possible to create a material that benefits from both advantages of starch and lignin. To the authors knowledge such investigation has not been made previously.

In this study, we report the development of a novel temperature-responsive material by combining the properties of starch and lignin with the advantages of the furan–maleimide DA reaction. The present work reports a new one-pot esterification at room temperature of starch using a solvent as a catalyst. Potato starch (St) was modified using 6-maleimidohexanoic acid (6-MHA), and kraft lignin (KL) was selectively modified at its phenolic chain ends using furfuryl glycidyl ether, introducing pendant maleimide and furan groups, respectively. These modifications were confirmed using spectroscopic methods (^{31}P and ^{1}H NMR, UV-Vis Absorption, and FTIR). Finally, furan and maleimide-grafted starch (St 6-MHA) and lignin (KL-Fu) were combined to perform the DA reaction, leading to formations of gels that returned to a liquid state upon triggering the reverse (retro) DA reaction. Our green method combines high carbon efficiency and one-pot/*in situ* synthetic methodologies, which significantly reduce the need to clean intermediate products. This, in turn, lowers energy demands and minimizes the extensive use of organic solvents.

2 Materials

Potato starch (St), kraft lignin (KL), oxalyl chloride, 6-maleimidohexanoic acid (6-MHA), dimethylacetamide (DMAc), dimethylsulfoxide (DMSO), furfuryl glycidyl ether (FGE), sodium hydroxide (NaOH), hydrochloric acid (HCl), lithium chloride, 2-chloro-4,4,5,5-tetramethyl-1,3,2-dioxaphospholane (TMDP, 95%), chromium(III) acetyl acetonate ($Cr(acac)_3$, 97%), cholesterol (greater than 99%), deuterated DMSO (DMSO-d_6), deuterated trifluoroacetic acid (TFA-d_1, 99.5% atom D),were purchased from Sigma-Aldrich (Stockholm, Sweden). All other solvents were American Chemical Society (ACS) grade and used as received.

3 Synthetic strategies

3.1 One-pot modification of starch

3.1.1 Preparation of acyl chloride. 6-MHA was dissolved in DMAc. Then, 1 equivalent of oxalyl chloride was added dropwise under ice bath. After adding, the reaction was conducted at room temperature under an inert atmosphere of argon for 3 h. Gaseous by-products (HCl, CO and CO_2) were allowed to escape the reaction mixture. At the end of reaction, the resulting acyl chloride was used without further purification.

3.1.2 Modification of starch with acyl chloride in solution. 3.2 g of oven dried St were placed in a round flask bottom containing 50 mL dry DMAc, the mixture was stirred at 140 °C for 1 h, then the temperature was lowered to 100 °C and 1 g of lithium chloride was added, the suspension instantly become transparent and the viscosity obviously rise to obtain a slurry. The solution was heated overnight to assess complete dissolution of St. The solution of St was added into the solution of acyl chloride in DMAc corresponding to 2 equivalent of hydroxyl group per anhydroglucose unit, and the reaction mixture was stirred at room temperature for 24 h under continuous flow of Argon. After reaction, the St was precipitated using methanol. Then, the modified St was washed/centrifuged with methanol 3–5 times, and then freeze-dried.

3.1.3 Functionalization of KL with furfuryl glycidyl ether. KL-Fu was synthetized based on previously reported method[23] without particularly considering a green approach. (1 g) was dissolved in water containing NaOH (200 mg, 5 mmol, corresponding to 1 eq. of total acidic groups in KL, *i.e.* phenolic OH and COOH). After 1 h of stirring, FGE was added (1.5 eq. of KL phenolic OH) and the reaction mixture was stirred at 50 °C for 24 h. After cooling to room temperature and acidifying to pH 2 using 10% (v/v) aqueous HCl, the suspension was centrifuged to recover the precipitated KL. The functionalized KL was then washed 3 times with 50 mL acidified water (pH 2) and subsequently freeze-dried.

4 Characterization

4.1 Amylose content of St

The amylose/amylopectin content of the St samples was determined by a colorimetric method previously described.[52] It consists of measuring the absorbance at 620 nm using ultraviolet-visible spectrophotometer (Lambda 35 UV/vis spectrometer, PerkinElmer, Waltham, USA) of a standard solution of pure amylopectin/amylose bound with iodine salt at different ratio to build a standard curve on the evolution of absorbance for the different amylose composition. The St amylose content was evaluated by the absorbance peak at 620 nm and compared with the standard curve. An amylose content of 17.1% was measured for St.

4.2 Spectroscopy

Spectrum Two FTIR (PerkinElmer, Waltham, USA) was equipped with an UATR Diamond accessory, which allows collection of FTIR spectra directly on a sample without any special preparation. The "pressure arm" of the instrument was used to apply a constant pressure (monitored by software) to the sample positioned on top of the diamond crystal to ensure a good contact between the sample and the incident IR beam. All FTIR spectra were collected at a spectrum resolution of 4 cm^{-1}, with 32 scans over the range from 4000 to 450 cm^{-1}.

All NMR spectra (^{1}H, ^{13}C, ^{13}C DEPT, ^{31}P, and 2D NMR spectroscopies) were recorded on a Bruker Avance III 600 MHz spectrometer (Billerica, USA). Samples were dissolved in DMSO-d_6.

For ^{31}P NMR spectroscopy, a 0.1 M solution of cholesterol in a pyridine/$CDCl_3$ anhydrous mixture (1.6 : 1) (v/v) was used as internal standard, Chromium(III) acetylacetonate was added into the internal solution as a relaxation agent. TMDP was used as phosphorylating agent, as described in standard protocols[53] 128 scans were recorded with 10 s delay and a spectral width of 100 ppm (180–100 ppm).

For ^{1}H NMR spectroscopic analysis, TMS was used as a reference. In this case, 16 scans were collected with 30 s delay. In a typical procedure for proper dissolution of St for ^{1}H NMR analyses, 100 to 150 mg of St were suspended in 800 μL of dry DMSO-d_6. The suspension was then shaken overnight on

a bidirectional mixer at 80 °C and finally transferred to a 5 mm NMR tube for analysis at room temperature. When TFA-d_1 was used, one to two drops were added to the solution just prior to measurement.

The degree of substitution (DS) of St-6-MHA was calculated by ^{1}H NMR spectroscopy, similarly to a commonly reported procedure.[54] It is based on the determination of the areas of the peaks assigned to grafted 6-MHA and those assigned to St backbone. After the addition of d_1-TFA, each α-D-glucopyranose unit contains seven protons. However, since St always contains traces of water that d-TFA wasn't able to deuterated, only the peak corresponding to the proton of the St at 5.19 ppm was usable. The DS was thus calculated using the following equation:

$$\mathrm{DS} = \frac{I_{\text{grafted 6-MHA}}}{2 \cdot I_{\text{starch}}} \quad (1)$$

where $I_{\text{grafted-6MHA}}$ and I_{starch} corresponds to the intensity of the protons from 6-MHA and to the intensity of the starch proton at 5.19 ppm, respectively.

4.3 Thermal stability

Thermogravimetric analysis (TGA) plots were carried out using a Mettler-Toledo TGA2 (Greifensee, Switzerland), under nitrogen with a flow rate of 40 mL min^{-1}. Around 5 to 10 mg of samples were put in alumina pans. The samples were heated from 30 to 650 °C at a heating rate of 10 °C min^{-1}.

4.4 Analysis of the DA and retro rDA reactions between St-maleimide and KL-furan

St-6-MHA and KL-Fu were dissolved in DMSO-d_6 with an equimolar ratio of maleimide and furan functions. The reaction was carried out at 65 °C for 4 days to ensure the total formation of the DA adduct. The intensity of the peak at 7.62 ppm assigned to furan double bonds protons was integrated to compare the area of the peak before and after reaction.

The retro DA of St–KL sample was analyzed using a DSC3+ differential scanning calorimeter (Mettler Toledo, city, Switzerland). A mixture containing St-6-MHA and KL-furan with an equimolarity of functionalizing group in DMSO were heated at 65 °C for 3 days to ensure that the DA reaction occurred. Approximately 5 mg of this mixture were accurately weighed by a balance with a resolution of 0.00001 g and put into an aluminum crucible of 100 μL with the empty aluminum crucible (with lead pierced) as reference. The samples were heated from −30 to 220 °C and subsequently cooled down to −50 °C for 5 min at a rate of 30 °C min^{-1}. Then, it was immediately heated from −50 to 200 °C at a rate of 30 °C min^{-1}. The first heating curve was use for functionalized materials when only the second heating curve was analyzed for raw materials. Dry nitrogen gas flow of 10 mL min^{-1} was used to purge the furnace chamber of the DSC instrument.

Modified St and KL were dissolved in DMSO with an equimolar ratio of maleimide and furan functions. DMSO was chosen as a solvent to minimize solvent evaporation during the measurement. The storage dynamic modulus (G') the loss modulus (G''), and viscosity were measured at 65 °C for 600 min using a rheometer (Haake Mars 60, Waltham, USA), equipped with a C35 1°/Ti measuring geometry at an oscillation frequency of 1 Hz. The sample was heated using a pelletier and temperature controller (MTMC Mars 60, Waltham, USA) and kept at a constant temperature using a water bath/circulator (Accel 500 LT, Waltham, USA).

4.5 E-factor

E-factor was calculated using the following equation:

$$\text{E-factor} = \frac{\text{total mass of waste from process}}{\text{total mass of product}} \quad (2)$$

By definition it takes into account waste such as byproducts of the reaction, unreacted reagents and solvent losses (anything else than the product of interest that can't be recovered for reuse). In the starch esterification process, we considered that potential wastes are the following:

- Lithium chloride used in starch dissolution.
- CO, CO_2 and HCl produced during acyl chloride formation.
- Excess of acyl chloride during starch esterification.
- DMAc used as solvent and methanol used to washed esterified starch.

Considering that the only wastes remaining in the solvent after starch modification is unreacted acyl chloride and starch residues, it is possible to recover DMAc and methanol by distillation. Thus DMAc and methanol were not included in E-factor.

5 Results and discussion

5.1 Analysis of the synthesized St-maleimide

The novelty of this esterification reaction (Scheme 1) is that it is performed in one pot at room temperature without the use of a harmful catalyst. We believe that the solvent also acts as a catalyst, similar to dimethyl formamide[55] and can be recovered at the end of the reaction. An E-factor of 1.2 was calculated under the assumption that both DMAc (b.p. 165 °C), used as the reaction solvent, and methanol (b.p. 64.7 °C), used for washing the final product, can be readily recovered through distillation. Consequently, the only likely residues in the process are LiCl, unreacted 6-MHA (b.p. 407 °C) and either native starch or St-6MHA. If we make the common assumption that 10%[56] of the solvents (DMAc and methanol) is lost, the E-factor raised up to 2.4. This raise the necessity for this reaction to be considered green to effectively recycle solvent.

Prior to St modification, 6-MHA was turn into its corresponding acyl chloride to increase its reactivity towards St hydroxyl groups. The reaction was carried under inert atmosphere to avoid the reaction of water present in the air with the newly form acyl chloride. Former studies reported the direct use of the synthetized acyl chloride without further purification.[23,57] We believe that it is hard to isolate the product and analyze it, as conventional FTIR is challenging to perform without hydrolyzing acyl chloride[23] because of the moisture present in the air.

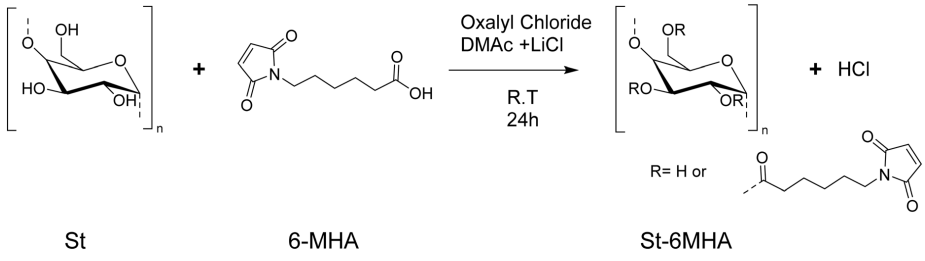

Scheme 1 Synthesis of St 6-MHA.

NMR has been done previously by other researchers.[42] Indeed, by evaporation of the solvent under vacuum followed by dissolution in deuterated solvent under inert atmosphere using septum, it is possible to transfer the product in NMR tube without any contact with the air. In order to minimize hydrolysis (potentially decreasing esterification yield), the acyl chloride was directly used without further purification, and the St solution in DMAc was added into it. The raw and modified St were analyzed by FTIR (Fig. 1).

Bands corresponding to the grafted 6-MHA St were observed at 1696, 1624 and 826 cm^{-1} respectively, attributed to maleimide N–C=O stretching, C=C bending and C–H ring bending. A band at 1740 cm^{-1} was attributed to ester C=O stretching confirming the esterification. Moreover, consumption of the hydroxyl after esterification was shown by the decrease of intensity of St hydroxyl groups stretching corresponding band around 3380 cm^{-1}. These results are consistent with previous work found in the literature.[58,59]

^{1}H and ^{13}C NMR of native (unmodified) St and St 6-MHA were recorded and peaks were assigned in details to confirm the success of the modification before performing the DA reaction. In order to confirm ^{1}H and ^{13}C NMR's assignments, 2D NMR of native and modified St was, ^{1}H–^{13}C HSQC and HMBC spectra can be found in SI (Fig. S2–S5).

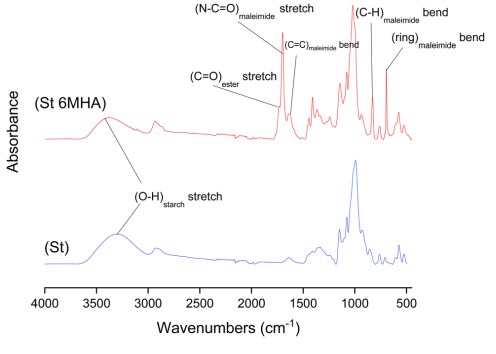

Fig. 1 FTIR absorbance spectra of unmodified St and 6-MHA grafted St.

The presence of maleimide groups grafted onto St was confirmed through ^{1}H (Fig. 2) and ^{13}C (Fig. 3) NMR. The ^{1}H NMR spectrograms show peaks corresponding to the protons of grafted 6-MHA St peak at 6.90 ppm, attributed to the protons on the maleimide ring. This signal was used to determine the degree of substitution (DS) after d_1-TFA addition, 0.97 ± 0.02. In theory, the addition of d_1-TFA enables to exchange OH protons with TFA-d_1 deuteron leading to shift all peaks corresponding to starch hydroxyl and water to a single peak around 8 ppm. Thus, allowing to simplify ^{1}H NMR spectrum in order to use St backbone protons to determine DS. This method was described by Morinval *et al.*[42] in order to calculate the degree of substitution of amylomaise St. Nonetheless, there is still traces of water trap into starch structure that doesn't exchange is proton with TFA-d_1. Indeed, unlike potato St, amylomaise has a high amylose content, and thus less crystalline, and be easier to solubilize and get rid of water into the St core. For this reason, only the peak at 5.19 ppm corresponding to one of the St proton was clear enough to be use in this purpose. Spectra of St-6-MHA in DMSO-d_6 are given in the SI.

On the ^{13}C NMR spectrum (Fig. 3), peaks between 171.5 and 173.2 ppm respectively corresponded to (C=O) carbons of maleimide and ester, indicating successful esterification.

On both ^{1}H and ^{13}C NMR spectra of St 6-MHA the peaks corresponding to the St native structure appeared broader and flattened. This decrease in peaks intensity is due to partial esterification of St, increasing the number of different equivalent groups of protons, and thus broadening the peak range while lowering intensity.[60] High scans number was required to make those peaks appeared on ^{13}C NMR as ^{13}C NMR is more sensitive to neighboring atoms than ^{1}H NMR and has a lower natural abundance of ^{13}C.

By integrating data from both 1D and 2D NMR spectroscopy, the observed peaks were successfully assigned to their respective hydrogen and carbon atoms. HMBC and HSQC of native St was performed (Fig. S2 and S3) to differentiate peaks from St and 6-MHA. The structure determination of St 6-MHA through HSQC (Fig. S5) and HMBC (Fig. S4) further confirmed the esterification. HSQC (Fig. S5) displayed peaks corresponding to the ring carbons and hydrogens of St when HMBC mostly shown the peaks corresponding to grafted FGE.

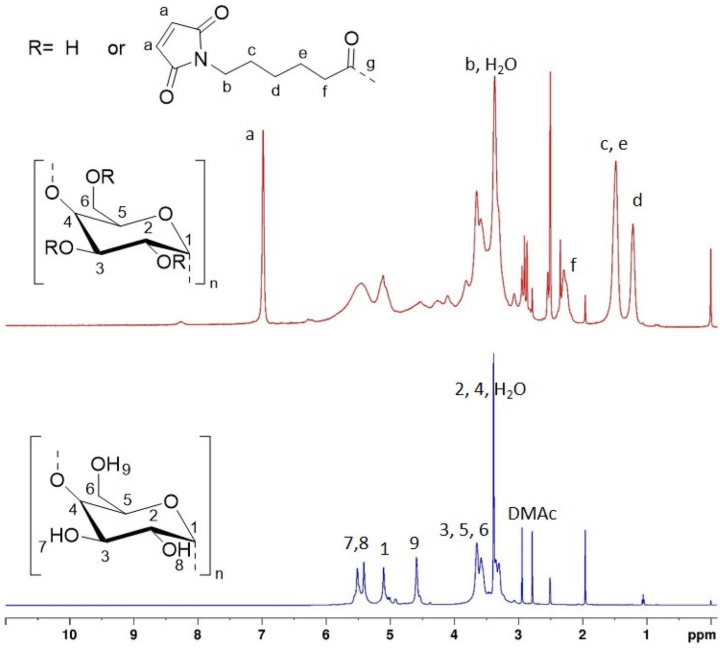

Fig. 2 ^{1}H NMR spectra of unmodified St and 6-MHA grafted St.

5.2 Analysis of the synthesized lignin-furan

KL was functionalized with FGE to introduce furan rings mostly at the phenolic chain ends, as illustrated in Scheme 2. The reaction was conducted in water with a stoichiometric amount of NaOH, calculated based on the total acidic groups in KL (both carboxyl and phenolic hydroxyl groups). Under these conditions, only carboxyl and phenolic OH groups were deprotonated, while aliphatic OH groups remained unaffected due to their significantly higher pK_a. As a result, phenolate ions acted as the reactive species, while carboxyl groups were inactive as carboxylates.

FTIR spectra of native KL and furan-grafted KL (KL-Fu) were recorded (see Fig. 4). Bands at $\nu = 1711$, 1588, 918 and 750 cm^{-1} were attributed to furan C=C stretching, C=C stretching, furan ring bending and C=C bending, respectively.[23] The furan grafting also cause an increase of intensity of the broad band between 3000 and 3600 cm^{-1}, corresponding to O–H stretching due to the epoxide ring opening leading to the formation of aliphatic hydroxyl groups.

^{1}H and ^{13}C NMR KL and KL-Fu were recorded and peaks were assigned to confirm the reaction. ^{1}H and ^{13}C NMR spectra of furfuryl glycidyl ether were also recorded to help in assignment of new peaks (Fig. S10).

The presence of maleimide groups grafted onto St was confirmed through ^{1}H (Fig. 5) and ^{13}C (Fig. 6) NMR. The ^{1}H NMR spectrograms show peaks corresponding to the protons of grafted 6-MHA St peak at 6.90 ppm, attributed to the protons on the maleimide ring.

The ^{1}H NMR spectra of the functionalized KL (Fig. 5), revealed two new peaks at 6.40 and 7.60 ppm, corresponding to the hydrogen atoms of the furan ring. Moreover, two peaks around 3.20 and 4.20 ppm corresponding to protons of the carbon chain of FGE could be observed.

The grafting of furan moieties onto KL was further confirmed through ^{13}C NMR (Fig. 6), and clear peaks associated to FGE after ring opening of the epoxide could be distinguished from broad and less intense peak from KL. Indeed, peaks corresponding to carbons of the furan ring were identified at 110, and 142 ppm. The peaks of the remaining carbon of FGE were present between 60 and 70 ppm (Fig. 6).

As illustrated in Scheme 2, the epoxide ring opening generates a new aliphatic hydroxyl group, leading to an increase in aliphatic OH content. This reaction results in the appearance of a new peak with high intensity in the ^{31}P NMR spectrum at 146 ppm, which is distinct from the original KL aliphatic OH signal, consistent with previous observations.[23] Indeed, 3 distinct area characteristic to KL ^{31}P NMR spectra: 134 to 136 ppm (carboxylic acid), 137 to 145 ppm (phenolic) and 145 to 150 ppm (aliphatic hydroxyl) are shown in Fig. 7.[53] Moreover, 3 sharp peaks with high intensities are displayed in ^{31}P NMR spectrum at 175, 144 and 132 ppm. They can be respectively attributed to the excess of TMDP, the cholesterol (internal

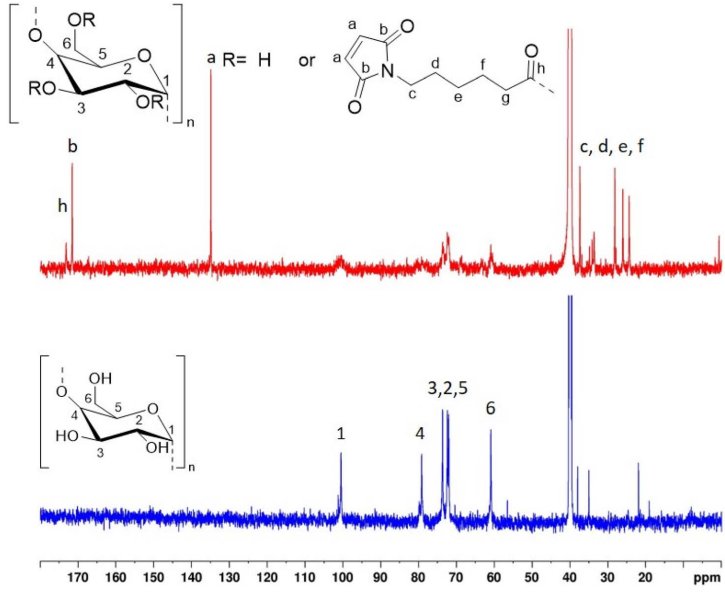

Fig. 3 ^{13}C NMR spectra of unmodified St and 6-MHA grafted St.

standard) and the hydroxylated-TMDP. The presence of these peaks confirmed the sample complete derivatization.[53]

As it could be seen on NMR spectra of St-6MHA, the peaks corresponding to the KL native structure appeared broader and flattened. This decrease in peaks intensity is due to partial modification of KL, increasing the number of different equivalent group of protons and thus broadening the peak range while lowering intensity. High scans number was required to make those peaks appeared on ^{13}C NMR as ^{13}C NMR is more sensitive to neighboring atoms than ^{1}H NMR and has a lower natural abundance of ^{13}C.

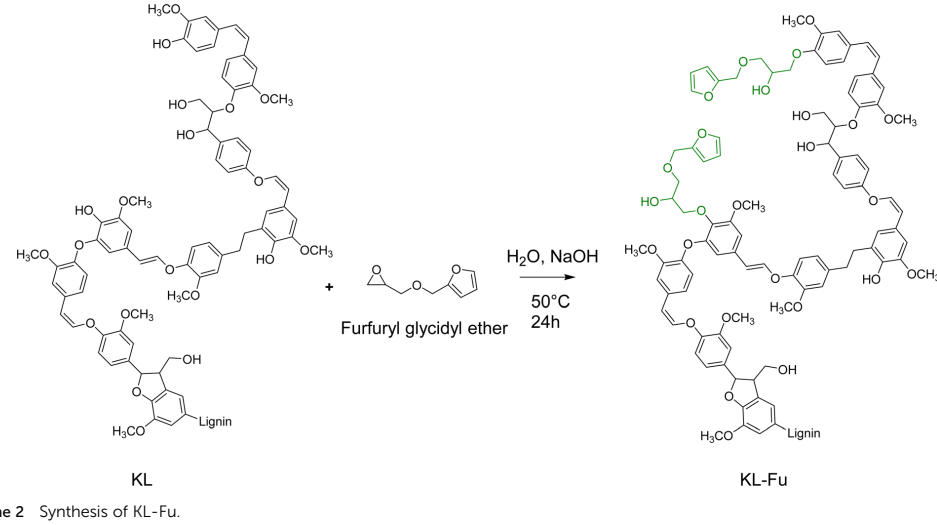

Scheme 2 Synthesis of KL-Fu.

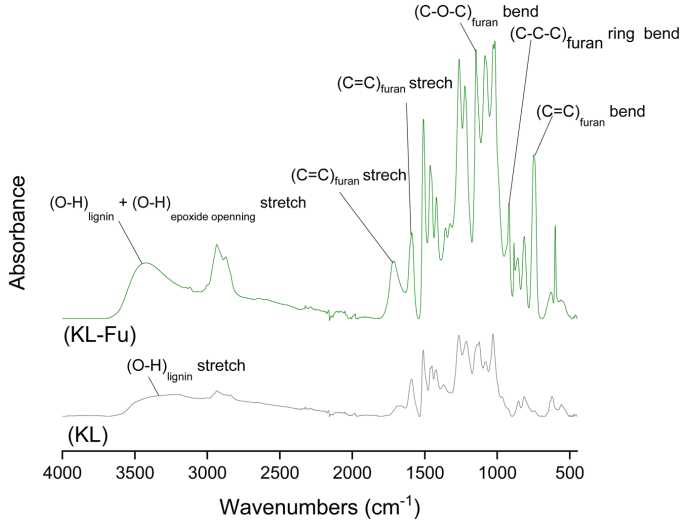

Fig. 4 FTIR absorbance spectra of unmodified KL and furan grafted KL.

The furan content of KL-Fu was measured through quantitative ^{31}P NMR following the procedure reported by Argyropoulos *et al.*[53] resulting as 2.30 mmol g^{-1}. This result aligned with previous work reported by Duval *et al.*[23] in which it was found that the total phenol content can react in the presence of a slight excess of FGE.

5.3 Analysis of the DA and rDA reactions between St-maleimide and KL-furan

The formation of DA network was investigated as we believe that such networks might show potential interest in the development of thermally responsive material such as on demand debonding adhesive. Moreover, this reversible network benefit

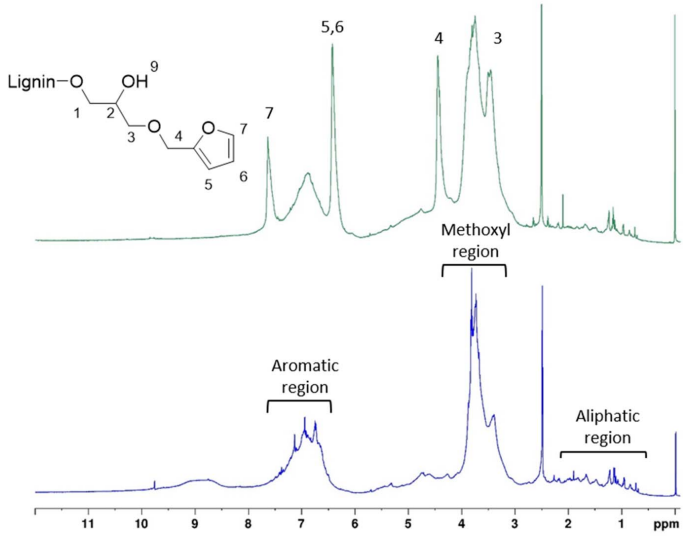

Fig. 5 ^{1}H NMR spectra of KL and furan grafted KL.

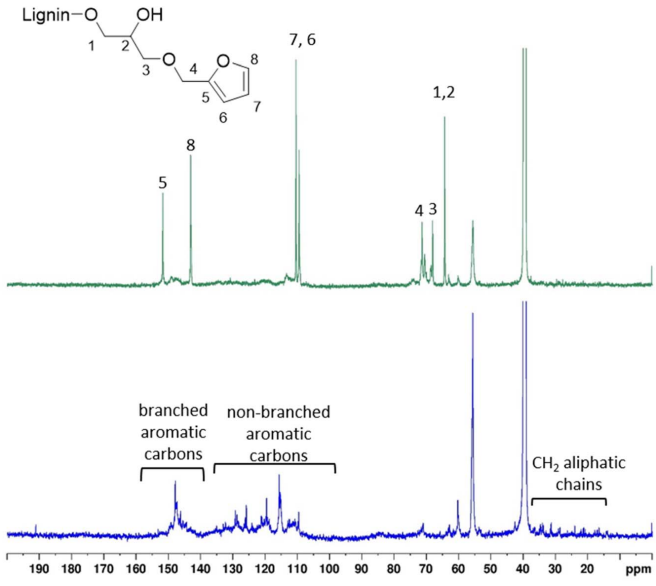

Fig. 6 ^{13}C NMR spectra of unmodified KL and furan grafted KL.

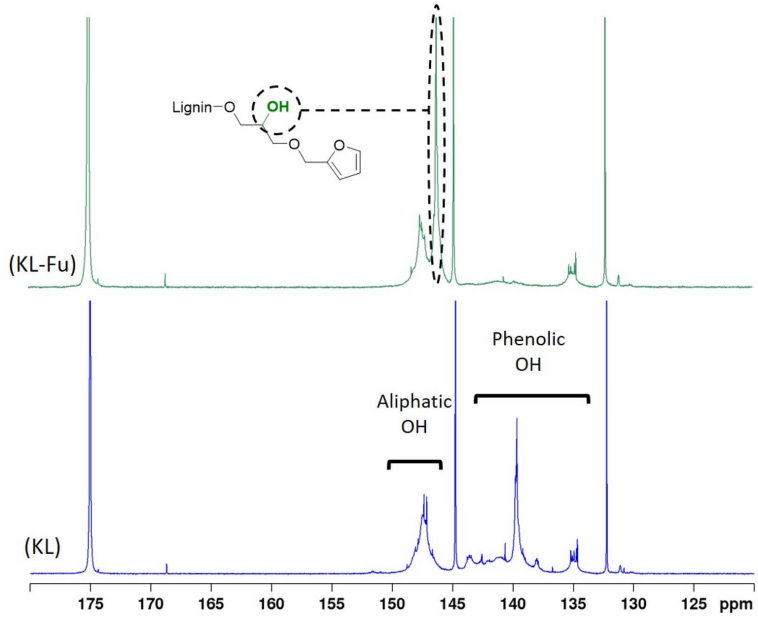

Fig. 7 ^{31}P NMR spectra of unmodified lignin and furan grafted lignin.

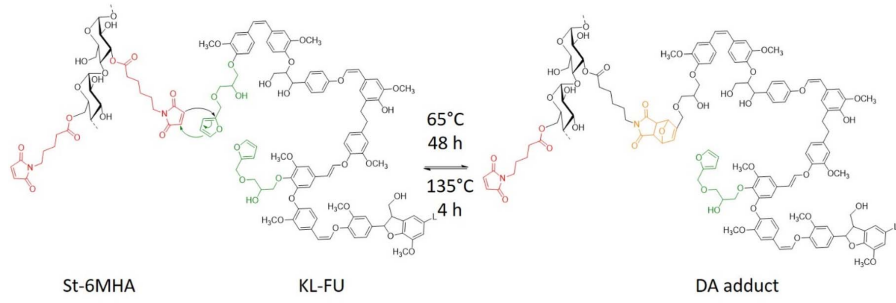

Scheme 3 St-6-MHA/KL-Fu DA network.

from the green aspect of the DA reaction, which provides a 100% atom economy, through click-chemistry (Scheme 3).

In order to demonstrate the cross-linking between the modified materials *via* DA cycloaddition, St 6-MHA and KL-Fu were mixed in a 1 : 1 maleimide to furan ratio and dispersed in DMSO to create a liquid with very low viscosity, facilitating observation of gel formation as the modified starch form a gel by itself at high concentration. This mixture was heated to 65 °C

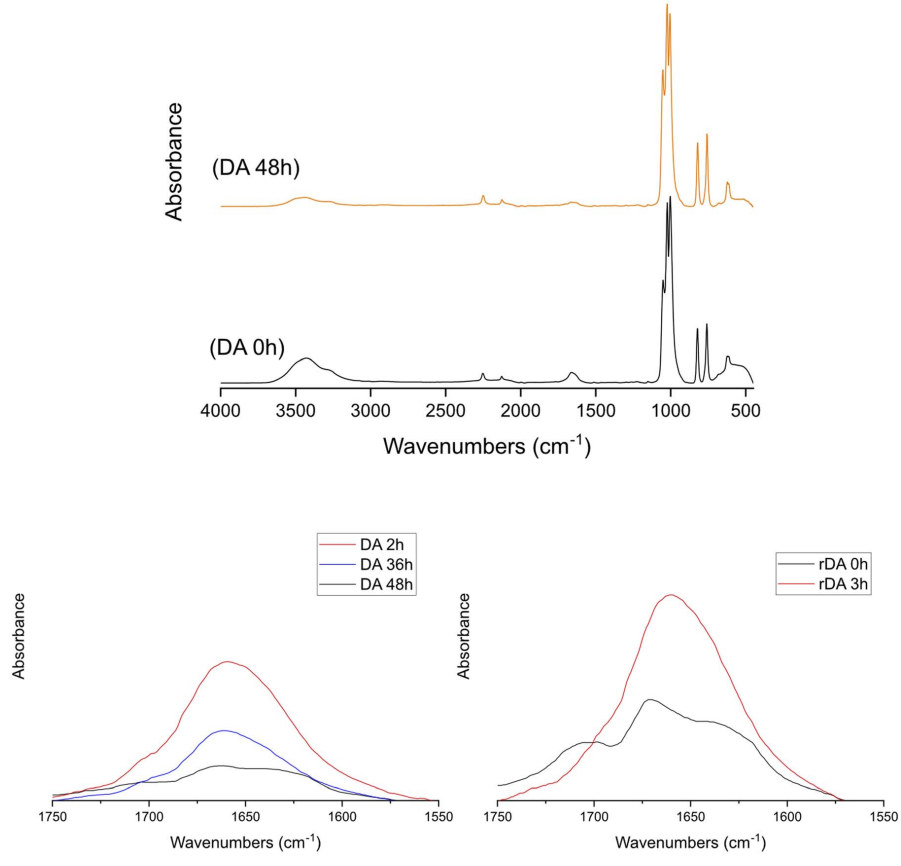

Fig. 8 FTIR absorbance spectra of St-6-MHA/KL-Fu mixture before and after heating at 65 °C for 48 h.

and stirred overnight. The gel formation was observed, and later disassembled upon heating to 135 °C for 2 h. A darker solution was obtained. When the mixture was too dilute, a phase separation between the gel formed and the excess of solvent could be observed.

To further confirm the forward and retro DA reactions, KL-Fu and St 6-MHA dispersed in DMSO and consecutively heated at 65 °C for 2 days and 135 °C for 3 hours, this sequence was repeated 2 times and FTIR spectra were recorded at regular time points. The decrease of intensity of the band around 1640–1680 cm^{-1} corresponding to the maleimide C=C bending, showed the formation of the DA adduct.[61] As can be seen on Fig. 8, the ratio between the intensity of this band and the band corresponding to the DMSO clearly confirmed the consumption of maleimide in the forward reaction and regeneration in the retro reaction.

The analysis of DA reaction was also confirmed by ^{1}H NMR (Fig. 9), and the modified St and KL were dissolved in DMSO-d_6 at low concentration to avoid gel formation to obtain a clear signal. The spectrum revealed a decrease of the peak intensity at 7.62 ppm corresponding to the furan double bonds. This observation is consistent with the disappearance of the furan double bonds during the formation of DA adduct. A 70% conversion was estimated by using peaks at 7.00 related to maleimide consumption aligning with the literature.[42]

The decomposition of DA adduct was investigated through Differential Scanning Calorimetry (DSC). A mixture of raw St and KL as well as the DA adduct were placed in 100 µL crucible and heated from 0 to 180 °C, and the obtained thermograms are presented in Fig. 10. In order to prove that the peaks observed in Fig. 10 do not correspond to individual behavior of St, St 6-MHA, KL and KL-Fu, their DSC thermograms were recorded and can be found in supported information (Fig. S6 and S7).

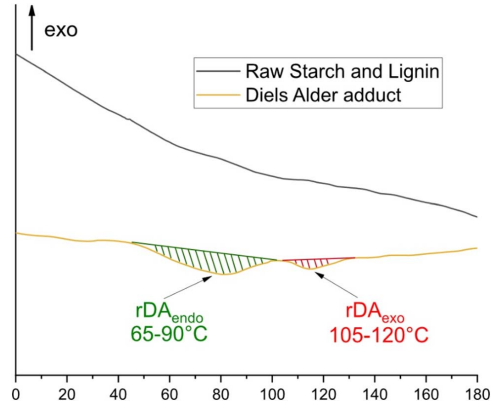

Fig. 10 DSC thermogram of St-6-MHA/KL-Fu mixture after heating at 65 °C for 48 h.

Moreover, to show the stability of all materials under this range of temperature, TGA and DTG thermograms of St, St 6-MHA, KL and KL-Fu were recorded between 30 and 630 °C (Fig. S8 and S9). As reported in previous work,[59] the thermal stability of St (Fig. S8) seems to be slightly better after modification. Moreover, the TGA thermograms of St showed a two-step degradation corresponding to the degradation of St backbone followed by the degradation of 6-MHA further confirming the success of esterification. Same observations were made for KL (Fig. S9). It was concluded that St 6-MHA and KL-Fu could both support the thermal condition of forward and retro-Diels–Alder reaction. This enabled to ensure preventing the degradation of renewable

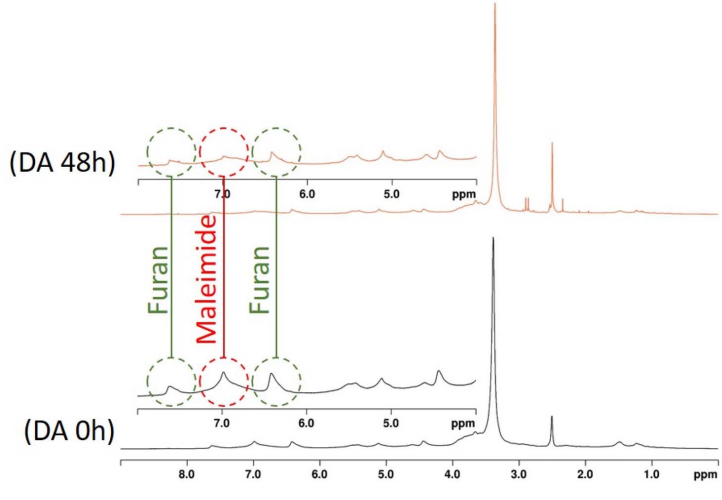

Fig. 9 ^{1}H NMR spectra of St-6-MHA/KL-Fu mixture before and after heating at 65 °C for 48 h.

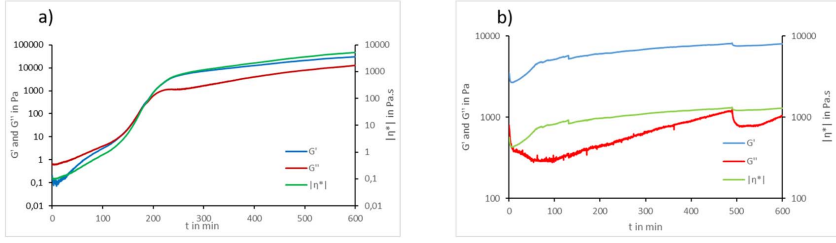

Fig. 11 Rheological analysis of a mixture of raw St and raw KL (a) and a mixture of St 6-MHA and KL-Fu (b) at 65 °C for 600 min.

feedstocks and maintaining the functional performance of bio-obased components.

While the DSC thermograms of initial materials (St mixed with KL) do not show the presence of any peaks (aligning with TGA's observations), the thermograms of DA adduct show the presence of two broad endothermic peaks around 80 and 110 °C. These two peaks correspond to the retro DA of the two DA adducts diastereoisomer. Indeed, in the DA reaction, two possible stereoisomeric products can be formed: the *endo* and *exo* products. The *endo* product arises when the electron-withdrawing group of the dienophile is oriented towards the diene, benefiting from secondary orbital interactions. This makes the *endo* pathway kinetically favored, meaning it forms more quickly due to a lower activation energy. In contrast, the *exo* product is often the thermodynamically more stable form but forms more slowly. As a result, the *endo* product is expected to dominate, especially at lower temperatures with bulky substrates.[62] It is well known that the *exo* diastereoisomer cleaved after the *endo* hence the higher temperature peak can be assigned to the *exo* diastereoisomer.[42]

The enthalpy energy of the contribution from *endo* and *exo* peaks was measured using star-e software (Metler Toledo, Greifensee, Switzerland), and it was calculated that the *endo* product has a significantly higher contribution with a factor 2.2. In the end, the DSC analysis enabled to further confirm the reversibility of the DA adduct.

The rheological behavior of a mixture of raw St and KL as well as St 6-MHA and KL-Fu was studied as a trial to confirm the forward DA reaction. It has to be noticed that, after 10 h at 65 °C, both mixtures had a completely different aspect. While the mixture of raw materials appeared as a slurry viscous solution, the mixture of modified materials appeared instead as a thin film coating the surface of the metal base of the rheometer apparatus.

The graphs in Fig. 11 show the evolution of storage modulus (G'), loss modulus (G'') and the modulus of complex viscosity $|\eta^*|$ of a mixture containing St and KL (11a) and a mixture containing St 6-MHA and KL-Fu (11b). When the DA material is heated to 65 °C, which corresponds to the forward DA reaction and possibly the gel-point temperature its loss modulus does not surpasses the elastic modulus, indicating a sol–gel behavior.[63] On the other hand, for the native materials mix, when heated to 65 °C in the same conditions, its viscous modulus surpasses the elastic modulus, indicating a liquid-like sol behavior.[63] The mixture of St and KL displayed an increase in both moduli and viscosity along time. Starch is known to exhibit shear-thickening behavior, wherein viscosity increases with shear frequency. Although the experimental frequency was held constant throughout our measurements. It was reported that shear-induced physical crosslinking[64] can happen in St dissolved in 90 : 10 DMSO : water solution. This can be seen as the formation of a highly entangled network of St itself as well as between St and KL. We also believe that a prolonged heating can induce solvent evaporation, leading to an increased concentration of starch and, consequently, a rise in viscosity. Moreover the fact that G' is higher than G'' indicated that the mixture tends to behave like a solid (elastic) rather than a liquid (viscous). We believe that upon heating, the starch and lignin components have the opportunity to interact *via* intermolecular hydrogen bonding. The hydroxyl groups of starch may form hydrogen bonds with both aliphatic and phenolic OH groups present in KL. As heating might cause a partial loosening of starch's granular structure (increase of chains distance with temperature),[65] improving its accessibility and increasing the likelihood of interfacial contact with lignin. This enhanced intermolecular bonding contributes to a denser network structure, which is expected to result in G' being higher than G''. Moreover, the starch gelatinization has been found to be dependent on hydrogen bond density in the solvent.[66] Adding KL to DMSO could decrease the volumetric density of intermolecular hydrogen bonds leading to an increase in St gelatinization temperature.

On the graph of DA (Fig. 11b) we can see twice the breakage of the materials resulting in two consecutive drastic drops after 120 and 480 min. This shows the different state of both materials. On one side, we have a viscous solution slowly turning into entangled network. On the other side we have a fast curing cross-linked gel. We believe that the curing is more efficient in the rheometer set up. The small sample thickness,[67] which is less than 1 mm, resulting in a higher surface-to-volume ratio in contact with the plates. This geometry allows heat to be transferred more rapidly and uniformly throughout the material, potentially resulting in faster curing.

6 Conclusions

In conclusion, a new thermally responsive and sustainable macromolecular system was successfully developed. Efficient

synthetic strategies for the functionalization of potato St and KL were established. St was first esterified through a one-pot synthesis, and the grafting of maleimide groups onto the starch backbone was clearly confirmed by FTIR and NMR spectroscopies. On the other hand, KL was modified with furfuryl glycidyl ether, as demonstrated by FTIR, ^{1}H, ^{13}C, and ^{31}P NMR spectroscopies. The two counterparts were conjugated through the DA reaction between the furan and maleimide functionalities of the two modified biopolymers. This reaction was confirmed through various spectroscopic and thermal analysis methods. Subsequently, the reversibility of the DA-conjugated network was examined thermally, and it was found that the retro DA reaction is possible through heating at 135 °C. Indeed, the adduct decomposition was shown by DSC and the reversibility was followed with the evolution of maleimide characteristic band by FTIR through successive heating cycles at 65 (DA) and 135 °C (rDA). By harnessing the advantages of the furan–maleimide DA reaction, this study highlights a sustainable approach on developing advanced biopolymer systems. The efficient synthetic methodologies reduce the need for intermediate cleaning steps, thus lowering energy demands and minimizing the use of organic solvents. This thermally responsive macromolecular system not only addresses environmental challenges posed by fossil fuel-derived materials but also contributes to the advancement of eco-friendly materials with enhanced functional properties.

Author contributions

Conceptualization R. P., S. A. and V. S.; methodology and experiments design, R. P., V. S.; validation, R. P. and S. A.; analysis, V. S.; investigation, V. S.; resources, S. A.; writing—original draft preparation, V. S.; writing—review and editing, R. P., V. S. and S. A.; visualization, V. S. All authors have read and agreed to the published version of the manuscript.

Conflicts of interest

The authors declare no conflict of interest.

Data availability

The data presented in this study are available from the corresponding author upon request.

Supplementary information includes: S1. ^{1}H NMR spectra of raw potato starch (blue) and St 6MHA (red) in DMSO-d_6 after adding TFA-d_1, S2. HMBC 2D NMR spectrum of raw potato starch in DMSO-d_6, S3. HSQC 2D NMR spectrum of raw potato starch in DMSO-d_6, S4. HMBC 2D NMR spectrum of St-6MHA in DMSO-d_6, S5. HSQC 2D NMR spectrum of St-6MHA in DMSO-d_6, S6. DSC thermogram of unmodified and modified Starch, S7. DSC thermogram of unmodified and modified Lignin, S8. TGA and DTG thermograms of unmodified and modified Starch, S9. TGA and DTG thermograms of unmodified and modified Lignin, S10. ^{1}H and ^{13}C NMR spectra of Furfuryl glycidyl ether in DMSO-d_6. See DOI: **https://doi.org/10.1039/d5ra02344k**.

References

1 M. Qamruzzaman, F. Ahmed and M. I. H. Mondal, *J. Polym. Environ.*, 2022, **30**, 19–50.
2 M. Norgren and H. Edlund, *Curr. Opin. Colloid Interface Sci.*, 2014, **19**, 409–416.
3 I. McKay, J. Vargas, L. Yang and R. M. Felfel, *Materials*, 2024, **17**, 4878.
4 K. M. Tavares, A. d. Campos, M. C. Mitsuyuki, B. R. Luchesi and J. M. Marconcini, *Carbohydr. Polym.*, 2019, **223**, 115055.
5 M. R. Sanghvi, O. H. Tambare and A. P. More, *Polym. Bull.*, 2022, **79**, 10491–10553.
6 M. A. Otache, R. U. Duru, O. Achugasim and O. J. Abayeh, *J. Polym. Environ.*, 2021, **29**, 1365–1379.
7 X. Wang, L. Huang, C. Zhang, Y. Deng, P. Xie, L. Liu and J. Cheng, *Carbohydr. Polym.*, 2020, **240**, 116292.
8 E. A. Agustiany, M. Rasyidur Ridho, M. R. D. N., E. W. Madyaratri, F. Falah, M. A. R. Lubis, N. N. Solihat, F. A. Syamani, P. Karungamye, A. Sohail, D. S. Nawawi, A. H. Prianto, A. H. Iswanto, M. Ghozali, W. K. Restu, I. Juliana, P. Antov, L. Kristak, W. Fatriasari and A. Fudholi, *Polym. Compos.*, 2022, **43**, 4848–4865.
9 R. Nadányi, A. Ház, A. Lisý, M. Jablonský, I. Šurina, V. Majová and A. Baco, *Energies*, 2022, **15**, 6520.
10 D. A. Ferreira-Filipe, A. Paço, A. C. Duarte, T. Rocha-Santos and A. L. Patrício Silva, *Int. J. Environ. Res. Public Health*, 2021, **18**, 7729.
11 M. P. Wilson and M. R. Schwarzman, *Environ. Health Perspect.*, 2009, **117**, 1202–1209.
12 A. Surendren, A. K. Mohanty, Q. Liu and M. Misra, *Green Chem.*, 2022, **24**, 8606–8636.
13 E. Ogunsona, E. Ojogbo and T. Mekonnen, *Eur. Polym. J.*, 2018, **108**, 570–581.
14 Z. u. Din, L. Chen, H. Xiong, Z. Wang, I. Ullah, W. Lei, D. Shi, M. Alam, H. Ullah and S. A. Khan, *Starch/Staerke*, 2020, **72**, 1900276.
15 T. Jiang, Q. Duan, J. Zhu, H. Liu and L. Yu, *Adv. Ind. Eng. Polym. Res.*, 2020, **3**, 8–18.
16 F. Liu, J. Ren, Q. Yang, Q. Zhang, Y. Zhang, X. Xiao and Y. Cao, *Int. J. Biol. Macromol.*, 2024, **260**, 129404.
17 Y. Zhang, C. Rempel and Q. Liu, *Crit. Rev. Food Sci. Nutr.*, 2014, **54**, 1353–1370.
18 L. do Val Siqueira, C. I. L. F. Arias, B. C. Maniglia and C. C. Tadini, *Curr. Opin. Food Sci.*, 2021, **38**, 122–130.
19 R.-C. Sun, *ChemSusChem*, 2020, **13**, 4385–4393.
20 R. Baghel, Lignin Waste Market Size & Share, by Product (Lignosulfonate, Kraft Lignin); Application (Concrete Admixtures, Animal Feed Binders, Dyestuff) - Global Supply & Demand Analysis, Growth Forecasts, Statistics Report 2025-2037, 2025, **https://www.researchnester.com/reports/lignin-waste-market/6166#:~:text=Around50milliontonsof,chemicalconversiontoproducelignosulfonates**.
21 J. J. Liao, N. H. A. Latif, D. Trache, N. Brosse and M. H. Hussin, *Int. J. Biol. Macromol.*, 2020, **162**, 985–1024.

22 S. Constant, H. L. Wienk, A. E. Frissen, P. De Peinder, R. Boelens, D. S. Van Es, R. J. Grisel, B. M. Weckhuysen, W. J. Huijgen and R. J. Gosselink, *Green Chem.*, 2016, **18**, 2651–2665.
23 A. Duval, H. Lange, M. Lawoko and C. Crestini, *Green Chem.*, 2015, **17**, 4991–5000.
24 P. Figueiredo, K. Lintinen, J. T. Hirvonen, M. A. Kostiainen and H. A. Santos, *Prog. Mater. Sci.*, 2018, **93**, 233–269.
25 M. H. Tran and E. Y. Lee, *J. Wood Chem. Technol.*, 2018, **38**, 460–478.
26 J. J. Meister, in *Chemical Modification of Lignocellulosic Materials*, Routledge, 2017, pp. 129–157.
27 S. Kim and H. Chung, *ACS Sustain. Chem. Eng.*, 2023, **11**, 1709–1719.
28 Y. Zhang, Y. Chen, G. Li, K. Shen and Y. Wu, *ACS Sustain. Chem. Eng.*, 2022, **10**, 15538–15549.
29 V. K. Thakur and M. K. Thakur, *Int. J. Biol. Macromol.*, 2015, **72**, 834–847.
30 J. A. Diaz-Baca and P. Fatehi, *Biotechnol. Adv.*, 2024, **70**, 108281.
31 M. H. Tran, D.-P. Phan and E. Y. Lee, *Green Chem.*, 2021, **23**, 4633–4646.
32 Z. Majeed, N. Mansor, Z. Man and S. A. Wahid, *E-Polymers*, 2016, **16**, 159–170.
33 A. Javed, P. Rättö, L. Järnström and H. Ullsten, *Polymers*, 2021, **13**, 1595.
34 R. Shi and B. Li, *Starch/Staerke*, 2016, **68**, 1224–1232.
35 X. Chen, A. Pizzi, B. Zhang, X. Zhou, E. Fredon, C. Gerardin and G. Du, *Wood Sci. Technol.*, 2022, **56**, 63–85.
36 Z. Rashedi, R. Mawhinney, W. Gao, A. Salaghi and P. Fatehi, *Carbohydr. Polym.*, 2025, **350**, 123044.
37 R. J. Wojtecki, M. A. Meador and S. J. Rowan, *Nat. Mater.*, 2011, **10**, 14–27.
38 S. Samanta, S. Kim, T. Saito and A. P. Sokolov, *J. Phys. Chem. B*, 2021, **125**, 9389–9401.
39 K. R. Mulcahy, A. F. Kilpatrick, G. D. Harper, A. Walton and A. P. Abbott, *Green Chem.*, 2022, **24**, 36–61.
40 C. J. Kloxin and C. N. Bowman, *Chem. Soc. Rev.*, 2013, **42**, 7161–7173.
41 J. A. Norton, *Chem. Rev.*, 1942, **31**, 319–523.
42 A. Morinval and L. Avérous, *Eur. Polym. J.*, 2023, **198**, 112391.
43 M. Thys, J. Brancart, G. Van Assche, R. Vendamme and N. Van den Brande, *Macromolecules*, 2021, **54**, 9750–9760.
44 B. F. Antunes, A. G. Ferreira, A. C. Amaral, A. J. F. Carvalho, A. Gandini and E. Trovatti, *Polym. Int.*, 2022, **71**, 1340–1346.
45 S. M. Morozova, *Gels*, 2023, **9**, 102.
46 B. F. Antunes, A. G. Ferreira, A. C. Amaral, A. J. F. Carvalho, A. Gandini and E. Trovatti, *Polym. Int.*, 2022, **71**, 1340–1346.
47 A. Gandini, A. J. F. Carvalho, E. Trovatti, R. K. Kramer and T. M. Lacerda, *Eur. J. Lipid Sci. Technol.*, 2018, **120**, 1700091.
48 K.-K. Tremblay-Parrado, C. Bordin, S. Nicholls, B. Heinrich, B. Donnio and L. Avérous, *Macromolecules*, 2020, **53**, 5869–5880.
49 P. van den Tempel, F. Picchioni and R. K. Bose, *Macromol. Rapid Commun.*, 2022, **43**, 2200023.
50 O. Diels and K. Alder, *Justus Liebigs Ann. Chem.*, 1928, **460**, 98–122.
51 A. Rammohan, A. P. Krinochkin, A. F. Khasanov, D. S. Kopchuk and G. V. Zyryanov, *Top. Curr. Chem.*, 2022, **380**, 43.
52 T. Zhu, D. S. Jackson, R. L. Wehling and B. Geera, *Cereal Chem.*, 2008, **85**, 51–58.
53 D. S. Argyropoulos, N. Pajer and C. Crestini, *J. Vis. Exp.*, 2021, **174**, e62696.
54 M. Elomaa, T. Asplund, P. Soininen, R. Laatikainen, S. Peltonen, S. Hyvärinen and A. Urtti, *Carbohydr. Polym.*, 2004, **57**, 261–267.
55 L. Mohammadkhani and M. M. Heravi, *ChemistrySelect*, 2019, **4**, 6309–6337.
56 R. A. Sheldon, *Green Chem.*, 2023, **25**, 1704–1728.
57 P. Buono, A. Duval, L. Averous and Y. Habibi, *ChemSusChem*, 2017, **10**, 984–992.
58 E. C. Aguiar, J. B. P. da Silva and M. N. Ramos, *J. Mol. Struct.*, 2011, **993**, 431–434.
59 V. Silveira, M. Jebrane, A. Letoffe and S. Adamopoulos, *Carbohydr. Res.*, 2025, **550**, 109401.
60 L. Junistia, A. K. Sugih, R. Manurung, F. Picchioni, L. P. B. M. Janssen and H. J. Heeres, *Starch/Staerke*, 2008, **60**, 667–675.
61 T. Wang, D. Gao, H. Yin, J. Zhao, X. Wang and H. Niu, *Polymers*, 2024, **16**, 441.
62 Y.-H. Li, J.-H. Chen and Z. Yang, *Chem.–Eur. J.*, 2024, **30**, e202304371.
63 B. J. Adzima, H. A. Aguirre, C. J. Kloxin, T. F. Scott and C. N. Bowman, *Macromolecules*, 2008, **41**, 9112–9117.
64 C. J. Carriere, *J. Polym. Sci., Part B: Polym. Phys.*, 1998, **36**, 2085–2093.
65 C. Zhiguang, H. Junrong, P. Huayin and W. Keipper, *Starch/Staerke*, 2022, **74**, 2100288.
66 R. G. M. van der Sman and L. J. Mauer, *Food Hydrocolloids*, 2019, **94**, 371–380.
67 C. Monteserín, M. Blanco, J. M. Laza, E. Aranzabe and J. L. Vilas, *J. Therm. Anal. Calorim.*, 2018, **132**, 1867–1881.

One-Pot Synthesis of Thermally reversible Materials Using Maleimide-Polysaccharide and Furan-Lignin Derivatives

Valentin Silveira[a], Raffaello Papadakis, and Stergios Adamopoulos[a,✉]

[a]*Department of Forest Biomaterials and Technology, Swedish University of Agricultural Sciences, Vallvägen 9C, 756 51 Uppsala, Sweden*

✉Stergios Adamopoulos, stergios.adamopoulos@slu.se, +46 73-572 27 86

Supporting Information

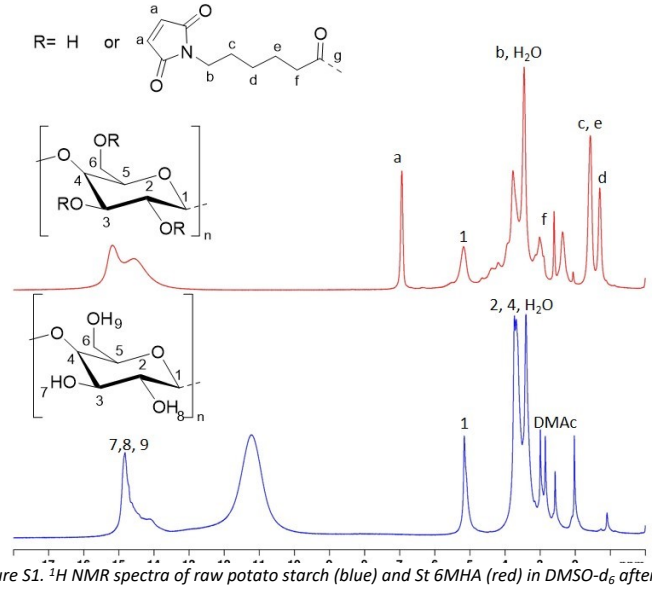

Figure S1. ^{1}H NMR spectra of raw potato starch (blue) and St 6MHA (red) in DMSO-d_6 after adding TFA-d_1

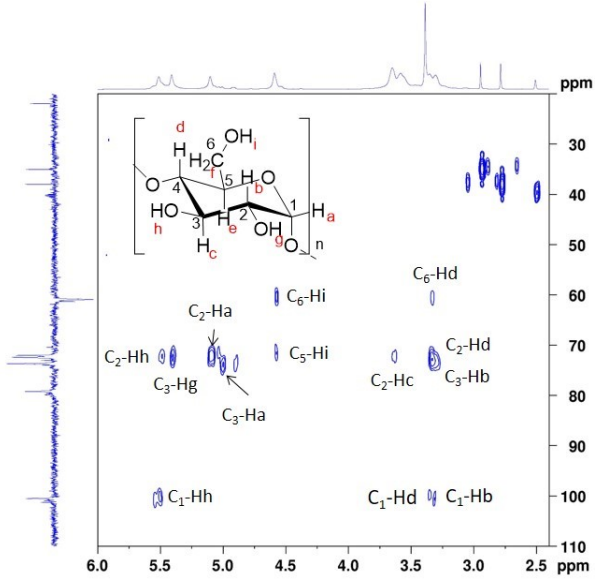

Figure S2. HMBC 2D NMR spectrum of raw potato starch in DMSO-d_6

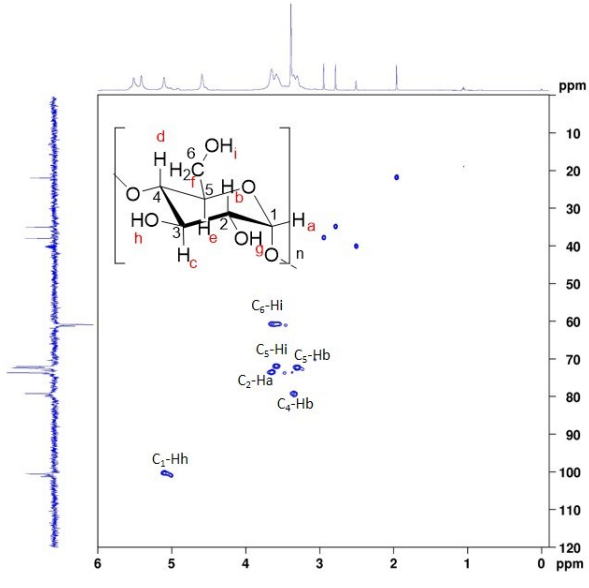

Figure S3. HSQC 2D NMR spectrum of raw potato starch in DMSO-d_6

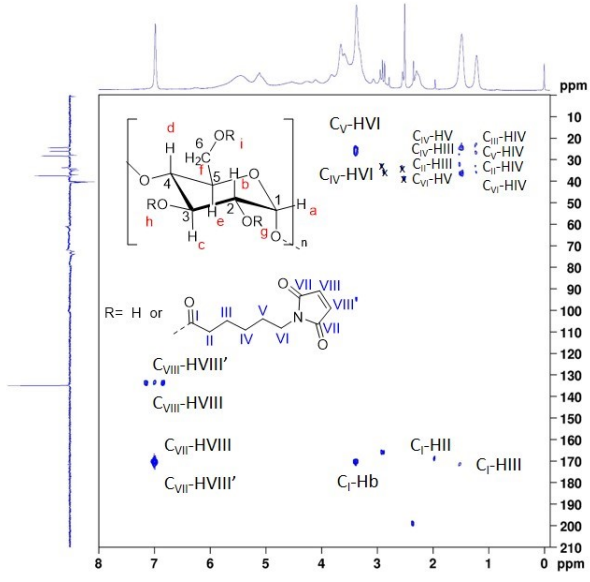

Figure S4. HMBC 2D NMR spectrum of St-6MHA in DMSO-d_6

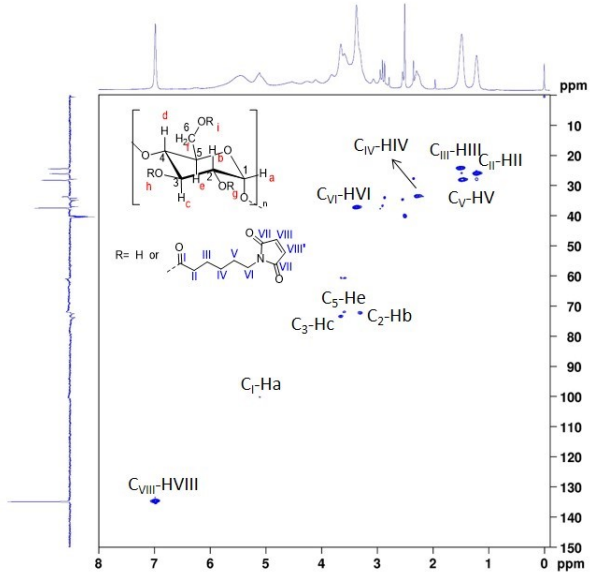

Figure S5. HSQC 2D NMR spectrum of St-6MHA in DMSO-d_6

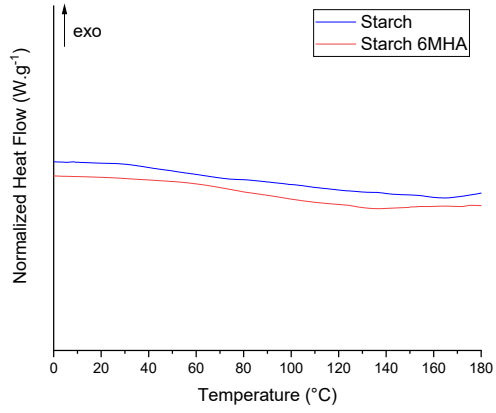

Figure S6. DSC thermogram of unmodified and modified Starch

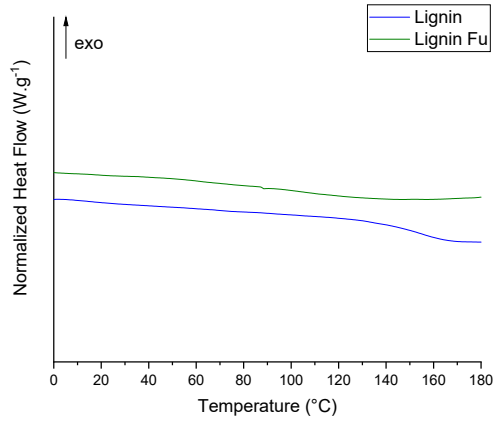

Figure S7. DSC thermogram of unmodified and modified Lignin

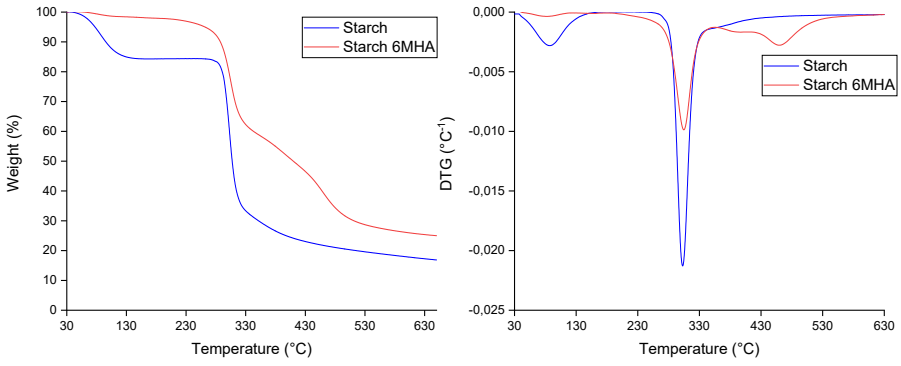

Figure S8. TGA and DTG thermograms of unmodified and modified Starch

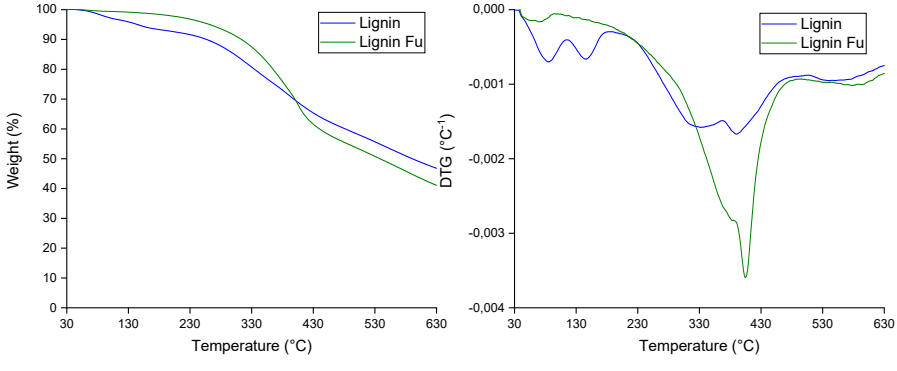

Figure S9. TGA and DTG thermograms of unmodified and modified Lignin

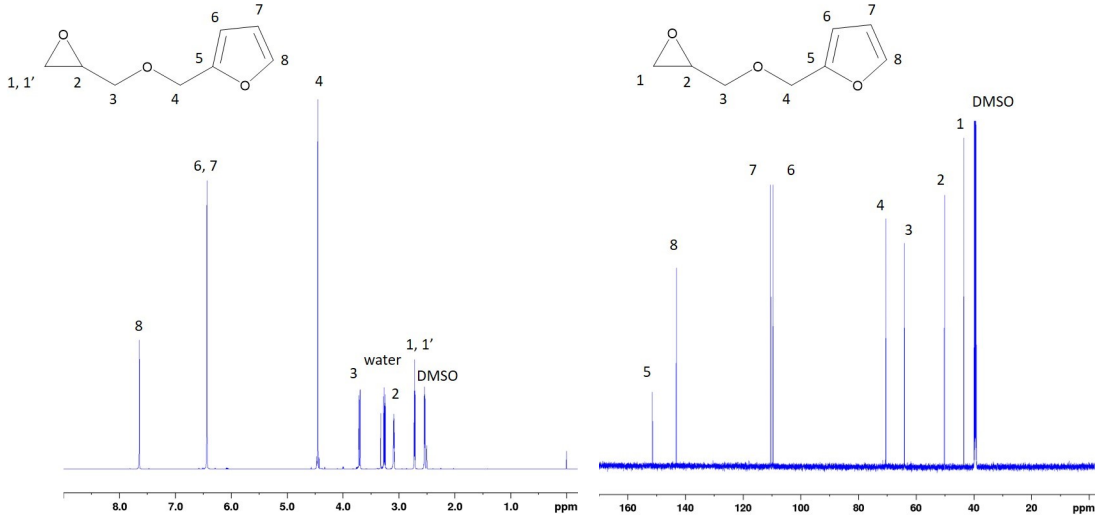

Figure S10. ^{1}H and ^{13}C NMR spectra of Furfuryl glycidyl ether in DMSO-d_6

IV

THE JOURNAL OF ADHESION
https://doi.org/10.1080/00218464.2025.2464051

Taylor & Francis
Taylor & Francis Group

Towards starch-based adhesives involving carbon dots as versatile crosslinkers

Valentin Silveira, Raffaello Papadakis, and Stergios Adamopoulos

Department of Forest Biomaterials and Technology, Swedish University of Agricultural Sciences, Uppsala, Sweden

ABSTRACT

In this study, biobased materials, Dialdehyde starch (DAS) and Carbon Dots (CDs) were synthesised to develop debondable adhesives via the formation of reversible imine networks between aldehyde and amine groups. Potato starch (St) was oxidised using Sodium periodate (NaIO4) and the modification was confirmed using FTIR spectroscopy, thermal analyses and Environmental scanning electron microscopy (ESEM). Two types of CDs were prepared: CD1, synthesized via a hydrothermal treatment of citric acid with formamide and aniline, and CD2, a post-functionalized version of CD1, prepared through a microwave-assisted reaction with polyethylenimine (PEI). CDs were characterized using XPS, fluorescence and absorbance spectroscopy, FTIR, TGA, DSC, as well as ESEM. DAS and CDs were reacted in DMAC to form DAS-CD conjugates through Schiff base formation. In the case of CD1, the reaction occurred through amino groups at the edges, while for CD2, the primary amino groups of PEI. The curing properties of these solutions with and without hexamethylenediamine (HMDA) as an auxiliary crosslinker were evaluated through ABES using beech veneer pressed at 160°C. Finally, debondability tests on veneer samples adhered with DAS-CD1 and DAS-CD2 were tested employing the reversibility of the Schiff-base connectivity motifs. Full debondability was achieved for DAS-CD1 after 1 hour in acidic solutions.

ARTICLE HISTORY
Received 9 December 2024
Accepted 2 February 2025

KEYWORDS
Carbon dots; starch; bio-based adhesives

1. Introduction

The development of bio-based adhesives is crucial for reducing environmental impact and decreasing dependence on petroleum resources.[1,2] Traditional petroleum-based adhesives contribute significantly to environmental pollution and are derived from non-renewable resources, which are becoming increasingly scarce. In contrast, bio-based adhesives are derived from renewable resources such as plants, which can be sustainably sourced and have a lower carbon footprint.[3,4] Moreover, bio-based adhesives often exhibit biodegradability, reducing the long-term environmental impact associated

CONTACT Raffaello Papadakis rafail.papadakis@slu.se Department of Forest Biomaterials and Technology, Swedish University of Agricultural Sciences, Vallvägen 9C, Uppsala 756 51, Sweden

with adhesive waste.[5] They also tend to be less toxic, making them safer for both human health and environment.[6] The shift towards bio-based adhesives aligns with the global sustainability goals and the principles of green chemistry, which emphasize the use of safer, renewable materials.[7] Recent advancements in the field have shown that bio-based adhesives can achieve performing characteristics comparable to their petroleum-based counterparts.[7]

Carbon dots (CDs) can play an important role in achieving this milestone due to their unique properties[8–10] and potential to enhance adhesive performance.[11–14] Indeed, the use of Carbon Dots as an additives for adhesive formulation has recently been explored in various ways. The versatility of carbon dots (CDs) has been explored as crosslinkers in bioadhesives, aiming to enhance drug delivery by increasing the porosity of gelatin-based gels while enabling optical tracking and photoactivated sterilization through their fluorescence.[15] Additionally, CDs have been investigated as crosslinkers in wood adhesives to improve the adhesion properties of conventional urea-formaldehyde (UF) adhesives.[12] By replacing hydrogen cohesive interactions within the UF resin with functionalized CDs (bearing amino, carboxyl, and hydroxyl groups), strong hydrogen bonds between the CDs and the polymer chains of UF can be achieved leading to enhancement of the original cross-linking structure and improvement of the micromechanical strength of bond lines.[12] Recent research also highlights the use of CDs as rigid nanofillers[11] to enhance energy dissipation and increase adhesive toughness, thereby improving resistance to failure. The surface functionalities of CDs, which provide excellent water dispersibility, make them a promising alternative to traditional nanofillers like silicon dioxide (SiO_2). Furthermore, the lower cytotoxicity of CDs has brought significant interest, and their fluorescence offers a valuable feature for routine safety checks during adhesive applications.

A wide variety of CDs derived from citric acid have been reported to date. Citric acid, a naturally occurring organic acid, is abundant, low-cost product, and exhibits excellent bioavailability and biocompatibility, making it an ideal precursor for CD synthesis[16,17] but also of novel bio-based adhesives.[18] Numerous CDs have been synthesized from citric acid, exhibiting high fluorescence quantum yields[19,20] and tunable photoluminescence, which are necessary for applications in energy conversion,[21] bioimaging,[22] sensing,[23] and optoelectronics. Additionally, citric acid derived CDs have been found to exhibit a corrosion inhibiting role[24] which is highly interesting for novel application in devices requiring high materials performance and endurance. Very interestingly, recent studies have demonstrated that citric acid-derived CDs can also significantly improve the performance of adhesives, showcasing their versatility.[12] Their incorporation into polysaccharide-based adhesives could enhance bonding strength and curing properties. In the context of wood adhesives, citric acid itself can play a crucial role. When

combined with starch, citric acid forms strong adhesive bonds through esterification and cross-linking reactions, improving adhesive properties and ensuring biodegradability and reducing toxicity.[25] As CDs often encompass moieties of their small-molecule precursors it is apparent that citric acid is a key ingredient for the development of CD-based adhesives.[15]

Embracing these findings, we report on the synthesis and post-functionalization of novel citric acid-derived CDs to enhance the curing properties of dialdehyde starch (DAS)-involving adhesives. Aiming to render them suitable for advanced adhesive formulations, we functionalized CDs with branched polyethyleneimine (PEI) to enhance crosslinking with dialdehyde starch (DAS). To improve the chemical stability and bonding of the intended adhesives, we developed a methodology that allows for the dynamic crosslinking of CDs with DAS in dimethylacetamide (DMAc) solvent. Additionally, we evaluated the need for an auxiliary crosslinker, hexamethylenediamine, to optimize adhesive performance. We applied mild conditions for curing and assessed the curing and bonding properties using the Automated Bond Evaluation System (ABES). To our knowledge, this approach has not been considered so far.

2. Results and discussion

2.1. Chemistry

For the needs of this study, carbon dots (CDs) were synthesized using citric acid, a bio-derived molecule widely recognized for its role in the development of graphene quantum dots and carbon dots.[26] Additionally, nitrogen-containing compounds (formamide and aniline) were employed to introduce N-doping into the CDs, delivering primary, secondary, or tertiary amino groups as well as corresponding amides. Similar synthetic approaches involving amines and citric acid have been recently reported.[27] This method was chosen to enhance the dipolarity of the CDs, thereby improving their dispersibility and solubility. Furthermore, these functionalities facilitate post-functionalization and crosslinking, which are crucial for developing novel adhesives. Specifically, CD1 was synthesized via a hydrothermal method using citric acid as the carbon source, along with significant amounts of formamide and aniline at 185°C (see Scheme 1).

After solvent removal following the hydrothermal process, CD1 was isolated and purified using size exclusion chromatography using Sephadex G-10, and eluted with MilliQ water. The collection criteria were based on the blue fluorescence of the desired CDs, monitored using a 365 nm UV-light source. The combined collected fractions were dried in a vacuum oven, yielding a yellow, shiny solid. This solid was then analyzed, and a portion of it was post-functionalized to product CD2. CD2 was synthesized via microwave

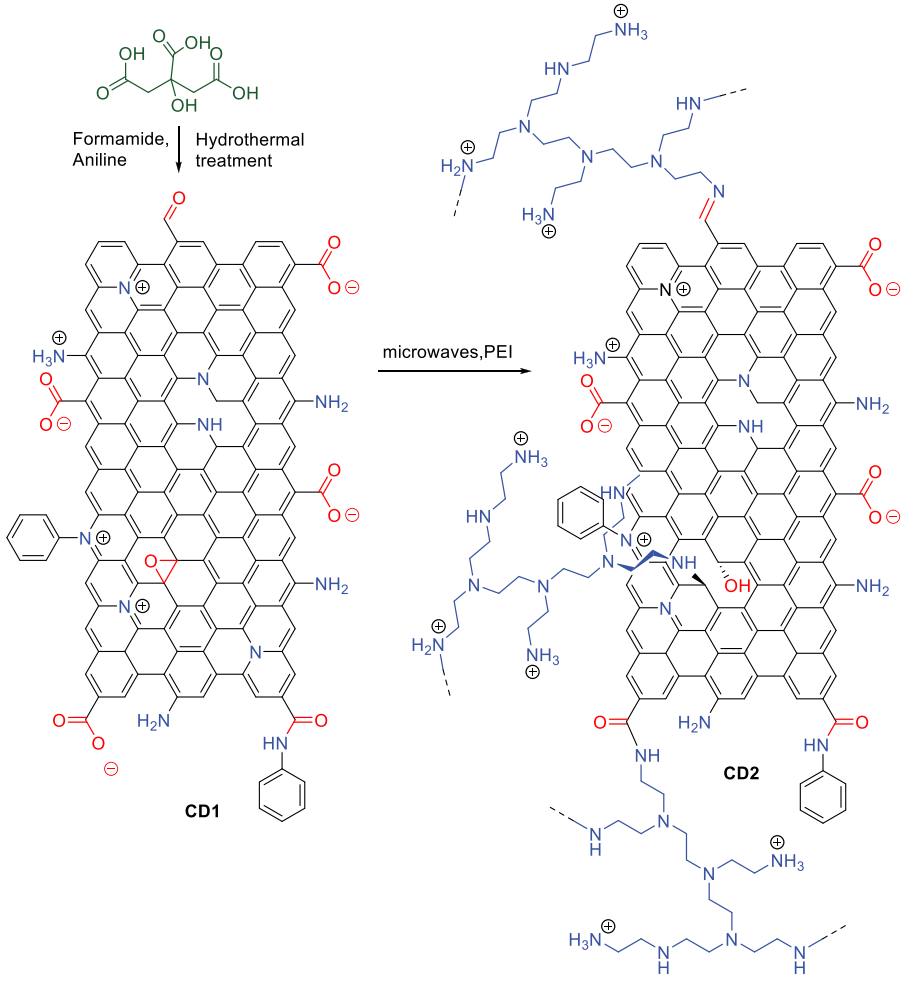

Scheme 1. The synthetic route used for the preparation of CD1 and CD2.

amidation of CD1 with branched polyethyleneimine (PEI). The synthesis was conducted in dimethylformamide (DMF), a solvent commonly used in similar microwave syntheses and proven to be effective for both CD1 and PEI. X-ray photoelectron spectroscopy (XPS) analysis suggests that further carbonization may have occurred during the post-functionalization process (*vide infra*). The proposed CDs have a quasi-spherical geometry (Figure 1) and a variety of functionalities as deduced through the different analytical methods used. Notably, connectivity motifs other than amide bonds might be present due to the occurrence of aldehyde or ketone functional groups appearing at the edges of the encompassed graphene layers in CD1 (see Scheme 1). While this model is mostly accepted by many research groups, a recent model developed by Boukhvalov et al. on the structure of carbon nanodots, which aligns with

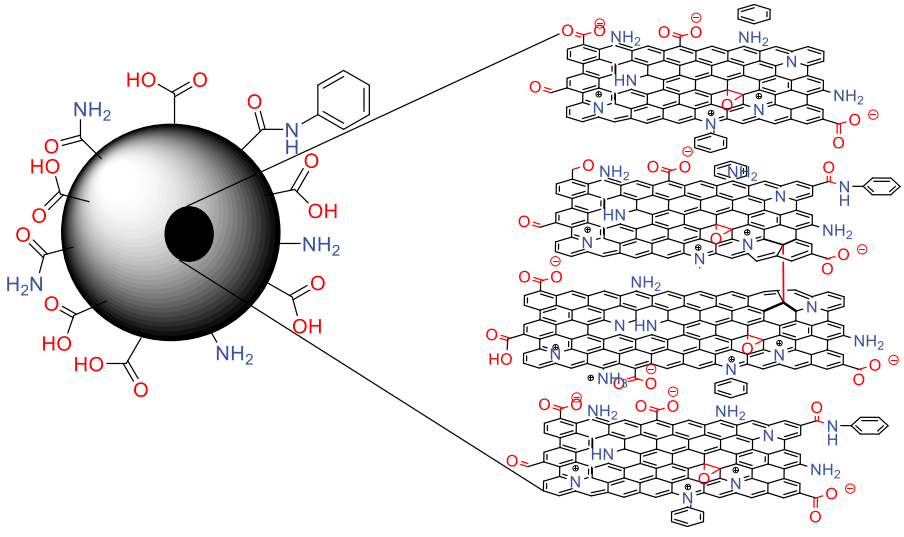

Figure 1. A schematic illustration of the spherical structure of CD1 with a hint of the structure of involved nano-graphene-like inner layers.

experimental observations (e.g. TEM studies) and is based on theoretical computations, suggests that CDs involve AA-stacked graphene layers with interlayer C – C covalent bonds and functional groups on their surface.[28] For instance, see the model in Figure 1, where the C – C interlayer bonds are marked in red.

Noteworthy, both CDs are very hygroscopic and they need to be stored under a dry atmosphere. While CD1 is readily soluble in water, CD2 becomes soluble only after heating above 50°C. Both CDs can be efficiently suspended in polar organic solvents such as DMSO, DMF, or DMAC.

The investigated adhesive formulations involve dialdehyde starch (DAS), a modified starch material prepared through the reaction of starch with sodium metaperiodate. This method was previously developed by our team.[29] We chose DAS as a key component of the adhesives due to its bioavailability (derived from starch) and its ability to undergo crosslinking with various crosslinkers such as amines, thanks to the presence of aldehyde groups. The DAS variant used in this study has been thoroughly analyzed (see Characterization) to fine-tune the reaction conditions, allowing for the optimal development of the DAS-CD adhesives.

For the development of the DAS-CD adhesives, a dynamic process was used involving condensation reactions between aldehyde units and the amino-groups of the two CDs (see Scheme 2). The role of such a dynamic conjugation methodology allowing for polysaccharide-graphene conjugations has been thoroughly discussed very recently.[30] In both cases (CD1 and CD2) CDs and DAS were suspended in DMAC and heated at 120°C overnight (16 h) with

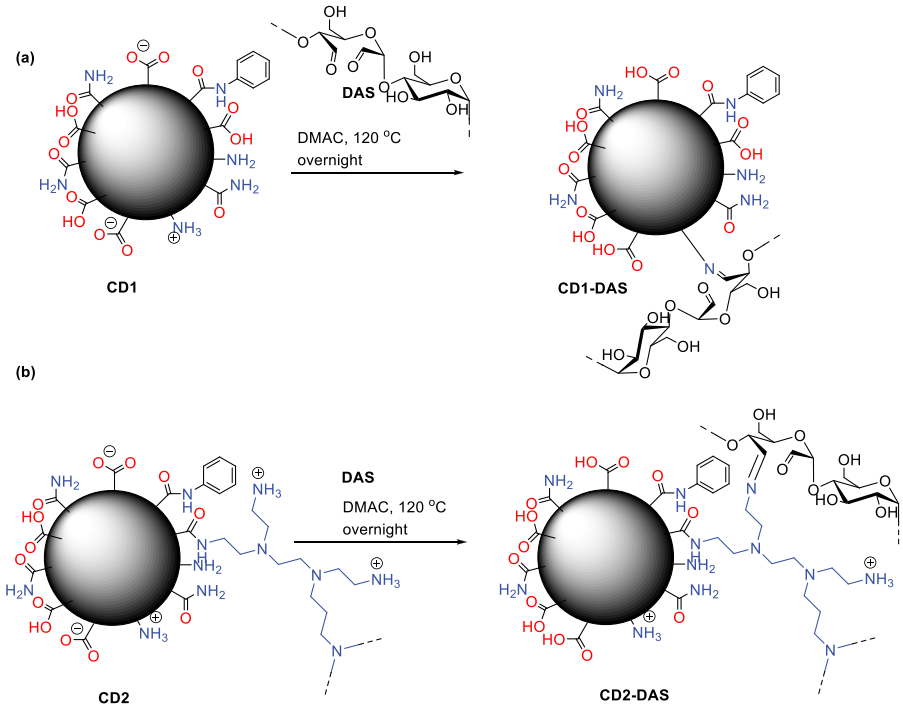

Scheme 2. Conjugation of CDs to DAS yielding CD1-DAS (a) and CD2-DAS (b).

CDs at 5% concentration relative to DAS. The dark brown solutions obtained using this process were used for ABES studies. As shown in Scheme 2, while conjugation of CD1 to DAS occurs through the amino-groups at its surface, in case of CD2, the corresponding Schiff base conjugation occurs through the primary NH_2 groups of the PEI units (which are covalently attached on CD2).

2.2. Characterization

2.2.1. X-ray photoelectron spectroscopy (XPS) analysis

X-ray photoelectron spectroscopy (XPS) is a surface-sensitive quantitative spectroscopic technique that can measure the topmost 200 atoms, (top 10 nm), of a surface. Given that the size of carbon dots (CDs) is typically less than 10 nm, XPS is a crucial technique for providing information on both the surface and the inner matter of a CD. In the case of CD1 and CD2, high-resolution (HR) C1s XPS spectra confirmed the presence of structures involving sp^2 and sp^3 hybridized carbon atoms, along with carbon atoms connected to nitrogen atoms (e.g., amines or amides) and distinct C=O bonding corresponding to the carboxylate and amide groups present in CD1 and CD2 (see Figure 2). The deconvolution of the measured HR-

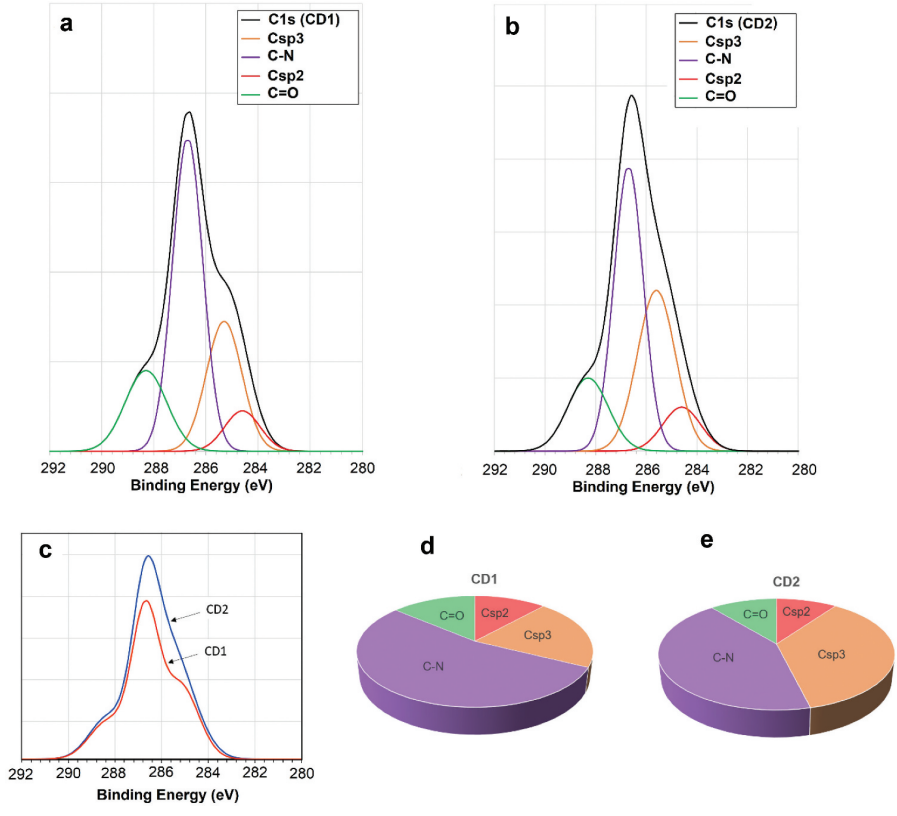

Figure 2. HR-C1s spectra of CD1 (a) and CD2 (b) and their deconvolution. (c) Superimposed HR-C1s XPS spectra of CD1 and CD2. Pie charts depicting the percentage contribution of each deconvolution signal in the HR-C1s XPS spectra of CD1 (D) and CD2 (E).

spectra for CD1 and CD2 revealed that, as expected, the post-functionalization of CD1 to CD2 resulted in enhanced C-N bonding (bands at 286.5 eV) due to the incorporation of PEI (a polyamine). It is noteworthy that CD1 has a substantial amount of N-involving groups (e.g. amides or amines) and this explains the large contribution of C-N bonding in the HR-C1s spectra of CD1 (more discussions on the types of groups in CD1 can be found in FTIR analysis below). This enhancement is evident from the significantly larger area of the C-N band in CD2 compared to CD1 (3.497 in CD1 and 3.897 in CD2; see Table 1 and Figure 2d,e). Additionally, the Csp3 signal (at 285.5 eV) increased after treatment with PEI. This increase aligns with the structure of branched PEI, which contains a large number of amino-methylene groups. Finally, distinct C=O bonding (broad bands at 288–288.5 eV) was identified through the HR-C1s spectra of both CDs examined. These bands are attributed to the presence of carboxylates, amides, or esters (all involving C=O bonds). Interestingly,

Table 1. Integrals and percentage contribution of the four deconvoluted signals of the HR-C1s and N1s XPS spectra of CD1 and CD2.

		CD1		CD2	
Signal	Band Energy (eV)	Integral	Percentage	Integral	Percentage
Csp2	285.0	0.759	11.7	0.899	9.9
Csp3	285.5	1.349	20.7	3.297	36.3
C-N	286.5	3.497	53.8	3.897	42.9
C=O	288.0–288.5	0.899	13.8	0.999	10.9
graphitic N	398.0–398.3	0.245	7.09	0.244	5.33
pyrrolic N	399.9–400.1	1.365	39.5	1.621	35.4
$-NH_3^+$	401.9–402.0	1.848	53.4	2.710	59.2

the C=O signal increased somewhat in the case of CD2 (see Table 1), presumably due to further carbonization and oxidation occurring under the microwave conditions applied to CD1.

The above small but important changes in the XPS of CD2 produced after the post-functionalization of CD1, lead to important changes in the shape and intensity of the spectra (see Figure 2 for comparison). The presence of PEI functionalities in CD2 is further supported through the FTIR analyses (*vide infra*).

Additional evidence of the introduction of PEI *via* condensation (amidation) on the surface of CD1 can be provided through a comparison of the High Resolution N1s-XPS of CD1 and CD2. The splitting of the various convoluted bands in this case allows for a better comparison due to the lower uncertainty upon deconvolution. As seen in Figure 3 (Panels A and B), a drastic increase of the band centered at 402 eV corresponding to $-NH_3^+$ groups is observed[31] in the N1s-XPS of CD2, corresponding to 59.2% of the entire convoluted N1s-XPS peak. At this level, the aforementioned band results in clear peak splitting. The corresponding contribution of this band in the N1s-XPS of CD1 was 53.4%, i.e., approximately 6% lower (Figure 3d and Table 1). Noteworthy, amino/ammonium groups are also present in CD1 since aniline was used in its hydrothermal production as an N-doping agent. The described finding is clear evidence of the introduction of PEI functionalities onto the CDs. Moreover, upon treatment of CD1 with PEI, the pyrrolic-N[32] and graphitic-N[32] content is retained at nearly the same levels (35–39% and 5.3–7.0%, respectively). The lowering of contribution of these peaks in CD2 is presumably associated with a "dilution effect" after the introduction of the PEI functionalities. Moreover, it also indicates that no drastic changes are observed on the CDs core upon treatment with PEI.

2.2.2. FTIR Analysis

2.2.2.1. CD1 and CD2. The complex FTIR spectrum of CD1 exhibits numerous signals attributed to the incorporation of a variety of functional groups in the structure. Most important is the presence of amide groups, with a sharp, strong signal at 1697 cm^{-1} corresponding to a typical C=O stretching band, as

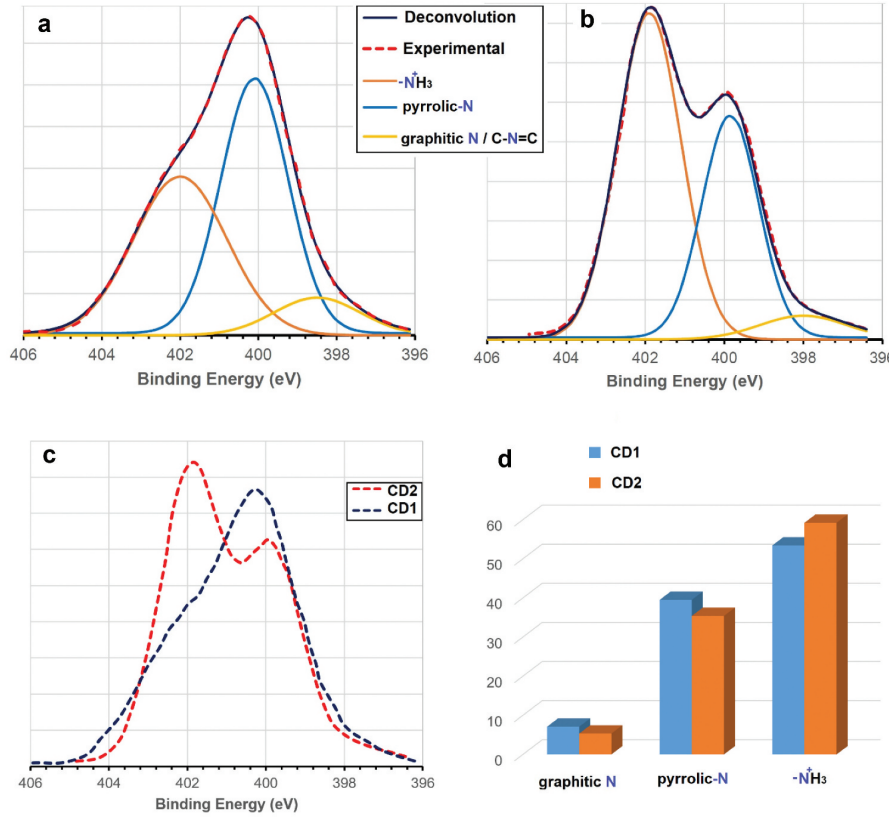

Figure 3. HR-N1s spectra of CD1 (a) and CD2 (b) and their deconvolution. (c) Superimposed HR-N1s XPS spectra of CD1 and CD2. Bar diagram depicting the percentage contribution of each deconvolution signal in the HR-N1s XPS spectra of CD1 (d).

well as carboxylate functionalities with symmetric C=O stretching bands at 1345 and 1399 cm^{-1}. Evidence of the presence of pyridinic nitrogen atoms (N-doping) is based on a signal centered at 1497 cm^{-1}. Additionally, CD1 involves amino groups with a distinct stretching N-H band at 3379 cm^{-1} and possibly N-H amine bending at 1635 cm^{-1}. The presence of aliphatic (sp^3 hybridized carbon; see also XPS analysis) is also apparent in a convoluted broadband with elements of peaks at 2928 and 2867 cm^{-1}, corresponding to the asymmetric stretching of C-H bonds in aliphatic chains. Additionally, aromatic amine-related functionalities are present (derived from aniline) with N-H stretching at 3379 cm^{-1} and convoluted aromatic C-H (phenyl rings) stretching bands around 3100–3000 cm^{-1}, and finally, aromatic C-H bending between 900–700 cm^{-1} (specifically at 884, 781, and 734 cm^{-1}).

On the other hand, the FTIR spectrum of CD2 indicated many similarities with that of its parent CD1. The spectrum exhibits various bands attributed to the incorporation of PEI in the CDs via amidation, the most important being

the N-H stretching broad band around 3366 cm^{-1}, indicative of N-H stretching vibrations from primary and secondary amines (see Figure 4). The C-H stretching peaks at 2858 and 2931 cm^{-1} correspond to the C-H stretching vibrations from the aliphatic chains of PEI. Additionally, N-H bending bands are present, such as a strong band at 1566 cm^{-1} and other convoluted bands between 1560 and Various C-N stretching bands are also observed between 1000 and 1300 cm^{-1}, for example, at 1074, 1136, and 1192 cm^{-1}, attributed to C-N stretching vibrations. The amide signals are also present in the spectra of CD2 as in CD1, specifically a strong sharp band at 1698 cm^{-1} (also present in CD1 at 1697 cm^{-1}; vide supra) and possibly other convoluted bands between 1640 and 1700 cm^{-1} at lower wavenumbers than the main peak at 1697 cm^{-1}. It is important to mention that the characteristic structures presented in Scheme 1 are mostly based on the findings of the XPS and FTIR analyses discussed above. 1600 cm^{-1}, which are associated with N-H bending vibrations.

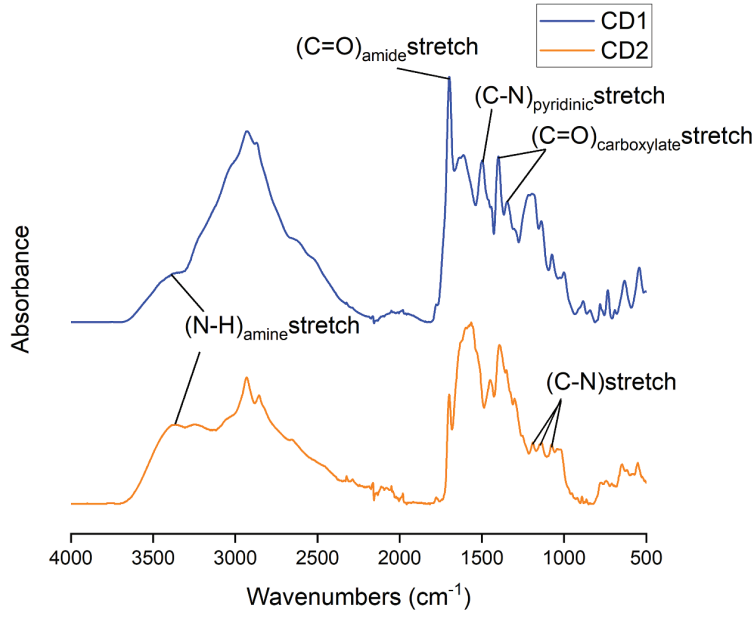

Figure 4. FTIR spectra of solid samples of CD1 and CD2.

2.2.2.2. Dialdehyde starch. The FTIR spectra show significant differences between DAS and Potato Starch (St), particularly in the carbonyl region and the 500–1000 cm^{-1} range. Specifically, the DAS spectrum exhibits peaks around 1729 cm^{-1} and 1679 cm^{-1}, associated with the carbonyl (C=O) stretching vibrations. These peaks are not present in the FTIR spectra of native St. The FTIR spectra of St (Figure 5) on the other hand showed three characteristic peaks at 990, 1075, and 1150 cm^{-1}, attributed to C-O bond stretching.

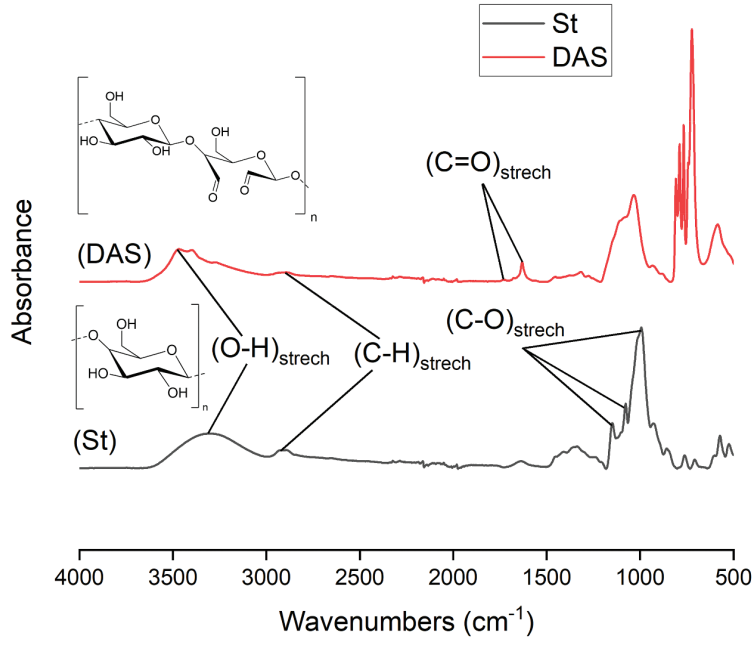

Figure 5. FTIR spectra of solid samples of DAS and St.

These peaks disappeared in the DAS samples after oxidation.[26] The absorption peaks in case of St at 1640 and 3290 cm^{-1} could be related to trapped moisture in the non-crystalline region of the starch structure or intermolecular hydrogen bonds.[26] Additionally, The peak at 2960 cm^{-1} in case of St assigned to CH group stretching, shifted slightly to 2880 cm^{-1} within the 2800–3000 cm^{-1} range, after the oxidation of St to DAS. Moreover, the DAS samples displayed a new stretching vibration at 1729 cm^{-1}, associated with carbonyl groups and a peak at 875 cm^{-1}, indicating hemiacetal bonds between dialdehyde groups and adjacent hydroxyl groups. The decrease of the intensity of the peak corresponding to hydroxyl groups around 3400 cm^{-1} corroborate the consumption of these latter toward the formation of aldehyde groups.

2.2.3. Spectrophotometric evaluation of the CDs

A clear proof of the formation of the CDs is provided through their measured emission properties. Both CDs emit light in an excitation dependent fashion (see Figure 7).[33,34] CD1 appears to be more emissive than CD2 when their emission properties are examined in aqueous solutions with about the same concentration. This is presumably associated with the presence of PEI units in case of CD2. The surface states responsible for CD-emission are drastically dependent on dopants, functional groups (especially bulky ones e.g. polymeric species).

The maximal emission in both cases is observed upon excitation at approx. 327 nm (near UV-light). Interestingly, CD2 exhibits some emission also in the visible region at around 620 nm as a result of a weak absorption band of CD2 at roughly 590 nm (see Figure 6). This absorption is clearly associated with the presence of PEI and accumulation of different unsaturated connectivity motifs e.g. imine (Schiff bases).

2.2.4. Thermal analysis

To be suitable for wood adhesive applications, CDs and DAS must exhibit thermal stability within the temperature range used in these processes. In this study, the temperature was set to 160°C. The thermal stability of the different materials was assessed using thermogravimetric (TG) and derivative thermogravimetric (DTG) analysis.

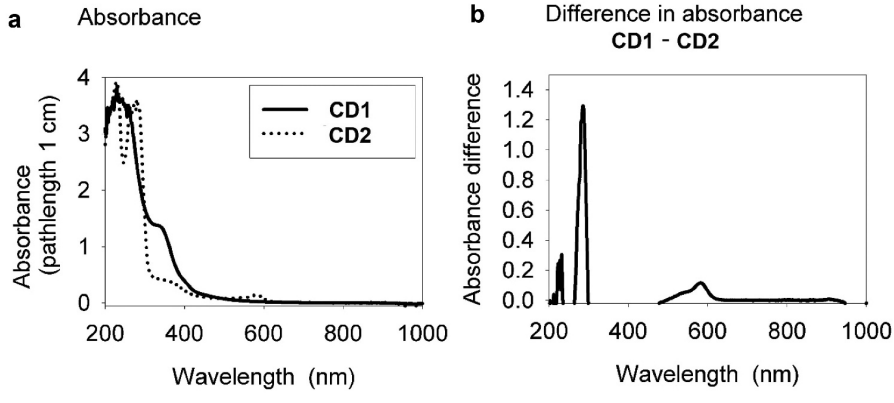

Figure 6. Absorption spectra of CD1 and CD2 (a) and difference in absorbance of CD1 and CD2 (b).

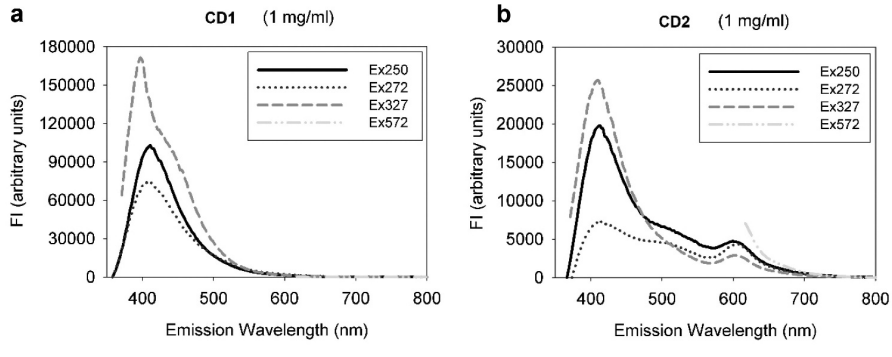

Figure 7. Emission spectra when dissolved in water at concentration 1mg/mL upon excitation at various wavelengths for CD1 (a) and CD2 (b).

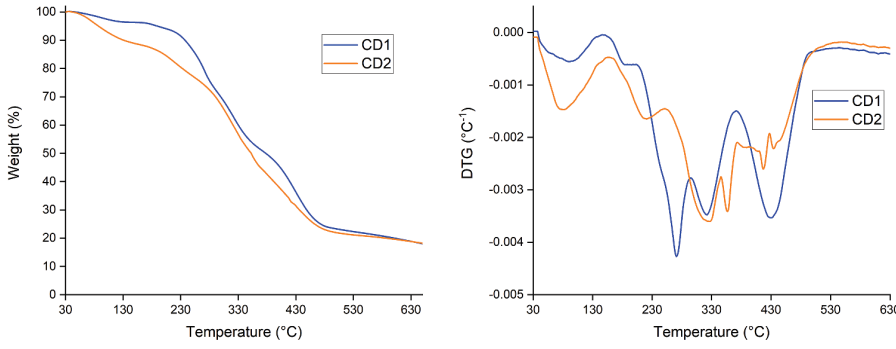

Figure 8. TG (left) and DTG (right) analyses of CD1 and CD2.

The TG and DTG analyses of the two CDs revealed that both are relatively stable up to temperatures close to 150°C (see Figure 8). The mass losses up to this temperature mostly correspond to the loss of trapped water. The TGA profiles of CD1 and CD2 are very similar, yet DTG indicates a range of thermal decomposition processes occurring at elevated temperatures (>200°C). Due to the high polydispersity of the CDs and the large range of encompassed functional groups, it is challenging to understand their multi-step thermal decomposition pathways at temperatures higher than 200°C. Generally, TGA results can be ambiguous when there are more than two peaks, as these peaks cannot be straightforwardly attributed to surface and core decomposition based solely on the temperature.[35] Nonetheless, for the scope of this work, their thermal behavior up to 160°C (the set temperature for the curing tests) indicates that both CDs are a good match for the design of resins/adhesives involving these CDs and DAS.

On the other hand, the thermograms of unmodified (St) and oxidized (DAS) (Figure 9) show fewer degradation steps. Unmodified starch displayed a two-step mass loss: the first at 100°C corresponds to approximately 5% mass

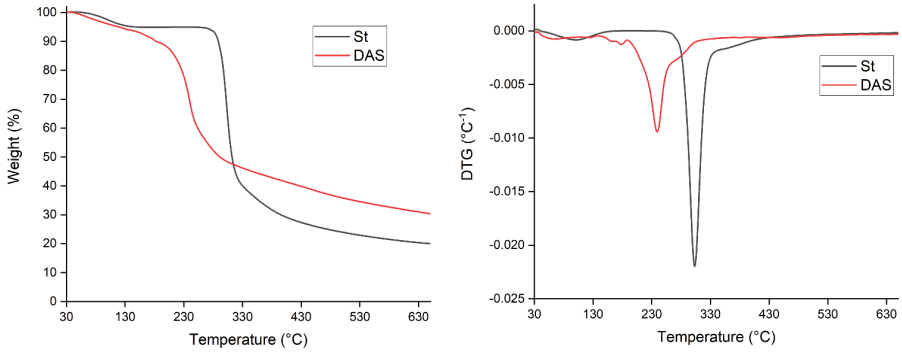

Figure 9. TG (left) and DTG (right) analyses of DAS and parent starch (St) material.

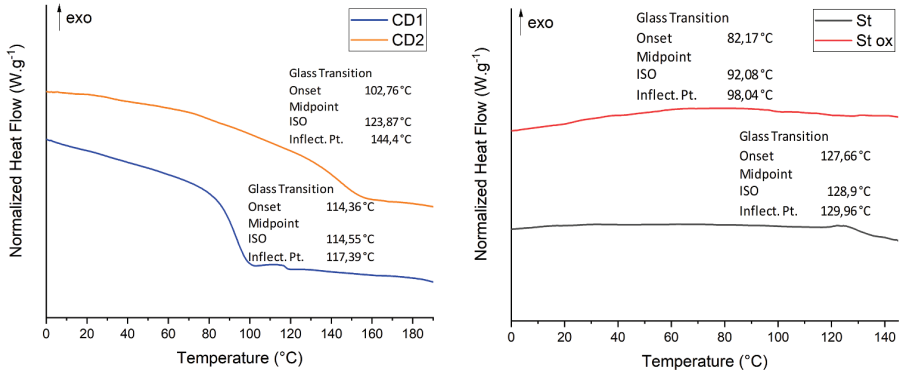

Figure 10. DSC analyses of CDs CD1 and CD2 (left panel) and of DAS and native St material (right panel).

loss of the water trapped in the starch structure. The second, occurring around 320°C is associated with the starch backbone thermal degradation, with an onset temperature of 205°C and a peak weight loss at 302°C. The residual weight was approximately 20%. The oxidized starch also displayed a two-step mass loss that can be interpreted in a similar way to native starch. However, the step corresponding to the starch degradation appeared at a lower temperature and started around 175°C with a peak weight loss at 240°C according to the DTG thermograms. It can be explained according to previous work[36] as the oxidation of starch results in the depolymerization of amylose and amylopectin chains, leading to a reduction in molecular weight and, consequently, a decrease in the thermal stability of starch. Moreover, it was reported that[37] Dialdehyde starch exhibits lower thermal stability compared to native starch, primarily due to the cleavage of the C2–C3 bonds in glucosyl units and the breaking of glycosidic bonds in the starch backbone.

Figure 10 shows the Differential scanning calorimetry (DSC) thermographs of CD and starch samples.

Both CDs exhibit glass transition temperatures (Tg) higher than 100°C, with CD2 showing a slightly higher Tg than CD1 (124°C vs. 115°C). CD2, with its higher Tg, is expected to exhibit slightly better mechanical properties after processing (thermal pressing at 160°C) compared to CD1. This could translate to slightly better performance in terms of rigidity and resistance to deformation under stress. Overall, the higher Tg of CD2 suggests a wider processing window, making it potentially more versatile and easier to handle during the adhesive formulation process. In terms of potential adhesive performance, both CDs are expected to perform well, with CD2 offering a slight edge in thermal and mechanical stability compared to CD1. The slightly higher Tg of CD2 can be explained by the restricted molecular mobility in CD2 compared to CD1. This restriction is due to pronounced H-bonding in CD2, attributed

to the presence of PEI units, which limits the mobility of polymer chains. Consequently, more energy (higher temperature) is required to achieve the molecular motion associated with the glass transition. Additionally, intermolecular interactions are more pronounced in CD2 due to H-bonding, contributing to the overall intermolecular forces within the material and generally leading to higher Tg values. Overall, both CDs are suitable for use at 160°C, but CD2 may provide marginally better performance due to its higher Tg.

On the other hand, the native potato starch displayed a Glass transition temperature of around 129°C. The Tg of unmodified starch was determined to be around 129°C. Previous research[38] has highlighted the significant influence of moisture content on the Tg of starch. Consequently, a lower moisture content of starch leads to higher Tg values compared to those reported in other studies. The oxidized starch showed a Tg around 92°C, this decreased value cannot be attributed to a different moisture content as the TGA analysis previously showed (see Figure 9) a similar moisture content of 5% for both starch. The significant decrease in Tg can be attributed to the formation of aldehydes during oxidation, which increases polymer mobility by reducing the number of hydroxyl groups and consequently weakening hydrogen bonding.[39]

2.2.5. Analysis of the morphology

2.2.5.1. Scanning electron microscopy (SEM) analysis of CD1 and CD2. CD1 (Figures 11a,b): The SEM images of CD1 reveal quasi-spherical particles with some of them merged to one another in varying sizes and relatively smooth textures. Similar morphologies have recently been reported for different CDs.[40,41] In Figure 11a, the particles are loosely aggregated and irregularly distributed across the field of view, with a scale marker at 100 µm. In contrast, Figure 11b which is an image realised at higher magnification (a scale marker of 50 µm) shows more distinct and larger quasi-spherical particles that are uniformly distributed, with smoother surfaces. The quasi-spherical shape and smooth surface of these particles is in line with the freeze-drying process[42] used for their fabrication which promotes spherical morphology.

CD2 (Figures 11c,d): The SEM images of CD2 depict densely packed, flake-like structures. Figure 11c shows these flakes arranged in a compact and possibly crystalline structure, with sharp, well-defined edges at a scale 20 µm. Figure 11d provides a closer view of a single flake-like structure, revealing its detailed geometry with smooth faces and sharp edges. The scale marker of 5 µm allows for a close examination of the flake's surface and edges, suggesting a high degree of regularity and precision in its formation. The flake-like morphology indicates a different formation process, such as exfoliation or layer-by-layer assembly, resulting in distinct layered and sharp-edged structures.

These morphological differences between CD1 and CD2 can significantly influence their properties and potential applications, with CD1's

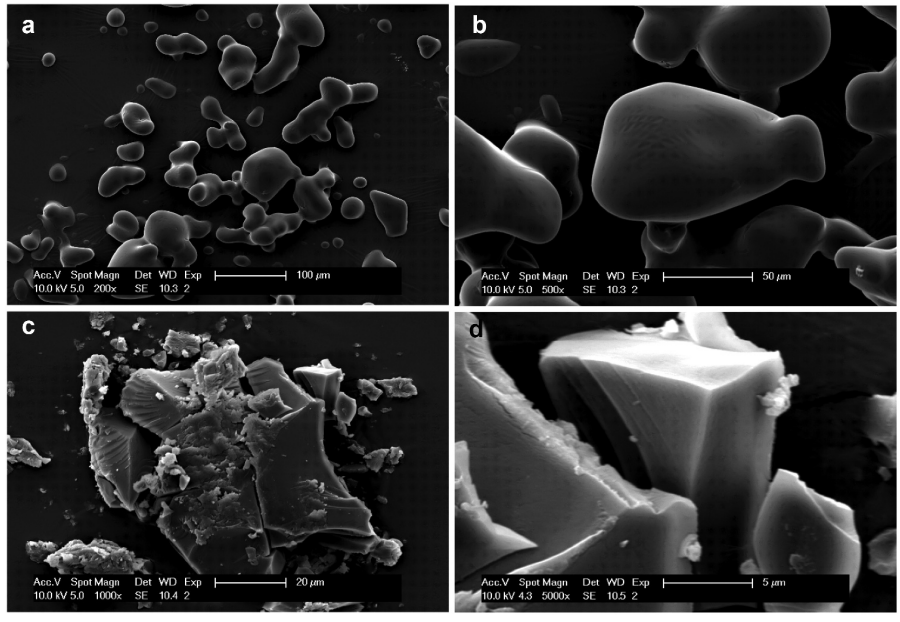

Figure 11. Scanning electron microscope (SEM) images of CD1 (a-b) and of CD2 (c-d).

quasi-spherical particles being suitable for applications requiring smooth, spherical morphologies, and CD2's flake-like structures being ideal for a wide range of adhesive applications needing layered, crystalline-like materials.

2.2.5.2. Scanning electron microscopy (SEM) analysis of DAS. The SEM images of Dialdehyde Starch (DAS) at 150× magnification (Figure 12a) reveal individual particles with a rough texture scattered across the field. At 1500× magnification (Figure 12b), a cluster of particles with more defined edges and intricate surface details, including tubular structures, is visible. These images illustrate a clear difference between DAS and the parent starch material (seen in Figure 12c,d), which exhibits smooth, oval to round-shaped particles densely packed together, a typical morphology encountered in starch. This drastic morphological change (which has been reported before upon oxidation of starch[43]) can significantly influence the miscibility and reactivity of DAS in the intended adhesive formulations (DAS-CD1 and DAS-CD2).

2.2.6. Adhesive bond strength development evaluation using ABES

2.2.6.1. Influence of pressing time. Pressing time is a critical factor as it influences bond strength, production speed, and energy consumption. To assess its impact on bonding strength, tests were conducted at a fixed pressing

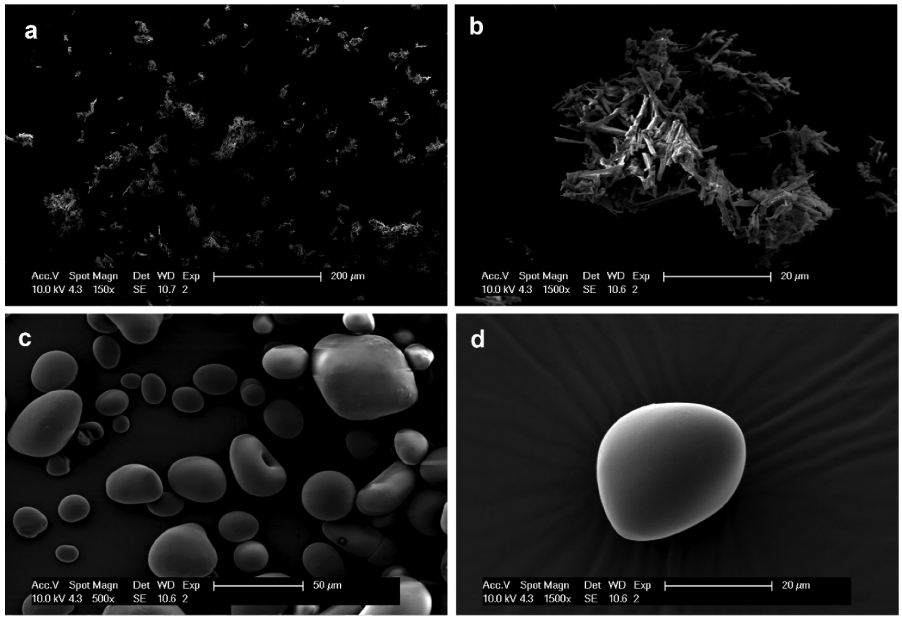

Figure 12. Scanning electron microscope (SEM) images of DAS (a-b) and of starch (c-d).

temperature of 160°C using the ABES system depicted in Figure 13. As anticipated, the results indicate that extended pressing times result in greater shear strength due to improved curing and solvent loss of the adhesives. This finding aligns with the observations of previous studies, which reported that longer pressing times enhance adhesive bonding, thereby increasing bond strength.[44]

2.2.6.2. Influence of HMDA. The prepared adhesive consists of a mix of linear and branched chains from DAS and Hexamethylenediamine (HMDA). The curing process is driven by the evaporation of the solvent (DMAc) and the cross-linking between the aldehyde groups of DAS and the amino groups of HMDA, resulting in the formation of imines. The internal cohesion is due to the formation of this imine network, while adhesion might be explained by the interlocking of starch chains in the wood structure and hydrogen bonding between hydroxyl groups from DAS, amino groups from HMDA, and hydroxyl groups present in the different components of wood (lignin, hemicellulose, cellulose).

As seen in Figures 14 and 15, solutions containing only DAS or only HMDA show adhesion with respective maximum shear strengths of 2.40 MPa ±0.11 and 2.95 MPa ±0.12. The formation of the imine network improves the bonding strength of DAS, achieving a maximum average shear strength of 3.63 MPa ±0.44.

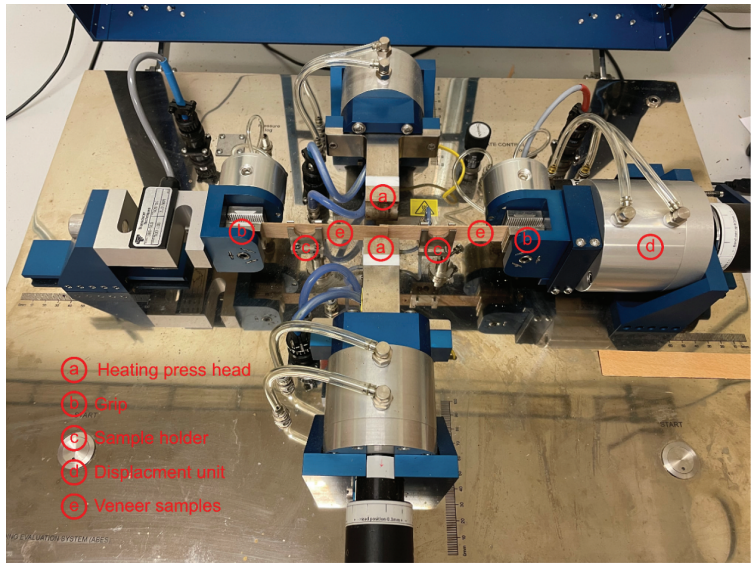

Figure 13. Top view of the ABES equipment used in this study.

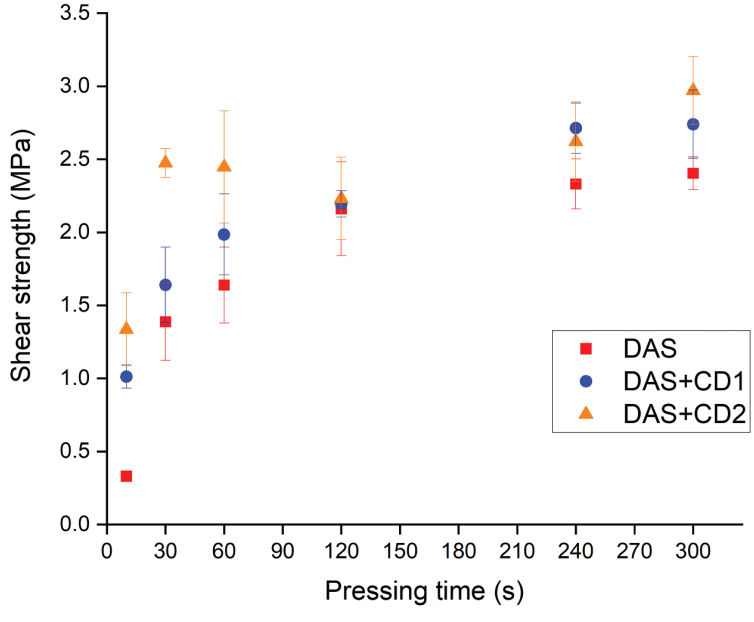

Figure 14. Plots of shear strength as a function of pressing time (at set temperature 160°C) for DAS, DAS+CD1 and DAS+CD2.

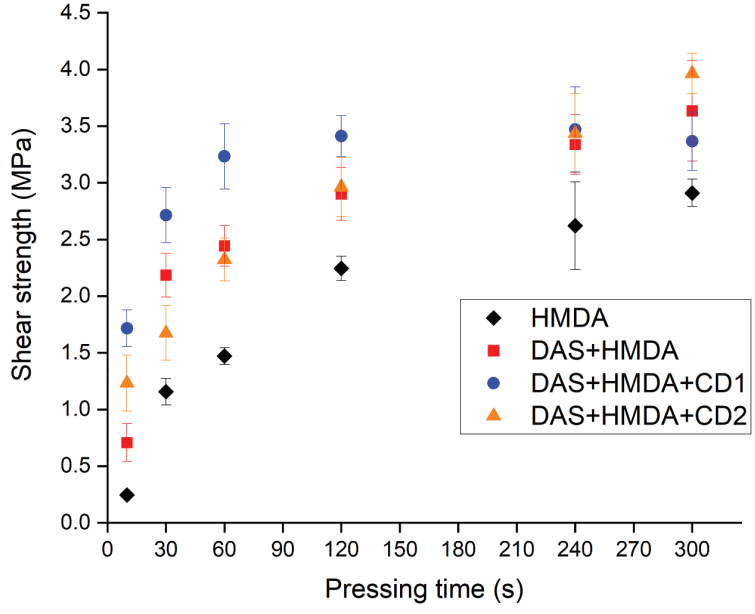

Figure 15. Plots of shear strength as a function of pressing time (at set temperature 160°C) for HMDA, DAS+HMDA, DAS+HMDA+CD1 and DAS+HMDA+CD2.

2.2.6.3. Influence of carbon dots. Figure 14 shows the evolution of shear strength over pressing time for Dialdehyde starch solution in the presence or not of the different synthetized Carbon dots. The Solution containing only DAS shows a continuous increase of shear strength over time reaching a maximum at around 240s with 2.3MPa ±0,17. The solutions containing CDs show faster curing, reaching the maximum shear strength of DAS solution at only 30s for CD2 with 2.47MPa ±0,10 and 120s for CD1 with 2.19MPa ±0,09. We believe that the amino groups present on both Carbon dots lead to the crosslinking of DAS enabling a better compatibility between the two materials. However, the amino groups of PEI grafted on CD2 might be more accessible due to the carbon chain length thus more reactive, improving the crosslinking between starch and CD2 compared to CD1. Moreover, in the presence of HMDA, we can observe a reverse trend, indeed, CD1 shows faster curing than CD2. We believe that this is due to the fact that the dialdehyde starch that has reacted with CD2 has less available reactive aldehyde than the one that as been crosslinked with CD1 allowing in a first step HMDA to crosslink more DAS+CD1 than DAS+CD2. However, after 300s we believe that the more hindered aldehyde present on DAS+CD2 is given enough time to react resulting in a higher shear strength of 3.96MPa ±0,18.

2.2.6.4. Reversibility test. The imine formation is known to be a reversible reaction.[45] Indeed, at acidic pH the imine can be hydrolysed leading back to

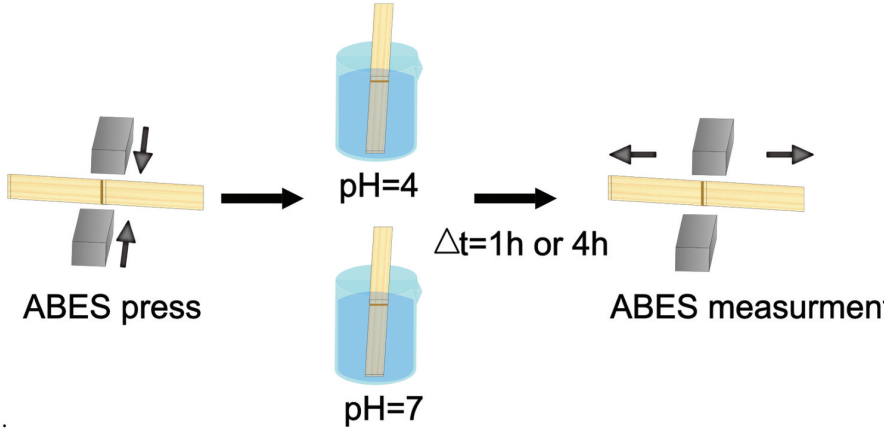

Figure 16. Illustration depicting the procedure followed for the reversibility tests on veneers adhered with resins **DAS+HMDA**, **DAS+HMDA+CD** (1 or 2).

Table 2. ABES results obtained after reversibility test performed at pH 4.

pH =4		
Time (h)	Average Maximum shear strength (Mpa)	Resin
1	1.49±0.21	DAS+HMDA
1	0	DAS+HMDA+CD1
1	1.06±0.05	DAS+HMDA+CD2
4	1.50±0.17	DAS+HMDA
4	0	DAS+HMDA+CD1
4	1.27±0.15	DAS+HMDA+CD2

the formation of amine and aldehyde. We expect that this will enable the adhesive to debond on demand in the presence of acidic conditions. The bond strength of veneer bonded with DAS+HMDA, DAS+HMDA+CD1 and DAS +HMDA+CD2 was then recorded using ABES after immersion in neutral water solution and acidic water solution. If in general the shear strength decreased after immersion in both solutions, only DAS+HMDA+CD1 was completely debonded after 1hour in an acidic solution (see Figure 16). Indeed, DAS+HMDA+CD2 will still show an average shear strength of 1.27MPa after 4 hours in acidic against 1.81MPa in neutral solution (detailed results are gathered in Tables 2 and 3). We believe this might be the result of the PEI chain making the system more water-resistant compared to CD1.

2.3. Experimental section

2.3.1. Materials

Citric acid monohydrate, aniline, formamide (FA), N,N-dimethylformamide (DMF), N,N-dimethylacetamide (DMAc), 1,6-Hexanediamine (HMDA), Sodium periodate (NaIO4), all of reagent grade were purchased from Sigma

Table 3. ABES results obtained after reversibility test performed at pH 7.

pH =7		
Time (h)	Average Maximum shear strength (Mpa)	Adhesive
1	1.95±0.21	DAS+HMDA
1	0.71±0.05	DAS+HMDA+CD1
1	2.11±0.20	DAS+HMDA+CD2
4	1.64±0.36	DAS+HMDA
4	0	DAS+HMDA+CD1
4	1.81±0.13	DAS+HMDA+CD2

Aldrich. Branched polyethylenimine (PEI) (average Mw ~ 25,000) and Potato Starch were also purchased from Sigma Aldrich. Purified water used in this research was produced using a Milli-Q® water purification system (Millipore). Beech veneer samples were cut at dimensions: 170 mm x 20 mm. For microwave treatment, a household microwave oven operating at scalable power with a maximal 900 MW power was used. Microwave reactions were carried out in Biotage 352,016 microwave reaction vials. Sephadex G-10 and G-25 (Medium) were purchased from Cytiva.

2.3.2. Synthesis

Carbon dots CD1 were synthesized using the following hydrothermal method. Citric acid (2.00 g) was wetted with 1.00 g of formamide and then 1 g of freshly distilled aniline (1.00 g) was added. The slurry was mechanically treated in a mortar and finally dissolved in 25 mL of MilliQ water. Subsequently, the solution was heated at 185°C for 24 h in a 50.0 mL Teflon-lined autoclave. After this process, the reaction mixture was transferred in a 100 mL round bottom flask (rbf) and the solvent was removed using rotary evaporation. The obtained dark orange product was purified through size exclusion chromatography (Sephadex G-10) to remove unreacted reagents and low molecular weight impurities. After this procedure, the obtained dialyzed sample was freeze-dried to obtain a fluffy deep-yellow colored powder. Final yield: 1.75 g.

Carbon Dots CD2 were synthesized via microwave-assisted post-functionalization (amidation) of CD1. Specifically, 0.50 g of CD1 was dissolved in 5 mL of DMF, and a fresh DMF solution of PEI (0.10 g in 5 mL) was added. The mixture was divided into four 5 mL Biotage microwave reaction vials, which were sealed and microwave-irradiated for 20 minutes at 300 W. After irradiation, the vials were allowed to cool to room temperature, and the contents were combined in a single 50 mL round-bottom flask. The resulting brown residue was separated using size exclusion chromatography (Sephadex G-25). The collected fractions were rotavaped to remove DMF solvent. The residue was collected and dried in a vacuum oven at 50°C for 16 hours. The final material (0.55 g) was not fully soluble in water and was analyzed using solid-state methods.

Dialdehyde Starch (DAS) was synthesized according to a published method by our group.[26] Specifically the method followed was the following: A 5% solution of oven-dried native potato starch (dried at 40°C for 48 hours in a vacuum oven) was initially dispersed in distilled water using a magnetic stirrer. Sodium periodate ($NaIO_4$) was then added to the mixture in a 1:1.65 weight ratio of potato starch to $NaIO_4$. To prevent light-induced decomposition of $NaIO_4$, the reaction vessel was wrapped in several layers of aluminum foil. The reaction was conducted at 35°C for 24 hours. The reaction was eventually quenched by adding acetone and centrifuged for 5 minutes at 5000 rpm. The precipitates were further washed with water and centrifuged at 5000 rpm, first for 5 minutes and then for 10 minutes. This was followed by washing with ethanol and centrifugation for 10 minutes at 5000 rpm to remove any remaining unreacted oxidative agents. The oxidized starch (DAS) was dried in a vacuum oven at 35°C for 48 hours. The as dried samples were used for analysis.

2.3.2.1. CD-DAS conjugates preparations. Different mixtures were prepared prior to ABES measurement. Dialdehyde Starch was dissolved in DMAc and divided in 4 portions. The two carbon dots were added to a Dialdehyde starch solution at 5% concentration relative to starch, then, the solution was heated at 120°C overnight. The reaction between aldehyde present on starch and amines present on CD2 was confirmed by the resulting homogeneous dark brown solution obtained, as CD2 is initially not soluble in DMAC. After testing that solution in ABES, an excess of Hexamethylenediamine was added (4:1, Amine: Aldehyde molar ratio) in order to crosslink DAS. A solution of 70% Hexamethylenediamine was also tested as a reference.

2.3.2.2. Reversibility tests. Samples of veneer were pressed using the ABES for 300s at 160°C with the different adhesives formulated. The bonded veneer was then immersed in different solutions. A first batch of bonded veneer was placed in a water solution at pH 7 and a second batch in a solution at pH 4. The shear strength was measured using ABES after 1 hour and 4 hours of immersion. Experiments were done in triplicates.

2.3.3. Characterization

UV-Vis spectra were recorded on a Varian CARY 1E UV – Vis spectrophotometer at 25 ± 1°C. Each measurement was repeated three times. Fourier-transform infrared spectroscopy: Infrared spectrum were recorded using a Fourier-transform infrared spectrophotometer (Spectrum Two, Perkin-Elmer, Llantrisant, UK) equipped with a Universal Attenuated Total Reflectance diamond. Fluorescence spectra were recorded on a HITACHI F-7000 fluorescence spectrophotometer.

All FTIR spectra were collected at a spectrum resolution of 4 cm^{-1}, with 32 scans from 4000 to 500 cm^{-1}. Thermogravimetric analysis: Thermograms were made with a Mettler-Toledo TGA2 (Mettler Toledo, Greifensee, Switzerland), under nitrogen with a flow rate of 40 mL min^{-1}, using alumina pans. 5 to 10 mg of each sample were put in a standard TGA alumina crucible pan and heated from 30°C to 600°C at a heating rate of 10°C min^{-1}.

The changes in glass transition temperature (Tg) of Carbon Dots and Starch were performed using a DSC analyzer (Mettler Toledo DSC3+ equipment, Columbus, USA). The samples were heated from – 30 to 200°C at a heating rate of 30°C min^{-1} followed by a cooling from 200 to – 30°C at – 20°C.min^{-1} under a nitrogen flow of 10 mL·min^{-1}. This cycle was repeated 3 times and only curves corresponding to the 2^{nd} or 3^{rd} heating were analyzed. Approximately 5 mg of priory oven-dried sample (at 50°C for 24 h) was used for each analysis.

The bond strength of the adhesives was evaluated using lab-shear bonds subjected to tensile loading through the ABES technique (Adhesive Bond Evaluation System, Corvalis., USA). This apparatus enables the assessment of strength development characteristics for various adhesive types in shear mode between two thin veneer pieces. It offers a rapid, cost-effective, and immediate method to characterize various bond-influencing parameters notably the curing speed of adhesives. The device consists of a pressing unit associated with a displacement module enabling to cure and test the adhesion on a single device, as shown in Figure 13. Adhesives were applied to a single side of one beech veneer (20×5 mm^2 overlapping area) using spatula to put approximatively around 20 mg of adhesive. The veneers were then hot-pressed under controlled conditions of temperature and time. The temperature was set to 160°C to enable solvent evaporation and avoid reagent evaporation. After curing, the pressure was released, and the bond was immediately subjected to shear testing. Shear strength was recorded at different pressing time. Each condition was tested with 10 replicates.

X-ray Photoelectron spectroscopy (XPS) X-ray photoelectron spectra of CVD graphene samples were recorded on a Quantum 2000 Scanning ESCA instrument) using a monochromatic Al K-Alpha X-ray (1486.7 eV) excitation source.

The morphology of CDs and DAS-CDs was visualized using an Environmental Scanning Electron Microscope (PhilipsXL-30 ESEM, HITACHI, Japan) at 10 KV, with a spot size of 4.3 using the secondary electrons detector for a magnification of 200 and 1000. Before observation, the samples were coated with gold using a sputter coater (Emitech k550X, Quorum Emitech, England).

3. Concluding remarks

We have developed two variants of carbon dots (CDs) with high hydrogen-bonding and covalent-bonding aptitude, suitable for new bio-based adhesive formulations when combined with dialdehyde starch (DAS). Both hydrothermal and microwave-assisted synthetic approaches were successfully employed. Thermal and physicochemical analyses of the CDs indicate high potential for efficient and safe thermomechanical treatment. The ABES study of combined formulations of DAS and CDs revealed significant influences on curing, with CDs assisting in achieving faster curing than DAS alone. Due to the potential of the CDs to act as crosslinkers in the presence of HMDA (an auxiliary crosslinker) at low concentrations, adhesion is enhanced by the imine network and hydrogen bonding offering additional options for adhesive formulations. Furthermore, we demonstrated that these resins can exhibit reversibility induced by an acidic environment, owing to the acidic hydrolysis of imine covalent bonds formed during the curing of the resins, within one hour of treatment.

Disclosure statement

No potential conflict of interest was reported by the author(s).

References

[1] Heinrich, L. A. Future Opportunities for Bio-Based Adhesives – Advantages Beyond Renewability. *Green Chem.* 2019, *21*(8), 1866–1888. DOI: 10.1039/c8gc03746a.

[2] Eisen, A.; Bussa, M.; Röder, H. A Review of Environmental Assessments of Biobased Against Petrochemical Adhesives. *J. Clean. Prod.* 2020, *277*, 124277. DOI: 10.1016/j.jclepro.2020.124277.

[3] Tenorio-Alfonso, A.; Sánchez, M. C.; Franco, J. M. A Review of the Sustainable Approaches in the Production of Bio-Based Polyurethanes and Their Applications in the Adhesive Field. *J. Polym. Environ.* 2020, *28*(3), 749–774. DOI: 10.1007/s10924-020-01659-1.

[4] Gonçalves, D.; Bordado, J. M.; Marques, A. C.; Galhano dos Santos, R. Non-Formaldehyde, Bio-Based Adhesives for Use in Wood-Based Panel Manufacturing Industry—A Review. *Polymers* 2021, *13*(23), 4086. DOI: 10.3390/polym13234086.

[5] Hemmilä, V.; Adamopoulos, S.; Karlsson, O.; Kumar, A. Development of Sustainable Bio-Adhesives for Engineered Wood Panels – a Review. *RSC Adv.* 2017, *7*(61), 38604–38630. DOI: 10.1039/c7ra06598a.

[6] Arias, A.; Feijoo, G.; Moreira, M. T. New Environmental Approach Based on a Combination of Planetary Boundaries and Life Cycle Assessment in the Wood-Based Bioadhesive Market. *ACS Sustainable Chem. Eng.* 2022, *10*(34), 11257–11272. DOI: 10.1021/acssuschemeng.2c03058.

[7] Ciastowicz, Ż.; Pamuła, R.; Białowiec, A. Utilization of Plant Oils for Sustainable Polyurethane Adhesives: A Review. *Materials* 2024, *17*(8), 1738. DOI: 10.3390/ma17081738.

[8] Zhang, S.; Liu, C.; Su, M.; Zhou, D.; Tao, Z.; Wu, S.; Xiao, L.; Li, Y. Development of Citric Acid-Based Biomaterials for Biomedical Applications. *J. Mater. Chem. B* 2024, *12*(45), 11611–11635. DOI: 10.1039/d4tb01666a.

[9] Pooresmaeil, M.; Javanbakht, S.; Namazi, H.; Shaabani, A. Application or Function of Citric Acid in Drug Delivery Platforms. *Med. Res. Rev.* 2021, *42*(2), 800–849. DOI: 10.1002/med.21864.

[10] Kasprzyk, W.; Świergosz, T.; Romańczyk, P. P.; Feldmann, J.; Stolarczyk, J. K. The Role of Molecular Fluorophores in the Photoluminescence of Carbon Dots Derived from Citric Acid: Current State-Of-The-Art and Future Perspectives. *Nanoscale* 2022, *14*(39), 14368–14384. DOI: 10.1039/d2nr03176k.

[11] Chen, S.; Li, X.; Bai, M.; Shi, S. Q.; Aladejana, J. T.; Cao, J. Oyster-Inspired Carbon Dots-Functionalized Silica and Dialdehyde Chitosan to Fabricate a Soy Protein Adhesive with High Strength, Mildew Resistance, and Long-Term Water Resistance. *Carbohydr. Polym.* 2023, *319*, 121093. DOI: 10.1016/j.carbpol.2023.121093.

[12] Yang, P.; Zhu, Z.; Wang, L.; Shen, A.; Tang, M.; Chen, M. Developing Carbon Dots as Green Modifiers for Improving the Bonding Performance of Low-Molar-Ratio Urea-Formaldehyde Resin. *Int. J. Adhes. Adhes.* 2023, *125*, 103416. DOI: 10.1016/j.ijadhadh.2023.103416.

[13] Samanta, S.; Banerjee, S. L.; Bhattacharya, K.; Singha, N. K. Graphene Quantum Dots-Ornamented Waterborne Epoxy-Based Fluorescent Adhesive via Reversible Addition–Fragmentation Chain Transfer-Mediated Miniemulsion Polymerization: A Potential Material for Art Conservation. *ACS Appl. Mater. Interfaces* 2021, *13*(30), 36307–36319. DOI: 10.1021/acsami.1c08812.

[14] Zhang, L.; Wang, W.; Jin, P.; Sun, Z.; Zhan, Y.; Jiang, B. Reactive Carbon Dots/Polysiloxane Composites Cross-Linked Silicone Resin Adhesives for Stable White LED Constructing. *Compos. Commun*. 2025, *53*, 102172. DOI: 10.1016/j.coco.2024.102172.

[15] Aggarwal, M.; Panigrahi, H.; Kotnees, D. K.; Das, P. Multifunctional Self-Healing Carbon Dot–Gelatin Bioadhesive: Improved Tissue Adhesion with Simultaneous Drug Delivery, Optical Tracking, and Photoactivated Sterilization. *Biomacromolecules* 2024, *25*(5), 3178–3189. DOI: 10.1021/acs.biomac.4c00313.

[16] Jelinek, R. *Carbon Quantum Dots: Synthesis, Properties and Applications*; Springer: Cham, 2017.

[17] Ren, J.; Malfatti, L.; Innocenzi, P. Citric Acid Derived Carbon Dots, the Challenge of Understanding the Synthesis-Structure Relationship. *C* 2020, *7*(1), 2. DOI: 10.3390/c7010002.

[18] Xu, D.; Li, C.; Pizzi, A.; Xi, X.; Wang, Z.; Du, G.; Chen, Z.; Lei, H. Self-Neutralizing Citric Acid–Corn Starch Wood Adhesives. *ACS Sustainable Chem. Eng.* 2024, *12*(35), 13382–13391. DOI: 10.1021/acssuschemeng.4c05590.

[19] Schneider, J.; Reckmeier, C. J.; Xiong, Y.; von Seckendorff, M.; Susha, A. S.; Kasák, P.; Rogach, A. L. Molecular Fluorescence in Citric Acid-Based Carbon Dots. *J. Phys. Chem. C* 2017, *121*(3), 2014–2022. DOI: 10.1021/acs.jpcc.6b12519.

[20] Dhenadhayalan, N.; Lin, K.-C.; Suresh, R.; Ramamurthy, P. Unravelling the Multiple Emissive States in Citric-Acid-Derived Carbon Dots. *J. Phys. Chem. C* 2016, *120*(2), 1252–1261. DOI: 10.1021/acs.jpcc.5b08516.

[21] Vallan, L.; Imahori, H. Citric Acid-Based Carbon Dots and Their Application in Energy Conversion. *ACS Appl. Electron. Mater.* 2022, *4*(9), 4231–4257. DOI: 10.1021/acsaelm.2c01021.

[22] Li, H.; Papadakis, R. Fluorescence Imaging Enhanced by Members of the Graphene Family: A Review. *Fluoresc. Imag. Recent Adv. Appl.* 2023. DOI: 10.5772/intechopen.113228.

[23] Meierhofer, F.; Dissinger, F.; Weigert, F.; Jungclaus, J.; Müller-Caspary, K.; Waldvogel, S. R.; Resch-Genger, U.; Voss, T. Citric Acid Based Carbon Dots with Amine Type Stabilizers: pH-Specific Luminescence and Quantum Yield Characteristics. *J. Phys. Chem. C* 2020, *124*(16), 8894–8904. DOI: 10.1021/acs.jpcc.9b11732.

[24] Ye, Y.; Yang, D.; Chen, H.; Guo, S.; Yang, Q.; Chen, L.; Zhao, H.; Wang, L. A High-Efficiency Corrosion Inhibitor of N-Doped Citric Acid-Based Carbon Dots for Mild Steel in Hydrochloric Acid Environment. *J. Hazard. Mater.* 2020, *381*, 121019. DOI: 10.1016/j.jhazmat.2019.121019.

[25] Mohamad Amini, M. A.; Hashim, R.; Sulaiman, N. S.; Mohamed, M.; Sulaiman, O. Citric Acid-Modified Starch as an Environmentally Friendly Binder for Wood Composite Making. *BioRes* 2020, *15*(2), 4234–4248. DOI: 10.15376/biores.15.2.4234-4248.

[26] Gao, F.; Ma, S.; Li, J.; Dai, K.; Xiao, X.; Zhao, D.; Gong, W. Rational Design of High Quality Citric Acid-Derived Carbon Dots by Selecting Efficient Chemical Structure Motifs. *Carbon* 2017, *112*, 131–141. DOI: 10.1016/j.carbon.2016.10.089.

[27] Song, Y.; Zhu, S.; Zhang, S.; Fu, Y.; Wang, L.; Zhao, X.; Yang, B. Investigation from Chemical Structure to Photoluminescent Mechanism: A Type of Carbon Dots from the Pyrolysis of Citric Acid and an Amine. *J. Mater. Chem. C* 2015, *3*(23), 5976–5984. DOI: 10.1039/c5tc00813a.

[28] Boukhvalov, D. W.; Osipov, Y. V.; Murzalinov, D.; Serikkanov, A.; Bi, H. A Comprehensive Model of Carbon Nanodots with 0.21 Nm Lattice Fringes Patterns. *Carbon* 2024, *225*, 119101. DOI: 10.1016/j.carbon.2024.119101.

[29] Neitzel, N.; Hosseinpourpia, R.; Adamopoulos, S. A Dialdehyde Starch-Based Adhesive for Medium-Density Fiberboards. *BioResources* 2023, *18*(1), 2155–2171. DOI: 10.15376/biores.18.1.2155-2171.

[30] Li, H.; Papadakis, R. Click Chemistry Enabling Covalent and Non-Covalent Modifications of Graphene with (Poly)saccharides. *Polymers* 2020, *13*(1), 142. DOI: 10.3390/polym13010142.

[31] Ederer, J.; Janoš, P.; Ecorchard, P.; Tolasz, J.; Štengl, V.; Beneš, H.; Perchacz, M.; Pop-Georgievski, O. Determination of Amino Groups on Functionalized Graphene Oxide for Polyurethane Nanomaterials: XPS Quantitation Vs. Functional Speciation. *RSC Adv.* 2017, *7*(21), 12464–12473. DOI: 10.1039/c6ra28745j.

[32] Lazar, P.; Mach, R.; Otyepka, M. Spectroscopic Fingerprints of Graphitic, Pyrrolic, Pyridinic, and Chemisorbed Nitrogen in N-Doped Graphene. *J. Phys. Chem. C* 2019, *123*(16), 10695–10702. DOI: 10.1021/acs.jpcc.9b02163.

[33] Siddique, A. B.; Hossain, S. M.; Pramanick, A. K.; Ray, M. Excitation Dependence and Independence of Photoluminescence in Carbon Dots and Graphene Quantum Dots: Insights into the Mechanism of Emission. *Nanoscale* 2021, *13*(39), 16662–16671. DOI: 10.1039/d1nr04301c.

[34] Mondal, M.; Pramanik, S. A Mechanism for Excitation-Dependent Emission from Carbon Nanodots. *Mater. Lett. X.* 2023, *18*, 100195. DOI: 10.1016/j.mlblux.2023.100195.

[35] Mintz, K. J.; Bartoli, M.; Rovere, M.; Zhou, Y.; Hettiarachchi, S. D.; Paudyal, S.; Chen, J.; Domena, J. B.; Liyanage, P. Y.; Sampson, R., et al. A Deep Investigation into the Structure of Carbon Dots. *Carbon.* 2021, *173*, 433–447. DOI: 10.1016/j.carbon.2020.11.017.

[36] Letoffe, A.; Hosseinpourpia, R.; Silveira, V.; Adamopoulos, S. Effect of Fenton Reaction Parameters on the Structure and Properties of Oxidized Wheat Starch. *Carbohydr. Res.* 2024, *542*, 109190. DOI: 10.1016/j.carres.2024.109190.

[37] Yong, H.; Liu, J. Recent Advances on the Preparation Conditions, Structural Characteristics, Physicochemical Properties, Functional Properties and Potential Applications of Dialdehyde Starch: A Review. *Int. J. Biol. Macromol.* 2024, *259*, 129261. DOI: 10.1016/j.ijbiomac.2024.129261.

[38] Chaudhary, V.; Panyoyai, N.; Small, D. M.; Shanks, R. A.; Kasapis, S. Effect of the Glass Transition Temperature on Alpha-Amylase Activity in a Starch Matrix. *Carbohydr. Polym.* 2017, *157*, 1531–1537. DOI: 10.1016/j.carbpol.2016.11.028.

[39] Hosseinpourpia, R.; Echart, A.; Adamopoulos, S.; Gabilondo, N.; Eceiza, A. Modification of Pea Starch and Dextrin Polymers with Isocyanate Functional Groups. *Polymers* 2018, *10*(9), 939. DOI: 10.3390/polym10090939.

[40] Ngafwan, N.; Rasyid, H.; Abood, E. S.; Abdelbasset, W. K.; Al-Shawi, S. G.; Bokov, D.; Jalil, A. T. Study on Novel Fluorescent Carbon Nanomaterials in Food Analysis. *Food Sci. Technol.* 2022, *42*, 42. DOI: 10.1590/fst.37821.

[41] Nezhad-Mokhtari, P.; Arsalani, N.; Ghorbani, M.; Hamishehkar, H. Development of Biocompatible Fluorescent Gelatin Nanocarriers for Cell Imaging and Anticancer Drug Targeting. *J. Mater. Sci.* 2018, *53*(15), 10679–10691. DOI: 10.1007/s10853-018-2371-8.

[42] Andreana, I.; Bincoletto, V.; Manzoli, M.; Rodà, F.; Giarraputo, V.; Milla, P.; Arpicco, S.; Stella, B. Freeze Drying of Polymer Nanoparticles and Liposomes Exploiting Different Saccharide-Based Approaches. *Materials* 2023, *16*(3), 1212. DOI: 10.3390/ma16031212.

[43] Wannous, A.; Milaneh, S.; Said, M.; Atassi, Y. New Approach for Starch Dialdehyde Preparation Using Microwave Irradiation for Removal of Heavy Metal Ions from Water. *SN Appl. Sci.* 2022, *4*(5), 4. DOI: 10.1007/s42452-022-05024-w.

[44] Gurr, J.; Barbu, M. C.; Frühwald, A.; Chaowana, P. The Bond Strength Development of Coconut Wood in Relation to Its Density Variations. *J. Adhes.* 2022, *98*(10), 1520–1533. DOI: 10.1080/00218464.2022.2091437.

[45] Zhang, H.; Su, Z.; Wang, X. Starch-Based Rehealable and Degradable Bioplastic Enabled by Dynamic Imine Chemistry. *ACS Sustainable Chem. Eng.* 2022, *10*(26), 8650–8657. DOI: 10.1021/acssuschemeng.2c02537.

Acta Universitatis Agriculturae Sueciae

Doctoral Thesis No. 2025:55

This research investigates polysaccharide-based systems for developing debondable adhesives in wood products. Thermally and pH-responsive networks were incorporated into starch-based adhesives to enable controlled debonding. Upon exposure to specific stimuli, a reduction in shear stress was observed, confirming the adhesives' ability to release bonded wood veneers. These findings represent a first step toward sustainable, debondable adhesive that facilitate the separation and recycling of bonded wood substrates, contributing to more environmentally friendly practices in wood product manufacturing and end-of-life material recovery.

Valentin Silveira received his doctoral education at the Department of Forest Biomaterials and Technology at the Swedish University of Agricultural Sciences in Uppsala. He holds an Engineer degree (MSc) in Chemistry from INP-ENSIACET Toulouse and a Master (MSc) degree in Green Chemistry from Toulouse University in France.

Acta Universitatis Agriculturae Sueciae presents doctoral theses from the Swedish University of Agricultural Sciences (SLU).

SLU generates knowledge for the sustainable use of biological natural resources. Research, education, extension, as well as environmental monitoring and assessment are used to achieve this goal.

ISSN 1652-6880
ISBN (print version) 978-91-8124-039-9
ISBN (electronic version) 978-91-8124-085-6